Universitat Autònoma de Barcelona

Carbon nanotube – inorganic hybrids: from synthesis to application

Laura Cabana Jiménez

DOCTORAL THESIS

Programa de Ciència dels Materials

Director: Dr. Gerard Tobias Rossell

Tutor: Dr. José Peral Pérez

Departament de Química

Facultat de Ciències

Universitat Autònoma de Barcelona

2015

Memòria presentada per aspirar al Grau de Doctor per:

Laura Cabana Jiménez

Vist i plau:

Dr. Gerard Tobias Rossell

Dr. José Peral Pérez

Bellaterra, 8 d'abril de 2015

Institut de Ciència de Materials de Barcelona
Consejo Superior de Investigaciones Científicas
Campus de la UAB
08193 Bellaterra, Barcelona

Acknowledgements

De totes les pàgines que podria omplir, això només és una breu pinzellada del meu profund agraïment cap a totes aquelles persones que poc o molt han deixat la seva empremta en mi i en aquesta tesi.

L'especial menció és per a tu, Gerard, per tot el que he après durant aquests anys i tot el que m'has aportat. No sóc capaç de plasmar com d'agraïda estic per la teva dedicació, bona orientació i recolzament. D'uns quants cafès i trobades casuals a una tesi doctoral, qui ho diria! Per mi és tot un honor ser la teva primera doctoranda.

Aquesta tesi ha estat financiada pel Consejo Superior de Investigaciones Científicas (CSIC) a través del programa de beques predoctorals JAE-Predoc. A més, voldria expressar la meva gratitud vers al Dr. José Peral per acceptar ser-ne el tutor.

Per altra banda, voldria agrair a tothom que ha fet aportació per als resultats d'aquest treball. Em sento molt afortunada d'haver pogut col·laborar amb gent de tots els àmbits i tots amb un alt nivell científic. A la Dra. Judith Oró-Solé i la Dra. Belén Ballesteros, pel treball en microscòpia. A la Dra. Khuloud Al-Jamal, la Dra. Julie T.W. Wang, al Maxime Bourgognon i al Houmam Kafa pels estudis biomèdics. Al Dr. Riccardo Rurali i a l'Eudar Batista pels estudis teòrics. A la Dra. Arantzazu González i la Dra. Rosario Núñez per la seva col·laboració en el treball amb carborans. Al Dr. Gustaaf Van Tendeloo, al Dr. Xiaoxing Ke, al Dr. César Magén i al Dr. Raúl Arenal pels estudis de microscòpia electrònica d'alta resolució. Al Dr. Dejan Kepic per la seva col·laboració en el treball de purificació de nanotubs de carboni. Al Prof. Josep Fontcuberta i la Dra. Anna Roig, per la seva aportació en les mesures de magnetisme. Al Dr. Abel Roige per les mesures d'espectroscòpia Raman. Al Bernat Bozzo per les mesures magnètiques. A la Roberta Ceravola i la Marixa Arnedillo per algunes de les mesures termogravimètriques. A l'Anna Crespi, Joan B. Esquius i el Francisco Javier Campos per les mesures de difracció de raigs X. Al Dr. Ángel Pérez del Pino i la Dra. Eniko Gyorgy, per la seva col·laboració ens els estudis de laser en nanotubs de carboni que, tot i no formar part d'aquesta tesi, han format part important en el període d'elaboració de resultats.

A la gent que forma part de l'ICMAB per la seva ajuda i bons moments, sobretot al Vicente per estar sempre alerta sense deixar de banda el bon humor i els riures.

I would like to kindly thank Dr. Khuloud Al-Jamal and all her group for accepting me during my three month stay at the Institute of Pharmaceutical Sciences, King's College

London. I have learned a lot from you, and your input was essential to get familiar with an area which was completely unknown to me. Thanks to your contribution I can say that this Thesis is an interdisciplinary work.

A partir d'aquí em permetré el luxe de parlar en un to més informal:

Gracias a todo el departamento de Química del Estado Sólido, en especial a mi grupo: "Carbon nanomaterials and inorganic nanostructures". Markus, Magdalena, Adem and Dejan, thanks for all the moments and scientific discussion. Stefania, mi *nanotube mate*, gracias por aguantar mis momentos límite en muchos ámbitos. Ela, no quiero contar cuantas muestras me has analizado, ni cuántos cafés/cervezas nos hemos tomado, pero espero que sean muchos más. Jorge o, mejor, Pérez, nos unió la música y encontré a un cómplice, un compañero para esos 'eventos rarunos' y conocí a dos soles: Elena y Sara.

De toda la gente que me podría haber cruzado en este tiempo, lo hice con la mejor: mi gente ON FIRE, a la que tengo que agradecer mucho y les debo aún más. Jess, yo no te hablaba y tú me has dicho más que nadie, eres mi negrita y mi bella, seguiremos reflexionando juntas. Nerea, alma inquieta como yo, tanto en común que ya somos casi gemelas (no solo por vestir igual), me has hecho de la recta final un simple paseíto. Marixa, mi *indioilo*, mi *polita*, has sido y eres mi mayor apoyo. Lo siento por descargarte mis "sufrimientos". ¡Nina! La *poppy* de Mollet pasó a ser la *chunga* de Mollet por cómo me acogiste desde el día uno, no tengo palabras por lo que has hecho por mí. Ana, nunca pensé que podría tener tanta compenetración con alguien como tú; que bien lo hemos pasado y 'que bien lo vamos a pasar'. Javi (Yabi), largas horas en el despacho con nuestra *music*, nuestras charlas, tantas fiestas, cervezas; eres mi *bigbro*. Jullieth, la meva petita, siempre estás ahí. Angie, tan cerca siempre (da igual donde), tan clara, tan cariñosa, tan… Julio, mi 'illo hipster', quiero ir más a *jisteá* contigo, del *tiri*. Sébastien, el tomàquet, con lo poco que hemos coincidido y lo mucho que hemos vivido. Ana Milena, llegué y te fuiste, pero a la vez te quedaste. El club de escaladores: Ashley: música, escapadas, la vida ¿de qué hablamos hoy mientras nos tomamos un te? y Alex, gracias por tu paciencia infinita, eres un padrazo.

Pero en el ICMAB hay mucha más gente a la que tengo que agradecer muchísimo. Mis *deivids*: Arancha, amiga y ¡colaboradora!, Romén, mi *yogui* siempre con una sonrisa, Marta y Cris (i les nostres converses, algunes censurables, i anades d'olla; us adoro tant!). Regina, des del principi amb mi, fins i tot a hores intempestives, has sigut un suport **fatal**. Maria, '¿dónde has estado todo este tiempo?', me arrastras siempre al lado oscuro, y eso me encanta. Pedro, llegaste tarde, pero lo hiciste bien, nuestros proyectos empiezan ya. Judith i les confessions i els *cotis* al TEM, vals or. Lidia, que bonita eres. Carlos Frontera,

Laura, Ilargi, Kumara, James, Diego, David, Marc, Guillem, mis *gabachis*: Alexis, Kévin, Gweltaz y William. A Roberta, Estela, Jessi *sexymami*, Quique, Mara, Alessandro, Juan Carlos, Muling, Berta, Blai, Justo, Elena, Ana (Feni), Mercedes… y una lista muy larga en la que aún me seguiría dejando gente, pero vosotros ya sabéis quienes sois.

I would like to thank all the people that made my stay in London one of my best memories, but I would like to specially mention the following: Maxime, part of this thesis has your name, you've been an incredible support. I miss our long hours together, our conversations and laughs. Magda, Abhinav and princess Vivi, I don't have enough words for you guys: you're very special to me. Houmam, my peculiar boy, you're an incredible person and someone to admire. Mis chicas del 'brownie club': Noelia y Raquel. Silvia, eres el mejor ejemplo de: calidad mejor que cantidad. Atiha, you're the best host. Y a la 'best roommate': Bea, eres fantástica, que no se te olvide nunca.

Pero mi vida no es solo el ICMAB y hay mucha gente que ha participado indirectamente en esta tesis. Mis amigas de siempre, les *Moquitos*: Alba (toda una vida juntas, sin importar la distancia), Núria, Anna, Muriel, Aida i Consu. Mis químicos, en especial: Mireia (y nuestras escapadas de *tupper* y *brunch*), Jose, las dos Crises, Arantxa (mi *proto*) e Isaac. Gente que se ha ido cruzando en mi camino de diferentes maneras: Rosa (no sé cómo habría escrito esta tesis sin tu compañía en 'les Aigües'), Marina, Sara, Matilde, Antonio… Mis Ribes's angels: Kasia, Montse, Laura y Beattie. Y sobre todo mi 'familia festivalera': Marta (¡mi querida cousin!), David, Xavi, Óscar y Mónica. También son una parte importante de todo en mi vida mis dos familias: el clan Cabana y los valientes Jiménez.

He dejado lo más importante para el final, vosotros os merecéis un espacio especial. Ni con todas las palabras del mundo podría describir lo que siento por vosotros y lo agradecida que estoy. Lucía y Elena, mis dos *peques*, que injusta es esta vida que no os puedo abrazar cada vez que me apetece y no os puedo ver crecer. Christina, eres una luchadora. Papa y mama, os debo mi vida. Sois el ejemplo del buen hacer y del sacrificio, quiero que llevéis la cabeza bien alta, pero no por vuestros dos hijos, sino por vosotros. Me siento la hija más afortunada del mundo. Y para acabar, agradecerte a ti Jordi, *broda*. Eres mi mentor en todos los sentidos. Con ser la mitad que tú, y no hablo solo de altura ni de ciencia, ya me doy más que por satisfecha. GRACIAS.

Abstract

This Thesis reports on the preparation of various carbon nanotube–inorganic hybrids for different applications, ranging from electronics to biomedicine. The purpose of the investigation has been to work on the functionalization of carbon nanotubes by both external decoration and endohedral filling with inorganic materials to obtain hybrids with functional properties.

Prior to the functionalization, a purification step must be conducted to remove undesired side products from the synthesis of CNTs. In this Thesis, a purification method using steam, a mild oxidizing agent, is proposed for multi-walled carbon nanotubes. We have investigated the effect of the steam treatment time on the degree of purification and shortening of the carbon nanotubes. Steam purification results in samples open-ended, high-quality nanotubes, which length can be easily modulated.

Once carbon nanotubes have been purified, we have prepared different types of hybrids by incorporating the material on the walls of the carbon nanotubes. We have externally decorated carbon nanotubes with superparamagnetic iron oxide nanoparticles by an *in situ* method. A dual imaging *in vivo* agent for both magnetic resonance and nuclear imaging has been achieved after labelling the nanoparticles with ^{99m}Tc. Moreover, it has been revealed that shorter carbon nanotubes enhance the magnetic properties of the hybrid, obtaining higher relaxivity values. On the other hand, we have covalently attached metallacarborane clusters on the walls of single walled carbon nanotubes to form a hybrid with high ^{10}B content that will be appropriate for boron neutron capture therapy. Different synthetic routes have been studied. The dispersibility of the resulting hybrid was higher than that of oxidized single-walled carbon nanotubes, and therefore the hybrid is a potential candidate for biomedical applications.

Finally, we have investigated the filling of multi-walled carbon nanotubes with a van der Waals solid by molten phase capillary wetting. We have reported on the formation of single-layered inorganic nanotubes inside carbon nanotubes for the first time. We have also investigated the dynamic transformation of the encaged nanomaterials under electron beam irradiation. Moreover the intrinsic stability of the single-layered inorganic nanotube has been demonstrated using density function theory.

The results presented within this Thesis further expand the capabilities of carbon nanotube–inorganic hybrids.

Resum

Aquesta Tesi descriu la preparació de varis híbrids formats per nanotubs de carboni i material inorgànic per a diferents aplicacions, que van des de l'electrònica fins a la biomedicina. El propòsit d'aquesta recerca ha estat treballar en la funcionalització de nanotubs de carboni mitjançant la decoració externa i l'emplenat amb materials inorgànics per obtenir híbrids amb propietats funcionals.

Com a pas previ a la funcionalització, els nanotubs de carboni s'han de purificar per a eliminar les impureses no desitjades. En aquesta Tesi, hem proposat un mètode de purificació per a nanotubs de carboni multicapa consistent en l'ús servir vapor d'aigua, que és un agent oxidant lleu. Hem investigat l'efecte del temps de tractament amb vapor d'aigua en el grau de purificació i escurçament dels nanotubs de carboni. Hem vist que la purificació amb vapor d'aigua genera mostres de nanotubs de carboni d'alta qualitat i amb les puntes obertes. A més, hem apreciat que la seva llargada pot ser modulada fàcilment.

Un cop purificats els nanotubs de carboni, hem preparat diferents tipus d'híbrids mitjançant la incorporació del material a les seves parets. Hem procedit a la decoració externa dels nanotubs de carboni amb nanopartícules d'òxid de ferro superparamagnètiques a través d'un mètode dut a terme *in situ*. S'ha aconseguit obtenir un agent de contrast dual tant per ressonància magnètica com per imatge nuclear a través del etiquetat de les nanopartícules amb ^{99m}Tc. A més, s'ha mostrat que l'ús de nanotubs de carboni més curts milloren les propietats magnètiques de l'híbrid, obtenint així valors de relaxivitat més elevats. D'altra banda, hem incorporat de manera covalent clústers de metalacarborans a les parets de nanotubs de carboni monocapa, formant un híbrid amb alt contingut de ^{10}B, que serà apropiat per la teràpia per captura neutrònica de bor. Diferents rutes sintètiques han estat investigades. La dispersabilitat de l'híbrid resultant ha estat més alta que en el cas dels nanotubs de carboni monocapa oxidats i, per tant, l'híbrid és un candidat potencial per a aplicacions biomèdiques.

Finalment, hem investigat l'emplenat de nanotubs de carboni multicapa amb un sòlid van der Waals per capil·laritat del material en la seva fase fosa. Hem reportat per primer cop la formació de nanotubs monocapa inorgànics dins dels nanotubs de carboni. Així mateix, hem investigat la transformació dinàmica dels nanomaterials encapsulats sota la irradiació amb un feix d'electrons. També hem demostrat, utilitzant la teoria de la funció de densitat, que els nanotubs monocapa inorgànics són estables.

Els resultats presentats en el marc d'aquesta Tesi expandeixen la capacitat dels híbrids formats per nanotubs de carboni i material inorgànic.

Resumen

Esta Tesis describe la preparación de varios híbridos formados por nanotubos de carbono y material inorgánico para diferentes aplicaciones, que van desde la electrónica hasta la biomedicina. El propósito de esta investigación ha sido trabajar en la funcionalización de nanotubos de carbono mediante la decoración externa y el llenado con nanotubos inorgánicos para obtener híbridos con propiedades funcionales.

Como paso previo a la funcionalización, los nanotubos de carbono se tienen que purificar para eliminar las impurezas no deseadas. En esta Tesis, hemos propuesto un método de purificación para nanotubos de carbono multicapa consistente en el uso vapor de agua, que es un oxidante leve. Hemos investigado el efecto del tiempo de tratamiento con vapor de agua en el grado de purificación y acortamiento de los nanotubos de carbono. Hemos visto que la purificación con vapor de agua genera muestras de nanotubos de carbono de alta calidad y con puntas abiertas. Además, hemos apreciado que su longitud puede ser modulada fácilmente.

Una vez que se han purificado los nanotubos de carbono, hemos preparado diferentes tipos de híbridos mediante la incorporación del material en sus paredes. Hemos procedido a la decoración externa de los nanotubos de carbono con nanopartículas de óxido de hierro superparamagnéticas a través de un método *in situ*. Se ha conseguido obtener un agente de contraste dual tanto para resonancia magnética como para imagen nuclear a través del etiquetado de las nanopartículas con ^{99m}Tc. Además, se ha mostrado que el uso de nanotubos de carbono más cortos mejoran las propiedades magnéticas del híbrido, obteniendo así valores de relajatividad más elevados. Por otro lado, hemos incorporado de manera covalente clústers de metalacarboranos en las paredes de nanotubos de carbono monocapa, formando un híbrido de alto contenido de ^{10}B, que será apropiado para la terapia por captura neutrónica de boro. Diferentes rutas sintéticas han sido investigadas. La dispersabilidad del híbrido resultante ha sido más alta que en el caso de nanotubos de carbono monocapa oxidados y, por lo tanto, el híbrido es un candidato potencial para aplicaciones biomédicas.

Finalmente, hemos investigado el llenado de nanotubos de carbono multicapa con un sólido van der Waals por capilaridad del material en su fase fundida. Hemos reportado por primera vez la formación de nanotubos inorgánicos monocapa dentro de los nanotubos de carbono. Asimismo, hemos investigado la transformación dinámica de los nanomateriales encapsulados bajo la radiación de un haz de electrones. También hemos

demostrado, usando la teoría de la función de densidad, que los nanotubos monocapa inorgánicos son estables.

Los resultados presentados en el marco de esta Tesis expanden la capacidad de los híbridos formados por nanotubos de carbono y material inorgánico.

Manuscript organization

According to the current regulations and prior acceptance by the PhD commission at Universitat Autònoma de Barcelona (UAB), this thesis is presented as a compendium of papers. These papers were published and presented to the PhD commission of UAB on March 2015. With the purpose of having a more completed report of the work conducted during the doctoral Thesis, submitted and under review articles, as well as papers in preparation are included as annexes. The studies included in the report are:

Article 1: *The role of steam treatment on the structure, purity and length distribution of multi-walled carbon nanotubes*. Laura Cabana, Dejan Kepic, Xiaoxing Ke, Judith Oro-Solé, Gustaaf Van Tendeloo, Gerard Tobias. *Under Review*

Article 2: *Magnetically decorated multiwalled carbon nanotubes as dual MRI and SPECT contrast agents*. Julie Tzu-Wen Wang,* Laura Cabana,* Maxime Bourgognon, Houmam Kafa, Andrea Protti, Kerrie Venner, Ajay M. Shah, Jane Sosabowski, Stephen J. Mather, Anna Roig, Xiaoxing Ke, Gustaag Van Tendeloo, Rafael T.M de Rosales, Gerard Tobias, Khuloud Al-Jamal. *Advanced Functional Materials*. **2014**. 24, 13, 1880-1894. *Equal contribution.

Article 3: *The Shortening of MWNT-SPION Hybrids by Steam Treatment Improves their Magnetic Resonance Imaging Properties In vitro and In Vivo*. Laura Cabana, Maxime Bourgognon, Julie Tzu-Wen. Wang, Andrea Protti, Rafael T. M. de Rosales, Ajay M. Shah, Josep Fontcuberta, Jane K. Sosabowski, Khuloud T. Al-Jamal, Gerard Tobias. *Submitted*.

Article 4: *Localized Metallacarboranes on Single-Wall Carbon Nanotubes for Boron Carriers*. Laura Cabana, Arantzazu Gonzalez-Campo, Xiaoxing Ke, Gustaaf Van Tendeloo, Rosario Núñez, Gerard Tobias. *In preparation*.

Article 5: *Synthesis of PbI_2 Single-layered inorganic nanotubes encapsulated within carbon nanotubes*. Laura Cabana, Belén Ballesteros, Eudar Batista, César Magén, Raúl Arenal, Judith Oró-Solé, Riccardo Rurali, Gerard Tobias. *Advanced Materials*. **2014**. 26, 13, 2016-2021.

In addition to the papers that have resulted in the present work, other papers have been published in parallel to the studies reported in this Thesis:

- *Deposition of functionalized single wall carbon nanotubes through matrix assisted pulsed laser evaporation*. Angel Pérez del Pino, Eniko György, Laura Cabana, Belén Ballesteros, Gerard Tobias. *Carbon*. **2012**. 50, 12, 4450-4458.

- *Effect of laser radiation on multi-wall carbon nanotubes: study of shell structure and immobilization process*. Eniko György, Angel Pérez del Pino, Jaume Roqueta, Belén Ballesteros, Laura Cabana, Gerard Tobias. *Journal of Nanoparticle Research*. **2013**. 15, 1852-1862.
- *Ultraviolet pulsed laser irradiation of multi-walled carbon nanotubes in nitrogen atmosphere*. Angel Pérez del Pino, Eniko György, Laura Cabana, Belén Ballesteros, Gerard Tobias. *Journal of applied physics*. **2014**. 115, 9, 093501.
- *IrO_x-carbon nanotube hybrids: A nanostructured material for electrodes with increased charge capacity in neural systems*. Nina M. Carretero, Mathieu P. Lichtenstein, Estela Pérez, Laura Cabana, Cristina Suñol, Nieves Casañ-Pastor. *Acta Biomaterialia*. **2014**. 10, 10, 4548-4558.

Table of contents **page**

Chapter 7. Published articles

Annex I. Submitted or under review articles

List of symbols abbreviations and acronyms

1D	One dimensional
2D	Two dimensional
BNCT	Boron neutron capture therapy
BP	Biphosphonate
BSA	Bovine serum albuminum
C_h	Chiral vector
CNT	Carbon nanotube
CVD	Chemical vapour deposition
CT	Computed tomography
DC	Direct current
DCC/HOBt	Dicylohexylcarbodiimide/hydroxibenzotriazole
DFT	Density function theory
DMSO	Dimethyl sulfoxide
DPA-ale	Dipicolylamine-alendronate
dsDNA	double stranded DNA
DTAB	dodecyltrimethylammoniumbromide
E_a	Magnetic anisotropy energy
EA	Elemental analysis
f-CNTs	Functionalized carbon nanotubes
FTIR	Fourier transform infrared spectroscopy
γ-Fe_2O_3	Maghemite
Fe_3O_4	Magnetite
FET	Field effect transistor
FFT	Fourier transform

HIV	Human immunodeficiency virus
HRTEM	High resolution transmission electron microscopy
ITO	Indium Tin Oxide
I.V.	intravenous
K_a	anisotropy constant
LDH	Lactate dehydrogenase
MR	Magnetic resonance
MRI	Magnetic resonance imaging
M_s	Saturation magnetization
MWCNT	Multi walled carbon nanotube
NIR	Near infrared
OLED	Organic light-emitting diode
PET	Positron emission tomography
r_1^*	Longitudinal relaxivity
r_2^*	Transversal relaxivity
R_1^*	Longitudinal relaxation rate
R_2^*	Transversal relaxation rate
RBM	Radial breathing mode
SDS	Sodium dodecyl sulphate
SPECT	Single photoemission computed tomography
SPION	Superparamagnetic iron oxide nanoparticle
SQUID	Superconducting quantum interference device
ssDNA	single stranded DNA
STEM	Scanning transmission electron microscopy
SWCNT	Single walled carbon nanotube
T_1	Longitudinal relaxation time

T_2	Transversal relaxation time
T_B	Blocking temperature
TEM	Transmission electron microscopy
TGA	Thermogravimetric analysis
TFT	Thin film transistor
XPS	X-ray photoelectron spectroscopy
XRD	X-ray diffraction
UV-Vis	Ultraviolet-visible
V	Volume
η	Chiral angle
$[3,3'\text{-}Co(C_2B_9H_{11})_2]^-$	cosane

1

Introduction

This chapter introduces the structure of carbon nanotubes, their properties and potential applications. In addition, different strategies for their purification and sidewall and endohedral functionalization are presented.

1.1. General aspects of carbon nanotubes

Nanomaterials provide new challenges for scientists. The nanotechnology field is being increasingly studied in the recent years, as many of the properties and applications of nanomaterials are yet to be discovered.[1]

When decreasing particle size, the surface area of the material is considerably increased, thus meaning that a larger amount of substance becomes in contact with the surrounding materials.[2] Moreover, quantum effects are observed at the nanoscale, as electrons are confined in a reduced volume and the behaviour of the material is ruled by quantum mechanics.[3] Hence, if the particle size is scaled down to nanometer dimensions, the chemical and physical properties of materials can be extremely modified with respect to their bulk structure. Nanotechnology is a promising field that is present in many different areas such as biotechnology, optics, photonics and storage technologies, among others.[4]

One of the nanomaterials that has defined the research field of nanotechnology are carbon nanotubes (CNTs). Since the report by Iijima in 1991,[5] there has been an explosion of interest in these type of nanomaterials.

Carbon nanotubes are quasi-one-dimensional structures that can be described as one or various rolled-up graphite layers, forming seamless cylinders. They are an allotropic form of carbon, together with diamond and graphite. The structure of a graphite layer consists on sp^2 hybridized carbon atoms in a hexagonal network with in-plane σ bonds and out of plane π orbitals.[6] Depending on the number of layers, either Single-Walled Carbon Nanotubes (SWCNTs) or Multi-Walled Carbon Nanotubes (MWCNTs) are formed (**Figure 1.1.**). Its diameter ranges from about one nanometer to tens of nanometers and its length range from less than 100 nm to several centimeters. Diameters of SWCNTs are typically between 0.8 to 2 nm, whereas MWCNTs have diameters typically of 5 to 100 nm. In the case of the MWCNTs the interlayer distance is 0.34 nm, which corresponds to that of graphite.[7] As a consequence of the increase in the number of carbon atoms when going to outer cylinders, there is no possibility to maintain the ABAB… stacking as in graphite. Depending on the technique used for its preparation, CNTs can be open-ended or closed by a hemispherical fullerene-like cap.

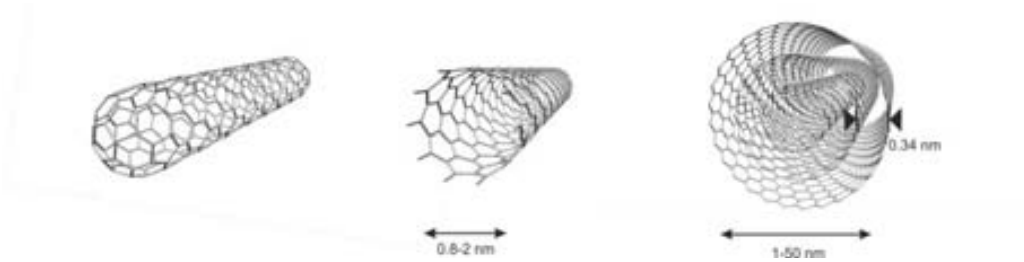

Figure 1.1. A schematic illustration of carbon nanotubes. A closed SWCNT with a hemispherical fullerene-type cap (left), an open-ended SWCNT (middle) and a MWCNT (right) are represented.

The classification of CNTs and their properties vary depending on the wrapping direction of the graphene sheet (**Figure 1.2.**).[7] The simplest way of specifying the structure of an individual tube is in terms of the chiral vector $C_{h,}$ that joins two equivalent points on the original graphene sheet, and the chiral angle η, defined as the angle the chiral vector forms with the abscissa. The vector C_h can be expressed as:

$$C_h = na + mb$$

where a and b are unit cell base vectors of the graphene sheet and each (n,m) integer represents a possible tube structure.

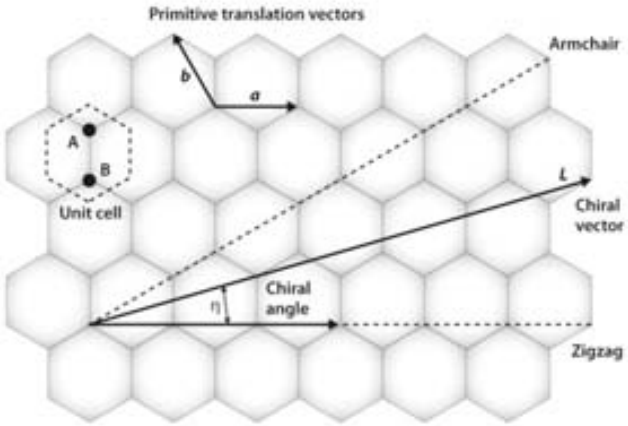

Figure 1.2. A 2D graphene sheet showing the unit cell, containing two carbon atoms (A,B), the chiral vector C_h (represented as L) the chiral angle η.[8]

The tube is formed by connecting the two points of the C_h and, therefore, the n, m units define the way in which the graphene sheet is rolled up to form a CNT, There are two possible high-simmetry structures known as 'zigzag', when n = 0 and m ≠ 0, and 'armchair', when n = m ≠ 0. Both of these structures are non-chiral.[9] If the n and m integers are different, then the CNT is chiral (**Figure 1.3.**).

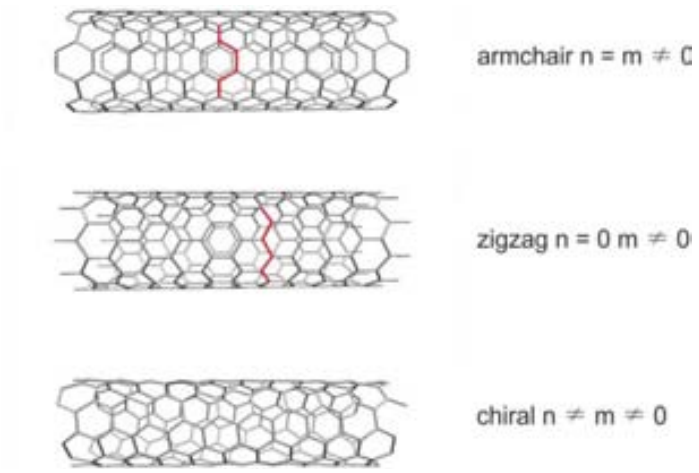

Figure 1.3. Different CNT structures. An armchair (6,6) SWCNT is shown at the top, a zigzag (10,0) in the middle and a chiral (6,4) at the bottom.

1.1.1. CNT synthesis

There are different techniques for the production of CNTs. The main and most commonly employed methods are arc discharge, laser ablation and chemical vapour deposition (CVD). Each technique has its peculiarities and the carbon nanotubes obtained differ between them. **Table 1.1.** contains a summary of all the different synthesis.

The CVD technique produces both SWCNTs and MWCNTs and employs a carbon source in the gas phase (usually methane, ethane, carbon monoxide or acetylene). The gas goes through a plasma or a resistively heated coil, which transfers the energy to the carbon molecule, cracking it into atomic carbon. Then the carbon diffuses towards the substrate. This substrate is coated with a catalyst (Ni, Fe or Co), and carbon is bound into it as the CNTs are formed on the metal catalyst. Depending on the nature of the catalyst and its size we can control the formation of SWCNT or MWCNT, their diameter, wall thickness, morphology and microstructure.[10, 11]

Arc discharge also allows the synthesis of both MWCNTs and SWCNTs.[12, 13] A direct current (DC; ~150 A/cm^2) with a voltage at ~20 V is applied across two graphite electrodes immersed in an inert gas such as He. The nanotubes are deposited as soot inside the chamber in the case of SWCNTs and formed on the negative electrode in the case of MWCNTs. In the case of SWCNTs a graphite anode containing a metal catalyst (Ni, Y) is used.[14]

Another way to synthesize CNTs, most commonly SWCNTs is the laser ablation.[15, 16] Here, a high power laser vaporizes carbon from a graphite target at high temperature

(~1200ºC). Under argon atmosphere the carbon target contains catalytic metal particles.[17] The argon carries the vapours generated from the high temperature chamber into a cooled chamber. When condensed, CNTs self-assemble on the walls of the flow tube.

Table 1.1. Summary of the more common CNT synthesis techniques. Adapted from Eder.[19]

synthesis technique	description	product	advantages	disadvantages	improvements
DC arc discharge	1991: Iijima[5] 1992: Ebbesen and Ajayan[14]	MWCNTs and SWCNTs (with catalyst)	easy design, few structural defects	short tubes and low yield, low purity, random diameters	magnetic field, rotating electrode, liquid N_2
laser ablation	1995: Smalley[15]	primarily SWCNTs	few defects, good control over diameter	most costly method, poor scalability, requires Class 4 lasers	ultrafast electron laser
chemical vapor deposition	1998: Endo[18]	both types	high yields, easy scalability, long tubes, alignment and pattern growth	some defects, medium purity	plasma enhanced, aerosol process, laser assisted, CoMoCat, HiPCo,

1.1.2. Physical properties of CNTs

CNT are being significantly studied mainly due to their exceptional properties. Its tubular structure entails a large surface area with structural integrity. Because of the low atomic weight of carbon CNTs have very low density and their high aspect ratio makes them very flexible.[20]

The attractive mechanical properties of the CNTs have its origin on the strong C=C double bonds.[21] This converts nanotubes in the stiffest and strongest fibers ever produced. If CNTs have no defects Young modulus that can reach values of 1.4 TPa in the axial direction of SWCNTs.[22, 23] The combination of an elongation-to-failure of 20-30 % along with their stiffness, confess them with tensile strength values above 100 GPa.[24] Yet, these are based on theoretical predictions, and experimental results have stated lower values.[25] The reason for the deviations in the experimental and theoretical values resides on the experimental method itself and the nature of CNTs, CNTs being nanosized materials, difficult their manipulation and measurement. On the other hand, the presence of defects on the wall of the CNTs also influence in the discrepancies with the theoretical calculations.[26]

The electronic properties of CNTs are determined by the wrapping direction of the graphene.[27] If the n and m index are equivalent the nanotubes will be metallic, whereas if $|n - m| = 3q$ those will be small band gap semiconductors. The rest of CNT will be moderate semiconductors, with a band gap depending on their diameter. In addition, the one dimensional (1D) size results in the removal of the electron collisions, being CNT ballistic conductors. Ballistic transport occurs when electrons pass along a conductor without experiencing any scattering from impurities or phonons. In other words, carbon nanotubes can conduct a large current without energy dissipation.[28]

Regarding the optical properties of CNTs, SWCNTs have been reported to be fluorescent.[29] A series of emission peaks can be observed in the near infrared spectroscopy, corresponding to the fluorescence across the band gap of semiconducting nanotubes. The fluorescence values depend on the nanotube structure. Raman spectroscopy is widely employed to study the CNT structure.[30-33] A Raman spectrum contains several characteristic peaks for CNTs (**Figure 1.4.**).

1- The region below 400 cm^{-1} is referred to as radial breathing modes (RBM). The peaks present in the RBM region provide information of the nanotube diameter (in SWCNTs).[34]
2- D-band at around 1340 cm^{-1}, corresponding to C sp^3, or disordered graphitic material. This band is commonly employed to assess the degree of defects and of impurities in the CNT sample.
3- A tangential mode vibration at 1550-1600 cm^{-1}, G-band, that arises from the C sp^2 of the CNT structure.
4- Second order harmonic of the D mode, known as 2D or G′ at 2600 cm^{-1}.

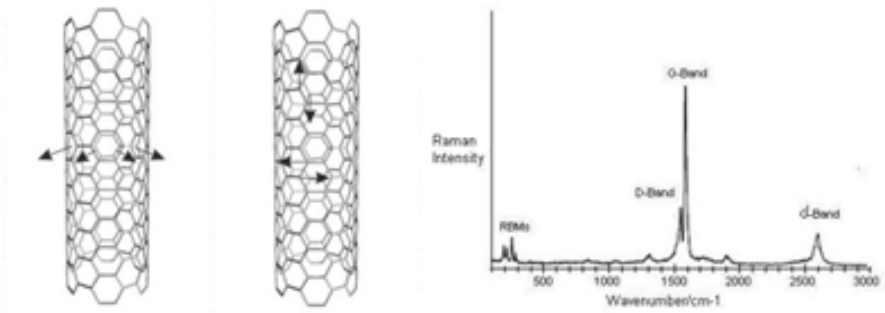

Figure 1.4. a) Scheme of the atomic displacements of the RBM (left) and the G-band (right) vibrations. b) Typical Raman spectrum of SWCNTs. Image from "Carbon Nanotubes" by A.R. Barron and D.J. Flood, licensed under CC BY 3.0.

The thermal properties of CNTs are also to be highlighted. CNTs transmit nearly twice as much heat as isotopically pure diamond. While pure diamond has a thermal conductivity of 2000-2500 $W{\cdot}m^{-1}{\cdot}K^{-1}$, theoretical calculations predicted room temperature thermal conductivities of individual SWCNTs of up to 6600 $W{\cdot}m^{-1}{\cdot}K^{-1}$.[35] Albeit, the highest experimental values obtained for individual MWCNTs up to date are 3000 $W{\cdot}m^{-1}{\cdot}K^{-1}$.[36]

Taking into account all the remarkable properties that a simple material combines, it is of no surprise that carbon nanotubes are being widely studied for many different applications. CNTs are promising materials for various scientific and technological and

biological areas. The next section will summarize some of the most outstanding applications that are already implemented or under development.

1.2. Applications of carbon nanotubes

As discussed in the previous section, CNTs have unique electronic, mechanic, optical and thermal properties that make them suitable for a wide range of applications. CNTs are promising nanomaterials for areas such as energy, information, aerospace and biomedicine. However, this is just the tip of the iceberg of the possibilities that these materials hold, and, though they are already being commercialized, there is still more to be discovered (**Figure 1.5.**).

Most CNT production at the industrial level is nowadays in bulk composite materials and thin films, taking advantage of the mechanical properties of CNTs. CVD is the most commonly employed technique when it comes to large scale production of CNTs. The CVD synthesis of SWCNTs requires much control than MWCNTs, and therefore bulk SWCNT prices are higher than their multiwalled counterparts. MWCNTs are thus more convenient for applications in which the diameter or the band gap values are not crucial. Among the composite materials that are employed, disordered MWCNT-polymer composites are of interest, as they can reach conductivities of 10.000 $S \cdot m^{-1}$.[37] The presence of MWCNTs also increases the stiffness, strength and toughness without affecting other mechanical properties of the polymer.[38] Some specific applications of these composites are in turbine blades and hulls for security boats.[39] CNT composites can also be employed as a multifunctional coating material as an alternative to other paints, especially in the maritime area, as CNTs are anticorrosive.[40] Also CNT yarns are fabricated for weight-sensitive applications where electrical and mechanical features are important.[41] These yarns can be knotted without losing strength, and even superconducting wires can be prepared.[42]

The electronic properties of CNTs are attractive in microelectronic applications. Their low electron scattering and a variable band gap depending on the nanotubes diameter and chirality make them suitable for transistors.[43] For instance, SWCNT are compatible for field effect transistors (FET). It has been shown that CNT arrays can increase output current and improve device uniformity and reproducibility. Also CNT thin film transistors (TFT) can be satisfactorily employed for driving organic light-emitting diode (OLED) displays; CNT have revealed higher mobility than amorphous silicon.[44]

In the field of energy storage and conversion, MWCNTs are being employed in lithium ion batteries for computers and mobile phones.[45] For this application, MWCNTs are mixed with active materials and a polymer binder, increasing the electrical connectivity and mechanical integrity, which in turn enhance the cyclability and rate capability. In addition, supercapacitors deploying forest-grown SWCNTs have exhibited impressive performance, with an energy density of 10 kW kg^{-1} and a power density of 10 kW kg^{-1}.[46] This is is of interest for applications in photovoltaics which could incorporate SWCNT transparent electrodes in the near future. A great effort is also being made to develop CNT-based transparent conductive films as an alternative to indium tin oxide (ITO).[47]

In the environmental area, CNTs can be for instance used in water purification. CNTs provide mechanically and electrochemically robust networks with porosity in the nanoscale range.[48] Moreover, CNTs allow flow through its structure, enabling lower energy cost for water desalination.[49]

A wide range of sensors are being developed with CNTs, SWCNT biosensors are based on a change in the electrical impedance or the optical properties of the sensor in the presence of a given payload.[50, 51] For instance, they can be used to detect microarrays for DNA and proteins, as well as gas and toxin detection of interest in the food industry among others.

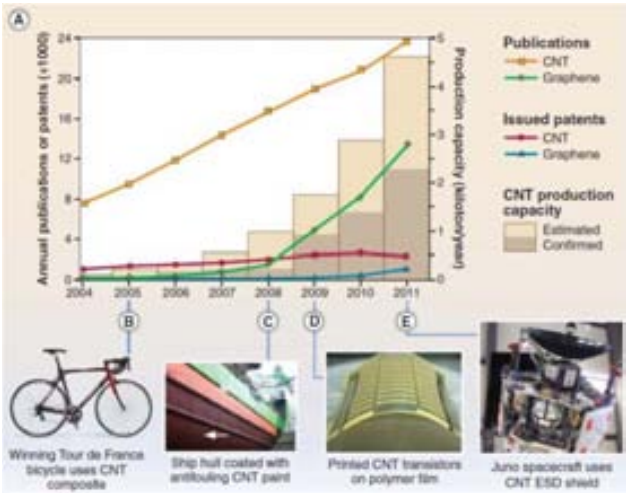

Figure 1.5. Trends in CNT research and commercialization. a) Journal publications and issued worldwide patents per year, along with estimated annual production capacity. b-e) Selected CNT related products: composite bicycle frame, antifouling coatings, printed electronics and electrostatic discharge shielding.[52]

One of the possible applications of the prepared carbon nanotubes-inorganic hybrids of this Thesis is the biomedical application. Therefore, further detail of this area of application is detailed in the following section.

1.2.1. Biomedical applications of carbon nanotubes

One of the major areas of research with CNTs is in the biomedical field. For instance, CNTs can be employed for biosensors.[53, 54] With sensors based on CNTs it is possible to achieve a large area to volume ratio thus increasing the interactions with the biomolecules of interest. Moreover, their electronic structure and ballistic conductivity allow a straightforward biosensing. In addition, the self-assembly possibilities of CNTs offer alternative routes for the construction of nanoscale devices.[55]

As previously mentioned, CNTs can be used as nanofillers of polymeric materials to create nanocomposites with improved mechanical properties.[56] This is also of interest in the biomedical field for tissue engineering. The use of CNT composites allows a controlled electrical stimulation.[57]

The diversity of chemistry that can be applied to CNTs and its cell-penetrating structure [58, 59] makes CNTs appropriate as carriers for the delivery of drugs, DNA, proteins, and other molecules.

1.2.1.1. Biocompatibility and toxicity of CNTs

When it comes to the *in vivo* application of CNTs it is imperative to rigorously investigate the toxicity and biocompatibility of these nanomaterials. Biocompatibility of a material implies an absence of inflammatory response, absence of deposition of the material in the body, absence of intoxication from possible metabolities and absence of adverse reactions such as apoptosis or necrosis when interacting with the biological medium both *in vivo* or *in vitro*.[60] Hence, it is compulsory to assure the health and safety of CNT exposure before the use of CNT-based materials becomes widespread.

First studies reported on the toxicity of as-made CNTs. CNTs were accelerating oxidative stress, loss of cell viability and morphological alterations to cellular structure. However, these initial studies were performed with as-produced, non-purified material, and the observed toxicity was likely due to the presence of metal catalyst nanoparticles, as well as the extreme length of the CNTs.[61-63] There is experimental evidence that shows that long and rigid CNTs should be avoided for *in vivo* applications (>15 μm). Despite there are contradictory reports with respect to CNT toxicity, and pharmacological studies are still in progress, there is agreement within the scientific community that the use of short and purified CNTs with biocompatible functionalization are essential to render CNTs biocompatible, eliminating any potential cytotoxicity.[64, 65]

One of the main issues that affect CNT toxicity and biocompatibility is the tendency of CNTs to aggregate and form bundles. This is due to the strong π-π intertubular interactions that results in the formation of bundles.[66] Consequently, the majority of the discrepancies in toxicity and biocompatibility reports have its origin on the different degree of CNT dispersion. Asbestos-like pathogenicity of long CNTs can be alleviated through the chemical functionalization.[62] This is a consequence of an improvement on the water dispersibility of the CNT by conducting a functionalization. There are several routes for the outer sidewall functionalization, which are described in section 1.4.

Biomedical imaging and drug delivery is a promising field for CNTs as long as purification, shortening and a good dispersion is achieved to render the CNTs biocompatible.

1.2.1.2. Applications of CNTs as molecular nanocarriers

The needle-like shape of CNTs enables them to have good flow dynamics and enhanced capacity to penetrate cellular membranes, making them especially suitable for biomedical imaging and drug delivery.

The intrinsic physical properties of CNTs, namely resonance Raman scattering, photoluminescence and strong NIR optical absorption already serve as good proves for biological tracking, detection and imaging. In addition, CNT can be functionalized with different agents, such as drugs for therapeutic applications, contrast agents for imaging purposes and targeting agents.[67] Moreover, CNTs have also empty hollow cavities that can be employed for encapsulation of a chosen payload. In this case, the external walls remain available for functionalization with selected moieties thus increasing their dispersibility and biocompatibility. If the external walls are functionalized with specific targeting agents, that target specific diseased cells, we move an step closer towards the development of smart drug delivery agent (**Figure 1.6.**).[68] Antibodies, folic acid and peptides are commonly employed to target and deliver the cargo to a chosen type of cell.[69] The inner cavity acts then as a nanovehicle avoiding the degradation of the cargo, preventing its interaction with the biological medium.

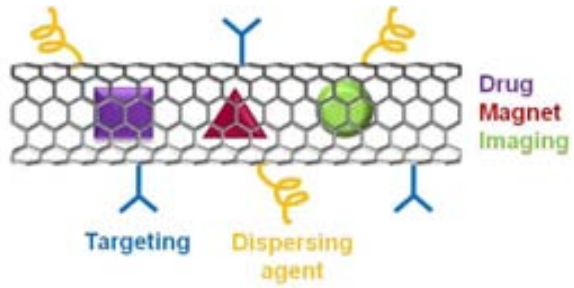

Figure 1.6. Schematic representation of the different agents that can be employed to modify carbon nanotubes, either by endohedral filling or external decoration.[70]

- **Drug delivery**: Drug delivery systems are materials designed to improve the pharmacological and therapeutic profile of a drug molecule. CNTs are a new emerging class of delivery systems for the transport and translocation of drug molecules through various mammalian cells.[71] CNTs with multiple functionalization with various moieties are being designed for the delivery of more than one therapeutic agents with recognition capacity.[72] As an example, the first study with CNTs for in vivo cancer treatment was described by Zhang et al. where positively charged SWCNTs were used to deliver therapeutic siRNA into cancer cells.[73]
- **Therapy**: Apart from drug delivery purposes, CNTs are suitable tools for other therapeutic purposes. For instance, they can be functionalized with boron containing molecules for boron neutron capture therapy (BNCT).[74] Actually, the intrinsic properties of CNTs can be directly exploited for thermotherapy. The strong optical absorption of CNTs in the NIR region makes them suitable for photothermal therapy.[75] CNTs have the ability to efficiently convert NIR into heat. When exposed to NIR, CNTs enter an excited state (hyperthermia) and release vibrational energy that is transformed into heat inducing cell death.[76] For instance, CNTs can arrive to a thermal destruction of tumors at 10-fold-lower doses and 3-fold-lower power than is needed for gold nanorods.[77, 78]
- **Imaging**: CNTs also serve as can be probes for biomedical imaging.[79] As already mentioned, one can benefit from the intrinsic physical properties of CNTs to afford imaging or develope of diagnostic agents based on the formation of hybrid nanostructures using CNTs. The cavity of the CNTs gives a versatile method to incorpore contrast agents, as they can be filled with a variety of materials.[80, 81] Another strategy consists of adding the contrast agent through external decoration with inorganic nanoparticles or molecular tags.[82, 83] There are several techniques that can be employed with CNTs for medical imaging

purposes including photoacoustic imaging, X-ray radiography, nuclear imaging (Single Photoemission Computed Tomography (SPECT), Positron Emission Tomography (PET)) and magnetic resonance imaging (MRI). Both MRI and nuclear imaging are the most widely employed clinical modalities when it comes to the diagnosis of diseases, and therefore observe special attention. Opposite to x-ray imaging, where radiation comes from an external source, nuclear medicine imaging is based on the radiation that is emitted from a radiopharmaceutical within the body. SPECT and PET are 3D nuclear medicine tomographic techniques that use gamma rays. A gamma camera gets information from different projections and can reconstruct them to create 3D information. When combined with a CT scanner, SPECT/CT is able to localize tumors.[84] On the other hand, MRI is a technique that uses a powerful magnet (in the radiofrequency range) to polarize and excite the protons in the water molecules of human tissues, producing a signal. When the radiofrequency pulse is switched off, the relaxation of the spins back to the lower state produces an amount of radiofrequency proportional to the received pulse. With the addition of contrast agents, the nuclear magnetic relaxation rate of the surrounding media is increased and the signal contrast is improved. The relaxation of the magnetic moments is mainly composed by two relaxation processes: T_1 the longitudinal relaxation time and T_2 the transversal relaxation time. Contrast agents based on gadolinium are known to be typical T_1 contrast agents whereas iron based materials are T_2 contrast agents.[85]

1.3. Purification of carbon nanotubes

As detailed, CNTs possess impressive properties and are remarkable candidates for a wide range of applications. Nonetheless, none of the synthesis techniques discussed in the previous section produces pure carbon nanotubes.

Bulk synthesis of CNTs typically results in samples that contain several impurities namely amorphous carbon, graphitic particles in the form of fullerenes or nano-onions, and metal nanoparticles used as catalyst. The amount of impurities depends on the method employed for the CNT growth, and usually increases when decreasing the diameter. For instance, in arc discharge and laser ablation methods the CNTs are formed by vaporization of graphite rods, also resulting in the formation of graphitic particles. Graphitic nano-onions with enclosed metal particles are also formed when CNTs are synthesized by CVD. These graphitic shells avoid the removal of metal nanoparticles.

Metal nanoparticles not only might induce cytoxicity[86-88] but can also dominate the electrochemical response of the material[89] along with graphitic particles.[90-92] On the other hand, the presence of amorphous carbon alter the adhesion properties of the nanotubes[93] and might lead to the formation of oxidation debris preventing the sidewall functionalization of CNTs.[94]

There has been a huge development of purification techniques the last couple of decades. The purification of CNTs is a key step since the properties of CNTs might also undergo a decrease of performance due to the presence of impurities. There are several methods for the CNT purification, with different effects on the material.[95] Usually, these methods take advantage of the differences in the aspect ratio and reactivity towards the oxidation between CNTs and the carbonaceous impurities. The purification of CNT samples can include one or more steps and can be classified as physical, liquid phase techniques or gas phase techniques. The main objective has been to develop reliable protocols with a high selectivity.

1.3.1. Physical techniques

The physical techniques are much less destructive than chemical methods. They do not involve oxidation treatments, meaning that no functionalities are incorporated onto the CNTs.

One route consists on the separation by filtration.[96] This method takes advantage of the differences in physical size, aspect ratio and dispersibility of CNTs with respect to the impurities present in the sample. For instance, graphitic carbon and fullerenes can be more easily dispersed in some organic solvents, meaning that by just immersing the sample and filtrating afterwards, the removal of the undesired carbon species can be achieved. However, the filters are often blocked by the material and surfactants are commonly needed to assure CNT suspension.

Centrifugation has also been investigated since the effect of gravity in the particles is different, as two particles of different weight settle down at different rates.[97] Then, amorphous and graphitic carbon are left in the sediment while CNTs remain in suspension. However, this technique requires the use of surfactants or nitric acid treatment, which oxidizes carbon and adds functional groups to the CNTs.

High temperature annealing can completely remove the metal particles, including the ones covered by graphitic particles. Graphitic structures are stable at 3000 ºC whereas metal evaporates at lower temperatures. By heating the material above the evaporation

temperature of the metal, this is eliminated.[98, 99] This treatment also increases the mechanical strength and thermal stability of CNTs. Albeit, the carbonaceous impurities still remain present in the sample, and an additional treatment is required. Therefore, purification by annealing can be employed in CNT samples with low carbonaceous impurities, and is mainly of interest for MWCNTs since SWCNTs start to coalesce above ~1400ºC.

1.3.2. Liquid phase techniques

Liquid phase treatments in oxidizing acidic conditions are the most widely used purification methods because they can produce pure CNTs in a high yield. The fundamental advantage is that this treatment can simultaneously remove both amorphous carbon and metal catalyst in only one step. The most commonly used oxidants are HNO_3,[100] H_2O_2 or a mixture of H_2O_2 and HCl,[101, 102] and $KMNO_4$.[103] Nevertheless, the inconvenience is that these agents react with CNTs and incorporate defects and functionalities on their structure.[104] This increases their dispersibility in water, but at the same time the damage onto the CNT structure can even result in the lost of a large amount of CNTs, in particular those with smaller diameter and length. The purity of the resulting material depends on the concentration of the acid, temperature and time of treatment. This approach can also benefit from a microwave-assisted acid treatment, where the acidic solution absorbs microwave energy improving its effectiveness. In this way metals can be dissolved in a shorter time, creating less damage on the CNTs.[105-107]

1.3.3. Gas phase techniques

In this purification method carbonaceous impurities are removed by oxidation at high temperature under an oxidizing atmosphere. Gas phase oxidation inflicts considerably less damage than liquid phase treatments, creating less structural defects and avoiding the formation of oxidation debris. On the other hand, its downside remains in the inability to remove metal particles, needing an additional step such as high temperature annealing or an HCl treatment.

Most frequently employed gases include air,[108, 109] oxygen, water,[110] carbon dioxide,[111] and hydrogen.[112, 113] The use of hydrogen and CO_2 for the purification of CNT samples is very limited. The air oxidation (or pure oxygen) has very limited selectivity between CNTs and carbonaceous impurities. Therefore when air is employed for the purification of CNT samples a careful optimization of the temperature and treatment time is necessary from batch to batch to avoid the complete oxidation and loss of the carbon material. In

contrast, steam, being a milder oxidizing agent, allows a better control of the purification with reactions with SWCNTs samples that can last for several hours.[114] Steam has also been combined with oxidizing acid treatments for the purification of cloth-like soot SWCNTs from arc discharge,[115] and it has been shown that it can even remove functionalities introduced by an oxidative acid treatment.[116]

1.3.4. Combined techniques

Gas phase, liquid phase, and physical techniques have their own advantages and disadvantages. Therefore, combination of chemical and physical purifications is being widely studied, as those incorporate the advantages of each individual method. Several techniques like oxidation, sonication, filtration or thermal annealing are added to a given purification procedure to obtain purer CNTs with a higher yield.

One effective merge is the sonication with oxidation. During ultrasonication, solvent molecules interact with CNTs thus removing amorphous and graphitic carbon that can be attached on the CNT walls. This can be done for instance with ethanol [117] or acid.[118]

Another strategy is the filtration in combination with oxidation. For instance, CNTs can be oxidized in air at high temperatures during a given period of time to remove where amorphous and graphitic carbon, followed by soaking the sample in concentrated HCl, to remove the metal particles.[119]

1.3.5. Shortening of CNTs

CNT shortening is an important aspect for some specific applications of these materials such as electrical devices[120] and biomedical applications.

The most widely used strategy to shorten CNTs is via liquid phase oxidative cutting. This is one of the treatments employed for purification purposes, but when employing strong concentrated acids their aggressive effect enables the CNT damage and shortening. This procedure involves the use of oxidative reagents, such as sulfuric acid, nitric acid or hydrogen peroxide.[121, 122] The downside the creation of a large number of structural defects and the introduction of functional groups.

Other strategies benefit from mechanical cutting via grinding, ball milling or sonication.[123, 124] These techniques do not incorporate functional groups on the walls of the nanotubes, but a great number of defects are created during the shortening. It is possible to combine both mechanical and liquid phase oxidative cutting.[125]

1.4. Modification of CNTs

Carbon nanotubes tend to align parallel to each other forming bundles due to Van der Waals interactions. These are insoluble in most organic solvents and aqueous solutions. They can be dispersed in some solvents by sonication, but precipitation immediately occurs when this process is interrupted, limiting the processability and application of the material. Therefore, modification of the CNT wall structure is in general needed to avoid the formation of bundles and to render this material dispersible.

CNT can interact with different classes of compounds,[126-129] and undergo functionalization. This allows the modification of the structural framework and the creation of supramolecular complexes. Therefore, their physicochemical properties are modulated enhancing their dispersibility, reactivity, processability, and even biocompatibility is enhanced. This enables the production of novel hybrid materials potentially suitable for the envisaged applications.

The functionalization consists on the attachment of organic or inorganic moieties on the tubular structure of the carbon nanotubes, and can be divided into four main groups: covalent functionalization, non-covalent functionalization, external decoration with inorganic materials, and endohedral filling (**Figure 1.7.**). A complete review of the functionalization strategies is outside the scope of the present Thesis. Therefore, each one of the four mentioned approaches will be described below, with some selected examples.

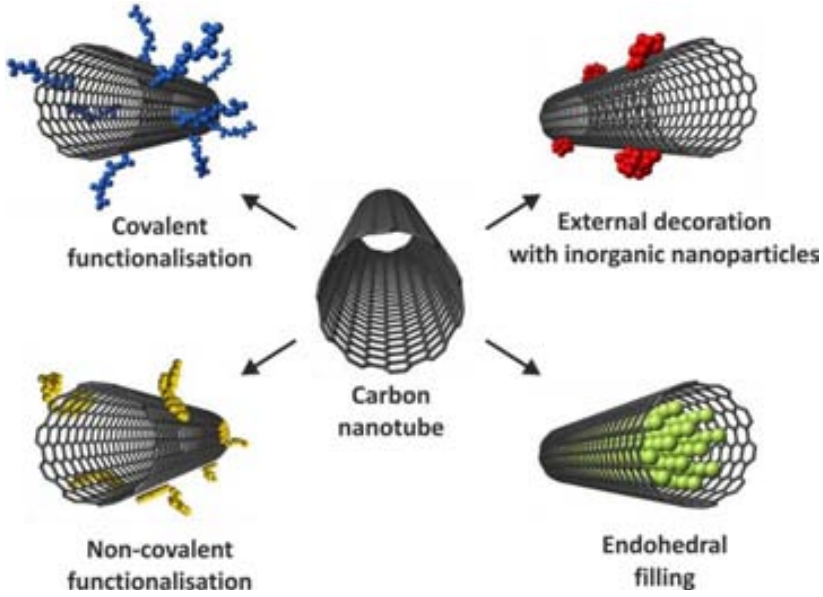

Figure 1.7. Schematic representation of the different strategies for the modification of CNTs.[70]

1.4.1. Covalent functionalization

Covalent functionalization of CNTs has been widely studied not only to increase their dispersibility but also for the purification, conjugation with biomolecules, preparation of polymeric composites, and to tune the properties of CNTs for specific applications (**Figure 1.8.**). The interesting feature of the covalent bond is that it is much more stable than other investigated methods such as surface adsorption on the surface. The major drawback is the disruption of the CNT sp^2 aromatic system, which can lead to the modification and degradation of the intrinsic properties of the material.

The approaches employed for covalent functionalization can be divided into two strategies: defect group functionalization and sidewall functionalization. Both procedures modify the CNT tubular structure, yet what differentiates one from another is that while defect functionalization is principally located at the CNT tips where oxidation is more favoured, sidewall reactions are conducted on the CNT sp^2 network.

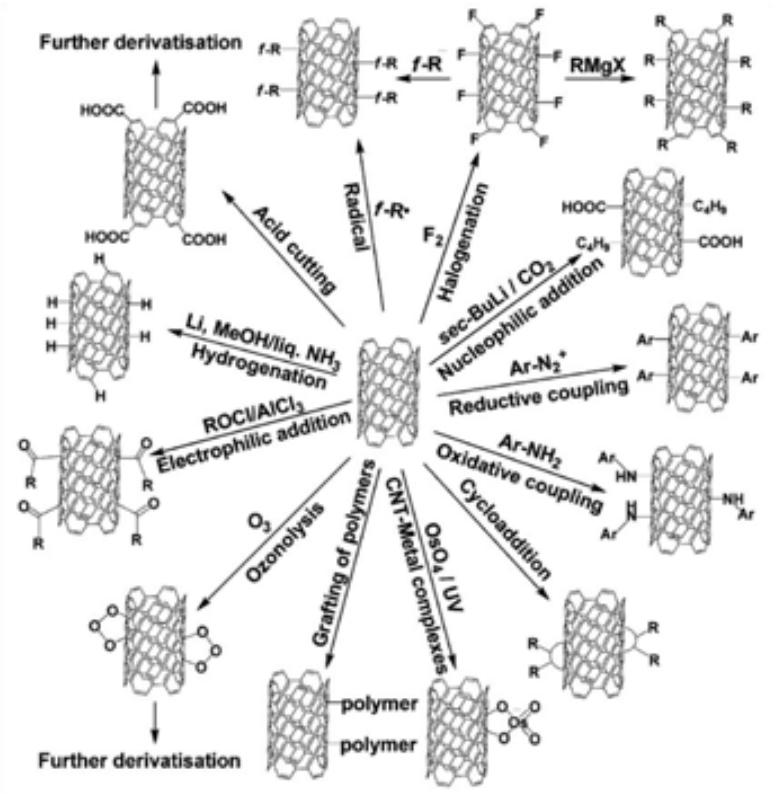

Figure 1.8. Examples of different strategies for the covalent functionalization of CNTs.[130]

1.4.1.1. Defect group functionalization

The defect group functionalization has the basis on the chemical transformation of defects, already present or generated via oxidation, to anchor the desired functionalities. The most common approach for the generation of defects is through oxidation either by liquid phase or gas phase reactions. Oxidation processes yield oxygen-bearing groups on the intrinsic defects and the CNT tips, which behave as precursors to introduce other functional groups through additional reactions. For instance, a commonly employed approach consists on the formation of amide bonds between carboxylated CNTs and amine-terminated functionalities.[131, 132]

1.4.1.2. Side-wall functionalization

Side-wall functionalization is based on the rehybridization of a sp^2 carbon atom of the CNT sidewall to an sp^3 configuration leading to the formation of a covalent bond with a chosen moiety.

There is a significant amount of synthetic routes to obtain covalent bonds on CNTs. Among the most common methods exists the halogenation, where the fluorination with C_2F is the most extensively used.[133, 134] The fluorinated CNTs are the starting point in many reactions where the fluorine atoms are replaced with other groups, such as alkyl groups via Grignard. Cycloaddition reactions are also extensively used methods to, for instance, increase dispersibility or to attach biomolecules. [2 + 1] Cycloaddition on pristine CNTs,[135, 136] 1,3-dipolar cycloaddition reaction[137] or Bingel [2 + 1] cyclopropanation[138] are just a few examples. The attachment of carbon radicals on the walls of CNTs has potential application in the formation of nanohybrids. A simple approach is by the radical addition of diazonium salts to prepare donor-acceptor systems.[139-141] There are numerous other methods for the sidewall functionalization of CNTs, namely electrophilic additions, ozonolysis, mechanochemical functionalizations or plasma activation.

1.4.2. Non-covalent functionalization

Non-covalent functionalization benefits from π-π stacking, van der Waals or charge-transfer interactions. Wrapping of the tubular surface with various functional molecules is capable to exfoliate CNT bundles and individualize the nanotubes. The interest of the non-covalent approach lies in the fact that the chemical molecules are weakly attached without altering the intrinsic properties of the CNTs. .

There are a wide range of compounds that interact with CNT walls.[142] Among those, surfactants are the most widely employed. Their hydrophilic parts interact with the solvent whereas the hydrophobic parts are adsorbed onto the nanotubes surface, avoiding the CNT aggregation.[143, 144] If the hydrophobic part contains an aromatic or naphtalenic group, the interaction is stronger as a consequence of the π-π stacking interactions. The surfactants can be anionic, cationic or non-ionic. Charged surfactants include sodiumdodecyl sulphate (SDS) or dodecyltrimethylammoniumbromide (DTAB) among others. Charge-neutral surfactants, such as Triton, suspend nanotubes depending on the size of the hydrophilic group.

Other non-covalent linkers include polymers, polynuclear aromatic compounds and biomolecules. Biomolecules are used mainly to disperse CNTs for biomedical applications since allow their integration into living systems. The biomolecules employed include saccharides, polysaccharides, proteins, olygopeptides, phospholipids and nucleic acids.[145, 146]

1.4.3. External decoration with inorganic materials

The preparation of carbon nanotubes–inorganic hybrids is an attractive area of research, as these possess unique properties that benefit from the synergy of both types of materials. In general, these nanocomposites are formed of inorganic nanoparticles decorating the external CNT sidewalls.[147] These nanocomposites hold potential in several nanotechnological applications, such as catalysis, sensors or devices. There are two strategies to prepare these hybrids: *ex situ* approach, where nanoparticles are pre-synthesized or *in situ* approach, where nanoparticles are formed directly on the CNT surface.

1.4.3.1. *Ex situ* approach

This method involves several steps. Firstly, the nanoparticles are synthesized, without the presence of CNTs. Hence, their size and shape are more rigorously controlled than when CNTs are present. The prepared NPs are typically coated with an organic shell that prevents their aggregation. CNTs are independently functionalized to allow the attachment of the nanoparticles to the CNT walls by covalent or noncovalent interactions.

Covalent bonding can be achieved through organic linkers or biomolecules. The advantage of this approach is that the amount of nanoparticles connected to the walls is controlled by the functionalities previously added to the surface of CNTs. There are a wide range of functional groups that can be incorporated, as it has been described in section 1.4.1. The bonds formed are well-defined chemical bonds, becoming the hybrid significantly stable and robust. There is a wide range of inorganic nanoparticles that have been covalently attached onto the CNTs, such as Au, CdSe, TiO_2, MnO_2, MgO or Fe_3O_4.[83, 148]

However, as stated above covalent functionalization may damage the structure of CNTs, losing their intrinsic properties. Through non-covalent decoration of CNTs, the CNT properties are well preserved. Besides, the synthetic procedure is usually very simple and in most of the cases involves only one step. The main drawback is that non-covalent interactions are not as robust as in the covalent approach and there is no control of the distribution on the CNT surface. Quantum dots (CdTe, CdSe), metals (Pt, Au) or metal oxides (TiO_2, SiO_2, Fe_3O_4) have been successfully added by non-covalent interactions.[149]

1.4.3.2. *In situ* approach

The *in situ* preparation of nanocomposites has as a characteristic that CNT act as templates and stabilizers for the formation of the nanoparticles. The positive aspect is that

it is a straightforward and effective method for the nanocomposite preparation. The degree of CNT coverage is extremely large and the nanoparticles are directly attached onto the surface of CNTs, without the presence of an organic shell. In addition, the degree of loading can go from discrete nanoparticles to a complete coverage of the CNTs. Nevertheless, the nanoparticles are not strongly bonded to the CNTs, as there is not a chemical linkage. Moreover, there is no control of the position of the nanoparticles, and their shape and dimensionality cannot be easily tuned.

There are different procedures that can be employed for the *in situ* approach: electrodeposition, sol-gel processing, hydrothermal treatment or gas-phase deposition are the most common. Metals, metal oxides, metal chalcogenides, metal carbides and metal nitrides are just a few examples of the nanoparticles that can be integrated on the CNT surface by the *in situ* approach.[150-152]

1.4.4. Endohedral functionalization: Encapsulation of materials inside CNTs

Endohedral filling is a completely different approach to functionalize CNTs, as the basis is the use of the inner cavity of the nanotubes. It is considered a method of CNT functionalization because the encapsulated compounds can also alter the properties of the nanotubes. There are several reports that show that it is possible to fill the hollow cavities of the CNTs, creating novel nanocomposites.[153, 154] The materials inside the nanotubes are confined in a very small volume, which result in the formation of new crystal structures and chemical compositions with novel properties. A large variety of compounds have been incorporated inside MWCNTs and SWCNTs.

There are different strategies for the filling, either during CNT synthesis or in a post-synthesis process. Depending of the physical properties of the filling material, it can be inserted in the solid, liquid or vapour phase.[155] The gas route is a straightforward methodology, as it consists on heating the material to be encapsulated above the sublimation temperature in the presence of open-ended CNTs.[156] In the same way, if the material is heated above the melting temperature, then it goes inside the CNT cavity in its molten state through capillary wetting. Another liquid state strategy is the solution filling, where open-ended CNTs are immersed in a solution of the chosen material.[157, 158] The solution gets inside the CNTs and afterwards the solvent is dried, leaving behind the CNTs and the desired material.

However, little is known of the properties and potential applications of these nanocomposites, and further studies are needed. For instance, filled CNTs are being

explored for nanoelectronic devices, as the band gap of carbon nanotubes can be modulated.[159] In addition, these nanocomposites can be employed in the biomedical field as they can be filled with therapeutic or imaging agents and at the same time the outer walls can be functionalized to enhance its dispersibility, biocompatibility or targeting capabilities.[160, 161]

1.4.4.1 Template-assisted growth of nanomaterials

Soon after the report of MWCNTs by Iijima in 1991,[5] Pederson and Broughton described with computer simulations that open-ended CNTs could behave as 'nanostraws' and encapsulate molecules either in gas phase or liquid phase.[162] As a consequence of this prediction, a great effort was dedicated to the encapsulation of materials inside MWCNTs. The initial reports were supported by electron microscopy techniques to readily detect the encapsulation of the material within the CNTs. It is to be noted that the filling of CNTs is only achieved when its ends are open, meaning that prior to the encapsulation of the material, an end-opening treatment must be conducted. The encapsulation of materials inside CNTs results in the formation of extremely narrow 1D nanowires that can go down to a chain of single atoms forming an "atomic necklace".[163] The new structures that were formed were 1D nanocrystals or nanoclusters which physical properties could differ from those of their bulk counterparts. Examples of these one dimensional nanostructures encapsulated in CNTs include KI[164], CoI_2[165], KCl and UCl_4[166] Not only inorganic nanocrystals have been formed within the CNT cavities, filling of SWCNTs with fullerene C_{60} was already reported back in 1998.[167] A large variety of materials have been encapsulated in CNTs, apart from inorganic salts,[156] organic molecules,[168] metals[169, 170] and water[171] have also been reported. Both the properties of the encapsulated structure and the properties of the CNTs can be modulated by filling.[172] These hybrids can be applied in many different fields, namely nanoelectronics as molecular magnets,[173] in biomedicine as drug delivery agents or contrast agents,[174] membranes, sensors, test-tubes or shielding of air sensitive materials.

Nonetheless, all the reported structures were in the form nanowires or nanoclusters, until a report from Wang et al in 2010 where they described the formation of inorganic nanoribbons encapsulated inside carbon nanotubes.[175] This showed that the formation of new systems consisting of one or few layers of an inorganic material was also possible within the CNT cavities. As a consequence of the seminal work by Geim and Novoselov,[176, 177] which reported on the properties of an isolated single-layer graphite flake, there is a heightened interest in the graphene related two-dimensional systems as well as in the formation of two dimensional materials of inorganic compounds. The report from Wang

and coworkers stated that these inorganic monolayered structures can be prepared inside a CNT, which is acting as a template.[175] The filling of CNTs with single-layered inorganic materials could have promising technological applications, as the electronic, optic and magnetic properties of single-layered materials differ from those presented in the bulk form.

1.5. References

1. C. Lieber, *MRS bulletin*, 2003, 28, 486-491.
2. C. N. R. Rao and A. K. Cheetham, *Journal of Materials Chemistry*, 2001, 11, 2887-2894.
3. G. A. Mansoori, *Principles of nanotechnology : molecular-based study of condensed matter in small systems*, World Scientific, New Jersey [etc.], 2005.
4. J. J. Ramsden, in *Nanotechnology*, ed. J. J. Ramsden, William Andrew Publishing, Oxford, 2011, 227-246.
5. S. Iijima, *Nature*, 1991, 354, 56-58.
6. R. Saito, G. Dresselhaus and M. S. Dresselhaus, *Physical properties of carbon nanotubes*, Imperial College Press, London, 1998.
7. C. N. R. Rao and A. Govindaraj, *Nanotubes and nanowires*, RSC Publishing, 2011.
8. T. Ando, *NPG Asia Mater*, 2009, 1, 17-21.
9. T. W. Ebbesen, *Annual review of materials science*, 1994, 24, 235-264.
10. H. Dai, *Accounts of Chemical Research*, 2002, 35, 1035-1044.
11. M. Anna, G. N. Albert and I. K. Esko, *Journal of Physics: Condensed Matter*, 2003, 15, S3011.
12. C. H. Kiang, M. S. Devries, G. Gorman, R. Savoy, D. S. Bethune, C. H. Klang, M. S. de-Vries, J. Vazquez and R. Beyers, *Nature*, 1993, 363, 605-607.
13. C. Journet, P. Bernier, W. K. Maser, A. Loiseau, M. L. de la Chapelle, S. Lefrant, P. Deniard, R. Lee and J. E. Fischer, *Nature*, 1997, 388, 756-758.
14. T. W. Ebbesen and P. M. Ajayan, *Nature*, 1992, 358, 220-222.
15. T. Guo, P. Nikolaev, A. Thess, D. T. Colbert and R. E. Smalley, *Chemical Physics Letters*, 1995, 243, 49-54.
16. W. K. Maser, E. Muñoz, A. M. Benito, M. T. Martı´nez, G. F. de la Fuente, Y. Maniette, E. Anglaret and J. L. Sauvajol, *Chemical Physics Letters*, 1998, 292, 587-593.
17. A. Thess, R. Lee, P. Nikolaev, H. Dai, P. Petit, J. Robert, C. Xu, Y. H. Lee, S. G. Kim, A. G. Rinzler, D. T. Colbert, G. E. Scuseria, D. Tománek, J. E. Fischer and R. E. Smalley, *Science*, 1996, 273, 483-487.
18. M. Endo, K. Takeuchi, S. Igarashi, K. Kobori, M. Shiraishi and H. W. Kroto, *Journal of Physics and Chemistry of Solids*, 1993, 54, 1841-1848.
19. D. Eder, *Chemical Reviews*, 2010, 110, 1348-1385.
20. S. Iijima, C. Brabec, A. Maiti and J. Bernholc, *The Journal of Chemical Physics*, 1996, 104, 2089-2092.
21. T. Hayashi, Y. A. Kim, T. Natsuki and M. Endo, *ChemPhysChem*, 2007, 8, 999-1004.

22. D. H. Robertson, D. W. Brenner and J. W. Mintmire, *Physical Review B*, 1992, 45, 12592-12595.

23. M. M. J. Treacy, T. W. Ebbesen and J. M. Gibson, *Nature*, 1996, 381, 678-680.

24. M.-F. Yu, B. S. Files, S. Arepalli and R. S. Ruoff, *Physical Review Letters*, 2000, 84, 5552-5555.

25. M. R. Falvo, G. J. Clary, R. M. Taylor, V. Chi, F. P. Brooks, S. Washburn and R. Superfine, *Nature*, 1997, 389, 582-584.

26. W.-J. Lee, J.-G. Chang, A.-C. Yang, Y.-T. Wang, W.-S. Su, C.-Z. Wang and K.-M. Ho, *Journal of applied physics*, 2013, 114, 144306.

27. J. W. G. Wildoer, L. Venema, A. Rinzler, R. Smalley and C. Dekker, *Nature*, 1998, 391, 59-62.

28. R. Martel, T. Schmidt, H. R. Shea, T. Hertel and P. Avouris, *Applied Physics Letters*, 1998, 73, 2447-2449.

29. M. J. O'Connell, S. M. Bachilo, C. B. Huffman, V. C. Moore, M. S. Strano, E. H. Haroz, K. L. Rialon, P. J. Boul, W. H. Noon, C. Kittrell, J. Ma, R. H. Hauge, R. B. Weisman and R. E. Smalley, *Science*, 2002, 297, 593-596.

30. M. S. Dresselhaus, G. Dresselhaus, R. Saito and A. Jorio, *Physics Reports*, 2005, 409, 47-99.

31. P. Puech, A. Bassil, J. Gonzalez, E. Flahaut, C. Power, S. Barrau, P. Demont, C. Lacabanne, E. Perez and W. Bacsa, *Physical review. B, Condensed matter and materials physics*, 2005, 72.

32. V. Kuznetsov, S. Bokova Sirosh, S. Moseenkov, A. Ishchenko, D. Krasnikov, M. Kazakova, A. Romanenko, E. Tkachev and E. Obraztsova, *Physica status solidi. B, Basic research*, 2014, 251, 2444-2450.

33. M. S. Dresselhaus, A. Jorio, M. Hofmann, G. Dresselhaus and R. Saito, *Nano Letters*, 2010, 10, 751-758.

34. A. M. Rao, E. Richter, S. Bandow, B. Chase, P. C. Eklund, K. A. Williams, S. Fang, K. R. Subbaswamy, M. Menon, A. Thess, R. E. Smalley, G. Dresselhaus and M. S. Dresselhaus, *Science*, 1997, 275, 187-191.

35. S. Berber, Y.-K. Kwon and D. Tománek, *Physical Review Letters*, 2000, 84, 4613-4616.

36. P. Kim, L. Shi, A. Majumdar and P. L. McEuen, *Physical Review Letters*, 2001, 87, 215502.

37. W. Bauhofer and J. Z. Kovacs, *Composites Science and Technology*, 2009, 69, 1486-1498.

38. T.-W. Chou, L. Gao, E. T. Thostenson, Z. Zhang and J.-H. Byun, *Composites Science and Technology*, 2010, 70, 1-19.

39. S. D. Thoppul, J. Finegan and R. F. Gibson, *Composites Science and Technology*, 2009, 69, 301-329.

40. A. Beigbeder, P. Degee, S. L. Conlan, R. J. Mutton, A. S. Clare, M. E. Pettitt, M. E. Callow, J. A. Callow and P. Dubois, *Biofouling*, 2008, 24, 291-302.

41. K. Koziol, J. Vilatela, A. Moisala, M. Motta, P. Cunniff, M. Sennett and A. Windle, *Science*, 2007, 318, 1892-1895.

42. M. D. Lima, S. Fang, X. Lepró, C. Lewis, R. Ovalle-Robles, J. Carretero-González, E. Castillo-Martínez, M. E. Kozlov, J. Oh, N. Rawat, C. S. Haines, M. H. Haque, V. Aare, S. Stoughton, A. A. Zakhidov and R. H. Baughman, *Science*, 2011, 331, 51-55.

43. Q. Cao and J. A. Rogers, *Advanced Materials*, 2009, 21, 29-53.

44. D.-m. Sun, M. Y. Timmermans, Y. Tian, A. G. Nasibulin, E. I. Kauppinen, S. Kishimoto, T. Mizutani and Y. Ohno, *Nat Nano*, 2011, 6, 156-161.

45. L. Dai, D. W. Chang, J.-B. Baek and W. Lu, *Small*, 2012, 8, 1130-1166.

46. M. Kaempgen, C. K. Chan, J. Ma, Y. Cui and G. Gruner, *Nano Letters*, 2009, 9, 1872-1876.

47. Z. Wu, Z. Chen, X. Du, J. M. Logan, J. Sippel, M. Nikolou, K. Kamaras, J. R. Reynolds, D. B. Tanner, A. F. Hebard and A. G. Rinzler, *Science*, 2004, 305, 1273-1276.

48. G. Gao and C. D. Vecitis, *Environmental Science & Technology*, 2011, 45, 9726-9734.

49. B. Corry, *The Journal of Physical Chemistry B*, 2007, 112, 1427-1434.

50. J. Wang, *Electroanalysis*, 2005, 17, 7-14.

51. N. Yang, X. Chen, T. Ren, P. Zhang and D. Yang, *Sensors and Actuators B: Chemical*, 2015, 207, Part A, 690-715.

52. M. F. De Volder, S. H. Tawfick, R. H. Baughman and A. J. Hart, *Science*, 2013, 339, 535-539.

53. B. Allen, P. Kichambare and A. Star, *Advanced materials*, 2007, 19, 1439-1451.

54. N. Yang, X. Chen, T. Ren, P. Zhang and D. Yang, *Sensors and actuators. B, Chemical*, 2015, 207, 690-715.

55. A. Vijayaraghavan, S. Blatt, D. Weissenberger, M. Oron Carl, F. Hennrich, D. Gerthsen, H. Hahn and R. Krupke, *Nano letters*, 2007, 7, 1556-1560.

56. S. C. Tjong, *Express polymer letters*, 2010, 4, 516-516.

57. C. F. de-Lannoy, D. Jassby, D. D. Davis, M. R. Wiesner and C. F. de Lannoy, *Journal of membrane science*, 2012, 415, 718-724.

58. D. Pantarotto, J.-P. Briand, M. Prato and A. Bianco, *Chemical Communications*, 2004, DOI: 10.1039/B311254C, 16-17.

59. N. W. Shi Kam, T. C. Jessop, P. A. Wender and H. Dai, *Journal of the American Chemical Society*, 2004, 126, 6850-6851.

60. A. Bianco, K. Kostarelos and M. Prato, *Chemical communications (London. 1996)*, 2011, 47, 10182-10188.

61. C. A. Poland, R. Duffin, I. Kinloch, A. Maynard, W. A. H. Wallace, A. Seaton, V. Stone, S. Brown, W. MacNee and K. Donaldson, *Nat Nano*, 2008, 3, 423-428.

62. H. Ali-Boucetta, A. Nunes, R. Sainz, M. A. Herrero, B. Tian, M. Prato, A. Bianco and K. Kostarelos, *Angewandte Chemie International Edition*, 2013, 52, 2274-2278.

63. A. Shvedova, V. Castranova, E. Kisin, D. Schwegler-Berry, A. Murray, V. Gandelsman, A. Maynard and P. Baron, *Journal of Toxicology and Environmental Health, Part A*, 2003, 66, 1909-1926.

64. D. Liu, L. Wang, Z. Wang and A. Cuschieri, *Nanoscale Res Lett*, 2012, 7, 361.

65. K. Kostarelos, *Nature biotechnology*, 2008, 26, 774-776.

66. Y. Maeda, S.-i. Kimura, Y. Hirashima, M. Kanda, Y. Lian, T. Wakahara, T. Akasaka, T. Hasegawa, H. Tokumoto, T. Shimizu, H. Kataura, Y. Miyauchi, S. Maruyama, K. Kobayashi and S. Nagase, *The journal of physical chemistry. B*, 2004, 108, 18395-18397.

67. Z. Liu, S. Tabakman, K. Welsher and H. Dai, *Nano Res.*, 2009, 2, 85-120.

68. W. Zhang, Z. Zhang and Y. Zhang, *Nanoscale Res Lett*, 2011, 6, 1-22.

69. D. A. Scheinberg, M. R. McDevitt, T. Dao, J. J. Mulvey, E. Feinberg and S. Alidori, *Advanced Drug Delivery Reviews*, 2013, 65, 2016-2022.

70. G. Tobias and E. Flahaut, *Smart materials for drug delivery; Chapter 16: Smart carbon nanotubes*, RSC Publishing edn., 2013.

71. J. M. Tan, P. Arulselvan, S. Fakurazi, H. Ithnin and M. Z. Hussein, *Journal of Nanomaterials*, 2014, 2014, 20.

72. W. Wu, S. Wieckowski, G. Pastorin, M. Benincasa, C. Klumpp, J.-P. Briand, R. Gennaro, M. Prato and A. Bianco, *Angewandte Chemie International Edition*, 2005, 44, 6358-6362.

73. Z. Zhang, X. Yang, Y. Zhang, B. Zeng, Z. Wang, S. Wang, T. Zhu, Y. Chen and R. Yang, *Clin. Cancer Res.*, 2006, 12, 4933-4939.

74. Z. Yinghuai, A. Peng, K. Carpenter, J. Maguire, N. Hosmane and M. Takagaki, *Journal of the American Chemical Society*, 2005, 127, 9875-9880.

75. R. Singh and S. Torti, *Advanced drug delivery reviews*, 2013, 65, 2045-2060.

76. N. W. S. Kam, N. W. Shi-Kam, M. O'Connell, J. A. Wisdom and H. Dai, *Proceedings of the National Academy of Sciences of the United States of America*, 2005, 102, 11600-11605.

77. J. Robinson, K. Welsher, S. Tabakman, S. Sherlock, H. Wang, R. Luong and H. Dai, *Nano Res.*, 2010, 3, 779-793.

78. Z. Liu, W. Cai, L. He, N. Nakayama, K. Chen, X. Sun, X. Chen and H. Dai, *Nat Nano*, 2007, 2, 47-52.

79. S. I. Pascu, R. L. Arrowsmith, S. R. Bayly, S. Brayshaw and Z. Hu, *Philosophical Transactions of the Royal Society A: Mathematical, Physical and Engineering Sciences*, 2010, 368, 3683-3712.

80. S. Datta, L. Marty, J. P. Cleuziou, C. Tilmaciu, B. Soula, E. Flahaut and W. Wernsdorfer, *Physical review letters*, 2011, 107, 186804.

81. J. Spencer, J. Nesbitt, H. Trewhitt, R. Kashtiban, G. Bell, V. Ivanov, E. Faulques, J. Sloan and D. Smith, *ACS nano*, 2014, 8, 9044-9052.

82. G. Lamanna, A. Garofalo, G. Popa, C. Wilhelm, S. Begin-Colin, D. Felder-Flesch, A. Bianco, F. Gazeau and C. Menard-Moyon, *Nanoscale*, 2013, 5, 4412-4421.

83. H. Zhou, C. Zhang, H. Li and Z. Du, *Journal of polymer science. Part A, Polymer chemistry*, 2010, 48, 4697-4703.

84. D. W. Jones, P. Hogg and E. Seeram, *Practical SPECT/CT in Nuclear Medicine*, Springer, 2013.

85. D. W. McRobbie, E. A. Moore, M. J. Graves and M. R. Prince, *MRI from Picture to Proton*, 2006.

86. S. Koyama, Y. A. Kim, T. Hayashi, K. Takeuchi, C. Fujii, N. Kuroiwa, H. Koyama, T. Tsukahara and M. Endo, *Carbon*, 2009, 47, 1365-1372.

87. J. M. Wörle-Knirsch, K. Pulskamp and H. F. Krug, *Nano Letters*, 2006, 6, 1261-1268.

88. H. Sharma, S. Hussain, J. Schlager, S. Ali and A. Sharma, in *Brain Edema XIV*, eds. Z. Czernicki, A. Baethmann, U. Ito, Y. Katayama, T. Kuroiwa and D. Mendelow, Springer Vienna, 2010, vol. 106, ch. 65, pp. 359-364.

89. C. E. Banks, A. Crossley, C. Salter, S. J. Wilkins and R. G. Compton, *Angewandte Chemie International Edition*, 2006, 45, 2533-2537.

90. M. C. Henstridge, L. Shao, G. G. Wildgoose, R. G. Compton, G. Tobias and M. L. H. Green, *Electroanalysis*, 2008, 20, 498-506.

91. A. Ambrosi and M. Pumera, *Chemistry – A European Journal*, 2010, 16, 10946-10949.

92. C. L. Scott and M. Pumera, *Electrochemistry Communications*, 2011, 13, 426-428.

93. Z. An, A. o. Furmanchuk, R. Ramachandramoorthy, T. Filleter, M. R. Roenbeck, H. D. Espinosa, G. C. Schatz and S. T. Nguyen, *Carbon*, 2014, 80, 1-11.

94. L. Shao, G. Tobias, C. G. Salzmann, B. Ballesteros, S. Y. Hong, A. Crossley, B. G. Davis and M. L. H. Green, *Chemical Communications*, 2007, DOI: 10.1039/b712614j, 5090-5092.

95. P.-X. Hou, C. Liu and H.-M. Cheng, *Carbon*, 2008, 46, 2003-2025.

96. J.-M. Bonard, T. Stora, J.-P. Salvetat, F. Maier, T. Stöckli, C. Duschl, L. Forró, W. A. de Heer and A. Châtelain, *Advanced Materials*, 1997, 9, 827-831.

97. A. Yu, E. Bekyarova, M. E. Itkis, D. Fakhrutdinov, R. Webster and R. C. Haddon, *Journal of the American Chemical Society*, 2006, 128, 9902-9908.

98. R. Andrews, D. Jacques, D. Qian and E. C. Dickey, *Carbon*, 2001, 39, 1681-1687.

99. G. Qiao Juan, L. He Jun, W. Xiang, L. Ke Zhi and Z. Xiu Lian, 2006, 64, 2365-2368.

100. H. Hu, B. Zhao, M. E. Itkis and R. C. Haddon, *The Journal of Physical Chemistry B*, 2003, 107, 13838-13842.

101. Y. Wang, H. Shan, R. Hauge, M. Pasquali and R. Smalley, *The journal of physical chemistry. B*, 2007, 111, 1249-1252.

102. Y. Feng, H. Zhang, Y. Hou, T. McNicholas, D. Yuan, S. Yang, L. Ding, W. Feng and J. Liu, *ACS nano*, 2008, 2, 1634-1638.

103. J. Zhang, H. Zou, Q. Qing, Y. Yang, Q. Li, Z. Liu, X. Guo and Z. Du, *The Journal of Physical Chemistry B*, 2003, 107, 3712-3718.

104. G. A. D. Briggs, J. G. Wiltshire, A. N. Khlobystov, L. J. Li, S. G. Lyapin and R. J. Nicholas, *Chemical Physics Letters*, 2004, 386, 239-243.

105. F.-H. Ko, C.-Y. Lee, C.-J. Ko and T.-C. Chu, *Carbon*, 2005, 43, 727-733.

106. R. Pelalak, M. Baniadam and M. Maghrebi, *Applied physics. A, Materials science & processing*, 2013, 111, 951-957.

107. K. MacKenzie, O. Dunens, M. Hanus and A. Harris, *Carbon*, 2011, 49, 4179-4190.

108. B. Bendjemil, E. Borowiak-Palen, A. Graff, T. Pichler, M. Guerioune, J. Fink and M. Knupfer, *Appl Phys A*, 2004, 78, 311-314.

109. N. Dementev, S. Osswald, Y. Gogotsi and E. Borguet, *Journal of materials chemistry*, 2009, 19, 7904-7908.

110. R. Sen, S. M. Rickard, M. E. Itkis and R. C. Haddon, *Chemistry of Materials*, 2003, 15, 4273-4279.

111. D. J. Babu, S. Yadav, T. Heinlein, G. Cherkashinin and J. J. Schneider, *The Journal of Physical Chemistry C*, 2014, 118, 12028-12034.

112. S. R. C. Vivekchand, A. Govindaraj, M. M. Seikh and C. N. R. Rao, *The Journal of Physical Chemistry B*, 2004, 108, 6935-6937.

113. L. Sheng, L. Shi, K. An, L. Yu, Y. Ando and X. Zhao, *Chemical Physics Letters*, 2011, 502, 101-106.

114. B. Ballesteros, G. Tobias, L. Shao, E. Pellicer, J. Nogues, E. Mendoza and M. L. H. Green, *Small*, 2008, 4, 1501-1506.

115. W. Guo, Z. Dou, H. Li, Z. Shi, H. Sun and Y. Liu, *Carbon*, 2010, 48, 3769-3777.

116. G. Tobias, L. Shao, C. G. Salzmann, Y. Huh and M. L. H. Green, *The Journal of Physical Chemistry B*, 2006, 110, 22318-22322.

117. P. Hou, C. Liu, Y. Tong, S. Xu, M. Liu and H. Cheng, *Journal of Materials Research*, 2001, 16, 2526-2529.

118. F. Li, G. Su, H. M. Cheng, Y. T. Xing and P. H. Tan, *Carbon*, 2000, 38, 2041-2045.

119. S. Bandow, S. Asaka, X. Zhao and Y. Ando, *Appl Phys A*, 1998, 67, 23-27.

120. J.-Y. Kim, M. Bae, S. Park, T. Jeong, S. Song, J. Lee, I. Han, J. Yoo, D. Jung and S. Yu, *Carbon*, 2012, 50, 170-174.

121. K. J. Ziegler, Z. Gu, H. Peng, E. L. Flor, R. H. Hauge and R. E. Smalley, *Journal of the American Chemical Society*, 2005, 127, 1541-1547.

122. M. V. Shuba, A. G. Paddubskaya, P. P. Kuzhir, S. A. Maksimenko, V. K. Ksenevich, G. Niaura, D. Seliuta, I. Kasalynas and G. Valusis, *Nanotechnology*, 2012, 23, 495714.

123. N. Pierard, A. Fonseca, Z. Konya, I. Willems and G. Van Tendeloo, *Chemical Physics Letters*, 2001, 335, 1-8.

124. K. L. Lu, R. M. Lago, Y. K. Chen, M. L. H. Green and P. J. F. Harris, *Carbon*, 1996, 34, 814-816.

125. F. Ren, S. Kanaan, F. Khalkhal, C. Loebick, G. Haller and L. Pfefferle, *Carbon*, 2013, 63, 61-70.

126. A. Hirsch, *Angewandte Chemie (International ed.)*, 2002, 41, 1853-1859.

127. K. Balasubramanian and M. Burghard, *Small*, 2005, 1, 180-192.

128. D. Tasis, N. Tagmatarchis, A. Bianco and M. Prato, *Chemical Reviews*, 2006, 106, 1105-1136.

129. N. Karousis, N. Tagmatarchis and D. Tasis, *Chemical Reviews*, 2010, 110, 5366-5397.

130. H.-C. Wu, X. Chang, L. Liu, F. Zhao and Y. Zhao, *Journal of Materials Chemistry*, 2010, 20, 1036-1052.

131. J. Chen, M. A. Hamon, H. Hu, Y. Chen, A. M. Rao, P. C. Eklund and R. C. Haddon, *Science*, 1998, 282, 95-98.

132. B. Li, Z. Shi, Y. Lian and Z. Gu, *Chemistry Letters*, 2001, 30, 598-599.

133. S. Kawasaki, K. Komatsu, F. Okino, H. Touhara and H. Kataura, *Physical Chemistry Chemical Physics*, 2004, 6, 1769-1772.

134. H. Touhara and F. Okino, *Carbon*, 2000, 38, 241-267.

135. K. Kamaras, M. E. Itkis, H. Hu, B. Zhao and R. C. Haddon, *Science*, 2003, 301, 1501.

136. H. Hu, B. Zhao, M. A. Hamon, K. Kamaras, M. E. Itkis and R. C. Haddon, *Journal of the American Chemical Society*, 2003, 125, 14893-14900.

137. N. Tagmatarchis and M. Prato, *Journal of Materials Chemistry*, 2004, 14, 437-439.

138. K. S. Coleman, S. R. Bailey, S. Fogden and M. L. H. Green, *Journal of the American Chemical Society*, 2003, 125, 8722-8723.

139. M. S. Strano, C. A. Dyke, M. L. Usrey, P. W. Barone, M. J. Allen, H. Shan, C. Kittrell, R. H. Hauge, J. M. Tour and R. E. Smalley, *Science*, 2003, 301, 1519-1522.

140. C. A. Dyke and J. M. Tour, *Journal of the American Chemical Society*, 2003, 125, 1156-1157.

141. P. R. Marcoux, P. Hapiot, P. Batail and J. Pinson, *New Journal of Chemistry*, 2004, 28, 302-307.

142. C.-Y. Hu, Y.-J. Xu, S.-W. Duo, R.-F. Zhang and M.-S. Li, *Journal of the Chinese Chemical Society*, 2009, 56, 234-239.

143. L. Vaisman, H. D. Wagner and G. Marom, *Advances in Colloid and Interface Science*, 2006, 128–130, 37-46.

144. R. Rastogi, R. Kaushal, S. K. Tripathi, A. Sharma, I. Kaur and L. Bharadwaj, *Journal of colloid and interface science*, 2008, 328, 421-428.

145. C. Klumpp, K. Kostarelos, M. Prato and A. Bianco, *Biochimica et Biophysica Acta (BBA) - Biomembranes*, 2006, 1758, 404-412.

146. G. Dieckmann, I. Musselman, S. Nielsen, E. Becraft and A. Klimenko, *Abstracts of papers - American Chemical Society*, 2009, 237.

147. X. Peng, J. Chen, J. A. Misewich and S. S. Wong, *Chemical Society Reviews*, 2009, 38, 1076-1098.

148. Y. Deng, C. Deng, D. Yang, C. Wang, S. Fu and X. Zhang, *Chemical Communications*, 2005, DOI: 10.1039/B511683J, 5548-5550.

149. L. M. Ang, T. S. A. Hor, G. Q. Xu, C. H. Tung, S. P. Zhao and J. L. S. Wang, *Carbon*, 2000, 38, 363-372.

150. J. Wan, W. Cai, J. Feng, X. Meng and E. Liu, *Journal of materials chemistry*, 2007, 17, 1188-1192.

151. P. C. Ma, B. Z. Tang and J.-K. Kim, *Carbon*, 2008, 46, 1497-1505.

152. M. Chun An, T. Jun Yan, L. Guo Hua and S. Jiang Feng, 2006, 64, 2123-2126.

153. M. Monthioux, E. Flahaut and J.-P. Cleuziou, *Journal of Materials Research*, 2006, 21, 2774-2793.

154. M. Monthioux, *Carbon*, 2002, 40, 1809-1823.

155. K. G. Ujjal, M. F. J. C. Pedro, B. Yoshio, F. Xiaosheng, L. Liang, I. Masataka and G. Dmitri, *Science and Technology of Advanced Materials*, 2010, 11, 054501.

156. P. Fedotov, A. Tonkikh, E. Obraztsova, A. Nasibulin, E. Kauppinen and A. Chuvilin, *Physica status solidi. B, Basic research*, 2014, 251, 2466-2470.

157. P. M. Ajayan and S. Iijima, *Nature*, 1993, 361, 333-334.

158. M. V. Kharlamova, L. V. Yashina, A. A. Eliseev, A. A. Volykhov, V. S. Neudachina, M. M. Brzhezinskaya, T. S. Zyubina, A. V. Lukashin and Y. D. Tretyakov, *physica status solidi (b)*, 2012, 249, 2328-2332.

159. M. d. C. Gimenez-Lopez, F. Moro, A. La Torre, C. Gomez Garcia, P. Brown, P. D. Brown, J. van Slageren, C. Gómez García and A. Khlobystov, *Nature communications*, 2011, 2, 407.

160. R. Marega and D. Bonifazi, *New Journal of Chemistry*, 2014, 38, 22-27.

161. M. Martincic and G. Tobias, *Expert Opinion on Drug Delivery*, 12, 1-19.

162. M. R. Pederson and J. Q. Broughton, *Physical Review Letters*, 1992, 69, 2689-2692.

163. R. Kitaura, R. Nakanishi, T. Saito, H. Yoshikawa, K. Awaga and H. Shinohara, *Angewandte Chemie International Edition*, 2009, 48, 8298-8302.

164. R. R. Meyer, J. Sloan, R. E. Dunin-Borkowski, A. I. Kirkland, M. C. Novotny, S. R. Bailey, J. L. Hutchison and M. L. H. Green, *Science*, 2000, 289, 1324-1326.

165. E. Philp, J. Sloan, A. I. Kirkland, R. R. Meyer, S. Friedrichs, J. L. Hutchison and M. L. H. Green, *Nat Mater*, 2003, 2, 788-791.

166. J. Sloan, A. I. Kirkland, J. L. Hutchison and M. L. H. Green, *Chemical Communications*, 2002, DOI: 10.1039/b200537a, 1319-1332.

167. B. W. Smith, M. Monthioux and D. E. Luzzi, *Nature*, 1998, 396, 323-324.

168. T. Takenobu, T. Takano, M. Shiraishi, Y. Murakami, M. Ata, H. Kataura, Y. Achiba and Y. Iwasa, *Nat Mater*, 2003, 2, 683-688.

169. F. Rossella, C. Soldano, V. Bellani and M. Tommasini, *Advanced materials*, 2012, 24, 2453-2458.

170. C. Soldano, S. Kar, S. Talapatra, S. Nayak and P. M. Ajayan, *Nano Letters*, 2008, 8, 4498-4505.

171. S. Cambré, S. M. Santos, W. Wenseleers, A. R. T. Nugraha, R. Saito, L. Cognet and B. Lounis, *ACS Nano*, 2012, 6, 2649-2655.

172. J. Lee, H. Kim, S. J. Kahng, G. Kim, Y. W. Son, J. Ihm, H. Kato, Z. W. Wang, T. Okazaki, H. Shinohara and Y. Kuk, *Nature*, 2002, 415, 1005-1008.

173. M. del Carmen Giménez-López, F. Moro, A. La Torre, C. J. Gómez-García, P. D. Brown, J. van Slageren and A. N. Khlobystov, *Nat Commun*, 2011, 2, 407.

174. S. Y. Hong, G. Tobias, B. Ballesteros, F. El Oualid, J. C. Errey, K. J. Doores, A. I. Kirkland, P. D. Nellist, M. L. H. Green and B. G. Davis, *Journal of the American Chemical Society*, 2007, 129, 10966-10967.

175. Z. Wang, H. Li, Z. Liu, Z. Shi, J. Lu, K. Suenaga, S.-K. Joung, T. Okazaki, Z. Gu, J. Zhou, Z. Gao, G. Li, S. Sanvito, E. Wang and S. Iijima, *Journal of the American Chemical Society*, 2010, 132, 13840-13847.

176. D. Jiang, K. S. Novoselov, A. K. Geim, S. V. Morozov, M. I. Katsnelson, I. V. Grigorieva, S. V. Dubonos and A. A. Firsov, *Nature*, 2005, 438, 197-200.

177. K. S. Novoselov, A. K. Geim, S. V. Morozov, D. Jiang, Y. Zhang, S. V. Dubonos, I. V. Grigorieva and A. A. Firsov, *Science*, 2004, 306, 666-669.

2

Objectives

In this chapter the general objectives to be achieved in this Thesis are presented.

Carbon nanotubes (CNTs) have received increased interest in the recent years as a consequence of their outstanding properties. They are promising candidates for a wide range of applications and they are already being commercially implemented. In view of the prospects of this new material, the motivation and aims of this Thesis were to provide further insight on the carbon nanotube chemistry and expand their range of application.

We have processed the material at different levels, starting from their purification up to their application. The following three main objectives have been addressed, each of them constituting a Thesis chapter:

1. Purification and shortening of multi walled carbon nanotubes with steam

As-made CNTs contain several impurities that should be removed prior to their application. Therefore, the first objective will be to develop a mild purification method for multi-walled carbon nanotubes (MWCNTs). We will investigate the effect of steam to eliminate the amorphous and graphitic carbon, as well as the catalyst employed in the CNT synthesis after a subsequent acid wash. The aim will be to obtain highly purified MWCNTs whilst preserving their wall structure. We will also study the effect of the steam treatment on the MWCNT length distribution.

2. Functionalization of carbon nanotubes for their use in biomedical applications

The second objective will be the modification of CNTs for their use in two relevant biomedical applications: imaging and Boron neutron capture therapy.

In terms of imaging we aim to develop a dual imaging contrast agent for both MRI and SPECT/CT that will have the benefits from both techniques. To do so we will investigate a synthetic procedure to externally decorate CNTs with radiolabelled inorganic nanoparticles. The aim of this work will be to obtain a hybrid that enhances the imaging properties while rendering the CNTs biocompatible.

On the other hand, we will investigate a method to covalently attach metallacarboranes on the CNT walls. The main purpose is to form a hybrid with high ^{10}B content that will be appropriate for Boron neutron capture therapy.

3. CNT filling with inorganic materials: inorganic nanotube formation

The third and last objective will be to develop a protocol that allows the growth of layered nanostructures inside CNTs.

The aim will be to form tubular single-layered materials by endohedral filling and to investigate the properties of the resulting compounds.

These objectives have motivated our research and a summary of the obtained results are presented separately in three chapters. All these results have been or are about to be published in international peer-reviewed journals. The published articles are appended in the main text and the submitted and under review articles are appended as an annex.

3

Results I:

Purification and shortening of MWCNTs with steam

In this chapter we present the results corresponding to the development of a purification and shortening method for MWCNTs. The optimized protocol will then be employed to prepare MWCNT samples suitable for both the external decoration with biomedical payloads (Chapter 4) and the filling of inorganic compounds (Chapter 5). The results here summarized have been reported in the following articles:

> **Article 1**: "The role of steam treatment on the structure, purity and length distribution of multi-walled carbon nanotubes". *Under review*.

3.1. Objectives

1. Optimize the steam-purification treatment time to purify MWCNTs.
2. Determine the influence of the steam on the wall structure of MWCNTs.
3. Develop a method that allows the modulation of length distribution of MWCNTs.

3.2. Summary

Since the report of Iijima back in 1991 on CNTs, these nanomaterials have driven a great deal of attention for a wide range of applications. A major drawback to benefit from the potential that CNTs hold is the presence of impurities from their synthesis; namely amorphous carbon, graphitic particles and metal catalyst nanoparticles.[1, 2] These not only can induce cytotoxicity which is a major concern for industrial scale applications, but can also affect the performance of the material. [3, 4]

As a consequence of the increased interest to obtain highly pure carbon nanotubes, several purification techniques are nowadays available. Most commonly liquid phase purification is employed, typically by oxidation with acids like nitric or sulphuric.[5, 6] An interesting alternative is the use of gas phase purification, being air the most widely used.[7] Notwithstanding, gas purification with other less oxidative gases has also been proposed to allow a better control of the process. For instance, the use of steam has been reported to allow both the purification and shortening of SWCNTs while preserving the wall structure of the material.

It is well established that during CVD synthesis the presence of water enhances the activity and lifetime. In addition, the formation of amorphous carbon is selectively diminished as a result of the low oxidizing effect of steam, which is capable of suppressing the formation of amorphous carbon, while the carbon nanotube structure remains undamaged.[8]

As mentioned, the post-synthesis treatment of SWCNTs is well demonstrated.[9, 10] Comparison of standard nitric acid purification and steam purification treatments on as-produced SWCNTs revealed that nitric acid is much more aggressive, creating a higher degree of defects onto the walls of the CNTs compared to steam.[11] Steam treatment, followed by an HCl wash, was found to remove the impurities present in the sample without having any effect on the tubular structure of SWCNTs. Neither defects nor functional groups were detected on the surface of the SWCNTs. Opening of the CNTs

ends was also observed followed by the shortening of the length of SWCNTs after a prolonged time of steam treatment.

The use of short CNTs is of interest for different applications including biomedicine,[12-15], sensors,[16] membranes[17] and electrode materials.[18] When it comes to their multi-walled counterparts, it has only been reported that steam removes the amorphous carbon and opens their ends.[9] But the role of steam on the degree of purity, length distribution and wall structure of the resulting CNTs has not been previously investigated and will be the focus of the present chapter

3.3. Steam treatment procedure

The MWCNTs employed in this study were CVD grown using Fe as catalyst (Thomas Swan Ltd). The MWCNT purification with steam involved two steps. Firstly, the as-received material was finely grounded with an agate mortar and pestle and spread on the center part inside a silica tube of 5 cm in diameter. The silica tube, opened at both ends, was then placed into the alumina tube of the furnace and purged with argon (150 mL min^{-1}) for 2 h to allow the complete removal of atmospheric oxygen. Steam was introduced by flowing the incoming argon through a bubbler with hot water (98 ^{o}C). Therefore, a mixture of Ar/steam gets in contact with the sample. A photograph of the employed system is presented in **Figure 3.1.** The temperature of the furnace was then increased up to 900 ^{o}C and dwelled for different periods of time between 1 to 20 h. Nonetheless, time points higher than 15 h resulted in the complete oxidation of the MWCNTs, leaving behind only the inorganic solid residue as a product. Therefore, further characterization was done only for samples treated between 1 to 15 h.

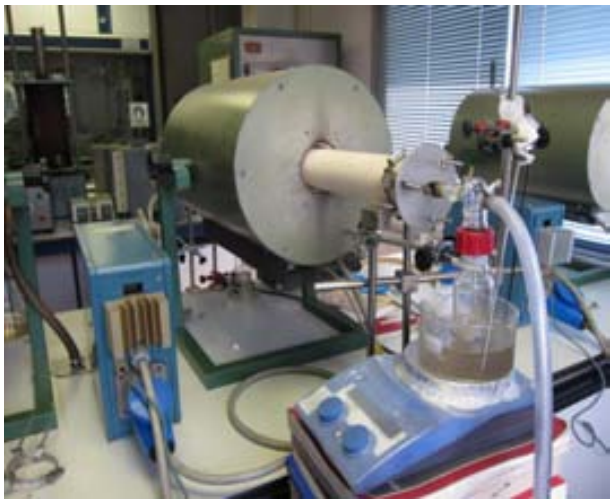

Figure 3.1. Photograph of the purification set-up. A bubbler filled with distilled water is placed on top of a heating plate and attached to a horizontal tubular furnace

The second step involved a treatment with 6 M HCl to remove any catalytic particles present in the sample. Finally the powder was collected by filtration through a 0.2 μm polycarbonate membrane and washed with distilled water until the pH of the filtrate was neutral.

3.4. Characterization and discussion

Thermogravimetric analysis

Thermogravimetric analysis (TGA) under flowing air was conducted from room temperature to 950 ºC for both as-received and steam purified samples for different periods of time: 1 h, 1.5 h, 2 h, 2.5 h, 5 h, 10 h and 15 h, followed by an HCl wash (**Figure 3.2**). TGA consists of a precision balance subjected to a controlled temperature program.

TGA provides information on the MWCNTs purity. On the one hand the value of the final wt% can be correlated with the amount of inorganic impurities and on the other hand the onset of combustion provides information on the type and amount of carbonaceous impurities. In a TGA under air conditions, all carbon species are oxidized to carbon dioxide, and any inorganic compound present form their corresponding oxides. Therefore, the residue from the TGA analysis must correspond to inorganic impurities from the synthesis of the nanotubes.

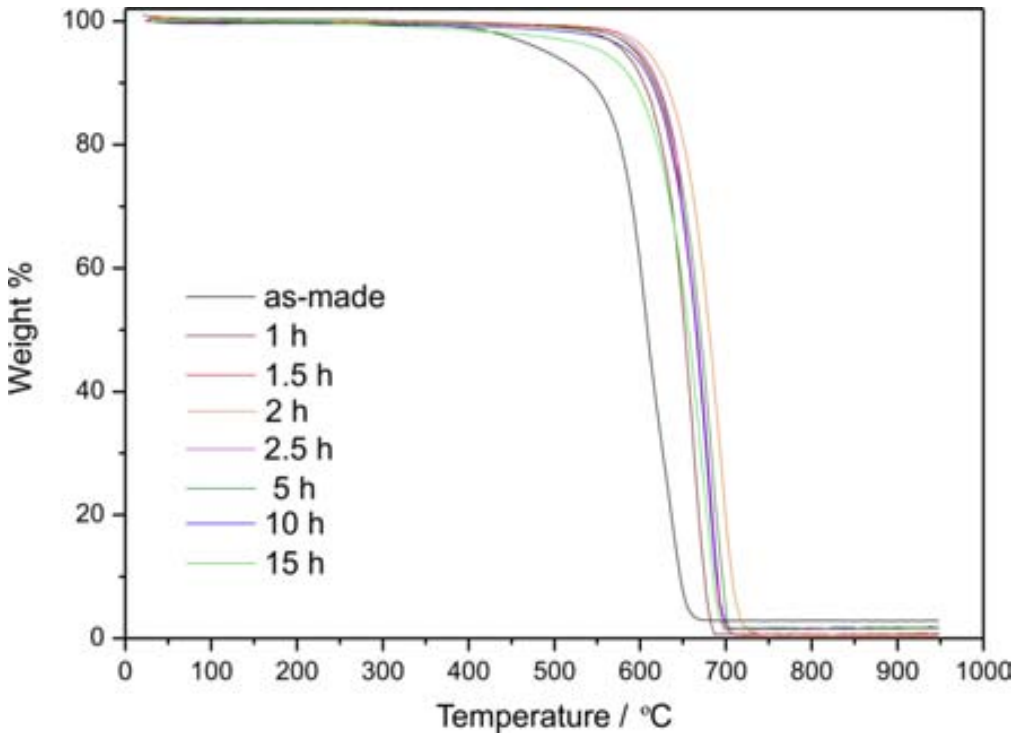

Figure 3.2. TGA in air of as-received MWCNTs and steam-purified MWCNTs from 1.5 h up to 15 h (after HCl wash).

It is clearly visible on **Figure 3.2.** that the onset of the combustion temperature is different for each sample. Both the amount of inorganic particles[19] and amorphous carbon[20] present in the samples of CNTs can influence the temperature at which carbon starts to oxidize. Amorphous the sample is more reactive towards oxygen than CNTs and graphitic particles and therefore its oxidation starts at much lower temperatures. Hence, MWCNTs with a higher degree of purification ought to start its oxidation at higher temperatures. This behaviour is in the TGA analysis of the samples, where raw MWCNTs have a much earlier onset of combustion than all steam-purified MWCNTs.

Compared to as-received material, which contains a 2.8 wt.% of inorganic solid residue, a decrease is observed up to 1.5 h of steam treatment, down to 0.5 wt.%. Longer treatments result in an increase of the inorganic content which levels off at about 1.9 wt.% for prolonged treatments (10-15 h). This reduction is explained by the fact that, after steam exposure, iron catalyst particles were exposed, as the graphitic particles surrounding them were completely eliminated by steam. Thus, it allows the complete removal of the catalyst used during the synthesis of the MWCNTs. The solid residue obtained after the thermogravimetric analysis of the samples in air is typically attributed to the oxidation of the metal employed for the growth of the CNTs. Therefore, in the

present case the residue would correspond to iron oxide (Fe_2O_3) since iron is used for the synthesis of the nanotubes. Taking this into account it is possible to determine the amount of catalytic particles (Fe) present in the prepared samples (**Figure 3.3.**). From this analysis the lowest iron content achieved is 0.17 wt% Fe (1.5 h steam), in contrast to 0.99 wt% for the as received material.

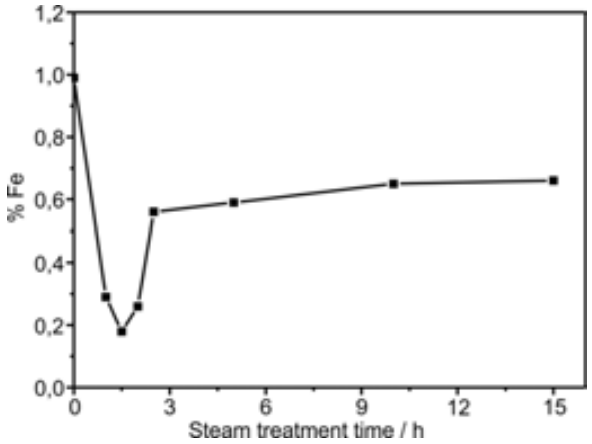

Figure 3.3. a) Amount of iron nanoparticles present in the MWCNTs samples before (0 h) and after steam treatment (1 h up to 15 h) followed by an HCl wash. Values are determined from the TGA residue assuming that corresponds to Fe_2O_3.

Magnetic measurements

Magnetic measurements were performed to independently assess the percentage of metal catalyst in all the steam-purified samples.[21] We analyzed the magnetic behaviour of iron, the metal catalyst employed in the synthesis of the CVD MWCNTs used in the present study. Therefore, was all the residue obtained from TGA to be Fe_2O_3 as expected, the percentage obtained with SQUID should match to the one determined by TGA.

Magnetic measurements are conducted with a Superconducting Quantum Interference Device (SQUID) magnetometer. In this case, the sample was placed inside a diamagnetic gelatine capsule and the data was acquired with an applied field from -50.000 Oe to +50.000 Oe at 10 K to obtain the hysteresis loops.

Figure 3.4. presents the hysteresis loops of both as-received MWCNTs and after 1.5 h steam purification followed by an HCl treatment. The as-received MWCNTs present a clear ferromagnetic behaviour from the iron superposed onto a paramagnetic contribution from the capsule, whereas in the purified sample the weak diamagnetic response from the holder starts to prevail. This illustrates a dramatic decrease in the amount of metal catalyst present in the purified sample.

Comparison of the saturation magnetization (M_s) obtained for as-received and purified MWCNTs and the bulk M_s of Fe (from bibliography) allows the determination of the amount of Fe present in the samples. Considering that the nature of the catalyst particles is pure Fe, and with iron having a bulk saturation magnetization of 221.7 emu·g^{-1},[22] the amount of metal catalyst in samples would be 0.99 wt.% for the as-received material and 0.022 wt.% for the 1.5 h steam purified sample. The quantity of Fe assessed by magnetic measurements in the steam purified MWCNTs turns out to be an order of magnitude lower than that determined by TGA. Even if the catalyst had reacted during the purification, either creating iron oxide due to an oxidation by the steam, or forming iron carbide from a reaction with carbon the inorganic residue obtained by SQUID measurements would still be below the ones revealed by TGA. Therefore, taking into account the Ms of Fe_3C (140 emu·g^{-1}), γ-Fe_2O_3 (87 emu·g^{-1}) and Fe_3O_4 (92 emu·g^{-1}) this was discarded.

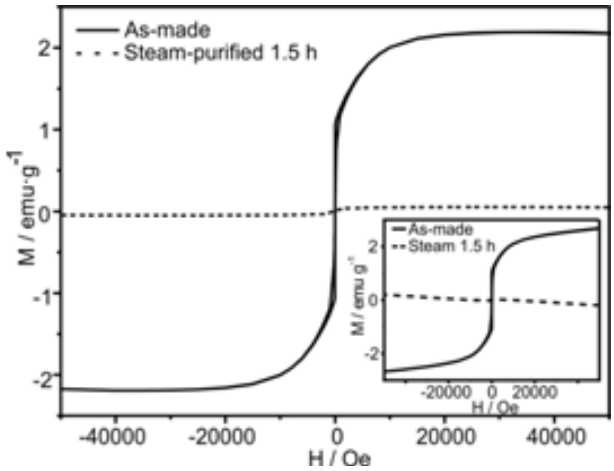

Figure 3.4. Hysteresis loops at 10 K for as-made MWCNTs and 1.5 h steam and HCl purified MWCNTs, after linear subtraction. Raw data is presented in the inset.

There is a clear mismatch between the metal content present in the MWCNT samples if we use TGA or SQUID. This means that not all the inorganic impurities present in the samples are magnetic SQUID cannot detect them. Thus, complementary technique was needed to fully assess the composition of the impurities present in the samples.

X-ray Photoelectron Spectroscopy

X-ray Photoelectron Spectroscopy (XPS) allows the determination of the elemental composition in a material. XPS measures the kinetic energy and the number of electrons that, after the irradiation with an X-ray beam, escape from a defined area on the surface of the material providing information of the chemical and electronic states of the

constituent elements. Survey-scan was conducted with a Pass Energy of 160 eV and high resolution scans at a Pass Energy of 20 eV We performed XPS analysis of the 10 h steam treated sample to determine the presence of any other inorganic species that can be present as impurities from the synthesis of MWCNTs. Whereas the amount of iron was below the detection limit of this technique, in agreement with the low level of catalyst determined by SQUID, an aluminium peak is clearly visible (**Figure 3.5.**). Most likely aluminium is present in the sample in the oxide form as alumina, a commonly employed refractory material for high temperature syntheses.[23] The presence of alumina impurities would indeed contribute to the TGA residue but not to the SQUID analysis, and accounts for the differences observed between both methods. This explains the fact that, after long purification treatments, magnetic measurements reveal the presence of a low amount of magnetic material (10 h 0.007 wt% Fe), whilst TGA analysis still showed wt% of inorganic residue. Most of the metal catalyst content is removed after the treatment and acid wash, though there is a little percentage that remains sheathed by thick graphitic layers that are difficult to be oxidized. On the other hand, alumina cannot be dissolved by an HCl wash and it will remain in the sample independently of the steam treatment time. Therefore, with the performed purification treatments is not possible to completely diminish the TGA residue.

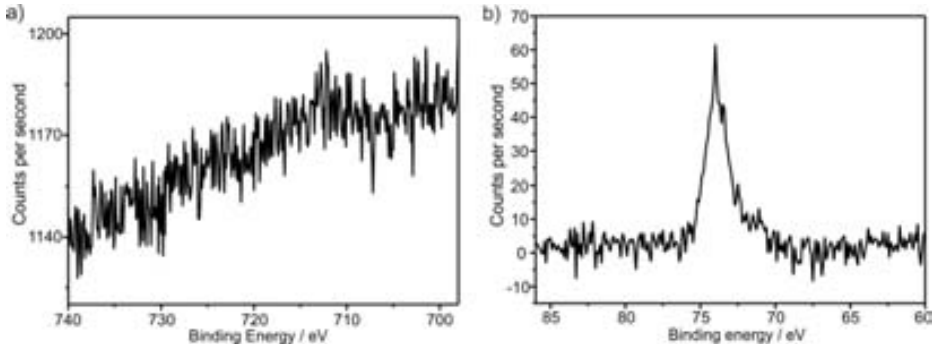

Figure 3.5. XPS spectra on the a) Al 2p region and b) Fe 2p region of steam-treated MWCNTs during 10 h followed by an HCl wash.

In addition to the determination of the inorganic compounds, the organic fraction can also be detected by XPS analysis, from the high resolution scans of the C1s and O 1s regions. (**Figure 3.6.**) Was oxygen to be identified, then the MWCNTs would contain functionalities added during the purification process. Similar levels of oxygen were found for both as-received and steam treated samples. Consequently, no oxygen-bearing functionalities were incorporated onto the MWCNT walls. The small percentage of oxygen observed is likely to arise from the alumina impurities and from absorbed atmospheric species. In addition, examination of the C1s peak also gives information of the oxygen

presence of functionalities, if any, which would appear as a shoulder of the main peak towards higher energies. Yet those were not detected in any of the analysed MWCNTs.

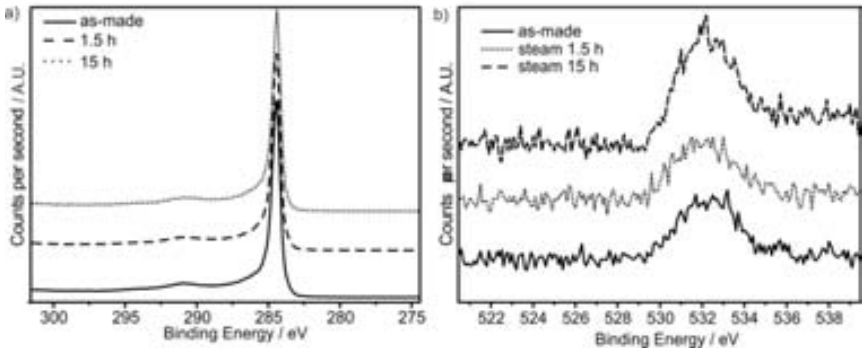

Figure 3.6. XPS spectra on the a) C 1s and b) O 1s regions of as-received MWCNTs and steam-purified MWCNTs during 1.5 h and 15 h. Spectra have been normalized for an ease of comparison.

Elemental analysis

Contrary to what happens to most commonly employed methods which use oxidizing agents,[5] XPS unveiled that steam is an efficient purification method that avoids the formation of any oxygen-based functionalities. However, apart from oxygen, hydrogen could also be incorporated into the MWCNTs structure as a result of the employed protocol. Elemental analysis (EA) gives information on the amount of C, N, H and S in the sample. Steam treated samples during 1.5 h and 15 h were measured after being treated in HCl (**Table 3.1.**). From these analyses it can be seen that the quantity of hydrogen in the samples is negligible (<0.2 wt.%), indicating that no functional groups containing this element are present on the MWCNTs. The threshold of <0.2 wt.% used for hydrogen quantification is the same than that of N and S which are certainly not expected in these samples.

Table 3.1. Amount of carbon, hydrogen, nitrogen, and sulfur obtained by elemental analysis of steam-treated samples for 1.5 h and 15 h (after HCl wash).

	at.% C	at.% H	at.% N	at.% S
Steam 1.5 h	97.79	<0.2	<0.2	<0.2
Steam 15 h	95.4	<0.2	<0.2	<0.2

Therefore, combining both XPS and elemental analysis we can conclude that no detectable functional groups are introduced in the MWCNT structure even after 15 h of steam exposure.

Raman Spectroscopy

Following the inspection of the degree of functionalization, and as a consequence of not finding any type of functional groups by either XPS or EA, we analyzed the samples by Raman spectroscopy.

Raman spectroscopy provides information on the CNT structure and purity. The Raman spectrum of MWCNTs contains two very characteristic peaks. The G-band arising at about 1575 cm^{-1} is related to well-ordered sp^2 graphite-type structures, whereas the D-band centered about 1341 cm^{-1} is commonly attributed to disordered sp^3-hybridized carbon material from defects and functionalities. The relative intensities of these peaks are probes of CNT wall integrity and degree of functionalization.[24] Beside those, in the Raman spectrum of MWCNTs it can be found a band at ~1620 cm^{-1} which appears as a shoulder on the G band and is denoted as D' band , a broad band at ~1200 cm^{-1}, and a band located between G and D band which is denoted as D'' band. D" band at ~1500 cm^{-1} originates only from the presence of amorphous carbon. Therefore, the intensity ratios of D@ and G bands can be used to estimate the purity of MWCNT samples.[25]

Figure 3.7. displays Raman spectra of the steam treated samples along with the as-received material for both green (514 nm; **Fig. 3.7.a**) and red lasers (633 nm; **Fig. 3.7.b**). The D/G intensity ratios derived from the presented spectra are summarized in **Figure 3.7.c**.

A moderate increase in the D/G ratio is observed for steam treated samples, no functional groups were detected by either XPS or EA, and we attribute this slight increase in the D/G ratio to the end-opening of the nanotubes. Contrary to other purification methods, for instance those employing strong oxidizing agents that react with all types of carbon without selectivity, steam being a mild oxidizing agent is less likely that reacts with carbon present on the tips, though it is far more reactive than the one placed at the walls. Since there is a continuous increase in the D/G ratio, this could indicate that shorter MWCNTs are present after long times of steam treatment. The amount of C sp^2 would be diminished (wall structure) with respect to the C sp^3 (ends) and this would be reflected as an increase of the D-band. Moreover, The D"/G ratios are presented in **Figure 3.7.d** to estimate the content of amorphous carbon in our samples. D"/G ratios decrease for the steam treated samples compared to as-received material, indicating that steam decreases the amount of amorphous carbon from the as-received MWCNTs.

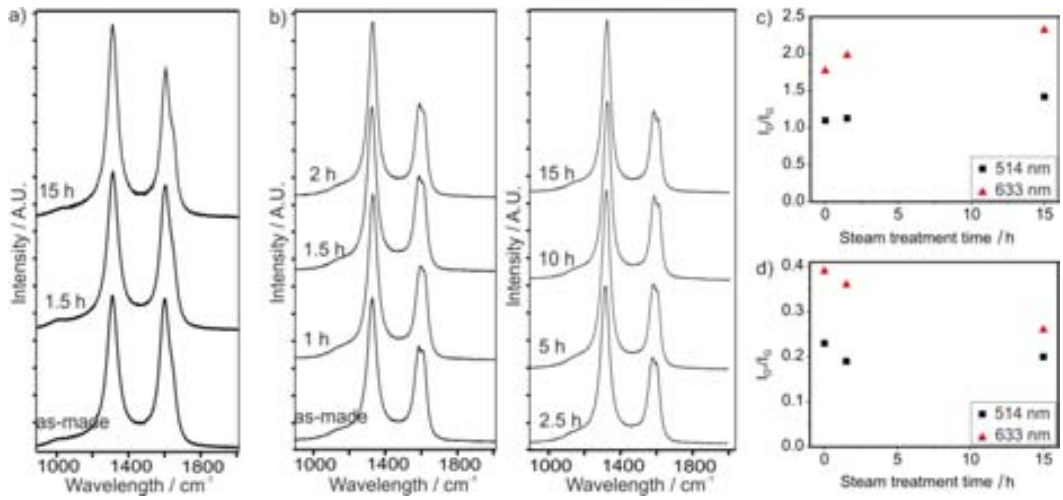

Figure 3.7. Raman spectra of as-made MWCNTs and steam-treated MWCNTs for different periods of time. a) Spectra obtained with green laser (514 nm). b) Spectra obtained with red laser (633 nm). c) Summary of the D/G band intensity ratio with respect of steam purification time for both lasers. d) Summary of the D″/G band intensity ratio with respect of steam purification time for both lasers.

Transmission electron microscopy

To get further insights on any structural changes that can take place during the purification treatment, we directly visualized the structure of the MWCNTs by High Resolution Transmission Electron Microscopy (HRTEM). HRTEM provides high magnification images where the CNT walls can be easily distinguished.[26, 27] Hence, if there were structural defects, these could be easily detected.[28] This technique can provide information down to the atomic scale.[29, 30]

Figure 3.8. displays HRTEM images of a MWCNT from the as-received material where the walls are clearly visible, and a MWCNT after a prolonged steam treatment (10 h). Albeit it is a long treatment, the MWCNT structure has been well preserved. The walls have no apparent breaks and the tubular structure remains intact. From a qualitative point of view the steam-treated MWCNTs have comparable structural integrity to as-received CNTs, which also natively contain defects. Therefore HRTEM confirms that the amount of defects introduced during the steam purification is sensibly low and that the observed increase in the D/G intensity ratio by Raman spectroscopy is most likely related to the end-opening and shortening of the MWCNTs.

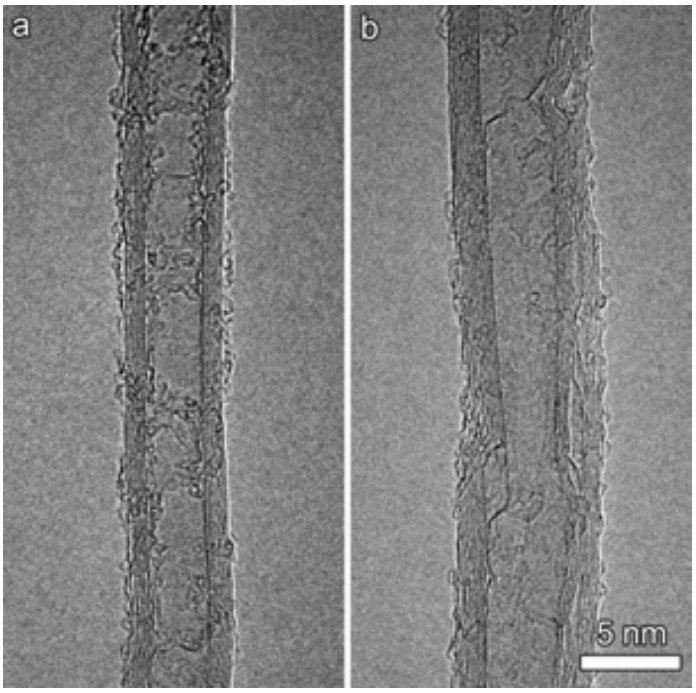

Figure 3.8. HRTEM images of a) as-received MWCNTs and b) Steam treated MWCNTs during 10 h.

According to the data obtained for MWCNT shortening seems to take place during the treatment. We therefore evaluated the length distribution of the MWCNTs for each steam treatment time. To do so, the length of MWCNT was determined from low magnification Transmission Electron Microscopy (TEM) images.

For comparison we analysed the as-received material, the sample presenting the lowest amount of solid residue (1.5 h steam), and three additional samples with longer steam treatments (5 h, 10 h and 15 h) (**Figure 3.9.**). For each sample, the length of 150-200 nanotubes was measured to, and the results are presented as histograms in the figure. When steam purification is carried out for a prolonged time, the length of the resulting MWCNTs is extremely diminished and a narrower length distribution is observed. For instance a median length of 0.58 μm is achieved for MWCNT samples treated with steam for 15 h. These results interestingly show that the length of the MWCNTs can be easily modulated and allows to create a guideline to obtain a specific MWCNT length distribution. We simply need to know which MWCNT length is needed for that specific application and applying a given steam treatment time to obtain the desired length distribution.

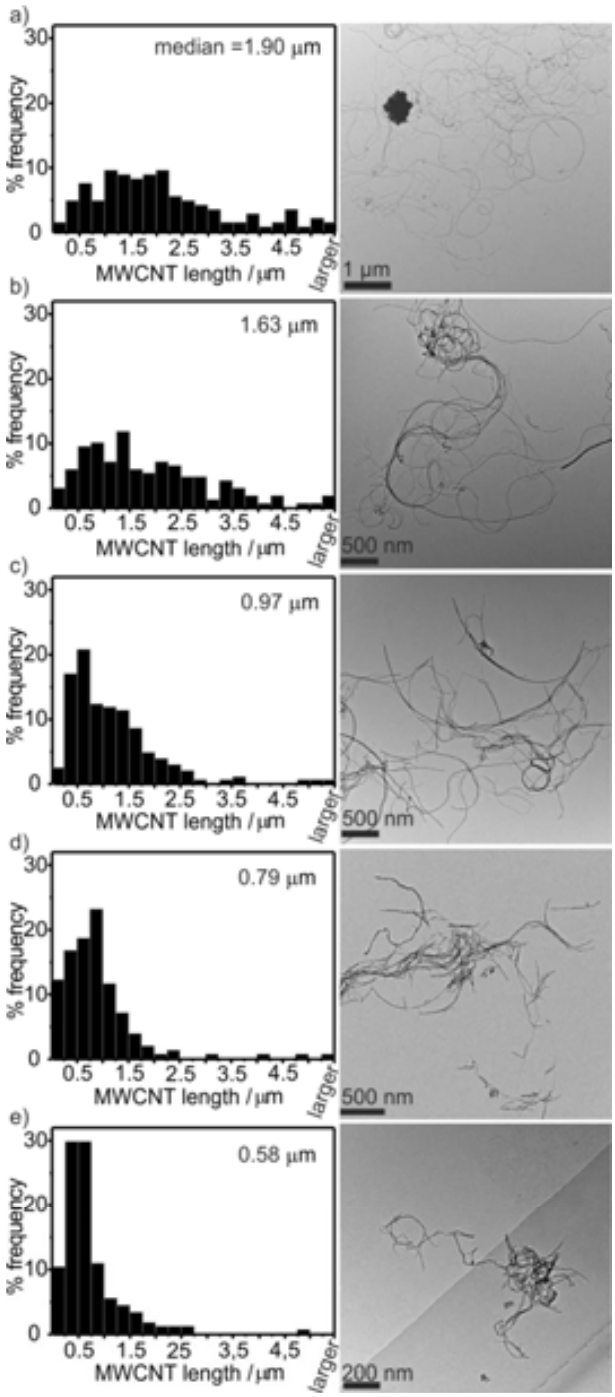

Figure 3.9. Low magnification TEM images and length distribution histograms of a) as-received MWCNTs, b) steam-treated MWCNTs for 1.5 h, c) 5 h, d) 10 h and e) 15h. All samples have undergone an HCl wash. Note that image magnification is different for each image to make more easily the MWCNTs visible.

3.5. Conclusions

Steam treatment was employed to afford both purification and shortening of multi-walled carbon nanotubes (MWCNTs). Firstly MWCNTs were heated up to 900ºC in an Ar/steam atmosphere for different periods of time. Then, the exposed iron catalyst particles were removed with HCl. We have investigated the role that the steam treatment time plays on the purification, wall structure and length distribution of MWCNTs.

- The low residual amount of iron particles after the steam and HCl treatments makes the whole range of steam-purified samples interesting for further application. Yet, not all the inorganic impurities presented magnetic behaviour and alumina, a refractory material employed for high temperature syntheses, was also present in the samples. A similar, and low, percentage of oxygen was detected for both as-received and steam treated MWCNTs, meaning that no functionalities were added during the purification process. In addition to that, no significant MWCNT wall defects were detected by either Raman or HRTEM, and the data was consistent with the end-opening of the MWCNTs.
- Steam treatment allows to modulate the length distribution of the MWCNTs. The longer the treatment the shorter the resulting MWCNTs will be.

Steam is a simple, economic, and environmentally friendly method that results in end-opened high-quality nanotubes, the length of which can be easily modulated by a mere change of the treatment time. Short CNTs are for instance desired in biomedical applications. On the other hand, open-ended CNTs with a low degree of functionalities are of interest for subsequent filling experiments since functional groups at the tips have been shown to block the entry ports of the nanochannels. Therefore, steam further expands the toolbox of purification, end-opening and shortening strategies that allow the preparation of tailored MWCNT samples for selected applications.

3.6. References

1. C. E. Banks, A. Crossley, C. Salter, S. J. Wilkins and R. G. Compton, *Angewandte Chemie International Edition*, 2006, 45, 2533-2537.
2. A. Ambrosi and M. Pumera, *Chemistry – A European Journal*, 2010, 16, 10946-10949.
3. S. Koyama, Y. A. Kim, T. Hayashi, K. Takeuchi, C. Fujii, N. Kuroiwa, H. Koyama, T. Tsukahara and M. Endo, *Carbon*, 2009, 47, 1365-1372.
4. Y. Liu, Y. Zhao, B. Sun and C. Chen, *Accounts of Chemical Research*, 2012, 46, 702-713.
5. H. Hu, B. Zhao, M. E. Itkis and R. C. Haddon, *The Journal of Physical Chemistry B*, 2003, 107, 13838-13842.
6. V. Datsyuk, M. Kalyva, K. Papagelis, J. Parthenios, D. Tasis, A. Siokou, I. Kallitsis and C. Galiotis, *Carbon*, 2008, 46, 833-840.
7. A. Suri and K. S. Coleman, *Carbon*, 2011, 49, 3031-3038.
8. K. Hata, D. N. Futaba, K. Mizuno, T. Namai, M. Yumura and S. Iijima, *Science*, 2004, 306, 1362-1364.
9. G. Tobias, L. Shao, C. G. Salzmann, Y. Huh and M. L. H. Green, *The Journal of Physical Chemistry B*, 2006, 110, 22318-22322.
10. B. Ballesteros, G. Tobias, L. Shao, E. Pellicer, J. Nogués, E. Mendoza and M. L. H. Green, *Small*, 2008, 4, 1501-1506.
11. M. T. Martínez, M. A. Callejas, A. M. Benito, M. Cochet, T. Seeger, A. Ansón, J. Schreiber, C. Gordon, C. Marhic, O. Chauvet and W. K. Maser, *Nanotechnology*, 2003, 14, 691-695.
12. M. Mahmood, Y. Xu, V. Dantuluri, T. Mustafa, Y. Zhang, A. Karmakar, D. Casciano, S. Ali and A. Biris, *Nanotechnology*, 2013, 24, 045102.
13. S. R. Ji, C. Liu, B. Zhang, F. Yang, J. Xu, J. Long, C. Jin, D. L. Fu, Q. X. Ni and X. J. Yu, *Biochimica et biophysica acta*, 2010, 1806, 29-35.
14. Z. Liu, W. Cai, L. He, N. Nakayama, K. Chen, X. Sun, X. Chen and H. Dai, *Nat Nano*, 2007, 2, 47-52.
15. B. Sitharaman, X. Shi, X. F. Walboomers, H. Liao, V. Cuijpers, L. J. Wilson, A. G. Mikos and J. A. Jansen, *Bone*, 2008, 43, 362-370.
16. X. Zhang, K. Jiao and X. Wang, *Electroanalysis*, 2008, 20, 1361-1366.
17. A. Fonseca, S. Reijerkerk, J. Potreck, K. Nijmeijer, Z. Mekhalif and J. Delhalle, *Desalination*, 2010, 250, 1150-1154.
18. X. Wang, J. Wang, H. Chang and Y. Zhang, *Advanced Functional Materials*, 2007, 17, 3613-3618.
19. B. Ballesteros, G. Tobias, M. A. H. Ward and M. L. H. Green, *The Journal of Physical Chemistry C*, 2009, 113, 2653-2656.

20. R. Brukh and S. Mitra, *Journal of Materials Chemistry*, 2007, 17, 619-623.

21. T. Kolodiazhnyi and M. Pumera, *Small*, 2008, 4, 1476-1484.

22. R. M. Cornell and U. Schwertmann, *The iron oxides: structure, properties, reactions, occurences and uses*, Wiley-VCH Verlag GmbH & Co., 2004.

23. A. Cassell, J. Raymakers, J. Kong and H. Dai, *The journal of physical chemistry. B*, 1999, 103, 6484-6492.

24. U. Kim, C. Furtado, X. Liu, G. Chen and P. Eklund, *Journal of the American Chemical Society*, 2005, 127, 15437-15445.

25. Y. C. Choi, K.-I. Min and M. S. Jeong, *Journal of Nanomaterials*, 2013, 2013, 6.

26. I. Suarez-Martinez, C. P. Ewels, X. Ke, G. Van Tendeloo, S. Thiess, W. Drube, A. Felten, J.-J. Pireaux, J. Ghijsen and C. Bittencourt, *ACS Nano*, 2010, 4, 1680-1686.

27. A. Felten, X. Gillon, M. Gulas, J.-J. Pireaux, X. Ke, G. Van Tendeloo, C. Bittencourt, E. Najafi and A. P. Hitchcock, *ACS Nano*, 2010, 4, 4431-4436.

28. C. S. Allen, A. W. Robertson, A. I. Kirkland and J. H. Warner, *Small*, 2012, 8, 3810-3815.

29. S. Y. Hong, G. Tobias, B. Ballesteros, F. El Oualid, J. C. Errey, K. J. Doores, A. I. Kirkland, P. D. Nellist, M. L. H. Green and B. G. Davis, *Journal of the American Chemical Society*, 2007, 129, 10966-10967.

30. F. Börrnert, S. Gorantla, A. Bachmatiuk, J. H. Warner, I. Ibrahim, J. Thomas, T. Gemming, J. Eckert, G. Cuniberti, B. Büchner and M. H. Rümmeli, *Physical Review B*, 2010, 81, 201401.

4

Results II:

Functionalization of carbon nanotubes for their use in biomedical applications

In this chapter we present the results corresponding to the modification of the CNT walls to form hybrids suitable for biomedical applications, in the areas of imaging and therapy. The results here summarized have been reported in the following articles:

Article 2: "Magnetically decorated multiwalled carbon nanotubes as dual MRI and SPECT contrast agents". *Advanced Functional Materials*. **2014**. 24, 13, 1880-1894.

Article 3: "The Shortening of MWNT-SPION Hybrids by Steam Treatment Improves their Magnetic Resonance Imaging Properties In vitro and In Vivo". *Submitted.*

Article 4: "Increased dispersion of Single-Walled Carbon Nanotubes by functionalization with metallacarborane cosane for Boron delivery in therapy". *In preparation*.

4.1. Objectives

1. Optimize the preparation of a dual-imaging agent for both Magnetic Resonance Imaging (MRI) and SPECT/CT tomography.
2. Study the effect of the MWCNT length on the imaging capabilities of the hybrid.
3. Functionalize SWCNTs to form a hybrid with high ^{10}B content with a high degree of SWCNT dispersibility.

4.2. Summary

Carbon nanotubes (CNTs) are considered as one of the most promising nanomaterials to be used for biomedicine applications in the areas of drug delivery, imaging and therapy. One of the main areas of research of MWCNTs for biomedical applications is their use in biomedical imaging. There is a huge effort being conducted in the development of imaging contrast agents to enhance the signal obtained.[1-3] MWCNTs can be employed as carriers of this contrast agents, as its needle shape has been proved to favour the internalization in cells.[4] One can benefit from their intrinsic properties, and use CNTs as optical tags or contrast agents for various imaging techniques.[5-7]

Nevertheless, their imaging capabilities can be greatly expanded *via* the incorporation, either covalently or non-covalently, of various imaging probes such as fluorophores, radiotracers or Magentic Ressonance Imaging (MRI) contrast agents.[8-10]

Many studies have been conducted to employ CNTs for MRI by incorporating paramagnetic gadolinium (Gd^{3+}) or superparamagnetic iron oxide nanoparticles (SPION) into CNTs. These two paramagnetic contrast agents are both clinically approved. Gd^{3+} serves mainly as a positive contrast agent which increases proton spin-lattice relaxation times (R_1); whereas iron oxide provides a negative contrast agent by increasing spin-spin proton transverse relaxation times R_2 and R_2*. For instance, iron oxide-CNTs hybrids have been recently investigated for *in vivo* MRI in the form of MWCNT-Fe_3O_4.[11] On the other hand, radiolabelled CNTs have also been tracked *in vivo* and even employed for cancer therapy.[12-15]

When it comes to therapeutic applications, carborane clusters have been reported to be appropriate ^{10}B-rich agents for Boron neutron capture therapy (BNCT). Those are delivered to tumours and their subsequent irradiation with low-energy neutrons causes the selective destruction of the targeted cells.[16, 17] By covalent reaction with SWCNTs a more site

specificity can be achieved for therapeutic applications.[18, 19] Therefore, SWCNTs could be useful boron delivery agents. It has been previously stated that functionalized SWCNTs with carborane-based derivatives were able to cross cell membranes and concentrate into the cytoplasm without toxic effects.[20]

In this chapter we have investigated strategies to incorporate biomedically relevant payloads onto the CNT walls. Those include covalent and noncovalent functionalization of the CNTs. The noncovalent functionalization was explored by decoration of MWCNTs with radiolabelled SPION. On the other hand, covalent functionalization was investigated via reaction of SWCNTs with metallacarborane clusters.

4.3. Magnetically decorated MWCNTs as dual imaging contrast agents

From material scientists' points of view, efforts have been made in the development of multimodal imaging contrast agents. The most spreaded clinical diagnostic techniques are magnetic resonance imaging (MRI) and nuclear imaging. MRI is already a standard medical imaging technique which offers excellent spatial and temporal resolution, and good soft tissue contrast.[21] Nuclear imaging including single photon emission computed tomography (SPECT) and positron emission tomography (PET) involves the use of radioisotopes and has the advantages over other modalities of high sensitivity and the possibility to perform functional imaging.[22] The development of a contrast agent that can be used in combination of these two techniques will combine the strong aspects of the two modalities. We propose magnetically decorated MWCNTs as dual MRI and SPECT contrast agents.

In here, we selected Superparamagnetic Iron Oxide Nanoparticles as an effective MRI contrast agent [23] and ^{99m}Tc as a radionuclide for SPECT/PET.[24] Those were successfully integrated to the MWCNT forming a hybrid structure.

4.3.1. Optimization of the hybrids

The synthesis of magnetic yet radioactive MWCNTs as dual MRI and SPECT contrast agents has not been previously reported. Therefore, the first part of the study was focused on the optimization of the hybrid in terms of proportion of MRI contrast agent versus MWCNTs. We wanted to examine how this was affecting the physicochemical properties of the hybrid, as well as the imaging response of the agent. Next, the R_2* magnetic properties and the efficiency of radio-labelling SPION-MWCNT hybrids were

examined. *In vivo* experiments were performed to characterize the hybrids as multimodal SPECT and MRI contrast agents.

4.3.1.1. Preparation of the SPION-MWCNT hybrids

The hybrid preparation requires different steps, namely, purification of the as-received MWCNTs, surface functionalization, decoration with MRI nanoparticles (NPs) and finally radiolabelling of the NPs.

Following the protocol described in the previous chapter, MWCNTs were purified and shortened using the steam treatment optimized in this Thesis. As steam purified MWCNTs during 1.5 h resulted in the lowest amount of inorganic content, we treated the as-received MWCNTs for this period of time. Therefore, we obtained MWCNTs of 1.63 μm length.

For the purpose of having well distributed nanoparticles along the wall of the MWCNTs we tried two different approaches. The first one consisted of incorporating the magnetic nanoparticles directly to the purified MWCNTs. Nonetheless, this resulted in hybrids with highly agglomerated nanoparticles and with a very big size (**Figure 4.1.**).

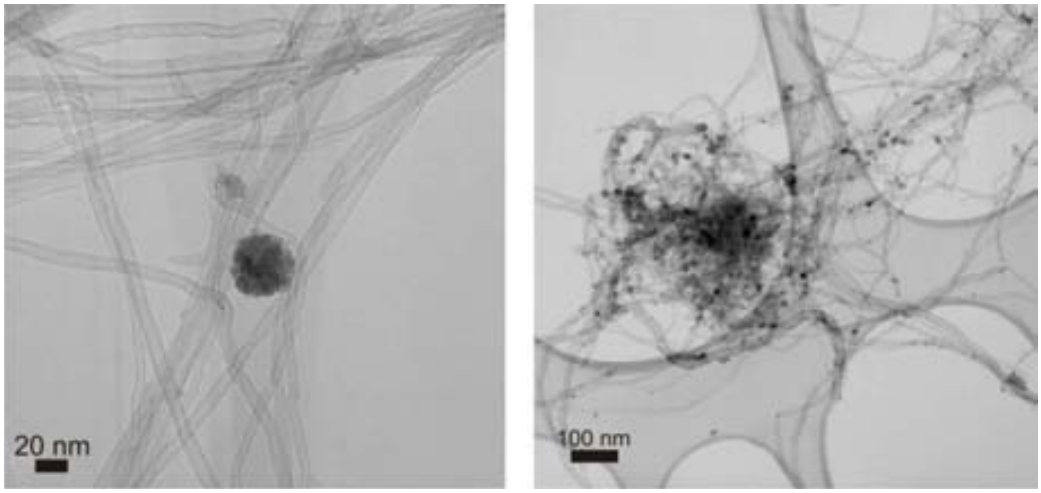

Figure 4.1. TEM images of magnetic nanoparticles-MWCNT hybrids with nanoparticles attached directly to steam purified MWCNTs.

The second approach consisted of adding oxygen-bearing functionalities, mainly carboxylic acid groups (–COOH), onto the steam-purified MWCNT tips and sidewalls. To do so, steam-purified MWCNTs were treated with a strong oxidizing agent, in this case nitric acid.[25] Briefly, MWCNT powder was added to a flask containing 3 M nitric acid and the system was heated at 130 ºC during 45 h. Magnetic nanoparticles-MWCNT hybrids

containing different amounts of iron oxide were then synthesized *in situ* by mixing the functionalized MWCNTs with an iron precursor for the formation of the nanoparticles (**Figure 4.2.**). It is known that when metal salts are dissolved in the presence of acid treated nanotubes, the metal ions interact with the surface groups present onto the MWCNTs. Such interactions were expected to occur in our samples when mixing iron acetate (precursor) with the functionalised MWCNTs, thus affording a homogeneous coverage of the iron atoms onto the surface of the MWCNTs. Subsequently, the samples were thermally treated and left exposed to air thus resulting in the formation of the iron oxide nanoparticles. This method results in better dispersed nanoparticles and with a higher degree of coverage of the MWCNT walls compared to the use of non-functionalized MWCNTs. Moreover, the size of the resulting NPs is smaller than for the previous method.

Once the magnetic nanoparticles had been attached to the walls of the MWCNT they were characterized to determine their structure. The final step was the incorporation the radioisotope by labelling the magnetic nanoparticles with ^{99m}Tc. Radio-labelling of magnetic nanoparticle-MWCNT hybrids was conducted as reported previously using a functionalized bisphosphonate (BP) namely dipicolylamine-alendronate (DPA-ale) as a linker between the magnetic nanoparticles and the radioisotope ^{99m}Tc.[26, 27] Roughly, the hybrids with different iron contents were first dispersed in 1 % Pluronic F127 to reach 1 mg/mL solutions. After that the dispersions were mixed with 1–10 MBq ^{99m}Tc-BP and incubated at 37 ºC for 30 min with gentle shaking. The radiolabelled hybrids were then separated from unbound ^{99m}Tc-BP by several centrifugation and washing with Pluronic F127 steps until no radioactivity was detected in the supernatant.

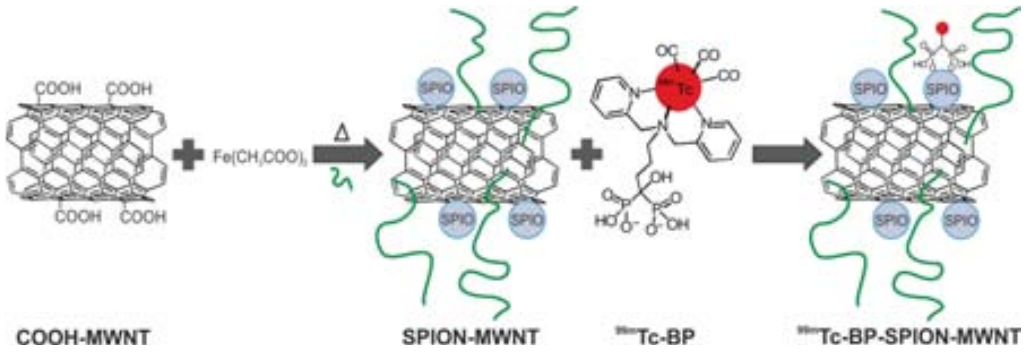

Figure 4.2. Scheme for the preparation of the MWCNT based hybrid.

4.3.1.2. Characterization and discussion

Thermogravimetric analysis

Initially, we optimized the proportion of Fe_xO_y:MWCNTs to get the major quantity of magnetic material possible without having very agglomerated nanoparticles. Hence, we prepared Fe_2O_3-MWCNT hybrids with different loadings of Fe_2O_3. The amount of iron oxide present in the hybrids was quantitatively determined by TGA carried out under flowing air (**Figure 4.3.**). The decrease in the onset of combustion temperature of the decorated nanotubes by about 150 ºC, compared to steam-purified MWCNTs, was an indicator of the presence of inorganic nanoparticles in the samples. The residue obtained after the complete combustion of carbon atoms at 600 ºC corresponded to the amount of iron oxide nanoparticles loaded onto the MWCNTs. Fe_xO_y-MWCNT hybrids containing 11.5, 28.0, 41.5 and 48.0 wt% of SPION (assuming Fe_2O_3) were obtained. Additional hybrids with more iron (II) acetate were also prepared. However, those lead to similar amounts of iron oxide between 40-50 wt% and not higher as one would expect. In addition, those hybrids contained far more agglomerated nanoparticles and were therefore not considered. Actually, Fe_2O_3-MWCNT with 48.0 wt% of iron oxide was found to be physically unstable in aqueous dispersions, and was also disregarded in further studies.

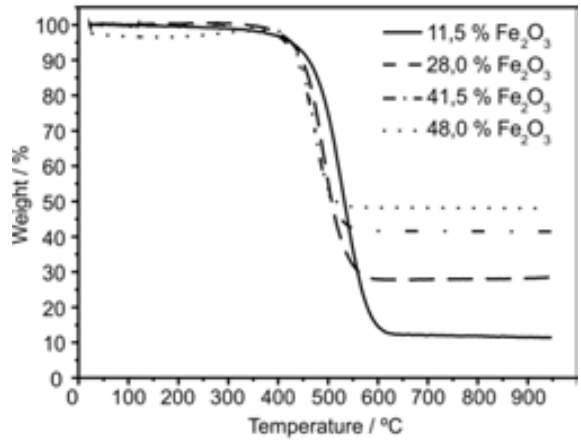

Figure 4.3. TGA of Fe_2O_3-MWCNTs in flowing air.

Magnetic measurements

Magnetic measurements were useful to clearly display the effect of the increasing amount of Fe_xO_y on the magnetic behaviour of the hybrid. **Figure 4.4.a** presents the hysteresis loop when applying a field of ±50000 Oe at 10 K of the different Fe_xO_y-MWCNT hybrids,

steam purified MWCNTs are also included as a control. Purified MWCNTs show an extremely weak magnetic signal, almost inappreciable in the figure, as expected for steam-treated MWCNTs with negligible amount of catalytic impurities.[28] In contrast to purified MWCNTs, a marked ferromagnetic behaviour was observed for the hybrids Fe_xO_y-MWCNT. As expected, samples with increasing amount of loaded Fe_2O_3 yielded higher saturation magnetization.

In order to determine whether the prepared nanoparticles presented a superparamagnetic behaviour, hysteresis loops at 300 K were recorded. As shown in **Figure 4.4.b**, no remnant magnetization was observed upon removal of the magnetic field, which is the typical behaviour of a superparamagnetic material. Collectively, it is confirmed that the MWCNTs were decorated with superparamagnetic γ-iron oxide nanoparticles (SPION). A superparamagnetic material has large magnetic susceptibility and in absence of external magnetic field there will be no reminiscent magnetization.

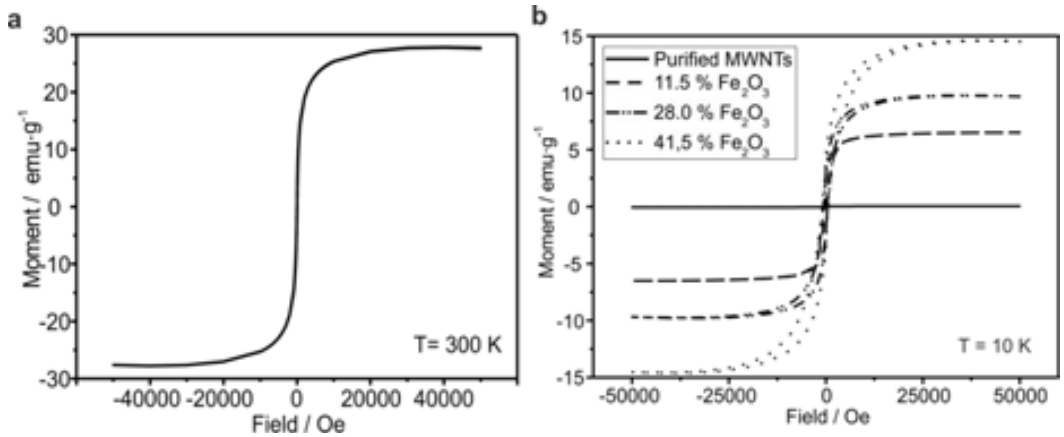

Figure 4.4. Hysteresis loops of SPION-MWCNTs a) at 10 K including purified MWCNTs for comparison and b) at 300 K for the sample containing 41.5 % Fe_2O_3. The linear background has been subtracted.

Transmission Electron Microscopy

Visual analysis of the sample by TEM allowed us to confirmed that we had formed nanoparticles and that these nanoparticles were nicely distributed and attached on the walls of the MWCNTs. TEM imaging was conducted on the different samples and in all of them SPION were found along the backbone of the carbon nanotubes (**Figure 4.5.a**). The size of SPION that decorated MWCNTs was determined based on TEM images analysis. The diameter of about 200 SPION was measured and the resulting histogram is presented in **Figure 4.5.b.** Independently of the percentage of Fe_xO_y present in the sample, the majority of the SPION have diameters between 4-8 nm, with a median value of 6.13 nm.

By HRTEM we studied the structure of the nanoparticles that were anchored to the MWCNTs. HRTEM analysis verified the presence of single-phase crystalline iron oxide nanoparticles and discarded the presence of core-shell nanoparticles (**Figure 4.5.c**). The structure was further studied by electron diffraction analysis of the nanoparticles and fast Fourier transform (FFT) of the HRTEM images, confirming that these NPs present cubic structure. The inset in **Figure 4.5.d** present the diffraction pattern of a nanoparticle corresponding to the [-233] zone axis, which corresponds to either γ-Fe_2O_3 (maghemite) or Fe_3O_4 (magnetite). However, we could not discern between the two structures, and complementary techniques were needed.

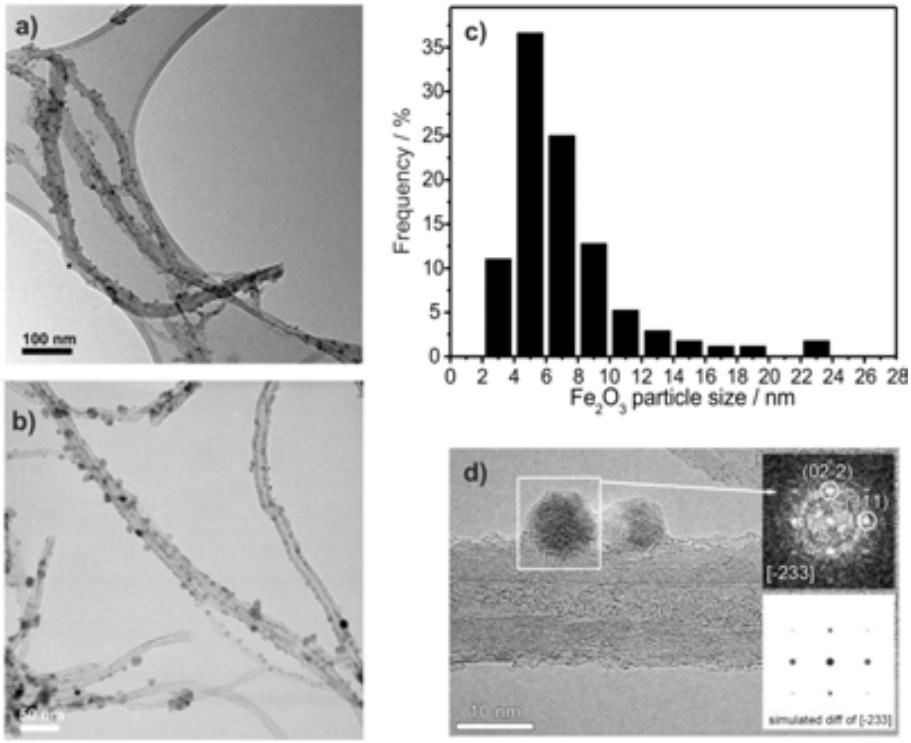

Figure 4.5. TEM analysis of SPION-MWCNTs: a,b) TEM images at two different magnifications; c) histogram of the nanoparticle size; d) HRTEM image of the hybrid; the inset presents the diffraction pattern of a nanoparticle and the simulated diffraction pattern along the zone axis.

X-Ray Diffraction and X-Ray Spectroscopy

The X-Ray Diffraction (XRD) of SPION-MWCNTs is presented in **Figure 4.6.a**. The observed peaks could be assigned to those of carbon (pdf –powder diffraction file– 750444) from carbon nanotubes and to either maghemite (γ-Fe_2O_3; pdf 391346) or magnetite (Fe_3O_4; pdf 740748). Hence, XRD could also not differentiate between the two compounds, as both γ-Fe_2O_3 and Fe_3O_4 possess spinel structures that belong to the Fm-3d space group.

Next, X-ray photoelectron spectroscopy (XPS) was performed to get further insight into the nature of the nanoparticles. A cumulative detailed scan performed over the Fe 2p region is presented in **Figure 4.6.b**. The position, shape and width of the XPS peaks and the presence of the "shake-up" satellite structure at 719.3 eV is distinctive of the γ-Fe_2O_3 structure.[29] Therefore, by XPS we could distinguish between the two structures and determine our SPION were actually maghemite.

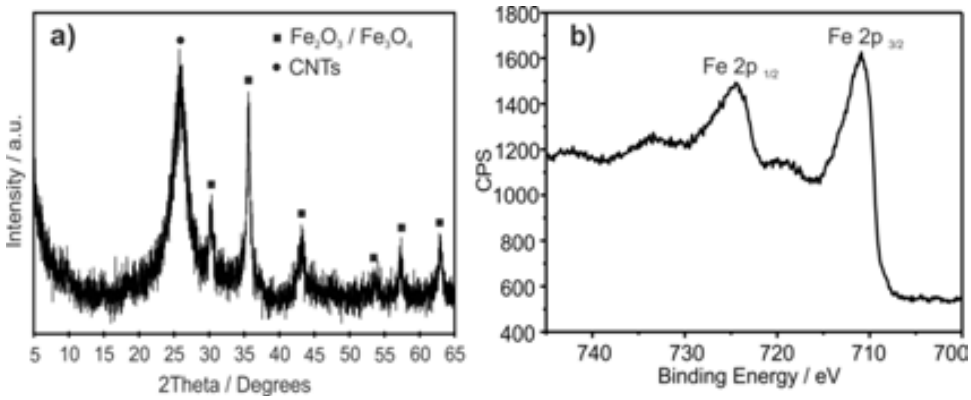

Figure 4.6. Characterization of the iron oxide nanoparticles decorating MWCNTs: a) X-ray diffraction pattern, b) X-ray Photoelectron Spectroscopy.

Biomedical studies of the hybrids

During this Thesis a short research stay was conducted during three months at the Institute of Pharmaceutical Sciences at King's College London, under the supervision of Dr. Khuloud T. Al-Jamal. There I performed the *in vitro* biomedical studies presented in this Thesis and became familiar with the *in vivo* work. The *in vivo* work was then completed by Dr. Julie T. Wang and Mr. Maxime Bourgognon.

Selection of the dispersing agent

One of the main problems for the use of carbon nanotubes comes from the fact that they cannot be dispersed in most solvents including aqueous media. For biomedical studies it is indispensable to have a uniform MWCNT dispersion. In an agglomerate state, nanomaterials may behave as large particles, hindering blood circulation and creating toxicity effects.[30]

To avoid the MWCNT precipitation in aqueous state, the use of dispersing agents is necessary.[31] For that reason, we have studied the dispersion of the SPION-MWCNT hybrids with different dispersing agents. The agents had to be biocompatible, as the main purpose was to use them for biomedical studies. Therefore we employed well stablished agents that had been previously investigated in both *in vitro* and *in vivo* studies of CNTs.

The dispersions were prepared with 1 % Pluronic® F-127 (a non-ionic triblock copolymer), 2.5 % Bovine Serum Albuminum (BSA), 0.7 mg/mL double-stranded DNA (dsDNA) and 1 mg/mL single-stranded DNA (ssDNA). 1 mg/mL SPION-MWCNTs were added to each of the dispersing agents and then bath sonicated for 30 minutes. The dispersions were left still and analyzed for 0, 10 min, 30 min, 24 h and 72 h. In **Figure 4.7.** dispersions after 30 minutes are displayed. Though it might not be clearly appreciated in the photograph, BSA and dsDNA achieved very pour dispersion and most of the material precipitated at the bottom of the vial. A slight improvement is observed for ssDNA, and a stable uniform solution is obtained with Pluronic® F-127, with no precipitated material. Hence, all the reported biomedical studies presented here have been conducted by dispersing the hybrids with 1 % Pluronic® F-127.

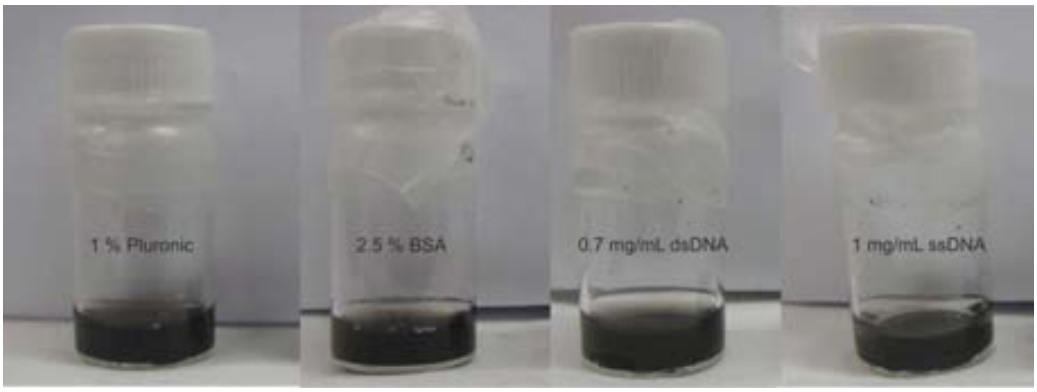

Figure 4.7. Photographs of dispersions of 1 mg/ml SPION-MWCNTs with different dispersing agents.

Magnetic Resonance Imaging and Relaxation measurements

SPION-MWCNT hybrids are promising candidates for imaging. Therefore, we did magnetic resonance (MR) studies to assess the signal obtained with the developed hybrids and compared it to "free" SPION, specifically with Endorem®, a clinically approved SPION.

The first study implied the MR measurement of the SPION-MWCNT dispersions. The transverse relaxation times (R_2*) of SPION-MWCNT with 28.0 and 41.5 % SPION dispersed in 1% agar and 0.5% Pluronic® F127 solution at different Fe concentrations was measured at 7 Tesla. SPION-MWCNTs with 11 wt% SPION were discarded because its dispersion was not ideal due to the high concentrations required to obtain an equivalent concentration of Fe to the other hybrids. Although the hybrids studied here displayed good dispersibility using 1% Pluronic® F127, phantom samples were prepared in agar to avoid any potential sedimentation of samples and thus achieve more accurate relaxation measurements. R_2^* values were calculated from their signal decay and were plotted against Fe concentration.

Figure 4.8.a shows the phantom MR imaging and R_2^* relaxation rate analysis of Endorem® and the hybrids SPION-MWCNTs containing 28.0 % and 41.5 % of Fe_2O_3 at different concentrations at an acquired echo time of 5 ms. By plotting the relaxation times versus concentrations of iron the following relaxivities (r_2^*) were calculated: 343 $s^{-1}mM^{-1}$, 425 $s^{-1}mM^{-1}$ and 325 $s^{-1}mM^{-1}$ for 28.0 % Fe_2O_3, 41.5 % Fe_2O_3 SPION-MWCNTs and Endorem respectively. Endorem® reported the lowest r_2* relaxivities while SPION-MWCNTs with 41.5 % Fe_2O_3 showed the highest r_2* making it an MR appealing probe for R_2* investigations. SPION-MWCNTs hold therefore potential for *in vivo* clinical studies. Having a higher r_2* relaxivity value implies that lower concentration of the SPION-MWCNTs will be required to achieve similar signals to that of Endorem®.

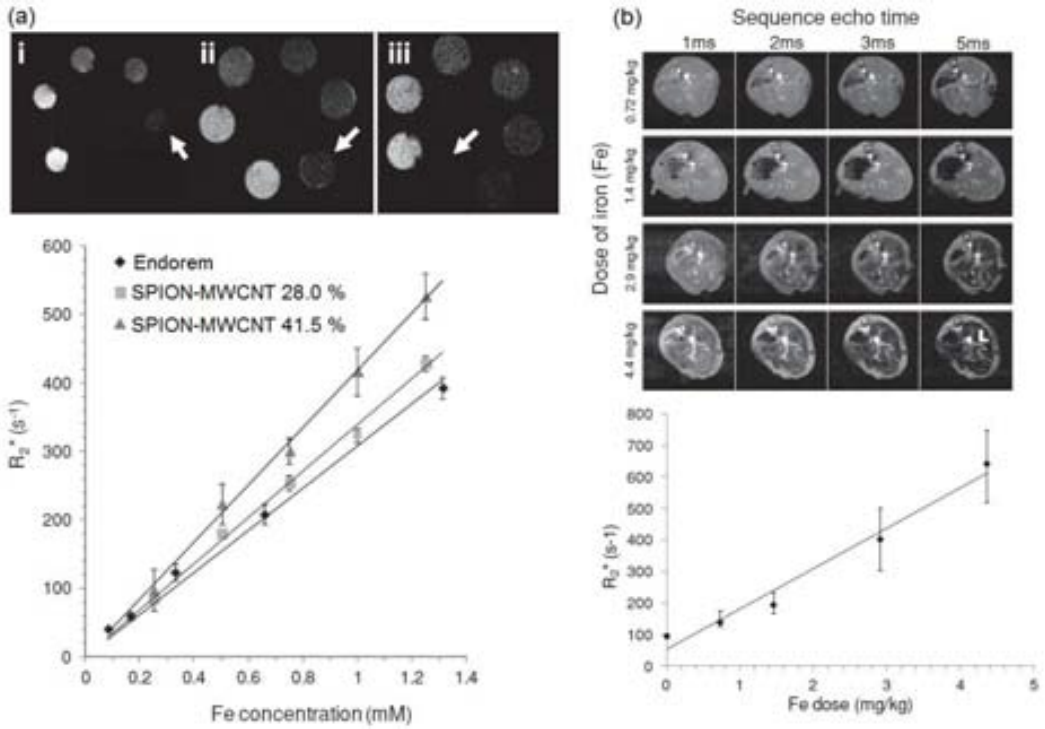

Figure 4.8. a) Phantom MR imaging of Endorem® and SPION-MWCNT containing 28.0 and 41.5 % Fe2O3 (top) and R2* relaxation time analysis as a function of Fe concentration (bottom); results are presented as mean ± S.D. (n=3); b) In vivo MR images of mouse liver 48h after injection with various doses of SPION-MWCNT containing 41.5 % Fe2O3 over time and R2* relaxation time measurements (bottom).

A high accumulation of the hybrids in the reticuloendothelial system (RES, e.g. liver and spleen) was observed after tail-vein injection of the hybrids in mice. Therefore, *in vivo* MRI was conducted in the liver to verify its behaviour as contrast agent (**Figure 4.8.b**). Liver images at different acquisition echo times against Fe concentration (mg/kg) interestingly showed a darkening of the MRI signals over time and increasing iron dosage. The

measured *in vivo* R_2* relaxation rates demonstrated time-dependent and concentration-dependent darkening in liver signals and an almost linear R_2* relaxation rate was obtained. Higher relaxation effects were observed with our constructs *in vivo* compared to previous reports that employed an equivalent amount of injected Fe.[11, 32] For instance, a reduction of 60% in R_2* was seen up by Wu et al[33] to 5 h after injection of 2.5 Fe mg/kg compared to a 69% reduction of R_2^* value obtained in our study at 48 h. Despite the different imaging time points which do not allow a direct comparison of the data, our study reveals SPION-MWCNTs enhanced liver MRI contrast and confirms that SPION-MWCNTs are suitable as a negative contrast agent.

As SPION-MWCNTs with 41.5 wt% of SPION presented the highest relaxivity values, this hybrid is the most convenient for utilizations as an imaging contrast agent. Consequently, the following studies were performed only for this hybrid.

TEM micrographs of liver and spleen sections

We next examined liver sections by TEM to confirm that the hybrid was indeed present in this organ and thus responsible for the enhanced relaxivity values. Histological examination was performed on tissues sampled at 24 h after intravenous (i.v.) injection of a dispersion containing 400 µg of SPION-MWCNTs (5.8 mg Fe/kg). Apart from liver, spleen was also investigated since both organs showed high accumulation of the hybrid. A series of TEM images were taken for hepatocytes and kupffer cells from the liver and spleen at different magnifications (**Figure 4.9.**). Hepatocytes are recognized by the presence of a substantial number of mitocondria. The analysis confirmed uptake of the hybrid not only in kupffer cells but also in hepatocytes of the liver. Co-localization of SPION and MWCNTs within the same endocytic vesicles was clearly observed in spleen cells, liver hepatocytes and kupffer cells at 24 h after injection. However, at 24 h, SPION were found dissociated from the MWCNTs perhaps due to the low pH of endocytic vesicles. These results provide sufficient evidence of the *in vivo* stability of SPION-MWCNT oxide hybrids so that they were taken up by the same cells as intact hybrids after intravenous injection.

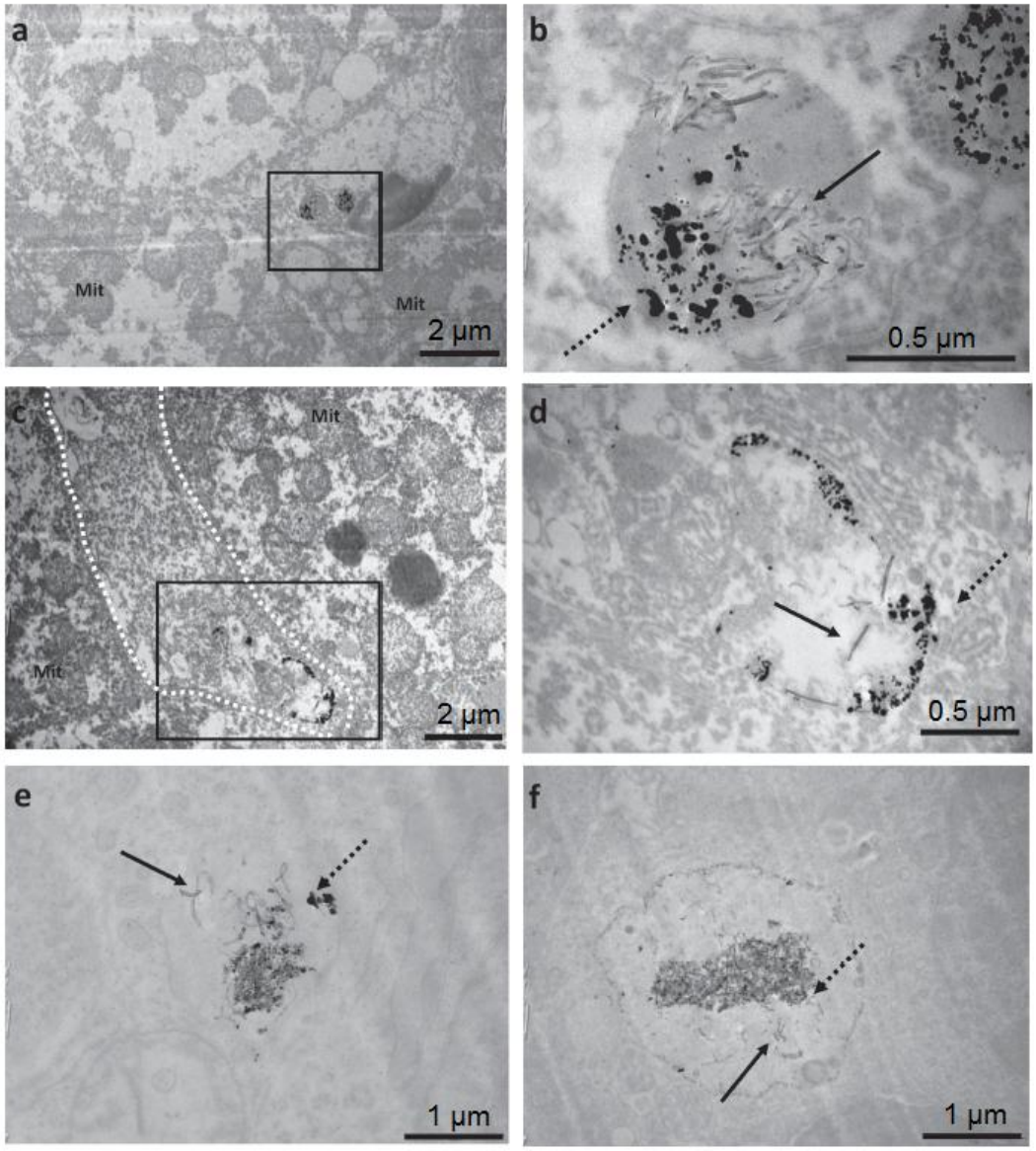

Figure 4.9. TEM micrographs of liver and spleen sections from animals injected with SPION-MWCNT with 41.5 wt% SPION at 24 h a,b) in hepatocytes, c,d) kupffer cells and e,f) spleen. (b) and (d) are higher magnification images from the inset rectangles in (a) and (c) respectively. Dashed arrows point SPION and solid arrows point MWCNTs. Mit: mitochondria.

In vivo SPECT/CT and biodistribution studies

In vivo biodistribution studies were performed byradio labelling the SPION with ^{99m}Tc-BP. The labelled hybrid is named ^{99m}Tc-BP-SPION-MWCNT. ^{99m}Tc is a γ-emitter and therefore allows *in vivo* body SPECT imaging in combination with computed tomography (CT). Post-

mortem γ-scintigraphy was conducted in parallel to SPECT/CT imaging to assess quantitatively the organ biodistribution of the hybrids over time.

^{99m}Tc-BP-SPION-MWCNT (4 MBq, 50 μg hybrid) and "free" ^{99m}Tc-BP (5 MBq) alone were intravenously injected in mice and studied at 30 min, 3 h and 24 h after injection (**Figure 4.10.a**). ^{99m}Tc-BP was mainly detected in bone, kidney and bladder at early time points (< 30 min and 3 h) due to the high affinity of bisphosphonates to bone minerals,[26] suggesting rapid renal clearance (**Figure 4.10.b**). ^{99m}Tc-BP-SPION-MWCNTs, however, showed predominant accumulation in lung, followed by liver and spleen within 30 min after injection. The signals in the liver remained constant after 4 h while a clear reduction in lung accumulation was observed over the first 4 h (**Figure 4.10.c**). The biodistribution of the ^{99m}Tc-SPION-MWCNTs is in agreement with previous reports that have observed prolonged uptake of CNT/iron oxide hybrids in lungs.[11] The lung accumulation may be also due to their tubular and long structure. Actually, long fibre particles tend to cause pulmonary toxicity and fibres with lengths above 10 μm were reported carcinogenic.[34] Nonetheless, in this work was employed much shortened MWCNTs, with a median length of 1.63 μm, to avoid toxicity.

Besides, we did a histological examination to assess the damage on the tissues. No histological abnormality was observed from different mice tissues treated with the hybrid up to 30 days, even though the dose used in histological examination was much higher (400 μg or 5.8 mg Fe/kg) than the doses for SPECT and MRI. This confirms the biocompatibility of the hybrid. Moreover, a fraction of the hybrid was even detected in the bladder after 30 min, indicating rapid clearance for some ^{99m}Tc-BP-SPION-MWCNT fractions.

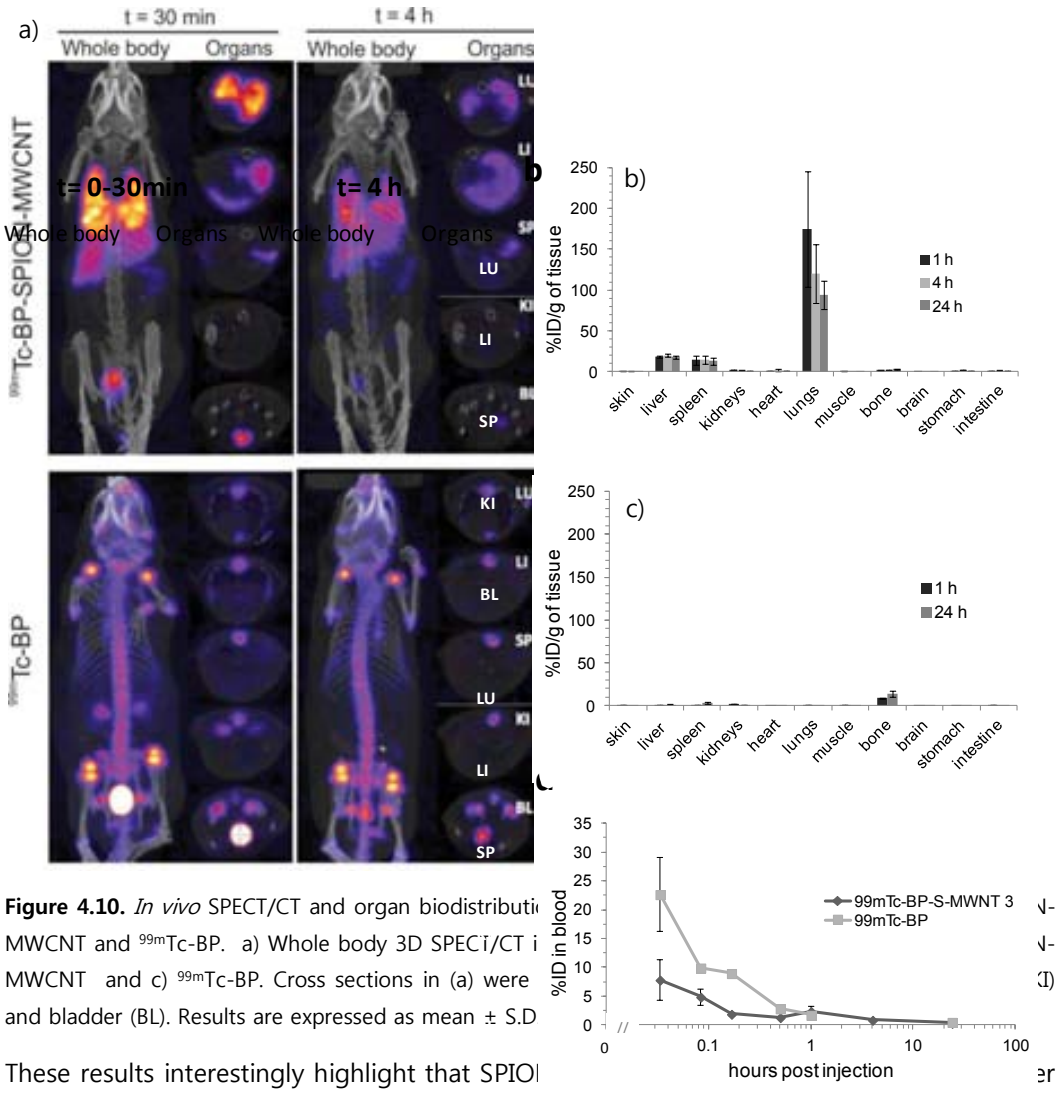

Figure 4.10. *In vivo* SPECT/CT and organ biodistributi MWCNT and ^{99m}Tc-BP. a) Whole body 3D SPECT/CT i MWCNT and c) ^{99m}Tc-BP. Cross sections in (a) were and bladder (BL). Results are expressed as mean ± S.D

These results interestingly highlight that SPIO diseases by enhancing the negative MRI signals and at the same time be detected by SPECT/CT when radiolabelled with ^{99m}Tc. Yet, though these hybrids were much shorter than toxic fibres, the toxicity concerns about long MWCNTs entailed us to use even shorter MWCNTs. Therefore, the next investigation involved the comparison of long and short MWCNTs for this application.

4.3.2. Effect of the shortening of MWCNT on the hybrid properties

It has been previously reported that apart from the CNT impurities, CNT length can be a source of cytotoxicity. Long nanotubes, which refers to rigid and with a significant length of more than 15 μm, have shown to behave like asbestos and induce acute and chronic peritoneal inflammation in mice.[34-38] Several reports have described that SWCNTs and

MWCNTs show biocompatibility after adequate shortening and surface functionalization.[38-40] However, not only is the cytotoxicity affected by the CNT length but also the biodistribution and their internalization by cells. It has also been shown that the percentage of cells containing MWCNTs is significantly higher when these are shorter.[41] Hence, for the development of CNTs for biomedical applications, we decided to prepare the same type of hybrid, but in this case using much shorter MWCNTs. Though we did not observe any tissue abnormality with the MWCNTs employed so far, we studied the effect that of shortening, has not only in terms of cytotoxicity but also with respect to their physicochemical properties and as contrast agents.

As explained in the introduction, there are different strategies that allow shortening of CNTs. In the present study we employed the steam treatment procedure optimized in this Thesis and described in Chapter 3.1. In order to compare the effect of the length distribution of MWCNTs on the performance of the hybrids, we prepared two different types of samples. One was steam treated during 1.5 h, with a median length of 1.63 μm, and it will be described during this section as long MWCNTs (L-MWCNTs). This is the same length distribution that has been employed for the studies reported so far in this Chapter. The other one was treated during 15 h, with a median length of 0.58 μm, and therefore mentioned as short MWCNTs (S-MWCNTs).

The hybrids were prepared following the same procedure described in the previous section. We firstly incorporated SPION on the MWCNT walls via an *in situ* method, and obtained two different samples: L-SPION-MWCNTs and S-SPION-MWCNTs. After its characterization and relaxivity measurements, we incorporated the radiotracer by radio-labelling the SPION with ^{99m}Tc-BP. We will refer to the final hybrids as: ^{99m}Tc-BP-L-SPION-MWCNTs and ^{99m}Tc-BP-S-SPION-MWCNTs.

4.3.2.1. Characterization and discussion

Characterization of the hybrids

The physicochemical characterization of the SPION onto L-SPION-MWCNTs and S-SPION-MWCNTs revealed similar results. TGA revealed that both long and short MWCNTs had similar loadings of Fe_2O_3 (34.0 wt% for L-MWCNTs and 30.0 wt% for S-MWCNTs). XRD and XPS confirmed that independently of the MWCNT length, the nanoparticles had the same structure.

The size, shape and distribution of the nanoparticles was examined by TEM (**Figure 4.11.**). The diameter of about 200 SPION was evaluated and a narrow distribution of sizes was

revealed. The size distribution of the SPION also appears to be similar, with median value of 6.13 nm for L-SPION-MWCNTs and 5.66 nm for S-SPION-MWNs.

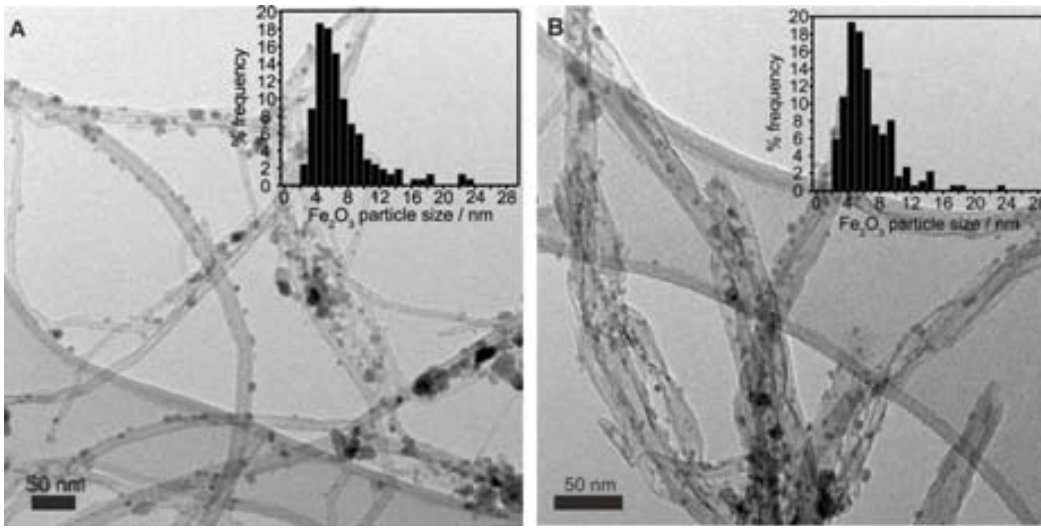

Figure 4.11. TEM images and SPION particle size distribution histograms of a) L-MWCNTs, b) S-MWCNTs.

Magnetic measurements

Both hybrids contain similar percentage of SPION with the same crystalline structure, which in turn also present a similar shape and size distribution. Therefore, we next performed magnetic measurements to determine if both hybrids would also give a similar response in MRI.

Hysteresis loops at 300 K (**Figure 4.12.a-b**) reveal the superparamagnetic behaviour of the SPION in both hybrids as expected, confirming that both long and short MWCNTs were decorated with superparamagnetic γ-Fe_2O_3 nanoparticles.

Next, zero-field cooling-field cooling (ZFC-FC) curves of the samples were recorded (**Figure 4.12.c-d**). The ZFC curve is measured by cooling down the sample without any applied field, whereas in the FC study there is an applied field of 100 Oe. The field cooling curve appears separated from the zero field cooling curve, which is expected for magnetically monodispersed materials presenting superparamagnetic properties. In the FC curve, the magnetization slightly increases when decreasing temperature, reflecting the reduction of the thermally-induced magnetic disorder. On the other hand, in the ZFC for SPIONs, the absence of magnetic field makes the spin directions randomly distributed and the overall magnetization is vanished. When warming up and measuring under field, the magnetization increases and displays a maximum (called the blocking temperature T_B) and

merges the FC curve. In a system of non-interacting SPIONs, T_B is determined by the magnetic anisotropy energy:

$$\boldsymbol{E_a = K_a V} \qquad (1)$$

Where K_a is the anisotropy constant of the nanoparticles and V is the volume. Both hybrids present identical SPION composition and their shape, size and size-distributions are also virtually identical. Therefore E_a and T_B should be similar. However, for L-SPION-MWCNTs Tb is clearly visible at ≈175 K and ZFC-FC approach each other at T>175 K, while in S-SPION-MWCNTs do not collapse up to 300 K. This conduct has been previously described for superparamagnetic systems with interacting particles.[42, 43] A large anisotropy is created by non-interacting single domain nanoparticles that depend on: its magnetocristallinity, surface and shape anisotropy. Nonetheless, our samples present a narrow and statistically similar size distribution. Consequently, differences in T_B should be related to the magnetic interactions among SPIONs. Since the amount of nanoparticles is similar in both samples, the distance between particles should also be similar in each nanotube. Therefore, interparticle interactions might arise from nanoparticles sitting on different nanotubes. During TEM analysis (**Figure 4.11.**) we observed that S-MWCNTs tend to form small bundles. Hence, the sample of short CNTs seems to present a higher degree of interaction between the CNTs both after steam purification and after being decorated with SPION. This interaction makes them to behave as a cluster, producing an increase of the blocking temperature.[44]

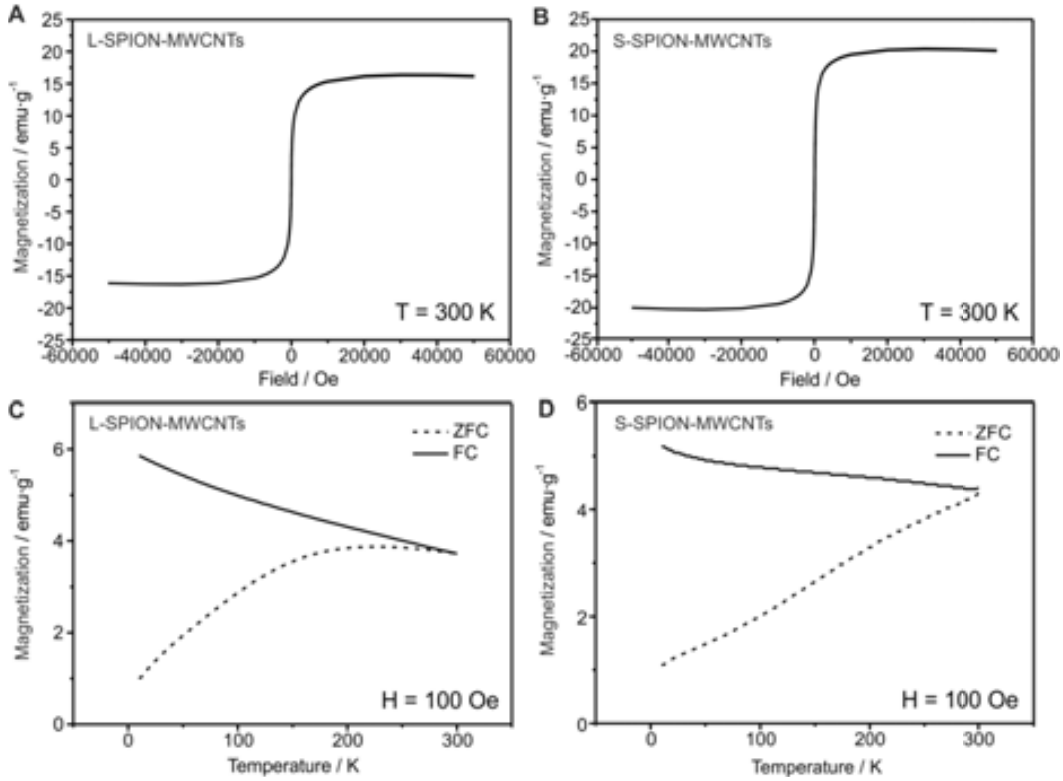

Figure 4.12. Hysteresis loops at 300 K after subtracting the linear background (top) and zero field-cooling-field-cooling curves at 100 Oe (bottom) of a,c) L-SPION-MWCNTs and b,d) S-SPION-MWCNTs.

Magnetic Ressonance Imaging

Phantom MR Imaging and R_2^* relaxation measurements

The difference observed in the magnetic properties of the hybrids was reflected in the MR imaging capabilities. Phantom MR imaging of the hybrids, with concentrations ranging from 0.125 to 1.25 mM (Fe), was conducted following the same protocol for phantom preparation as in the previous section (**Figure 4.13**.). S-SPION-MWCNT exhibited higher r_2^* value (530 s^{-1} mM^{-1}) compared to L-SPION-MWCNT (417 s^{-1} mM^{-1}) and both hybrids displayed higher r_2^* values compared to Endorem® (308 s^{-1} mM^{-1}).

This could be explained by the high interaction between the SPION when MWCNTs have shorter length as we have stated with the magnetic measurements. As a result of this big interaction, the cluster itself might be considered as a large magnetized sphere. The total magnetization is aligned to the magnetic field and because of having a large size the secular term of the relaxation rate is affected.

$$\boldsymbol{R_2 = \frac{1}{T_2} = \frac{16 f_a \Delta\omega^2 \tau_D}{45}} \qquad (2)$$

The secular contribution derives from the the outersphere diffusion theory.[45] This refers to $\Delta\omega\tau_D < 1$, where $\Delta\omega$ is the difference between the frequencies of the local field experienced by a proton in the cluster surface and the one experienced by a proton in the bulk and τ_D is the diffusion time around the cluster, which increases with cluster size.[46] In equation 1, f_a is the volume fraction occupied by the cluster. This secular contribution significantly describes an increase in R_2 values at high fields.[47, 48] Consequently, for S-SPION-MWCNTs the obtained values were higher than for L-SPION-MWCNTs, which have a more diffused cluster.

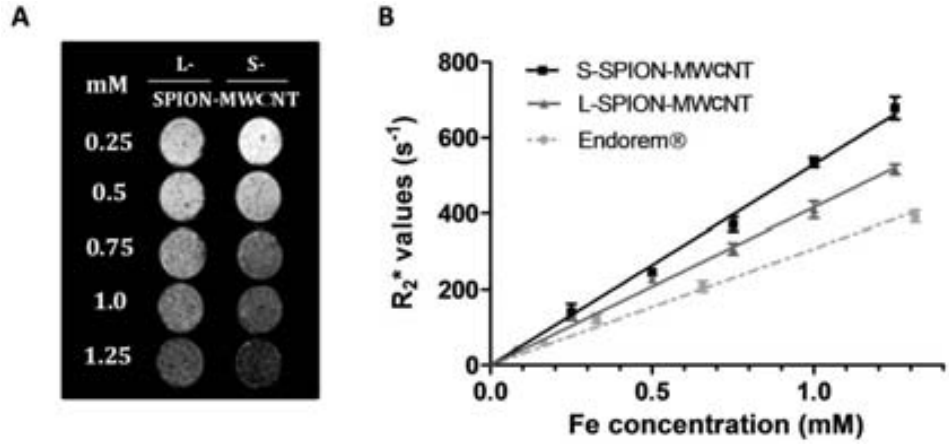

Figure 4.13. Phantom MR imaging and R_2^* relaxation rate of Endorem®, S-SPION-MWCNT and L-SPION-MWCNT.

In Vitro MR Imaging and Uptake Ability of Hybrids by ICP-MS in J774A.1 cells

After observing an increase in the relaxivity values in the phantom of short MWCNTs, we studied the cell internalization of the hybrids and the MRI behaviour *in vitro*. L-SPION-MWCNT, S-SPION-MWCNT and Endorem® were incubated with J774A.1 cells at 12 and 24 μg_{Fe}/mL for 24h. Perls' staining confirmed the co-localization of CNTs and Fe within J774A.1 cells (**Figure 4.14.a**).

To measure the MR imaging properties of internalized hybrids, J774A.1 cells were detached, fixed and resuspended in 0.5 % Agarose solution at a final density of 1 x 106 cells per 200 µL and imaged at 7 Tesla (**Figure 4.14.b**). J774A.1 treated with the hybrids presented higher relaxation rate than Endorem®. In addition, S-SPION-MWCNT displayed higher R_2^* than cells exposed to L-SPION-MWCNT and Endorem® at 24 µg/mL. These results confirmed that the shortening of SPION-MWCNT increased the *in vitro* negative contrast imaging properties of the hybrids.

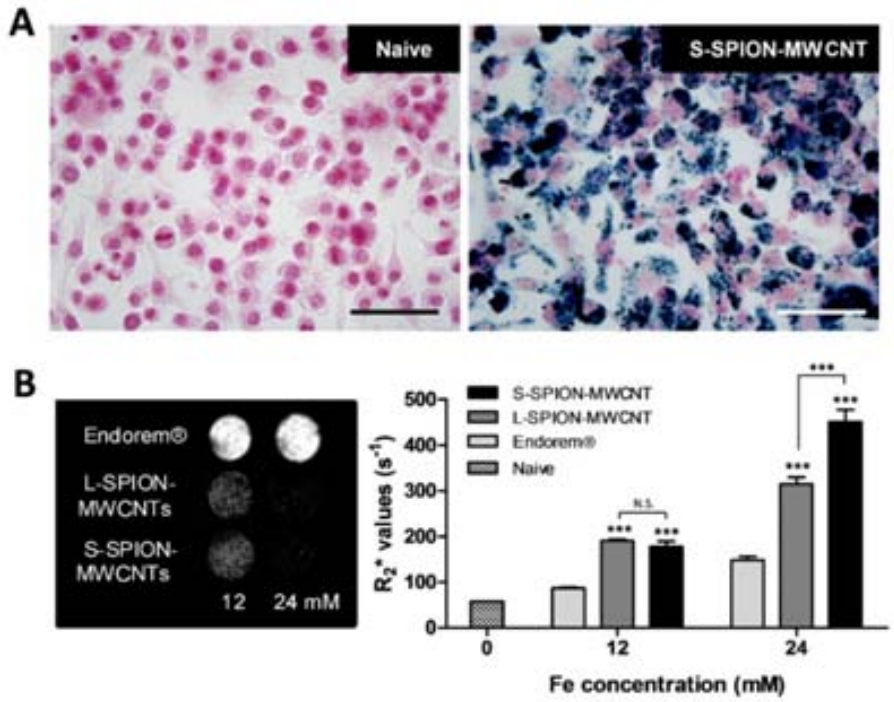

Figure 4.14. In vitro MR imaging of J774A.1 cells exposed to SPION-MWCNT and Endorem®; a) Perl's staining of J774A.1 cells exposed to 24 μg/ml (Fe) of S-SPION-MWCNT for 24 h; b) In vitro T2*-weighted MR images and R2* relaxation rate measurements of J774A.1 cells exposed to SPION-MWCNT and Endorem®.

MR imaging in mice

As the short hybrids have exhibited higher relaxivity values *in vitro* than the long ones, we next investigated their performance *in vivo*. Previous report using L-SPION-MWCNTs showed a high presence of the hybrid in the liver. Therefore, magnetic properties of S-SPION-MWCNT and Endorem® were compared in liver tissue after intravenous injection of both hybrids at 1.4 mg_{Fe}/kg in mice (**Figure 4.15.**). At early timepoints, higher relaxation rates were observed in Endorem® than S-SPION-MWCNTs. However, as it will be stated later in the biodistribution studies, S-SPION-MWCNTs present high accumulation in the lungs and, therefore, less amount of iron will be in the liver. Interestingly, 24 h after injection, the relaxation rate of liver injected with S-SPION-MWCNT (347.1 ± 26.2 s^{-1}) was comparable to that of Endorem® (316.9 ± 15.9 s^{-1}). The high R_2^* values on the liver for S-SPION-MWCNTs, though having accumulation of the hybrid in the lungs, reflect the higher MR response of the S-SPION-MWCNTs than Endorem®. Furthermore, the relaxation rate of liver treated with S-SPION-MWCNT was consistently higher than that of Endorem® at 8 days.

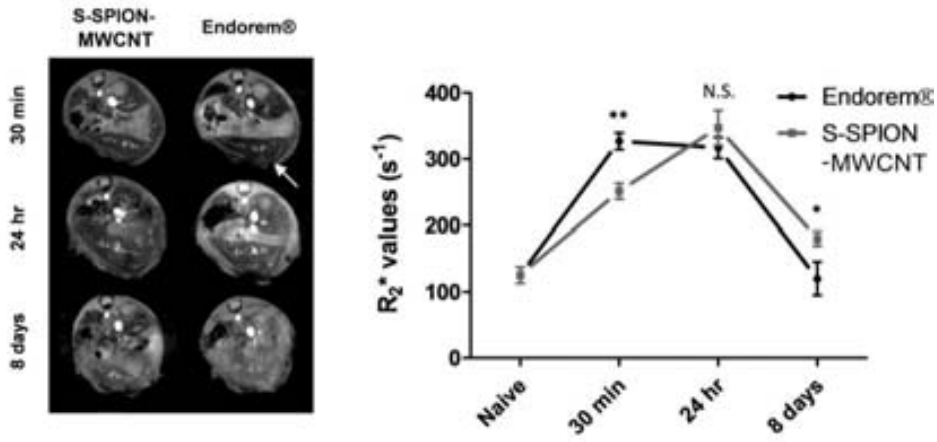

Figure 4.15. *In vivo* T_2*-weighted MR images and *in vivo* R_2* relaxation rate measurements in liver after intravenous injection of 1.4 mg_{Fe}/kg S-SPION-MWCNT and Endorem®.

***In vivo* SPECT/CT and biodistribution studies**

Having revealed a higher MR signal for hybrids using short MWCNTs, we proceeded to the radio-labelling in order to obtain a dual imaging agent and assess their biodistribution profile. The procedure was the same than in the previous studies and adopted from Rosales *et al.*[22, 26] The final hybrid consisted then of ^{99m}Tc-BP-S-SPION-MWCNTs.

To confirm its dual imaging ability, whole body SPECT/CT imaging was conducted (**Figure 4.16.a**) at 30 min, 4 h and 24 h after intravenous injection of ^{99m}Tc-BP-S-SPION-MWCNT (4 MBq, 10 mg/kg hybrid) or ^{99m}Tc-BP (10 MBq) alone in C57BL/6 mice. As in the previous report, ^{99m}Tc-BP was accumulated into bone tissue and the bladder and the signal within the bladder revealed its predominant urinary excretion. In contrast, ^{99m}Tc-BP-S-SPION-MWCNT accumulated mostly into lungs, followed by liver and spleen after 30 min of injection. A small fraction of ^{99m}Tc-BP-S-SPION-MWCNT was found in the bladder, indicating that a fraction of the hybrid was excreted *via* the urinary tract. Because of the rapid decay of ^{99m}Tc (half-life = 6 h), the "virtual" loss of radioactivity was compensated by adjusting the signal intensity of later time points. At 4 and 24 hr, ^{99m}Tc-BP-S-SPION-MWCNT was translocated from lungs to the liver and spleen.

To quantitatively assess the organ biodistribution profile of S-SPION-MWCNT, post-mortem γ-scintigraphy was conducted (**Figure 4.16.b**). Major mouse organs were excised at 1, 4 and 24 h time points. As observed with SPECT/CT, lung, liver and spleen were the organs showing the highest accumulation. Despite significant accumulation of ^{99m}Tc-BP-S-SPION-MWCNT into the lungs, the hybrid was progressively cleared from this organ. On

the other hand, in agreement with the *in vivo* relaxation rates, there is no clearance observed for liver and spleen.

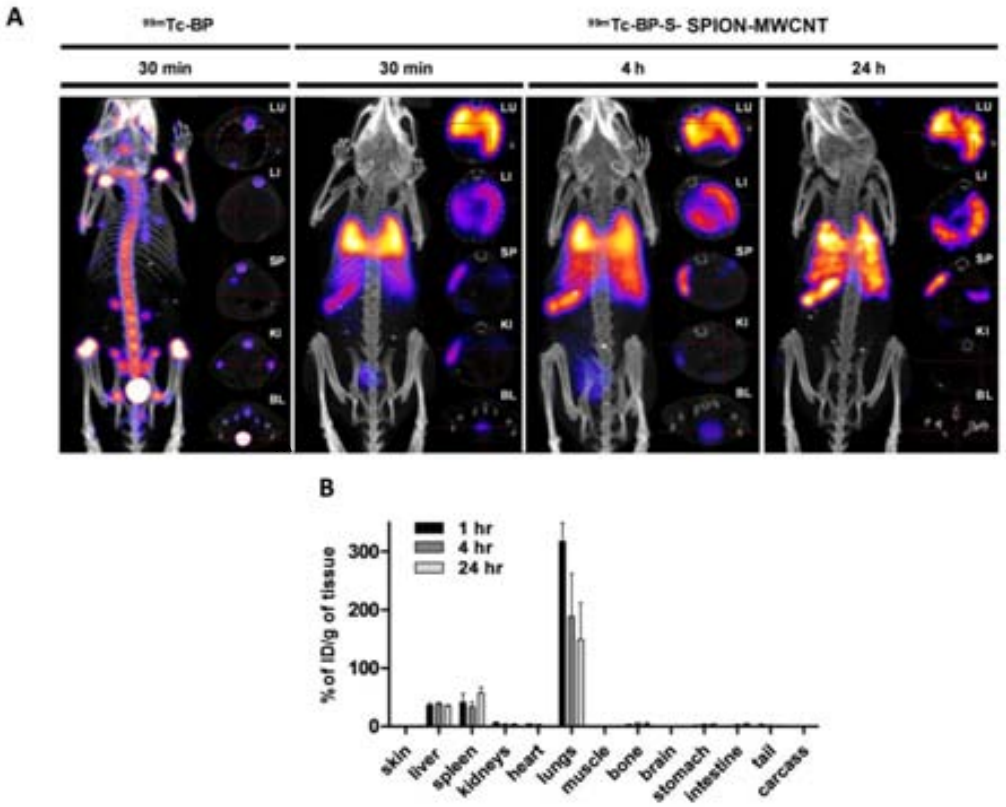

Figure 4.16. a) Whole body 3D SPECT/CT imaging of 99mTc-BP-S-SPION-MWCNT; b) Organ biodistribution of ^{99m}Tc-BP-S-SPION-MWCNT by γ-counting.

Modified LDH assay

The cytotoxicity of the hybrids was determined with the modified lactate dehydrogenase assay (LDH assay). More common methods, such as MTT and LDH, have been demonstrated to give false positives when employed with MWCNTs.[49] This false interaction comes from the fact that CNTs have interaction with the formazan crystals used in the assays. In the modified LDH assay, the MWCNTs are excluded from the reaction medium to eliminate the risks of interference. This is achieved by lysing cells that were not damaged and centrifuge the cell lysate to precipitate and remove the CNTs to avoid interference. Moreover, the LDH assay cannot be conducted for long time points, as the half life of the LDH released by the cells is not longer than 9 hours. On the other hand, with the modified LDH assay longer cell incubations can be studied because of measuring the LDH in living cells.[50]

Briefly, macrophages (J774A.1) cells were incubated for 24 and 72 h with S-SPION-MWCNTs and L-SPION-MWCNTs at 10, 50 and 100 µg/mL. After cell incubation, media was aspirated. Cells were then lysed with a lysis buffer (0.9% v/v Triton X-100) and incubated for 60 minutes to obtain cell lysate. Afterwards the plate was centrifuged (16000/g for 5 minutes) to pellet down the MWCNTs and the cell membrane. The supernatant of the cell lysate was then mixed with LDH substrate and incubated for 15 minutes. The absorbance was read at 490 nm using a plate reader and the percentage of cell survival was calculated by comparison of the absorbance of untreated cells.

Figure 4.17. displays the cell viability when cells are incubated with L-SPION-MWCNTs and S-SPION-MWCNTs. Positive and negative controls are included (control, which are untreated cells, and 10 % dimethyl sulfoxide (DMSO)). Treatment with Pluronic® F-127 block copolymer alone did not exhibit any signs of toxicity as expected, indicating the biocompatibility of this copolymer. No cytotoxicity was observed for neither long nor short hybrids at 24 hours. Different concentrations of the hybrid were employed with a slight decrease of the cell viability. At 24 h the decrease is very low for both hybrids, yet at 72 h higher concentrations show less living cells (around 80 %). There are not big variations in the cell viability when using long or short MWCNTs. However, by increasing the incubation time to 72 h, L-SPION-MWCNT showed the highest reduction in intracellular LDH.

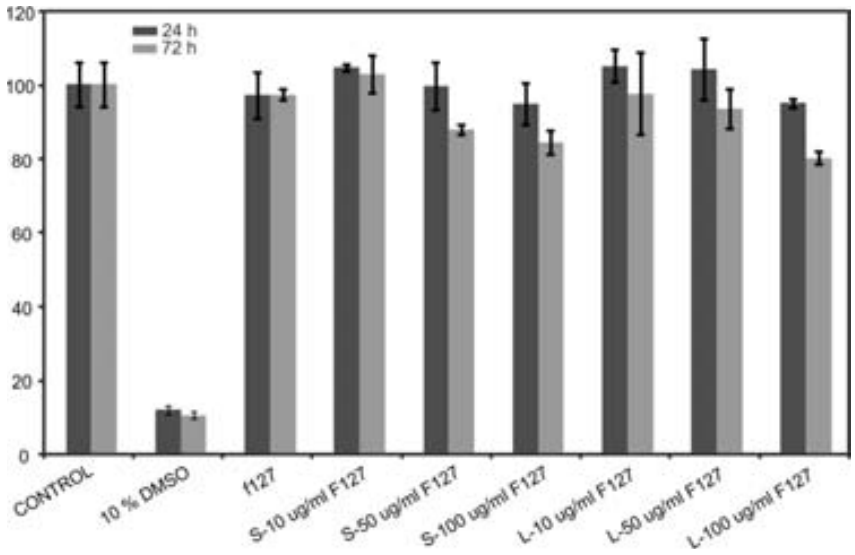

Figure 4.17. Modified LDH assay of J774A.1 cells incubated with S-SPION-MWCNT and L-SPION-MWCNTs with concentrations of 10, 50 and 100 µg/mL during 24 and 72 hours. LDH content was quantified (n=3).

It has been demonstrated that the use of shorter MWCNTs to prepare a dual imaging hybrid not only might play a role in the biodistribution profile and the toxicity of the

material but also to an enhanced the MR signal. This research introduces for the first time the influence of the length distribution of the CNTs on the contrast properties of the resulting material which is of interest for biomedical imaging area.

4.4. SWCNT functionalization with carboranes as B-rich carrier agents

Boron neutron capture therapy (BNCT) is a chemo-therapeutic technique that involves selective delivery of ^{10}B-rich agents to tumours and their subsequent irradiation with low-energy neutrons causes the selective destruction of the targeted cells.[16, 17] Carborane boron clusters are good candidates for boron delivery, as they are thermally and chemically stable while having low toxicity.[51] Moreover, the interest in these clusters stands in the fact that contain a large amount of B atoms, very convenient for BNCT, which requires a great number of radioactive ^{10}B atoms. From all of them, the cobaltabisdicarbollide sandwich anion, $[3,3'\text{-}Co(C_2B_9H_{11})_2]^-$ (cosane), has emerged as a suitable building block for the preparation of boron carrier drugs. It has been used in medicine as specific inhibitor of the human immunodeficiency virus (HIV) protease and for boron neutron capture therapy (BNCT).[52] Moreover, its structure allows the attachment of functional groups with specific functionalities.

On the other hand, Single-Walled Carbon Nanotubes (SWCNTs) are promising materials for biomedical applications,[53-55] as they are able to penetrate biological barriers and to be internalized by the nucleus without any toxic effects.[56-59] Because of its high surface area it is possible to chemically modify them to increase its biocompatibility.[60-63] However, the main drawback of this family of nanomaterials is that their biomedical applications are discouraged due to their tendency to form bundles and their hydrophobicity.[64] Many studies have been conducted with the purpose to increase dispersibility of SWCNTs in water [55, 65] with the aim to reduce any possible toxicity coming from their agglomeration.[66] Strategies include covalent[67] and non-covalent[68] functionalization with surfactants or polymers.

The combination of carborane clusters and SWCNTs could entail an improvement in the group of tumour-targeting biomolecules for the BNCT.[69] SWCNTs can achieve more site specificity than boron clusters, as they are even able for instance to cross the blood-brain barrier and concentrate in the cytoplasm. First attempts of incorporation of boron clusters to SWCNTs have been made.[70, 71] Nonetheless an improvement of the dispersibility of the SWCNTs upon attachment with carborane clusters has not been stated to date.

The aim of this work was to develop several strategies to chemically functionalize SWCNTs with metallacarborane clusters. Furthermore, we also wanted to determine whether an enhancement in the water dispersibility of SWCNTs could be achieved by incorporation of these clusters.

4.4.1. Synthetic protocols for the functionalization of SWCNTs with cosane

Before incorporation of the metallacarborane cosane, SWCNTs must be purified in order to remove all the impurities present in the as-received material to remove the carbonaceous species present in the sample, such as amorphous carbon and graphitic particles. It has been shown that the presence of amorphous carbon hiders sidewall functionalization of SWCNTs.[72] Therefore, we used the method developed during this Thesis, the steam purification of CNTs, but for SWCNTs, which had been previously reported.[73, 74]

The purified SWCNTs were then oxidized by reflux with nitric acid to introduce oxygen bearing functionalities onto the SWCNT tips and sidewalls, mainly carboxylic acid groups (-COOH).[25] In order to remove any possible atmospheric humidity absorbed onto the SWCNTs, they were heated overnight in a round bottom flask at 100 ºC. Afterwards, the flask was pump-filled with argon for 3 times to remove any residual oxygen. Then, sample was left under vacuum for 6 hours at 100 ºC to finally obtain a completely dry powder.

The functionalization of SWCNTs with cosane has not been previously reported. Therefore, we explored three different methods to determine the best route for the incorporation of the cluster with a high yield (**Figure 4.18.**).

The first method consisted in the activation of SWCNTs with a strong base. Following literature methods,[75] acid treated SWCNTs were mixed with a solution of 10 M NaOH in water for 5h at 90 ºC. Then, the collected CNTs-COONa were dried under vacuum at 60ºC. Afterwards, pump filled for 3 times with Ar to remove any residual oxygen and a solution of carborane **1** in anhydrous DME was added drop wise. The mixture was then stirred at room temperature for 72h. The solvent was removed and the final [Co]Na-SWCNTs were washed with EtOH, filtered through a polycarbonate membrane, washed with MeOH and dried. The sample obtained will be named [Co]Na^+-SWCNTs in this Thesis.

In the second method SWCNTs were activated with thionyl chloride.[76] Briefly, acid treated SWCNTs were heated at 65 ºC in thionyl chloride for 24h. The solvent was then removed

under vacuum and a solution of carborane **2** in dry DMF was added to the activated SWCNTs. After 96h, the mixture was cooled down at room temperature and MeOH was added. The product was filtered through the polycarbonate membrane, washed with MeOH and dried.

In the last method a one-pot synthesis was performed.[76] Notice that in this case the counterion after functionalization will be a H^+ instead of a Na^+. Acid treated SWCNTs were pre-activated with Dicylohexylcarbodiimide/hydroxibenzotriazole DCC/HOBt in dried DMF. After 45 min, a solution of carborane **2** in dry DMF was added. The mixture was then stirred at room temperature for 72h. After this time, the solvent was removed under vacuum and MeOH was added. The final mixture was filtered through a polycarbonate membrane, washed with MeOH and dried. The sample obtained is named [Co]H^+-SWCNTs during the report.

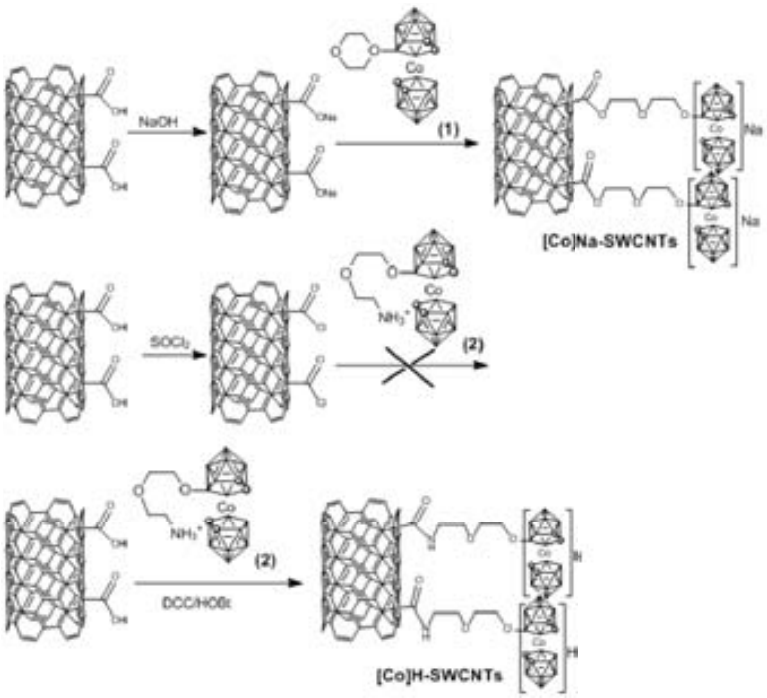

Figure 4.18. Scheme of the different explored routes for the functionalization of SWCNTs with carborane clusters.

4.4.2. Characterization and discussion

Fourier Transform Infrared Spectroscopy

We performed Fourier Transform Infrared Spectroscopy (FTIR) to assess the functionalization of the SWCNTs (**Figure 4.19.**). FTIR measures the light absorption of the

sample at each wavelength, and can determine the chemical structure of the sample. The carborane clusters present a distinctive B–H vibration (at~2500 cm^{-1}) and therefore FTIR arises as a convenient technique for the characterization of this type of materials. In the case of the second synthesis method, after characterization of the sample no functionalization was detected in the FTIR characterization. We considered a reaction between the precursors, and for that reason a mixture of thionyl chloride with **2** was done. This resulted in a very exothermic reaction, increasing the solution temperature and even some gases were detected. We conducted a $^{11}B\{^1H\}$-NMR in deuterated DMSO after 3 days of reaction. The obtained spectra reflected a mixture of compounds and the presence of unfunctionalized cosane. Moreover, the range of the spectrum was narrower than for **2**, indicating an elimination of the NH_2-terminated alkyl chain of **2**. This was a clear indicator of the decomposition of the compound to a mixture of different compounds, including cosane. Therefore, this route was completely discarded for following characterization.

Both the [Co]Na^+-SWCNTs and [Co]H^+-SWCNTs samples present the B–H vibration band at 2535 and 2525 cm^{-1}, which is a clear indicator of the presence of the carborane clusters in these samples. Furthermore, both the oxidized and functionalized SWCNTs with carboranes present the C=O stretching peak is seen at 1740 cm^{-1}, and a decrease of the relative intensity was detected for the functionalized SWCNTs with cosane. Moreover, the C=C stretching band is downshifted to 1587 cm^{-1} with respect to the purified material. The sidewall covalent functionalization is also confirmed in the [Co]H^+-SWCNT sample with the signal at 1621 cm^{-1}, that is attributed to the stretching of N−C=O.

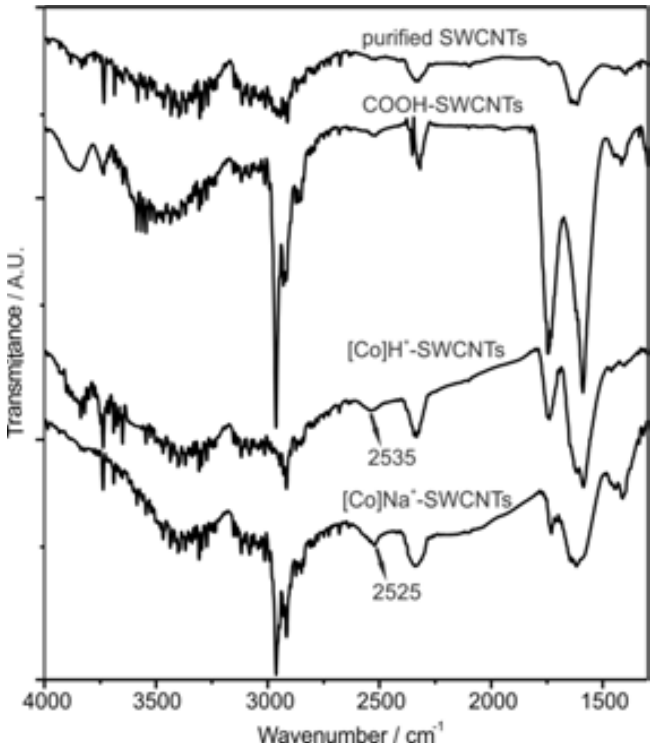

Figure 4.19. Infrared spectra of purified SWCNTs oxidized SWCNTs and functionalized SWCNTs with carboranes.

Transmission Electron Microscopy

FTIR being a bulk technique provides evidence of the formation of covalent bonds but cannot discern between functional groups attached to the sidewalls of the CNTs or to other carbonaceous impurities that might still be present after the steam purification. Therefore, we next analyzed the samples by HRTEM since this technique allows direct visualization of the functional groups attached to the walls of the SWCNTs (**Figure 4.20.a**).[76] Dark field Scanning Transmission Electron Microscopy (STEM) imaging a z-contrast image is obtained, which scales to a power of the atomic number. Therefore, heavier elements will appear with brighter contrast. In this image a bundle of SWCNTs is observed. Along the bundle, various bright dots are detected surrounding the walls of the SWCNTs. Those correspond to the Co atoms present on the carborane structure, as they are much heavier than the rest of the elements in the sample (C,N,H,B). To better display the attachment of the cluster to the nanotube, High Resolution TEM (HRTEM) imaging was performed (**Figure 4.20.b**). In this image, one DWCNT is observed, containing several aggregates along its walls. In HRTEM, Co present in the carborane structure will originate dark contrast. HRTEM simulation (inset in the image), that illustrates how the Co atoms

with a dark contrast are surrounded by lower contrast atoms from the cluster structure. The image simulation is in good agreement with the experimental HRTEM image confirming the presence of the cluster along the wall of the CNT. Hence, we provide direct evidence that the SWCNTs have been successfully functionalized with the carboranes.

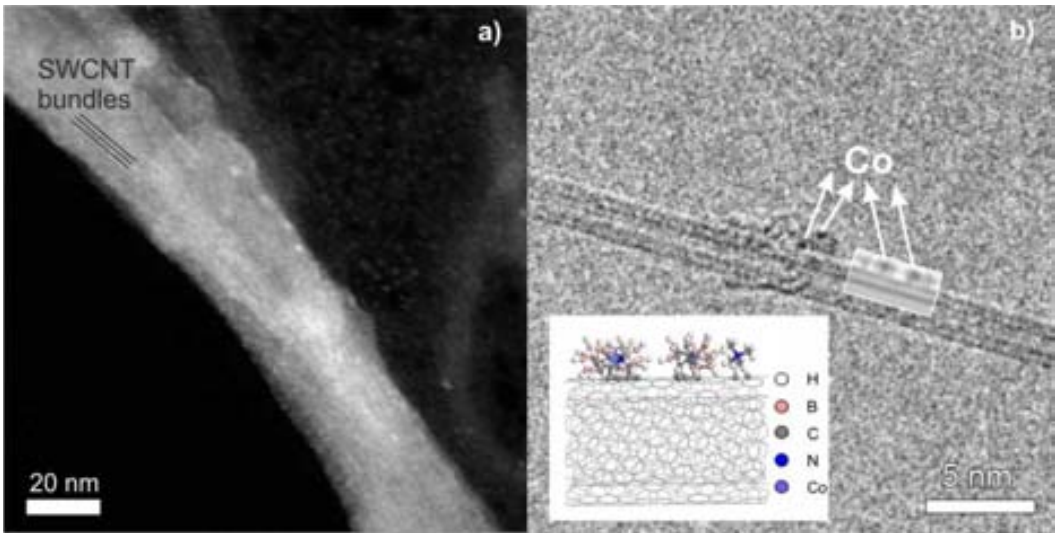

Figure 4.20. STEM and HRTEM analysis of the material a) Dark field STEM image of SWCNTs functionalized with carborane clusters. b) HRTEM of a carborane cluster attached to the wall of a DWCNT with the corresponding simulation (right inset) and the employed model (left inset).

Ultraviolet-Visible Spectroscopy

One of the main issues when using CNTs for biomedical applications is its lack of dispersibility in aqueous media. To complete this study the dispersibility of the carborane functionalized CNTs was assessed by preparing dispersions of 1mg/mL in water (**Figure 4.21.a**). UV-Vis spectroscopy of the supernatant was conducted comparing the two hybrids with oxidized nanotubes, which are known to present good dispersibility in water. (**Figure 4.21.**). UV-Vis allows to quantitatively determine the amount of sample present in solution, After functionalization of SWCNTs with the carborane clusters there are different scenarios. **2** presented two bands with maximum absorbance at 213 nm and 300 nm. [Co]Na^+-SWCNTs has no absorbance in the UV-Vis region due to the poor dispersibility of this sample. On the contrary, [Co]H^+-SWCNTs show two peaks with a maximum absorbance at 217 and 256 nm. While the band at 217 nm indicates the presence of cobaltabisdicarbollide anion, the broad band at 256 nm exhibits higher intensity and was shifted with respect to the COOH-SWCNTs. Interestingly, the absorbance of this hybrid is much higher, even overtaking the one of oxidized SWCNTs. This indicates that SWCNTs

are better dispersed after being functionalized with carboranes (with H+ as counterion) than the oxidized nanotubes by nitric acid. In addition, the counterion used is essential to define the properties and the further application of the functionalized SWCNTs.

To check the stability of the prepared dispersions these were left standing for 3 months (**Figure 4.21.b**). After this period of time the [Co]Na^+-SWCNTs precipitated at the bottom of the vial, confirming the poor dispersibility of the hybrid as observed by UV-Vis. On the contrary, both oxidized SWCNTs and [Co]H^+-SWCNTs present a dark dispersion after three months. Moreover, in the naked eye, the [Co]H^+-SWCNTs solution appears to be even darker than the acid treated one, which starts to present some deposited powder at the bottom of the vial.

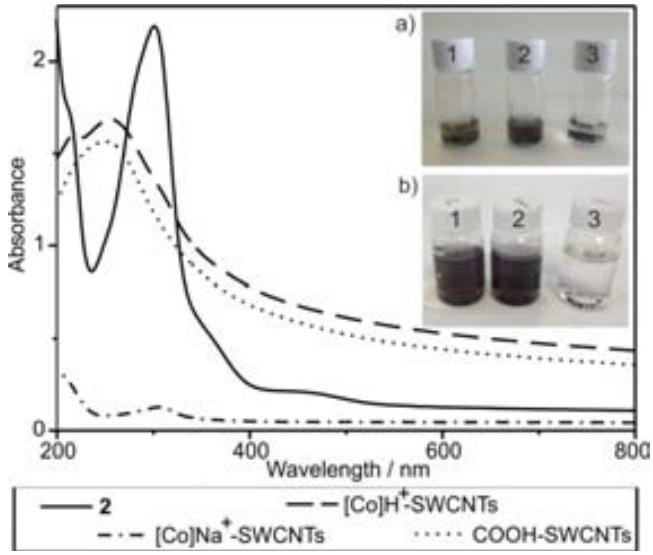

Figure 4.21. UV-Vis spectra of freshly prepared dispersions of oxidized SWCNTs, 2, [Co]H^+-SWCNTs and [Co]Na^+-SWCNTs. The inset presents a picture of 1 mg/mL dispersions of oxidized SWCNTs (1), [Co]H^+-SWCNTs (2), [Co]Na^+-SWCNTs (3) when a) freshly prepared and b) after 3 months.

We have demonstrated that it is possible to covalently attach carborane clusters to the walls of SWCNTs. The resulting hybrids present good water dispersion ability, even higher than oxidized SWCNTs, which is the most commonly route employed to render SWCNTs dispersible. Therefore, this hybrid arises a promising agent for boron carrier for biomedical applications.

4.5. Conclusions

We have prepared different types of inorganic CNT hybrids by external decoration of the CNT walls.

- Hybrids of SPION-MWCNT have been prepared by *in situ* generation, followed by the radiollabelling of the SPION with ^{99m}Tc through a BP derivative. High r_2 relaxivities were obtained in both phantom and *in vivo* MRI compared to the clinically approved SPION Endorem®. SPECT/CT imaging and γ-scintigraphy allowed to quantitatively assess the biodistribution in mice. TEM images of liver and spleen tissues showed the co-localization of SPION and MWCNT within the same intracellular vesicles, indicating good *in vivo* stability of the hybrids after intravenous injection. The results demonstrated the capability of the present ^{99m}Tc-SPION-MWCNT hybrids as dual MRI and SPECT contrast agents for *in vivo* application.
- Enhanced R_2 relaxivities have been obtained *in vitro* and *in vivo* when employing short SPION-MWCNTs, which is attributed to a larger degree of interparticle interaction when compared to the lon SPION-MWCNTs.
- Metallacarborane clusters have been attached to the walls of the SWCNTs. Both STEM and HRTEM confirm the presence of the clusters along the SWCNT walls.The hybrid dispersibility of the resulting hybrid is higher than that of oxidized SWCNTs, which is one of the most commonly used routes to render SWCNTs dispersible in water. A better dispersibility entails more biocompatible CNTs and therefore this hybrid is a suitable agent for boron delivery for BNCT.

4.6. References

1. J. Chen, F. Saeki, B. J. Wiley, H. Cang, M. J. Cobb, Z.-Y. Li, L. Au, H. Zhang, M. B. Kimmey, Li and Y. Xia, *Nano Letters*, 2005, 5, 473-477.
2. J.-L. Bridot, A.-C. Faure, S. Laurent, C. Rivière, C. Billotey, B. Hiba, M. Janier, V. Josserand, J.-L. Coll, L. Vander Elst, R. Muller, S. Roux, P. Perriat and O. Tillement, *Journal of the American Chemical Society*, 2007, 129, 5076-5084.
3. X. Li, N. Anton, G. Zuber and T. Vandamme, *Advanced Drug Delivery Reviews*, 2014, 76, 116-133.
4. M. Foldvari and M. Bagonluri, *Nanomedicine*, 2008, 4, 183-200.
5. P. Cherukuri, S. M. Bachilo, S. H. Litovsky and R. B. Weisman, *Journal of the American Chemical Society*, 2004, 126, 15638-15639.
6. D. A. Heller, S. Baik, T. E. Eurell and M. S. Strano, *Advanced Materials*, 2005, 17, 2793-2799.
7. A. De La Zerda, C. Zavaleta, S. Keren, S. Vaithilingam, S. Bodapati, Z. Liu, J. Levi, B. R. Smith, T.-J. Ma, O. Oralkan, Z. Cheng, X. Chen, H. Dai, B. T. Khuri-Yakub and S. S. Gambhir, *Nat Nano*, 2008, 3, 557-562.
8. J. V. Jokerst and S. S. Gambhir, *Accounts of chemical research*, 2011, 44, 1050-1060.
9. S. K. Nune, P. Gunda, P. K. Thallapally, Y. Y. Lin, M. L. Forrest and C. J. Berkland, *Expert Opinion on Drug Delivery*, 2009, 6, 1175-1194.
10. D. Tasis, N. Tagmatarchis, A. Bianco and M. Prato, *Chemical reviews*, 2006, 106, 1105-1136.
11. H. Wu, G. Liu, Y. Zhuang, D. Wu, H. Zhang, H. Yang, H. Hu and S. Yang, *Biomaterials*, 2011, 32, 4867-4876.
12. J. S. Choi, J. C. Park, H. Nah, S. Woo, J. Oh, K. M. Kim, G. J. Cheon, Y. Chang, J. Yoo and J. Cheon, *Angew. Chem.-Int. Edit.*, 2008, 47, 6259-6262.
13. C. Glaus, R. Rossin, M. J. Welch and G. Bao, *Bioconjugate Chemistry*, 2010, 21, 715-722.
14. L. Sandiford, A. Phinikaridou, A. Protti, L. K. Meszaros, X. J. Cui, Y. Yan, G. Frodsham, P. A. Williamson, N. Gaddum, R. M. Botnar, P. J. Blower, M. A. Green and R. T. M. de Rosales, *ACS Nano*, 2013, 7, 500-512.
15. N. Kohler, C. Sun, A. Fichtenholtz, J. Gunn, C. Fang and M. Q. Zhang, *Small*, 2006, 2, 785-792.
16. R. N. Grimes, in *Carboranes (Second Edition)*, ed. R. N. Grimes, Academic Press, Oxford, 2011, 1053-1082.
17. R. F. Barth, J. A. Coderre, M. G. H. Vicente and T. E. Blue, *Clin. Cancer Res.*, 2005, 11, 3987-4002.
18. M. L. H. Green, D. Morgan, J. Sloan and M. L. H. Green, *Chemical communications (London. 1996)*, 2002, 2442-2443.
19. Z. Yinghuai, A. Peng, K. Carpenter, J. Maguire, N. Hosmane and M. Takagaki, *Journal of the American Chemical Society*, 2005, 127, 9875-9880.

20. G. Calabrese, A. C. N. M. Gomes, E. Barbu, T. G. Nevell and J. Tsibouklis, *Journal of Materials Chemistry*, 2008, 18, 4864-4871.

21. D. W. McRobbie, E. A. Moore, M. J. Graves and M. R. Prince, *MRI from Picture to Proton*, 2006.

22. J. T. W. Wang, L. Cabana, M. Bourgognon, H. Kafa, A. Protti, K. Venner, A. M. Shah, J. K. Sosabowski, S. J. Mather, A. Roig, X. X. Ke, G. Van Tendeloo, R. T. M. Rosales, G. Tobias and K. T. Al-Jamal, *Advanced Functional Materials*, 2014, 24, 1880-1894.

23. A. Leblanche, E. Schoumanclaeys, C. Chambon, O. Clement, A. Le Blanche, E. Schouman Claeys and G. Frija, *Magn. Reson. Imaging*, 1993, 11, 509-519.

24. E. Even Sapir, U. Metser, E. Mishani, G. Lievshitz, H. Lerman and I. Leibovitch, *The Journal of Nuclear Medicine*, 2006, 47, 287-297.

25. G. Tobias, L. Shao, B. Ballesteros and M. L. H. Green, *Journal of nanoscience and nanotechnology*, 2009, 9, 6072-6077.

26. R. T. M. de Rosales, C. Finucane, S. J. Mather and P. J. Blower, *Chemical Communications*, 2009, DOI: 10.1039/b908652h, 4847-4849.

27. R. T. M. de Rosales, R. Tavare, A. Glaria, G. Varma, A. Protti and P. J. Blower, *Bioconjugate Chemistry*, 2011, 22, 455-465.

28. T. Kolodiazhnyi and M. Pumera, *Small*, 2008, 4, 1476-1484.

29. A. P. Grosvenor, B. A. Kobe, M. C. Biesinger and N. S. McIntyre, *Surface and Interface Analysis*, 2004, 36, 1564-1574.

30. K. Donaldson, F. Murphy, R. Duffin and C. Poland, *Part. Fibre Toxicol.*, 2010, 7, 5.

31. R. Rastogi, R. Kaushal, S. K. Tripathi, A. Sharma, I. Kaur and L. Bharadwaj, *Journal of colloid and interface science*, 2008, 328, 421-428.

32. C. Chambon, O. Clement, A. Leblanche, E. Schoumanclaeys and G. Frija, *Magn. Reson. Imaging*, 1993, 11, 509-519.

33. H. X. Wu, G. Liu, Y. M. Zhuang, D. M. Wu, H. Q. Zhang, H. Yang, H. Hu and S. P. Yang, *Biomaterials*, 2011, 32, 4867-4876.

34. K. Donaldson, F. A. Murphy, R. Duffin and C. A. Poland, *Part. Fibre Toxicol.*, 2010, 7.

35. C. A. Poland, R. Duffin, I. Kinloch, A. Maynard, W. A. H. Wallace, A. Seaton, V. Stone, S. Brown, W. MacNee and K. Donaldson, *Nat Nano*, 2008, 3, 423-428.

36. J. Palomäki, E. Välimäki, J. Sund, M. Vippola, P. A. Clausen, K. A. Jensen, K. Savolainen, S. Matikainen and H. Alenius, *ACS Nano*, 2011, 5, 6861-6870.

37. K. Kostarelos, *Nature biotechnology*, 2008, 26, 774-776.

38. H. Ali-Boucetta, A. Nunes, R. Sainz, M. A. Herrero, B. Tian, M. Prato, A. Bianco and K. Kostarelos, *Angewandte Chemie International Edition*, 2013, 52, 2274-2278.

39. H. Dumortier, S. Lacotte, G. Pastorin, R. Marega, W. Wu, D. Bonifazi, J.-P. Briand, M. Prato, S. Muller and A. Bianco, *Nano Letters*, 2006, 6, 1522-1528.

40. B. Sitharaman, X. Shi, X. F. Walboomers, H. Liao, V. Cuijpers, L. J. Wilson, A. G. Mikos and J. A. Jansen, *Bone*, 2008, 43, 362-370.

41. C. Bussy, M. Pinault, J. Cambedouzou, M. J. Landry, P. Jegou, M. Mayne-L'hermite, P. Launois, J. Boczkowski and S. Lanone, *Part Fibre Toxicol*, 2012, 9, 46.

42. O. M. Lemine, K. Omri, M. Iglesias, V. Velasco, P. Crespo, P. de la Presa, L. El Mir, H. Bouzid, A. Yousif and A. Al-Hajry, *Journal of Alloys and Compounds*, 2014, 607, 125-131.

43. L. M. Malkinski, J.-Q. Wang, J. Dai, J. Tang and C. J. O'Connor, *Applied physics letters*, 1999, 75, 844.

44. S. Si, A. Kotal, T. Mandal, S. Giri, H. Nakamura and T. Kohara, *Chemistry of Materials*, 2004, 16, 3489-3496.

45. R. A. Brooks, *Magnetic resonance in medicine : official journal of the Society of Magnetic Resonance in Medicine / Society of Magnetic Resonance in Medicine*, 2002, 47, 388-391.

46. P. Gillis, F. Moiny and R. A. Brooks, *Magnetic resonance in medicine : official journal of the Society of Magnetic Resonance in Medicine / Society of Magnetic Resonance in Medicine*, 2002, 47, 257-263.

47. Y. Matsumoto and A. Jasanoff, *Magn Reson Imaging*, 2008, 26, 994-998.

48. D. X. Chen, E. Taboada and A. Roig, *Journal of Magnetism and Magnetic Materials*, 2011, 323, 2487-2492.

49. H. Ali-Boucetta, K. Al-Jamal and K. Kostarelos, in *Biomedical Nanotechnology*, ed. S. J. Hurst, Humana Press, 2011, vol. 726, ch. 19, pp. 299-312.

50. H. Ali Boucetta, K. Al Jamal, K. Müller, S. Li, A. Porter, A. Eddaoudi, M. Prato, A. Bianco and K. Kostarelos, *Small*, 2011, 7, 3230-3238.

51. G. Calabrese, J. J. Nesnas, E. Barbu, D. G. Fatouros and J. Tsibouklis, *Drug Discovery Today*, 2011, 17, 153-159.

52. P. Cígler, M. Kožíšek, P. Řezáčová, J. Brynda, Z. Otwinowski, J. Pokorná, J. Plešek, B. Grüner, L. Dolečková-Marešová, M. Máša, J. Sedláček, J. Bodem, H.-G. Kräusslich, V. Král and J. Konvalinka, *Proceedings of the National Academy of Sciences*, 2005, 102, 15394-15399.

53. A. Bianco, K. Kostarelos, C. D. Partidos and M. Prato, *Chemical Communications*, 2005, DOI: 10.1039/b410943k, 571-577.

54. Z. Liu, S. Tabakman, K. Welsher and H. J. Dai, *Nano Res.*, 2009, 2, 85-120.

55. M. Adeli, R. Soleyman, Z. Beiranvand and F. Madani, *Chem Soc Rev*, 2013, 42, 5231-5256.

56. N. W. S. Kam, M. O'Connell, J. A. Wisdom and H. J. Dai, *Proceedings of the National Academy of Sciences of the United States of America*, 2005, 102, 11600-11605.

57. C. Klumpp, K. Kostarelos, M. Prato and A. Bianco, *Biochimica et Biophysica Acta (BBA) - Biomembranes*, 2006, 1758, 404-412.

58. K. Kostarelos, L. Lacerda, G. Pastorin, W. Wu, WieckowskiSebastien, J. Luangsivilay, S. Godefroy, D. Pantarotto, J.-P. Briand, S. Muller, M. Prato and A. Bianco, *Nat Nano*, 2007, 2, 108-113.

59. M. Mahmood, Y. Xu, V. Dantuluri, T. Mustafa, Y. Zhang, A. Karmakar, D. Casciano, S. Ali and A. Biris, *Nanotechnology*, 2013, 24, 045102.

60. N. W. S. Kam, M. Shim, N. Shi Kam, R. Chen, Y. Li and H. Dai, *Nano Letters*, 2002, 2, 285-288.

61. A. Battigelli, C. Ménard-Moyon, T. Da Ros, M. Prato and A. Bianco, *Advanced Drug Delivery Reviews*, 2013, 65, 1899-1920.

62. P. Luksirikul, B. Ballesteros, G. Tobias, M. Moloney and M. L. H. Green, *Journal of materials chemistry*, 2011, 21, 19080-19085.

63. M. Prato, K. Kostarelos and A. Bianco, *Accounts of chemical research*, 2007, 41, 60-68.

64. M. O'Connell, P. Boul, L. Ericson, C. Huffman, Y. Wang, E. Haroz, C. Kuper, J. Tour, K. Ausman and R. Smalley, *Chemical Physics Letters*, 2001, 342, 265-271.

65. C. G. Salzmann, B. T. T. Chu, G. Tobias, S. A. Llewellyn and M. L. H. Green, *Carbon*, 2007, 45, 907-912.

66. G. M. Mutlu, G. R. Budinger, A. A. Green, D. Urich, S. Soberanes, S. E. Chiarella, G. F. Alheid, D. R. McCrimmon, I. Szleifer and M. C. Hersam, *Nano Lett*, 2010, 10, 1664-1670.

67. P. Singh, S. Campidelli, S. Giordani, D. Bonifazi, A. Bianco and M. Prato, *Chemical Society Reviews*, 2009, 38, 2214-2230.

68. P. Bilalis, D. Katsigiannopoulos, A. Avgeropoulos and G. Sakellariou, *RSC Advances*, 2014, 4, 2911-2934.

69. Z. Yinghuai, A. T. Peng, K. Carpenter, J. A. Maguire, N. S. Hosmane and M. Takagaki, *Journal of the American Chemical Society*, 2005, 127, 9875-9880.

70. S. N. Yannopoulos, G. D. Zouganelis, S. Nurmohamed, J. R. Smith, N. Bouropoulos, G. Calabrese, D. G. Fatouros and J. Tsibouklis, *Nanotechnology*, 2010, 21, 85101.

71. P. A. Jelliss, S. S. Graham, A. Josipovic, S. Boyko, S. D. Minteer and V. Svoboda, *Polyhedron*, 2013, 50, 36-44.

72. L. Shao, G. Tobias, C. G. Salzmann, B. Ballesteros, S. Y. Hong, A. Crossley, B. G. Davis and M. L. H. Green, *Chemical Communications*, 2007, DOI: 10.1039/B712614J, 5090-5092.

73. B. Ballesteros, G. Tobias, L. Shao, E. Pellicer, J. Nogues, E. Mendoza and M. L. H. Green, *Small*, 2008, 4, 1501-1506.

74. G. Tobias, L. Shao, C. G. Salzmann, Y. Huh and M. L. H. Green, *The Journal of Physical Chemistry B*, 2006, 110, 22318-22322.

75. B. Zhao, J. Wang, Z. Li, P. Liu, D. Chen and Y. Zhang, *Materials letters*, 2008, 62, 4380-4382.

76. Y. H. Sung, S. Hong, G. Tobias, B. Ballesteros, F. El Oualid, J. Errey, K. Doores, A. Kirkland, P. Nellist, M. L. H. Green and B. Davis, *Journal of the American Chemical Society*, 2007, 129, 10966-10967.

5

Results III:

CNT filling with inorganic materials: inorganic nanotube formation

In this chapter we present the results corresponding to the formation of single-layered inorganic nanotubes by using MWCNTs as templates. The results here summarized have been reported in the following article:

> **Article 5**: "Synthesis of PbI_2 single-layered inorganic nanotubes encapsulated within carbon nanotubes" *Advanced Materials* **2014**, 26, 2016–2021.

5.1. Objectives

1. Fill in carbon nanotubes with a Van der Waals solid (lead iodide) by molten phase capillary wetting.
2. Study the PbI_2 structure when encapsulated inside the MWCNTs.
3. Develop a protocol that allows the growth of single-layered crystals.

5.2. Summary

A large number of layered materials are characterized by its strong in-plane bonding and weak van der Waals interplanar interactions. Examples of these include graphite, metal dichalcogenides and hexagonal-BN.[1] Since the report on graphene, individual layer of graphite back in 2004, there is a growing interest on the synthesis and properties of van der Waals bonded layered compounds. These unique layered materials, known as van der Waals solids, significantly exhibit interesting physical properties.[2] One method to obtain inorganic single-layered materials is through the synthesis of inorganic nanotubes.[3] The formation of a single-layered nanotubes, that combines the characteristics of two-dimensional (2D) and one-dimensional (1D) materials.[4] A major problem for the formation of single-layered inorganic nanotubes comes from the fact that their multi-walled counterparts are preferred during their growth. For that reason, most reports on inorganic nanotubes are on multi-layered structures.[5] The formation of PbI_2 nanostructures is getting an increased attention. For instance, the use of supramolecular cages has been employed for the template-assisted growth of PbI_2 nanoclusters.[6]

It is well established that CNTs can be employed as templates for the assisted growth of inorganic nanostructures.[7] Their internal space and outer surface allows the formation of tailored nanostructures.[8] There are numerous studies on the formation of narrow 1D nanowires using CNTs as templates.[9] However, the use of the inner cavities for the growth of single-layered inorganic materials has not been realized to date. Interestingly, the formation of inorganic nanotubes (PbI_2) has been reported using other tubular templates such as WS_2 nanotubes.[10, 11] In this case multi walled PbI_2 nanotubes were observed.

The purpose of this chapter was to explore whether single-layered inorganic nanotubes could be synthesized by using MWCNTs as hosts. We chose lead iodide (PbI_2) as a van der Waals solid for the present study. Lead iodide is a semiconductor that presents electroluminescence, photoluminiscence and non-linear optical effects.[12] It is a good

candidate for X-ray and X-ray detectors, thin film transistors and, more recently, organolead iodide perovskites are employed in efficient hybrid solar cells.[13]

5.3. Hybrid preparation

The first step consists in opening the ends of the MWCNTs. To do so, we proceeded with the steam treatment of MWCNTs described in Chapter 3. We steam-treated MWCNTs during 1.5 h followed by an HCl wash to ensure purification, end-opening and shortening of the nanotubes. After that, we proceeded with the filling by a previously reported method, the molten phase capillary wetting.[14] Briefly, MWCNTs and PbI_2 were ground with an agate mortar and pestle until the mixture presented a uniform colour. PbI_2 was added in excess, to increase the amount of material that gets into the nanotubes. The mixture was transferred to a silica ampoule. This was conducted in a glove box with an Ar atmosphere to avoid the presence of oxygen, which would oxidize the compounds when treated at high temperature. The silica ampoule was sealed under vacuum, to reduce the risk of ampoule breaking due to the gas pressure generated inside upon annealing. Then, the ampoule was placed in a furnace and heated up at a given temperature (500 or 800 ^{o}C), above the melting point of PbI_2., where it dwelled for different periods of time (from 10 min up to 86 h). Therefore, PbI_2 gets within the MWCNTs by capillarity.[15] The sample is then cooled down to room temperature. Different annealing treatments were employed. The temperature of the sample was either increased at a constant rate or the mixture was inserted into a furnace with an already set temperature. The target temperature was kept for different time points from 10 min to 86 h. Finally, different cooling rates were also employed, from very slow cooling down lasting for several days (1 ^{o}C/h) or hours (30 ^{o}C/h), until quenching. **Table 5.1.** rigorously illustrates the different conditions that were studied.

Table 5.1. Different temperature ramp combinations for the molten phase filling of MWCNTs.

Heating rate (°C/h)	Final temperature (°C)	Plato (hours)	Cooling rate (°C/h)
300	500	12	30
300	500	12	4
300	500	12	1
300	500	86	30
300	500	12	quench
300	800	12	30
0	500	0.16	quench
0	500	86	quench

After the treatment molten PbI_2 solidifies and it needs to be grinded. Due to the large excess of PbI_2 employed, some yellow crystals of PbI_2 appear on the wall of the quartz ampoule when the sample is cooled down.

5.4. Characterization and discussion

Transmission electron microscopy

Samples were initially analysed by low resolution TEM imaging (**Figure 5.1.**). The filling of PbI_2 occurs in a fast and effective manner and can be achieved after annealing the bulk metal halide in the presence of carbon nanotubes in only 10 minutes. Higher encapsulation efficiencies are obtained after annealing for longer periods of time. The encapsulation of PbI_2 mainly occurs in the form of a nanorod, yet those were also accompanied by single layered PbI_2 tubular structures. Several nanotube to nanorod junctions can be simply observed in the images.

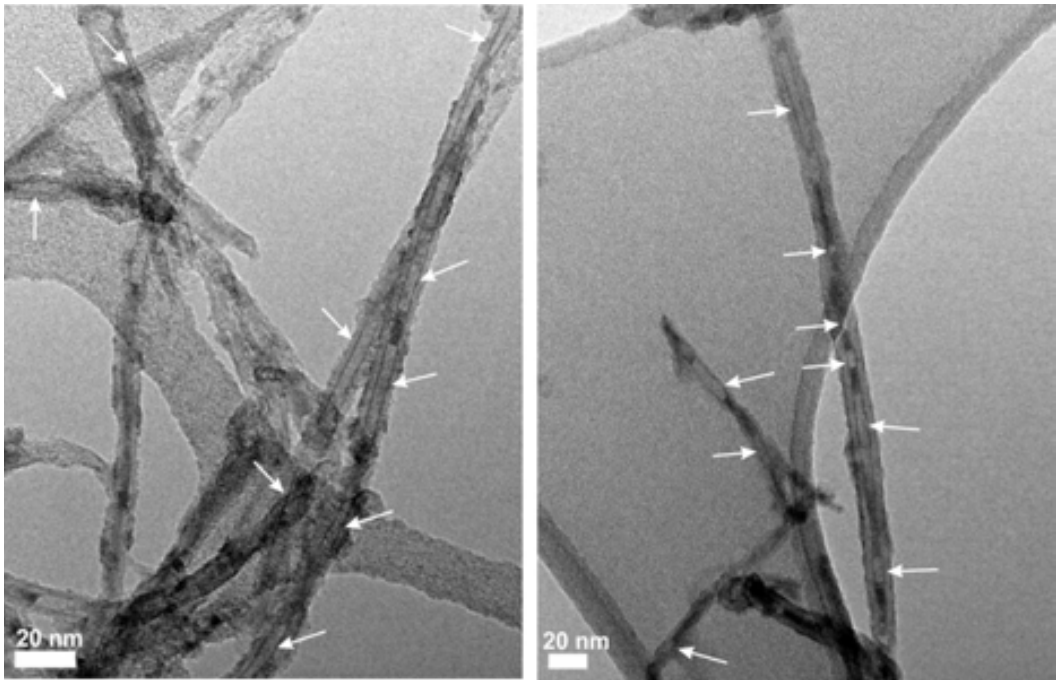

Figure 5.1. low resolution TEM images of MWCNTs filled with PbI_2. White arrows indicate the formation of PbI2 nanotubes within the MWCNTs. Areas with darker contrast inside the MWCNTs display the formation of PbI_2 nanowires.

Even though several experimental conditions (as detailed in **Table 5.1.**) were studied, we could not clearly assess a tendency of forming of either a nanorod or a nanotube. Hence, further studies are necessary to encounter a manner to modulate the formation of one specific structure.

By low magnification TEM we observed the formation of PbI_2 nanotubes inside MWCNTs. Yet, to rigorously confirm that this nanotube was single layered, we studied this new structure by scanning TEM (STEM) and HRTEM.

HRTEM analysis (**Figure 5.2.**) confirms the presence of both types of structures, the complete filling of MWCNTs with PbI_2 to form a nanowire and PbI_2 nanotubes. The formation of PbI_2 nanowires can be detected with a darker contrast in the MWCNT cavity. Though the PbI_2 has been confined in a defined space, the material is capable to remain its layered structure. The different layers of the PbI_2 nanowire can be clearly observed in **Figure 5.2.** The PbI_2 nanotube is detected by observation of the empty cavity within the MWCNT, yet having an internal layer with much darker contrast than the MWCNT layers.

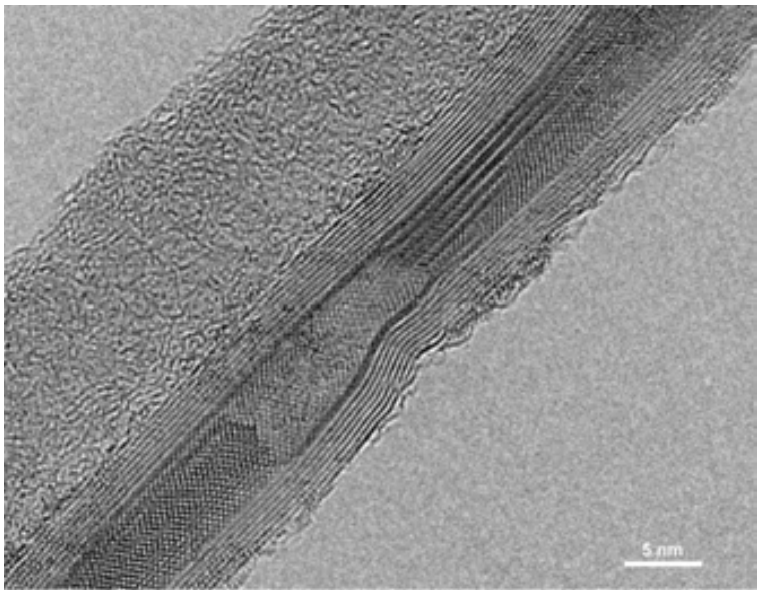

Figure 5.2. HRTEM image of a MWCNT filled with PbI_2. The formation of a PbI_2 nanowire and PbI_2 nanotube is observed.

High-angle annular dark field (HAADF) imaging in high resolution scanning TEM (STEM) images were also obtained (**Figure 5.3.**). HAADF imaging provides Z-contrast images which scale with a power of the atomic number, thus facilitating the detection of heavy elements confined within carbon nanotubes or attached to their external walls down to the atomic scale.[16, 17] Therefore in HAADF STEM a large contrast is observed between PbI_2 and C from the host. This feature makes it easy to premise the wall thickness of the PbI_2 nanotube that has been formed, simply measuring the area of highest intensity in the intensity line profile. The wall thickness measured in the HAADF STEM image is about 0.4 nm, consistent with the formation of a single layer of PbI_2, confirming the mono-layered nature of the PbI_2 nanotube.

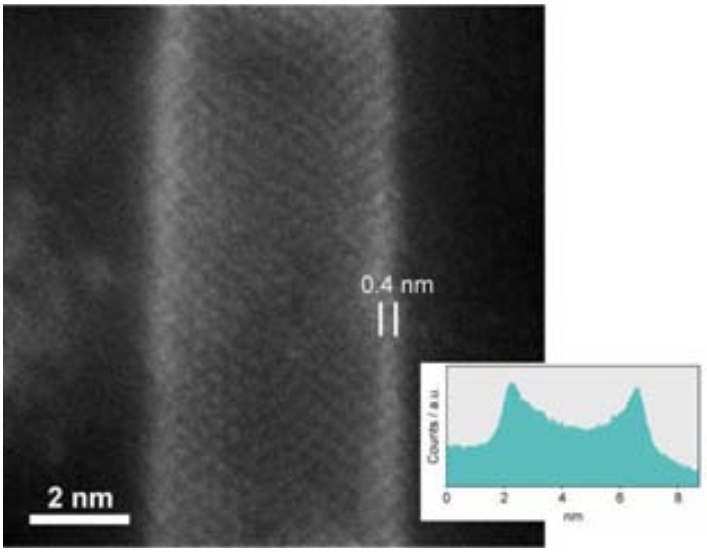

Figure 5.3. HAADF HRSTEM image, with its corresponding intensity line profile (integrated along 25 pixels), of a single-layered PbI_2 nanotube.

Though it seems by the HRTEM imaging that the PbI_2 nanowire occupies the whole MWCNT cavity, HAADF STEM images (**Figure 5.4.**) remarkably reveal that those nanowires can be composed of narrower nanowires confined within a single-layered PbI_2 nanotube. A spacing of darker contrast between this nanowire and the single-walled PbI_2 nanotube reveals this kind of structure.

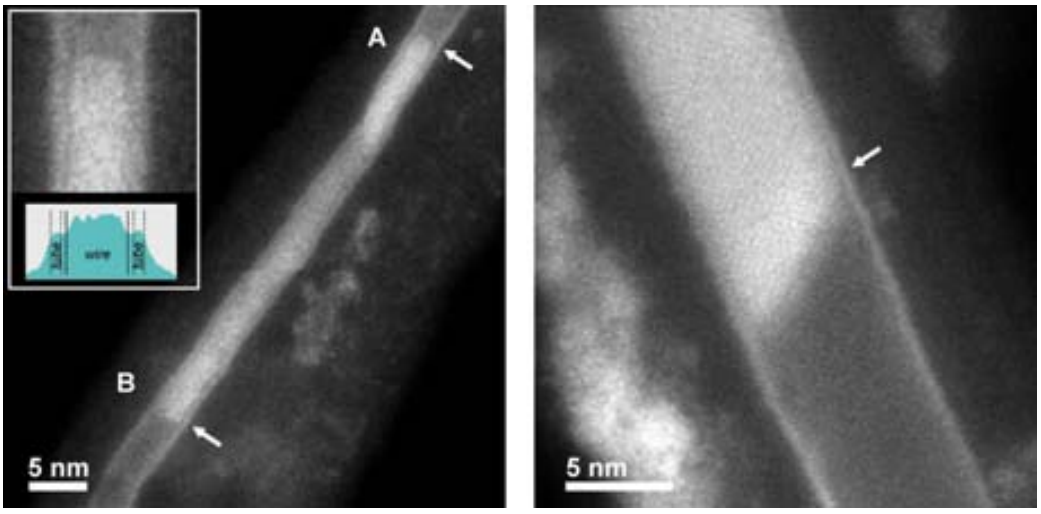

Figure 5.4. HAADF STEM images of nanotube nanorod junctions. In both images a PbI2 nanorod appears to be confined within a PbI2 nanotube. The arrows point at the end of the nanorods. The inset shows a higher magnification image of area A with its corresponding line intensity profile (integrated along 25 pixels).

Figure 5.5.a displays a HRTEM image a single-layered nanotube with an outermost external diameter of 3.94 nm. Taking into account that each layer of PbI_2 is actually composed by a I-Pb-I repeating unit in which a layer of Pb atoms is sandwiched between two layers of I atoms, an external diameter of 3.94 nm actually corresponds to a nanotube of about 3.5 nm (taking Pb as the central point). We will therefore refer to the diameter of the PbI_2 nanotubes to this central Pb layer. The PbI_2 SWNT formed was seen to have a stable structure, being able to adapt its diameter to the one of the host. Moreover, with HRTEM we can appreciate that PbI_2 crystallinity and also display the PbI_2 nanotube curvature. The simulated image is included as an inset of **Figure 5.5.a** and its structure perfectly matches with the experimental results obtained. The selected simulated image is the one that got best agreement in terms of focus, and corresponds to a focal length of -8 nm. **Figure 5.5b** satisfactorily exhibits a model that has been constructed to schematically represent this new structure.

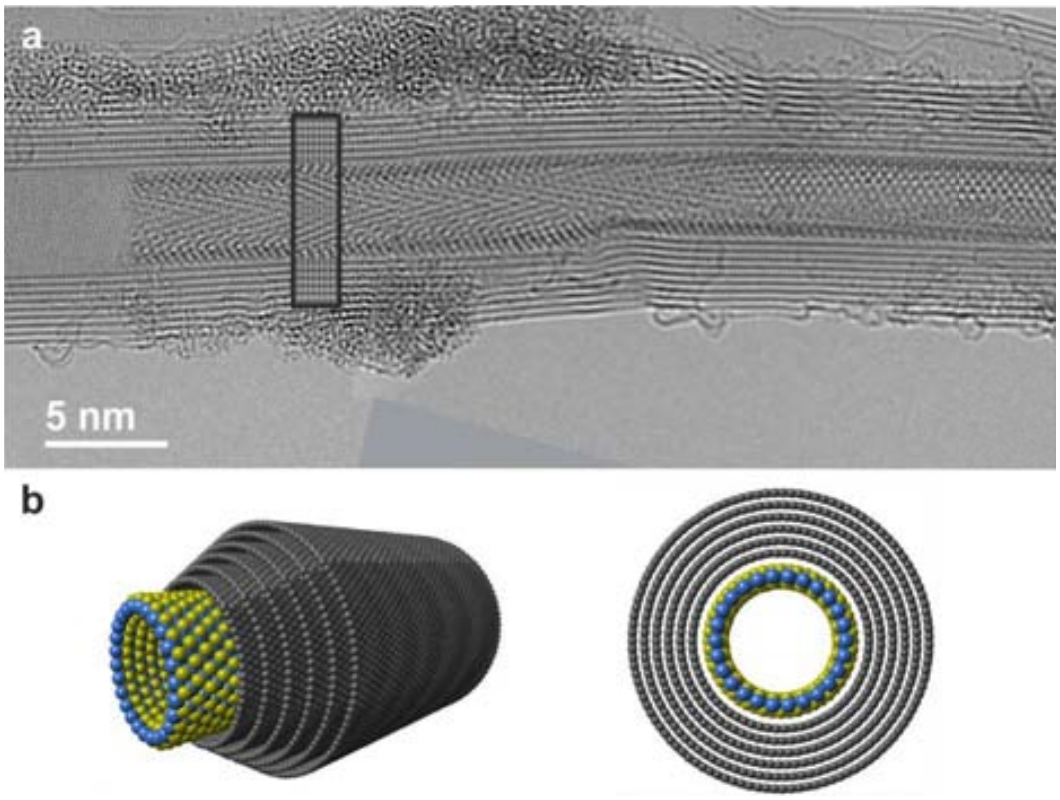

Figure 5.5. a) HRTEM image of a PbI2-SWNT@MWCNT. The black square displays the corresponding simulation of the area selected. b) Schematic representation of the grown single-layered PbI2 tubular materials (cyan and green spheres representing Pb and I atoms, respectively) within the inner cavities of a multiwalled carbon nanotube (grey spheres). A cross section across the main axis of the tube is also included for clarity.

The simulated image presented as an inset of **Figure 5.5.a** is selected by previously constructing the same image with different focal lengths. To illustrate the analysis, **Figure 5.6.** presents images calculated for various focal lengths, ranging from -20 nm to +20 nm. By doing an observation of the images in detail, it can be appreciated that the simulation that shows more similarities to the experimental result is the one with a focal length of -8 nm.

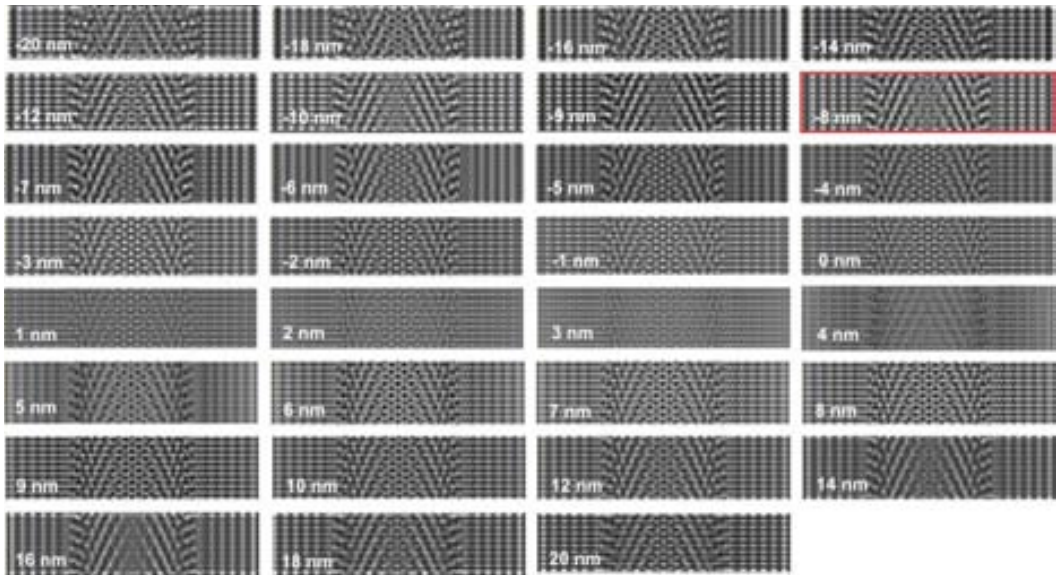

Figure 5.6. Simulated images of the PbI_2-SWNT@MWCNT with different focal lengths, going from –20 nm to +20 nm.

X-ray energy dispersive spectroscopy (EDS) experiments give elemental profiles of a region of the sample when STEM imaging is conducted (**Figure 5.7**). When conducted in an area with tubular contrast (**Figure 5.7.a**), a higher intensity of both constituent elements, I and Pb, is detected at the edges compared to the central space confirming the tubular nature of the grown material. For comparison, we also analyzed an area which a nanowire of PbI_2 was formed within the MWCNT (**Figure 5.7.b**). Herein, The highest intensity of both I and Pb is located at the center of the linear profile, as expected for the nanowire formation inside the CNT.

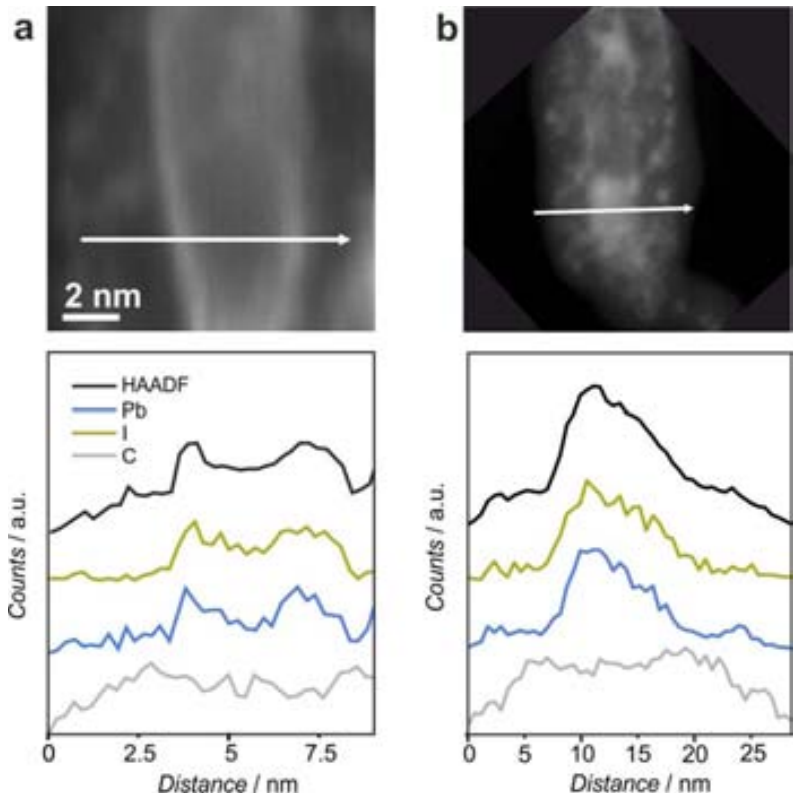

Figure 5.7. HAADF HRSTEM image with its corresponding intensity STEM -EDS line profile (integrated along 25 pixels) confirming a) the presence of a PbI_2 nanotube or b) the presence of a PbI_2 nanowire.

The sample of MWCNTs contained nanotubes with inner diameters ranging from 1.5 nm to 9 nm. Therefore, we could study the role of the host in the formation of the inorganic nanotubes and whether there were any diameter constraints. We measured the diameter of the inner cavity of the CNT host when either a nanorod or a single-layered nanotube was present and the resulting histograms are plotted in **Figure 5.8.** Interestingly, despite the confined growth of nanorods can take place irrespective of the diameter of the host, the formation of nanotubes preserve a threshold at 4 nm. Taking into account that the grown PbI_2 nanotubes are about 0.5 nm narrower than the host, single-layered PbI_2 nanotubes from 3.5 to 7.5 nm in diameter can be successfully prepared with this approach.

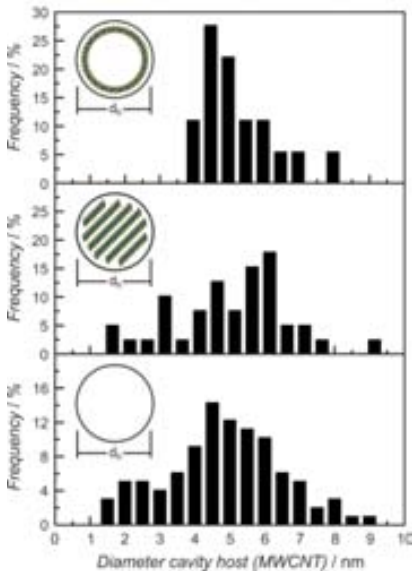

Figure 5.8. Histograms of the MWCNT cavity (cavity of the host), when PbI_2 nanotubes (top) or PbI_2 nanorods (center) are observed; empty MWCNTs (bottom) are also included for comparison.

During the TEM inspection of the samples, we detected physical transformations of the PbI_2 confined within the MWCNTs. Because of the high interest that these kind of nanoscale transformations present, [18, 19] we studied the dynamic effect of electron beam irradiation on several nanotube-nanorod junctions. In **Figure 5.9.a** a series of images are displayed, in which a PbI_2 nanorod is confined between PbI_2 nanotubes. When irradiating with the electron beam at 80 kV, a continuous blending of the nanorod onto the nanotube takes place until its complete dissolution, thus resulting in the formation of a continuous PbI_2 nanotube. The opposite procedure, in which a PbI_2 nanotube is converted to a PbI_2 nanorod was also observed in several areas and an example is displayed in **Figure 5.9.b**. The transformation from one type of nanostructure to the other takes place due to the irradiation by the electron beam. HAADF-STEM analysis in **Figure 5.4.** revealed that nanowires could be accommodated within single-layered PbI_2 nanotubes. Thus meaning that to allow the accommodation of additional lead and iodine atoms into the tubular structure an atomic migration within the top/bottom part of the nanotube was necessary. There were some empty MWCNT areas that became filled when lead and iodine atoms are displaced due to the irradiation. In some previous reports where metal halides had been encapsulated within CNTs, electron been irradiation has even lead to chemical changes.[20, 21]

For this reason, the mechanism of transformation from nanotubes to nanorods and viceversa needs further investigation and even chemical changes cannot be disregarded at

this stage. Therefore the use of low voltage is desired when investigating these systems under the electron beam if we want to preserve the initial structure without including any changes.

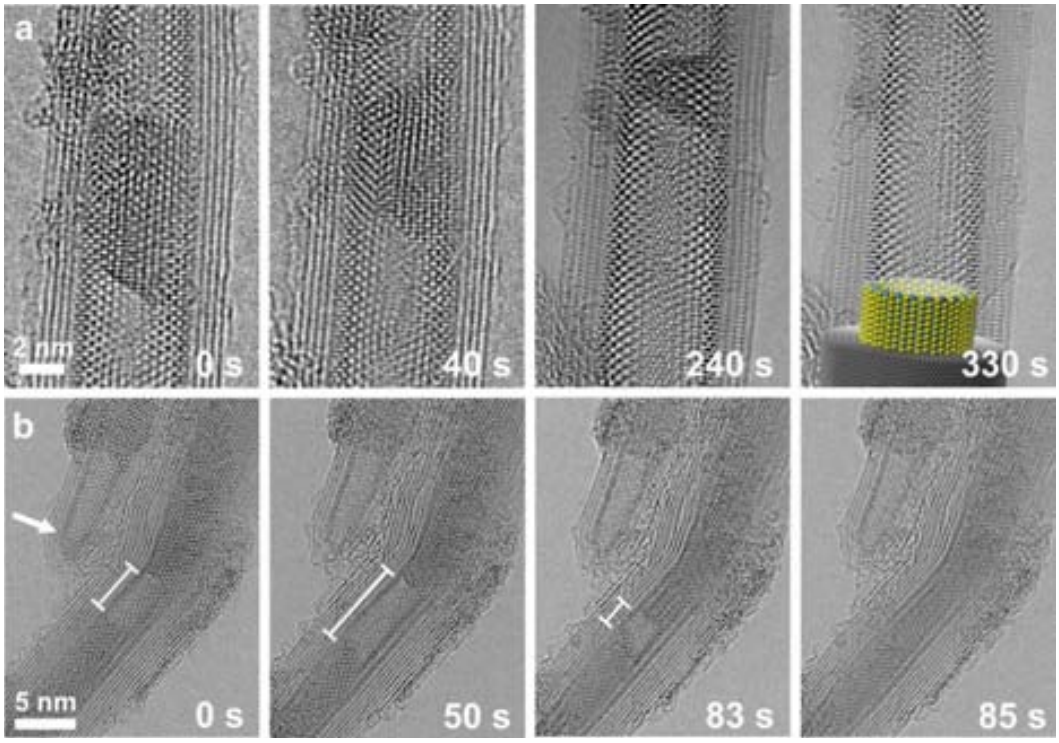

Figure 5.9. Dynamics under the electron beam radiation. Sequence of images showing the transformation from a nanorod fragment onto a single layered nanotube using an electron dose of ~$0.6 \cdot 10^4$ e^- $Å^{-2}$. A schematic representation is included in the last image; cyan, green and grey spheres representing Pb, I and C atoms, respectively.

First principle electronic structure calculations

The possibility to form inorganic single-walled nanotubes was assessed with first principle electronic structure calculations using the Density Function Theory (DFT) implemented in the SIESTA code.[22] The metal halide nanotubes were modeled by rolling up a fragment (of variable size) of an individual layer of bulk PbI_2 (**Figure 5.10.a**).[23] The energy cost of the wrapping is rather moderate (it is larger than 1 eV per nanotube unit cell only for the narrower systems investigated) and, as expected, it decreases as the diameter of the nanotube increases. This energy is always largely exceeded by the encapsulation energy of the PbI 2 nanotubes, the van der Waals PbI_2–C interlayer interaction that we found to be approximately 2.75 eV nm^{-2}. The higher energy at smaller diameters makes the synthesis of narrow tubes less likely, favouring the higher relative stability of PbI_2

nanorods in such a size range. This is in good agreement with the analysis performed in **Figure 5.8**. where the formation of PbI_2 single-layered nanotubes is only observed above 4 nm. The theoretical calculations also predict stability for the single-layered PbI_2 nanotubes in case the template was removed: all the stand-alone nanotubes considered turned out to be stable.

Because of PbI_2 being a band gap semiconductor, we studied the energy band gap of the PbI_2 in the form of a SWNT (**Figure 5.10.b**). This was seen to be very similar to the one of bulk PbI_2 (2.3-2.6 eV)[24] and scarcely dependent on the tube diameter or wrapping axis. Yet, in very narrow diameters, the energy starts to drop but these would correspond to unrealistic diameters as for the work presented in this study.

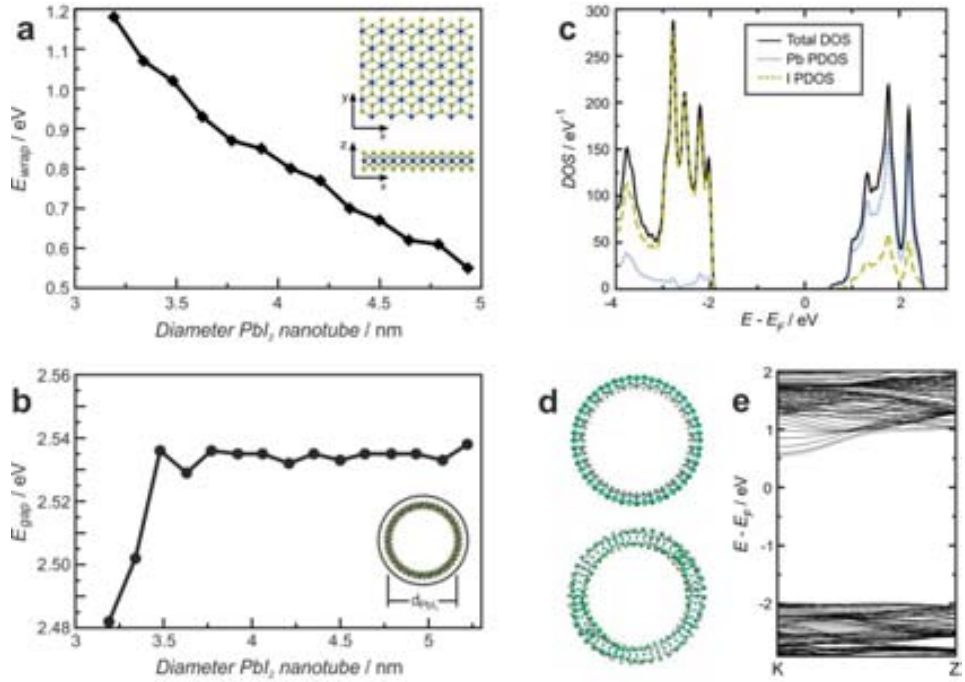

Figure 5.10. a) Wrapping energy as a function of the PbI_2 nanotube diameter. The wrapping energy is defi ned as $E_{wrap} = E_{NT} - E_{ML}$, where E_{NT} is the total energy of the PbI_2 nanotube and E_{ML} is the total energy of a flat stand-alone PbI_2 monolayer of the same size, i.e. the unrolled nanotube. The wrapping axis is x (inset) and the energy is given for unit cell of the nanotube. Note that the x, y, z axis correspond to the fragment of PbI_2 layer used to model the nanotubes and not to the bulk PbI_2 structure. b) Band-gap vs diameter of the PbI_2 single-layered nanotube. c) Total density of states and projections on Pb and I atoms. d) The wave-function of HOMO (bottom) and LUMO (top) shows the different localization: on I atoms the former, on Pb atoms the latter. e) Band structure diagram. The data presented correspond to a nanotube of 3.77 nm in diameter.

The projections of the density of states (DOS) were next displayed to study the behaviour of PbI_2 as a band gap semiconductor (**Figure 5.10.c**). These reveal a peculiar localization

of the band-edge states of different layers. Valence states are almost exclusively made of I orbitals, while conduction states are mostly made of Pb orbitals. This behaviour has been previously reported for SiGe heterostructures.[25] This was also evident in the real space representation (**Figure 5.10.d**) of the valence and conduction bands. The efficient charge separation present in this compound can be exploited for electronic applications such as solar cells. For these devices, the recombination of the electron-hole pair must be minimized, and this new material is a good candidate for that.

Additionally, we observed that the conduction states exhibit a larger dispersion than the rather flat valence band (**Figure 5.10.e**), thus electrons are expected to be more efficient charge carriers than holes in these tubular systems.

5.5. Conclusions

- The formation of single-layered inorganic nanotubes inside CNTs has been reported for the first time.
- A solvent-free high temperature route has been developed for the formation of high-quality single-crystalline inorganic nanotubes.
- The formation of these single-walled inorganic nanotubes was observed for diameters bigger than 3.5 nm and is dependent on the diameter of the host.
- Inorganic nanotubes of a given diameter can be prepared by simply using a sample of CNTs with uniform inner diameter.
- The dynamic transformation from an inorganic nanorod to an inorganic nanotube can be displayed by irradiating with an electron beam.
- The prepared single-layered nanotubes are found to be stable even without the presence of the hosting template (as per DFT calculations).

These 1D nanostructures will offer very promising technological applications where materials having well defined electronic, optic or optoelectronic properties are required. The method is highly versatile opening up new horizons in the preparation of single-layered nanostructures of a wide variety of materials.

5.6. References

1. Y.-C. Lin, N. Lu, N. Perea-Lopez, J. Li, Z. Lin, X. Peng, C. H. Lee, C. Sun, L. Calderin, P. N. Browning, M. S. Bresnehan, M. J. Kim, T. S. Mayer, M. Terrones and J. A. Robinson, *ACS Nano*, 2014, 8, 3715-3723.
2. G. Gao, W. Gao, E. Cannuccia, J. Taha-Tijerina, L. Balicas, A. Mathkar, T. N. Narayanan, Z. Liu, B. K. Gupta, J. Peng, Y. Yin, A. Rubio and P. M. Ajayan, *Nano Letters*, 2012, 12, 3518-3525.
3. J. Goldberger, R. Fan and P. Yang, *Accounts of Chemical Research*, 2006, 39, 239-248.
4. R. Tenne, *Front. Phys.*, 2014, 9, 370-377.
5. C. N. R. Rao and A. Govindaraj, *Advanced Materials*, 2009, 21, 4208-4233.
6. Y. Liu, C. Hu, A. Comotti and M. D. Ward, *Science*, 2011, 333, 436-440.
7. R. Kitaura, N. Imazu, K. Kobayashi and H. Shinohara, *Nano letters*, 2008, 8, 693-699.
8. D. Eder, *Chemical Reviews*, 2010, 110, 1348-1385.
9. M. Monthioux, *Carbon*, 2002, 40, 1809-1823.
10. R. Kreizman, S. Y. Hong, J. Sloan, R. Popovitz-Biro, A. Albu-Yaron, G. Tobias, B. Ballesteros, B. G. Davis, M. L. H. Green and R. Tenne, *Angewandte Chemie International Edition*, 2009, 48, 1230-1233.
11. R. Kreizman, A. N. Enyashin, F. L. Deepak, A. Albu-Yaron, R. Popovitz-Biro, G. Seifert and R. Tenne, *Advanced Functional Materials*, 2010, 20, 2459-2468.
12. L.-M. Wu, X.-T. Wu and L. Chen, *Coordination Chemistry Reviews*, 2009, 253, 2787-2804.
13. J.-Y. Jeng, Y.-F. Chiang, M.-H. Lee, S.-R. Peng, T.-F. Guo, P. Chen and T.-C. Wen, *Advanced Materials*, 2013, 25, 3727-3732.
14. R. R. Meyer, J. Sloan, R. E. Dunin-Borkowski, A. I. Kirkland, M. C. Novotny, S. R. Bailey, J. L. Hutchison and M. L. H. Green, *Science*, 2000, 289, 1324-1326.
15. P. M. Ajayan and S. Iijima, *Nature*, 1993, 361, 333-334.
16. S. Y. Hong, G. Tobias, B. Ballesteros, F. El Oualid, J. C. Errey, K. J. Doores, A. I. Kirkland, P. D. Nellist, M. L. H. Green and B. G. Davis, *Journal of the American Chemical Society*, 2007, 129, 10966-10967.
17. X. Fan, E. C. Dickey, P. C. Eklund, K. A. Williams, L. Grigorian, R. Buczko, S. T. Pantelides and S. J. Pennycook, *Physical Review Letters*, 2000, 84, 4621-4624.
18. V. C. Holmberg, M. G. Panthani and B. A. Korgel, *Science*, 2009, 326, 405-407.
19. P. M. F. J. Costa, U. K. Gautam, Y. Bando and D. Golberg, *Nat Commun*, 2011, 2, 421.

20. J. L. Hutchison, N. Grobert, R. M. Zakalyukin, A. A. Eliseev, M. V. Chernisheva, A. S. Kumskov, Y. V. Grigoriev, A. V. Krestinin, B. Freitag and N. A. Kiselev, *AIP Conference Proceedings*, 2008, 999, 79-92.

21. A. Ilie, J. S. Bendall, K. Nagaoka, S. Egger, T. Nakayama and S. Crampin, *ACS Nano*, 2011, 5, 2559-2569.

22. G. Kresse and J. Furthmüller, *Computational Materials Science*, 1996, 6, 15-50.

23. B. Palosz, W. Steurer and H. Schulz, *Journal of physics. Condensed matter*, 1990, 2, 5285-5295.

24. A. Ferreira da Silva, N. Veissid, C. Y. An, I. Pepe, N. Barros de Oliveira and A. V. Batista da Silva, *Applied Physics Letters*, 1996, 69, 1930-1932.

25. M. Amato, S. Ossicini and R. Rurali, *Nano Letters*, 2010, 11, 594-598.

6

Conclusions

In this chapter the general conclusions are described.

The main achievements of this Thesis can be structured into three different sections:

1. Purification and shortening of MWCNTs using steam

We have investigated the role of steam on the purification, wall structure and length distribution of MWCNTs. Steam is capable of removing amorphous carbon and graphitic particles that sheath the metal catalyst employed for the CNT growth. Therefore, these metal nanoparticles could be efficiently removed by a subsequent HCl wash, leading to samples with very low residual amount of metal catalysts (0.013 wt%)

The MWCNT wall structure was found to remain intact after the steam treatment, with no detectable oxygen- and hydrogen- bearing functionalities

Furthermore, the length distribution could also be modified by the time of steam treatment. Higher steam exposition times resulted into shorter MWCNTs. Steam is a simple, economic, and environmentally friendly method that results in high-quality nanotubes, the length of which can be easily modulated by a mere change of the treatment time.

2. Functionalization of carbon nanotubes for their use in biomedical applications

Two different strategies have been developed for the modification of the CNT walls: a non-covalent and a covalent functionalization with inorganic payloads of interest for biomedical applications.

Non-covalent functionalization of MWCNTs with SPION has been achieved by *in situ* generation. Smaller particles and better distribution onto the MWCNT walls was exhibited when using oxidized MWCNTs. The prepared SPION-MWCNT hybrids turn out to be better contrast agents than Endorem®, a clinically approved contrast agent.

A dual imaging agent for MRI and SPECT/CT with good *in vivo* stability has been developed by radiolabelling the SPION with ^{99m}Tc. This constitutes the first report on the use of CNTs for dual MRI/SPECT imaging.

An enhanced MRI signal can be obtained by using short MWCNTs, containing the same type, amount and distribution of SPION nanoparticles than a sample of long MWCNTs. This is due to a higher interaction of the nanoparticles when incorporated onto short CNTs. *In vitro* cytotoxicity studies of the hybrids revealed that the developed agents are biocompatible.

Covalent functionalization of CNTs was achieved *via* incorporation of metallacarborane clusters onto SWCNT with an amide bond. The synthesized hybrid was presented a higher

dispersibility in water than oxidized SWCNTs, an essential feature for biomedical applications. Therefore, this hybrid holds potential for boron delivery for Boron Neutron Capture Therapy.

3. CNT filling with inorganic materials: inorganic nanotube formation

The formation of single-layered PbI_2 nanotubes within the CNT cavities has been achieved by molten phase capillary wetting. HRTEM and STEM analysis confirms presence of high-quality single-crystalline structures.

The diameter of the single-layered inorganic nanotube synthesized can be modulated by changing the diameter of the hosting CNT template. The narrowest inorganic nanotube observed was of 3.5 nm in diameter.

Theoretical calculations predict the stability of the prepared PbI_2 nanotubes, even without the presence of the hosting CNT template. The prepared single-layered PbI_2 nanotubes are band gap semiconductors with similar band gap energies than bulk PbI_2.

An efficient charge separation between the valence and conducting bands is observed, suggesting that these 1D nanostructures are potential candidates for technological applications such as solar cells.

7

Published articles

FULL PAPER

Magnetically Decorated Multiwalled Carbon Nanotubes as Dual MRI and SPECT Contrast Agents

Julie Tzu-Wen Wang, Laura Cabana, Maxime Bourgognon, Houmam Kafa, Andrea Protti, Kerrie Venner, Ajay M. Shah, Jane K. Sosabowski, Stephen J. Mather, Anna Roig, Xiaoxing Ke, Gustaaf Van Tendeloo, Rafael T. M. de Rosales, Gerard Tobias, and Khuloud T. Al-Jamal**

Carbon nanotubes (CNTs) are one of the most promising nanomaterials to be used in biomedicine for drug/gene delivery as well as biomedical imaging. This study develops radio-labeled, iron oxide-decorated multiwalled CNTs (MWNTs) as dual magnetic resonance (MR) and single photon emission computed tomography (SPECT) contrast agents. Hybrids containing different amounts of iron oxide are synthesized by in situ generation. Physicochemical characterisations reveal the presence of superparamagnetic iron oxide nanoparticles (SPION) granted the magnetic properties of the hybrids. Further comprehensive examinations including high resolution transmission electron microscopy (HRTEM), fast Fourier transform simulations, X-ray diffraction, and X-ray photoelectron spectroscopy assure the conformation of prepared SPION as γ-Fe_2O_3. High r_2 relaxivities are obtained in both phantom and in vivo MRI compared to the clinically approved SPION Endorem. The hybrids are successfully radio labeled with technetium-99m through a functionalized bisphosphonate and enable SPECT/CT imaging and γ-scintigraphy to quantitatively analyze the biodistribution in mice. No abnormality is found by histological examination and the presence of SPION and MWNT are identified by Perls stain and Neutral Red stain, respectively. TEM images of liver and spleen tissues show the co-localization of SPION and MWNTs within the same intracellular vesicles, indicating the in vivo stability of the hybrids after intravenous injection. The results demonstrate the capability of the present SPION–MWNT hybrids as dual MRI and SPECT contrast agents for in vivo use.

1. Introduction

Nanomaterials constitute a new class of imaging agents in biomedical imaging. Because of the possession of large surface area per unit and the capability of further engineering, they often serve as a platform to facilitate imaging via the incorporation, either covalently or non-covalently, of various imaging probes such as fluorophores, radiotracers or magnetic resonance (MR) imaging contrast agents.[1–4] Carbon nanotubes (CNTs) are considered one of the most promising nanomaterials to be used for biomedicine applications as delivery vectors for drugs or genes.[5–7] CNTs have also been employed for in vivo imaging either through conventional linking to the above mentioned imaging molecules or can be captured directly using Raman spectroscopy,[8] NIR fluorescence microscopy,[9] photoacoustic imaging[10] or ultrasonography[11] all relying on their inherent physical properties. However, satisfactory sensitivity and spatial resolution remain the major challenges.

Although optical imaging is still the leading imaging modality in

Dr. J. T.-W. Wang, M. Bourgognon, H. Kafa, Dr. K. T. Al-Jamal
Institute of Pharmaceutical Science
King's College London
London, SE1 9NH, UK
E-mail: gerard.tobias@icmab.es
L. Cabana, Dr. A. Roig, Dr. G. Tobias
Institut de Ciència de Materials de Barcelona (ICMAB-CSIC)
Campus UAB, 08193, Bellaterra, Barcelona, Spain
E-mail: khuloud.al-jamal@kcl.ac.uk
Dr. A. Protti, Dr. R. T. M. de Rosales
Division of Imaging Sciences and Biomedical Engineering
King's College London
St. Thomas' Hospital, London, SE1 7EH, UK
Dr. A. Protti, Prof. A. M. Shah
Cardiovascular Division, James Black Centre
King's College London British Heart Foundation Centre of Excellence
London, SE5 9NU, UK
K. Venner
UCL Institute of Neurology
University College London
London, WC1N 3BG, UK
Dr. J. K. Sosabowski, Prof. S. J. Mather
Centre for Molecular Oncology
Barts Cancer Institute,
Queen Mary University of London
London, EC1A 7BE, UK
Dr. X. Ke, Prof. G. Van Tendeloo
Electron Microscopy for Materials Research (EMAT)
University of Antwerp
Groenenborgerlaan 171, B-2020, Antwerp, Belgium

DOI: 10.1002/adfm.201302892

laboratory-based biomedical research mainly due to its convenience and low cost,[12] magnetic resonance imaging and nuclear imaging are currently the mainstream clinical diagnostic approaches. MRI is already a standard medical imaging technique which offers excellent spatial and temporal resolution, and good soft tissue contrast.[13] Nuclear imaging including single photon emission computed tomography (SPECT) and positron emission tomography (PET) involves the use of radioisotopes and has the advantages over other modalities of high sensitivity and the possibility to perform functional imaging.[14] The concept to establish multimodality imaging techniques is not new since each imaging modality has its own strength and weaknesses. From material scientists' points of view, efforts have been made in the development of multimodal imaging contrast agents.[15] Here we propose magnetically decorated multi-walled CNTs (MWNTs) as dual MRI and SPECT contrast agents.

Many studies have been conducted to employ CNTs for MRI by incorporating paramagnetic gadolinium (Gd^{3+}) or superparamagnetic iron oxide nanoparticles (SPION) into CNTs.[16–22] The two contrast agents are both clinically approved although showing opposite effect on a MR image. Gd^{3+} serves mainly as a positive contrast agent which increases proton spin-lattice relaxation rates (R_1); iron oxide instead is a negative contrast agent by increasing spin-spin proton transverse relaxation rates R_2 and R_2*. Although Gd^{3+}-based contrast agents (GBC) are generally considered safe after chemical conjugation with organic chelating ligands, concern remains in their in vivo stability as free gadolinium ions are toxic.[23] There are also reports of adverse effects on using GBC in patients with impaired renal function.[24] In this regard, iron oxide nanoparticles which exhibit superparamagnetic properties have been used as negative MRI contrast agents in the clinic since they are biodegradable and can be incorporated into normal iron metabolism in the body.[25,26] A Gd^{3+}-conjugated ultra-short single-walled CNT (SWNT) nanocomposite was reported as a CNT-based MRI contrast agent for the first time in 2005.[16] Together with a subsequent study,[17] this type of Gd^{3+}-SWNTs induced low toxicity in vitro and reported both high R_1 and R_2 relaxation properties. The first approach to employ CNT/iron oxide for MR imaging was described by Choi et al. who utilized $Fe(CO)_5$ as the iron-containing catalyst precursor for the growth of SWNTs.[18] The process resulted in the attachment of iron oxide nanoparticles to one end of the nanotubes, allowing MR imaging. The constructs were imaged using MRI and NIR spectroscopy in cells. CNTs/iron oxide hybrids applied for in vivo MRI were also recently studied by Wu et al. in the form of MWNT-Fe_3O_4 hybrids.[19] The hybrids accumulated in lung, liver and spleen and the T_2-weighted MRI revealed significantly reduced signals in liver and spleen. Chen and the colleagues developed a 'layer-by-layer' approach to assemble CNTs/iron oxide hybrids with quantum dots for in vitro magnetic-fluorescence dual imaging.[20] There was also a study using carboxylated SWNTs containing traces of iron for in vivo MRI.[21] Recently, Yin et al. demonstrated an *in vitro* targeting effect of CNTs/iron hybrids conjugated to the tumour targeting ligand folic acid.[22] Targeted constructs accumulated more in folate receptor positive cells compared to the non-targeted counterparts and thus displayed a darker MR image.

Since SPION has been shown to be an effective MRI contrast agent, there have been studies to broaden the potential of iron oxide in biomedical imaging by merging with a radionuclide to combine MRI and SPECT/PET.[27–36] Such integration was often performed through polymeric coating which may not have desirable stability, especially in vivo.[31,32] A new approach has been introduced by de Rosales et al. using bisphosphonates (BPs) to link SPION with radionuclides.[33,35,36] With regards to the strong binding ability of BPs to the surface of SPION, radiolabelled-BPs were successfully conjugated to the iron oxide core and permitted quantitative biodistribution studies as well as dual SPECT/PET-MR imaging.[33,35,36]

In the present study, we have exploited this novel approach to synthesize magnetic yet radioactive MWNTs as dual MRI and SPECT contrast agents. To the best of our knowledge, this is the first study documenting the use of CNTs/iron oxide hybrids for dual MRI and nuclear imaging. In this work, the R_2* magnetic properties and the efficiency of radio-labelling SPION/MWNT hybrids were examined. In vivo experiments were performed to characterize the hybrids as multimodal SPECT and MRI contrast agents.

2. Results

2.1. Synthesis of SPION–MWNT Hybrids

The as-received MWNT materials were firstly purified by steam and HCl to remove some impurities, namely amorphous carbon, graphitic particles (carbon nanomaterials having few graphitic layers) and some metal particles. These metal particles, from the catalyst used for the growth of the MWNT, are covered by graphitic shells which inhibit their direct dissolution in an acidic media. Steam removed the amorphous carbon present in the samples and the graphitic shells covering the metal particles.[37] The removal of the amorphous carbon is essential to allow an efficient sidewall functionalization of the carbon nanotubes.[38] Purified MWNTs were then treated with nitric acid to introduce oxygen bearing functionalities (mainly carboxylic acid groups (–COOH)) onto the MWNT tips and sidewalls.[39,40] SPION–MWNT hybrids containing increasing amount of iron content were synthesized in situ by mixing the functionalized MWNTs with a precursor for the formation of the nanoparticles. It is known that when metal salts are dissolved in the presence of acid treated nanotubes, the metal ions interact strongly with the surface groups present onto the MWNTs.[41] Such interactions were expected to occur in our samples when mixing iron acetate (precursor) with the functionalised MWNTs, thus affording a homogeneous coverage of the iron atoms onto the surface of the MWNTs. Subsequently, the samples were thermally treated and left exposed to air thus resulting in the formation of the iron oxide nanoparticles.

2.2. Physicochemical Characterization of SPION–MWNT Hybrids

The amount of SPION present in the hybrids was quantitatively determined by thermogravimetric analysis (TGA) carried out under flowing air (**Figure 1**A). As shown in the

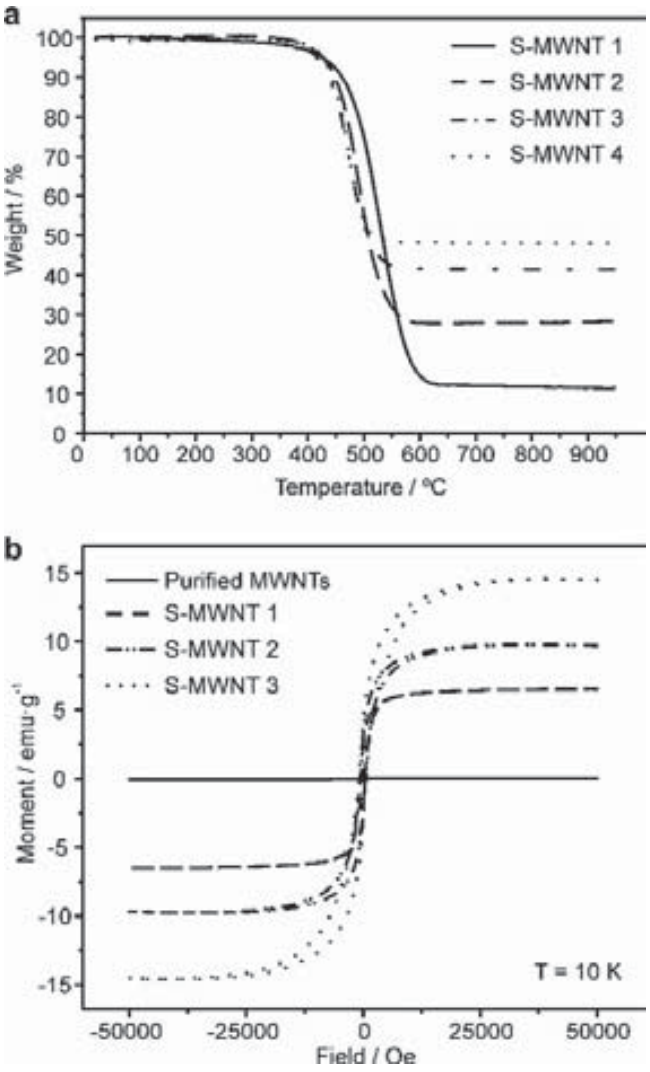

Figure 1. Physicochemical characterisation of SPION–MWNT hybrids. A) Thermogravimetric analysis of S-MWNTs in flowing air; B) Hysteresis loops of S-MWNT **1–3** at 10 K after subtracting the linear background; purified MWNTs were included for comparison.

TGA curves, oxidation of the samples took place at around 450 °C. Therefore, the residue obtained after the complete combustion of carbon atoms at 600 °C corresponded to the amount of iron oxide nanoparticles loaded onto the MWNTs. SPION–MWNT hybrids containing 11.5, 28.0, 41.5, and 48.0 wt% of SPION (assuming Fe_2O_3) were obtained and named S-MWNT **1–4** respectively from now on, where S refers to the superparamagnetic properties of the iron oxide nanoparticles deposited on the MWNTs. The superparamagnetic properties are described in the later section. S-MWNT **4** was found to be physically unstable in aqueous dispersions, as will be described later, thus was disregarded in further studies. Magnetic measurements at 10 K were performed to evaluate the effect of the increasing amount of SPION. Figure 1B shows the hysteresis loops for S-MWNT **1–3** and steam purified MWNTs which was included as a control. Purified MWNTs showed extremely weak magnetic signals, almost inappreciable in the figure, which was expected for samples with negligible catalytic impurities.[42] This was in agreement with TGA data under flowing air of the purified material that confirmed an almost unappreciable amount of residual metal catalyst (Figure S1). Samples with a metallic content below 1 wt% are dubbed as "high quality" in terms of catalyst content (impurities from the synthesis of the carbon nanotubes.[43] In contrast to purified MWNTs, a marked ferromagnetic behavior was observed for hybrids S-MWNT **1–3** at 10 K. As expected, samples with increasing amount of loaded SPION yielded higher saturation magnetization. Values for the saturation magnetization were measured as 6.5, 9.7, and 14.6 emu per total gram of sample (emu·g^{-1}) for S-MWNT **1–3** respectively.

2.3. Phantom MR Imaging and R_2* Relaxation Measurements

The transverse R_2* relaxation rates of S-MWNT **2-3** dispersed in 1% agar and 0.5% Pluronic F127 solution at different Fe concentrations were measured at 7 Tesla (7T). Although the hybrids studied here displayed good dispersibility using 1% Pluronic F127 solution before dilution with agar, phantom samples were prepared by dispersing the materials in agar to avoid the sedimentation of samples and thus achieve more accurate relaxation measurements. The same preparation and measurements using Endorem, a clinically approved SPION, were carried out for comparison. S-MWNT **1** with the lowest iron content was not investigated here since the dispersion was not ideal due to high sample concentrations required to achieve equivalent Fe amount to the other hybrids and thus for reliable MR imaging. **Figure 2**A shows MRI of Endorem (i) and S-MWNT **2-3** (ii-iii) at different concentrations at an acquired echo time of 5 ms. Some of the vials reported none or little signal due to fast signal decay effects when imaged at increased echo times. By sampling such signal shortenings, R_2* values were determined. The relaxation times of S-MWNT **2-3** and Endorem were plotted versus concentrations of iron (Figure 2B), reporting good linear correlations. The r_2* relaxivities were calculated as 343 $s^{-1}mM^{-1}$, 425 $s^{-1}mM^{-1}$ and, 325 $s^{-1}mM^{-1}$ for S-MWNT **2-3** and Endorem respectively. Endorem reported the lowest r_2* relaxivities while S-MWNT **3** showed the highest r_2* making it an MR appealing probe for R_2* and R_2 investigations.

2.4. Characterization of S-MWNT 3

Further characterization was performed for S-MWNT **3** since it was found to be the hybrid with the best r_2 relaxivity. **Figure 3**A,B and Figure S2 display transmission electron microscopic (TEM) images of S-MWNT **3** where SPION were shown along the backbone of the carbon nanotubes. High resolution TEM (HRTEM) analysis (Figure 3C) confirmed the presence of crystalline nanoparticles attached to the walls of carbon nanotubes. Electron diffraction analysis of these and other nanoparticles along with fast Fourier transform (FFT) simulations confirmed that the structure of the nanoparticles fit a cubic structure. The FFT pattern of one of the nanoparticles is shown as the inset in Figure 3C. Indexation of this pattern and its corresponding simulation are in good agreement with the [–233]

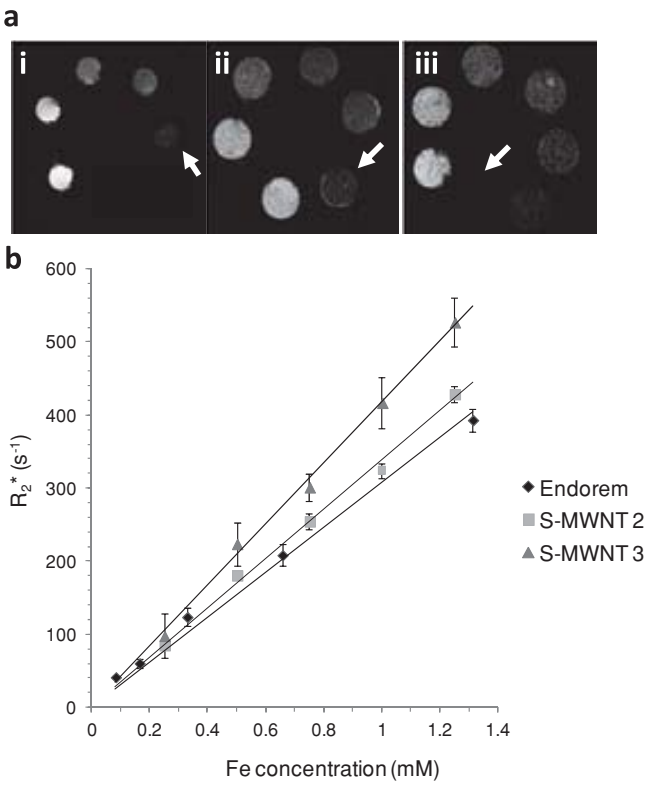

Figure 2. Phantom MRI studies. A) Phantom MR imaging of Endorem (i) and S-MWNT **2-3** (ii-iii). Samples are arranged clockwise from lowest (brightest) to highest (white arrows) iron concentration; B) R_2* relaxation time analysis as a function of Fe concentration. A 7 Tesla magnet was engaged for image acquisition. r_2* relaxivities of the hybrids were obtained from the different slopes. Results are presented as mean ± S.D. (n = 3).

zone axis. This allowed us to narrow the nature of the SPION to either γ-Fe_2O_3 or Fe_3O_4, and all other oxide possibilities can be excluded.

The size of SPION that decorated MWNTs was determined based on TEM images analysis. The diameter of about 200 SPION was measured and the resulting histogram is presented in **Figure 4**A. The majority of the SPION have diameters between 4–8 nm, with a mean value of 6.5 ± 4.0 nm. The presence of small particles was responsible for the low signal to noise ratio showing in the X-ray diffraction (XRD) pattern of the hybrid (Figure 4B). The observed peaks in Figure 4B could be assigned to those of carbon (pdf –powder diffraction file– 750444) from carbon nanotubes and to either maghemite (γ-Fe_2O_3; pdf 391346) or magnetite (Fe_3O_4; pdf 740748). No peaks for iron (II) acetate which was used as a precursor were observed indicating a successful decomposition by the thermal treatment. Further evidence for the complete decomposition of iron acetate was provided by TGA analysis performed under flowing nitrogen where no weight loss at low temperature is observed (Figure S3). The sharp drop at 710 °C for S-MWNT **3** was in good agreement with the percentage weight loss expected from the carbothermal reduction of the iron oxide nanoparticles by carbon (from the CNTs). Although the synthesis of the nanoparticles was performed under reducing conditions (Ar/H_2 mixture), the posterior exposition of the samples in air led to the complete oxidation of the nanoparticles. X-ray photoelectron spectroscopy (XPS) was performed to get further insight into the nature of the nanoparticles. A cumulative detailed scan performed over the Fe 2p region is presented in Figure 4C. The position, shape and width of the XPS peaks and the presence of the "shake-up" satellite structure at 719.3 eV is distinctive of the γ-Fe_2O_3 structure.[44]

In order to determine superparamagnetic properties of the SPION, hysteresis loops at 300 K were recorded. As shown in Figure 4D, no remnant magnetization was observed when there was no applied magnetic field, which is the typical behavior of a superparamagnetic material. Collectively, it is confirmed that the MWNTs were decorated with superparamagnetic γ-Fe_2O_3 nanoparticles (SPION).

2.5. Radio-Labelling Efficiency and Serum Stability Studies

Radio-labelling of SPION–MWNT hybrids was conducted as described previously using a functionalized bisphosphonate (BP) namely dipicolylamine-alendronate (DPA-ale) as a linker between SPION and the radioisotope ^{99m}Tc[34] (**Scheme 1**). DPA-ale is described as BP in the following sections. To investigate the possible influence of iron content on the radio-labelling efficiency, pristine MWNT (p-MWNT)

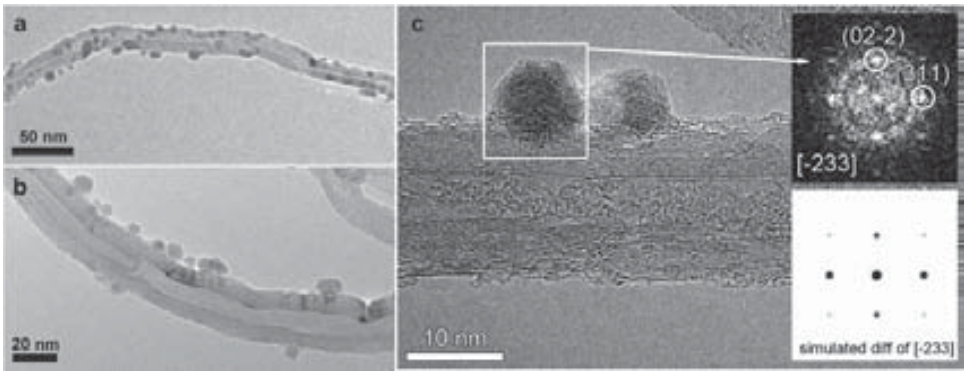

Figure 3. TEM analysis of S-MWNT **3**. A,B) TEM images at two different magnifications; and C) a high resolution transmission electron microscopy (HRTEM) image of S-MWNT **3**; the inset presents the diffraction pattern of a nanoparticle and the simulated diffraction pattern along the zone axis [–233].

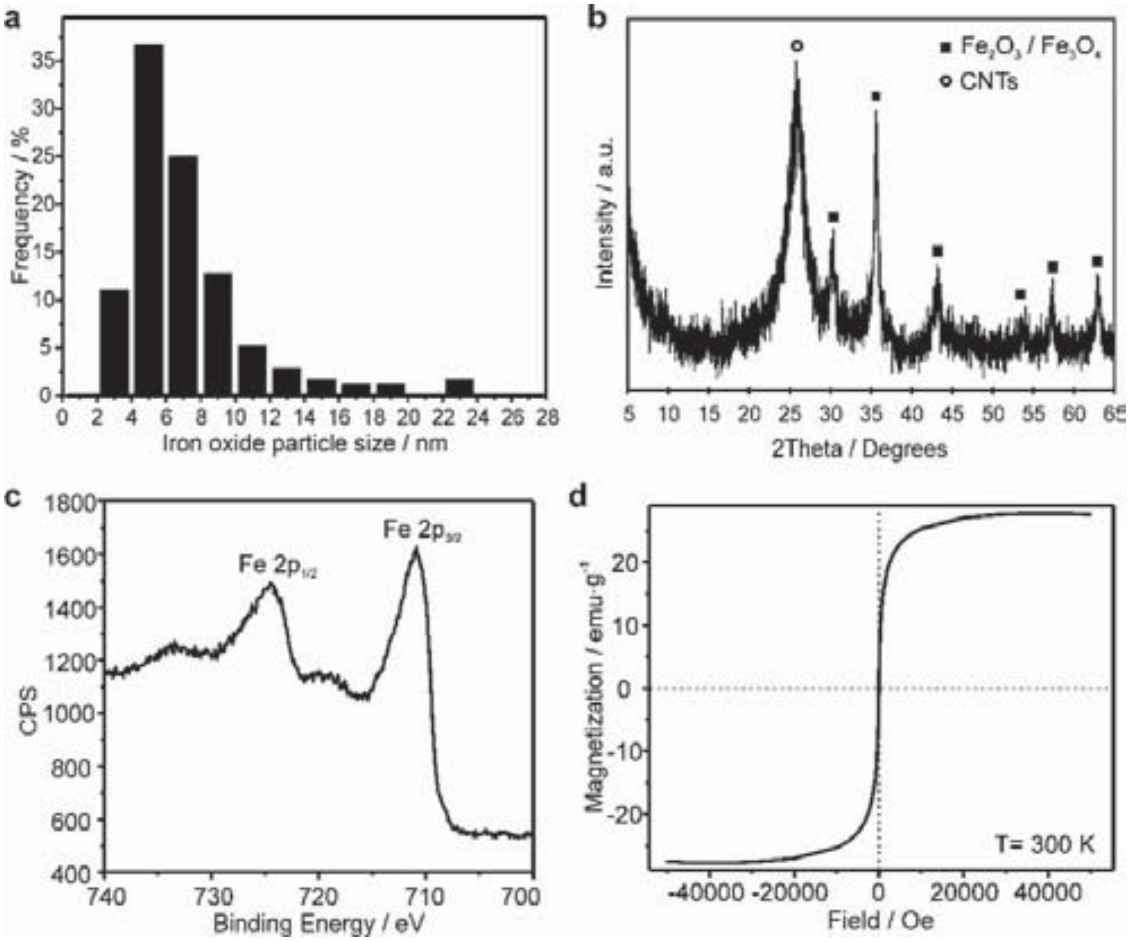

Figure 4. Characterization of the iron oxide nanoparticles decorating MWNTs. A) Histogram of the nanoparticle size, B) X-ray diffraction pattern, C) X-ray photoelectron spectroscopy, and D) hysteresis loops at 300 K.

without SPION and S-MWNT **1–3** with increasing iron contents were radio-labelled. As shown in **Figure 5**A, low radio-labelling efficiency was observed in p-MWNT in contrast to the S-MWNT hybrids where labelling yields were obtained above 57.5% ± 2.3. The low radio-labelling yield for p-MWNT could be due to non-specific adsorption of ^{99m}Tc-BP to the graphitic backbone of CNTs. The best labelling efficiency was achieved for S-MWNT **2** and **3** with values of 82.5 ± 3% and 79.3 ± 3%, respectively. The results indicated that, as expected, the amount of iron content has an impact on the radio-labelling efficiency, and hybrids with higher SPION contents exhibited higher radio-labelling yields.

Stability studies were assessed by incubating the labelled hybrids in either human serum or PBS (50% final concentration) at 37 °C for 24 h. The results demonstrated high stability of all radio-labelled S-MWNTs in either human serum or PBS (Figure 5B). Most of ^{99m}Tc was still bound to the hybrids (more than 90%) after 24 h incubation. Since S-MWNT **3** displayed the best radio-labelling yields and stability in serum, it was selected to be used in the subsequent dual in vivo imaging and organ biodistribution studies.

2.6. Whole Body 3D SPECT/CT Imaging of Mice Injected with ^{99m}Tc-BP-S-MWNT 3

Whole body SPECT imaging in combination with computed tomography (CT) scanning was carried out to study the organ biodistribution of the radio-labelled ^{99m}Tc-BP-S-MWNT **3** (4 MBq, 50 µg hybrid) or ^{99m}Tc-BP (5 MBq) alone at 30 min, 3 h, and 24 h after i.v. injection in mice. As shown in the bottom panel in **Figure 6**A, ^{99m}Tc-BP was mainly detected in bone at the early time points (<30 min and 3 h) which is expected due to the high affinity of bisphosphonates to bone minerals.[34] Accumulation in kidney and bladder was detected in mice treated with ^{99m}Tc-BP within 30 min after injection suggesting rapid renal clearance. ^{99m}Tc-BP-S-MWNT **3**, however, showed predominant accumulation in lung, followed by liver and spleen (top panel in Figure 6A) within 30 min after injection. The signals in the liver remained constant after 4 h while a clear reduction in lung accumulation was observed over the first 4 h. Similar to ^{99m}Tc-BP, a small fraction was detected in the bladder after 30 min indicating rapid clearance for some ^{99m}Tc-BP-S-MWNT fractions. Low SPECT signals were detected

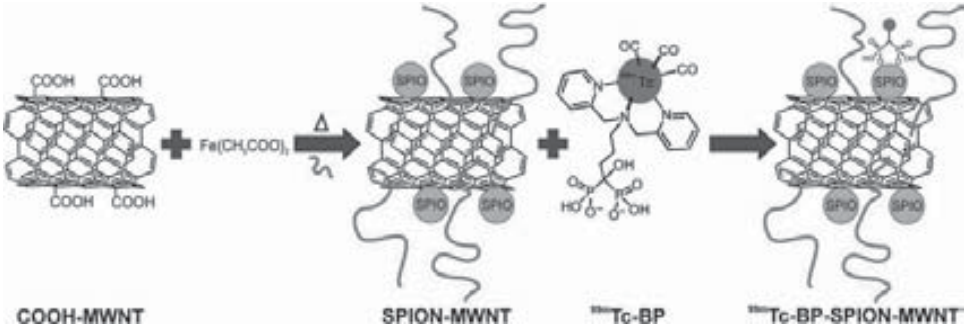

Scheme 1. Radio-labelling of SPION–MWNT hybrids with technetium-99m (^{99m}Tc) via a linker. The Radio-labelling was conducted using ^{99m}Tc-dipicolylamine-alendronate (^{99m}Tc-DPA-ale, referred to ^{99m}Tc-BP thereafter) as described previously.[34]

in both mice at 24 h post administration (Figure S5). The 'virtual' loss of radioactivity is most likely due to the decay of the radionuclide (half-life for ^{99m}Tc, 6 h) as is the case of short, half-lived radioisotopes. Therefore, post-mortem γ-scintigraphy was conducted in parallel to SPECT/CT imaging to assess quantitatively the organ biodistribution of the hybrids over time.

2.7. Organ Biodistribution and Blood Clearance Profile of ^{99m}Tc-BP-S-MWNT 3 in Mice After i.v. Injection

Organ biodistribution of ^{99m}Tc-BP-S-MWNT **3** or ^{99m}Tc-BP alone in major mice organs was examined at 1, 4, and 24 h after i.v. injection. The results correlated well with the SPECT images that lung, liver, and spleen were the major organs of accumulation (Figure 6B and Figure S6A). In view of organ biodistribution over time, the hybrid seemed to retain in liver and spleen tissues up to 24 h post injection as the percentage of injection dose (%ID) per gram tissue remained constant (Figure 6B). Despite the reduction in %ID per gram lung tissue observed, substantial amount of the hybrid (i.e., 12.8% ± 1.9 ID/organ) was still detected in the lung after 24 h.

On the contrary, a markedly different organ biodistribution profile was observed for ^{99m}Tc-BP. A typical bisphophonate pharmacokinetics was featured with profound accumulation in the bone and minimal exposure to other tissues (Figure 6C and Figure S6B). The results indicated successful conjugation of ^{99m}Tc-BP to SPION-MWNT hybrids, as shown by the altered organ biodistribution pattern in vivo.

Different blood clearance profiles were found for ^{99m}Tc-BP and ^{99m}Tc-BP-S-MWNT **3** (Figure 6D). Despite less than 2.9% ± 0.3 of ID was measured in blood at 30 min after i.v. injection in the case of the hybrid, the amount of ^{99m}Tc-BP detected at the earliest time point (2 min) was approximately 3 times higher than that of ^{99m}Tc-BP-S-MWNT **3**.

2.8. In Vivo MR Imaging and liver R2* Relaxation Time Measurements

Since SPECT imaging demonstrated accumulation of the hybrid in the reticuloendothelial system (RES, e.g., liver and spleen), MRI was engaged in the liver in order to verify the correct multimodality effect of the hybrid. **Figure 7**A shows axial

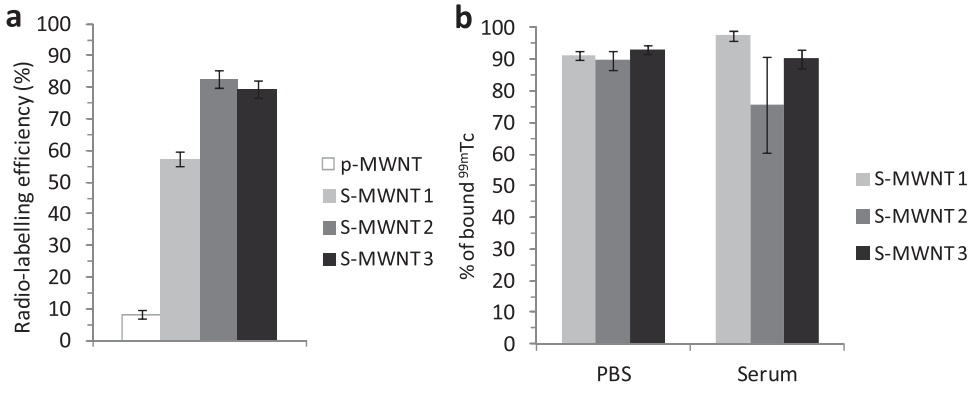

Figure 5. Radio-labelling efficiency and stability of SPION–MWNT hybrids. A) Radio-labelling efficiency of pristine MWNT (p-MWNT) and S-MWNT **1–3**. Hybrids dispersed in 1% Pluronic F127 solution at 1 mg/mL concentration were mixed with ^{99m}Tc-BP at 37 °C for 30 min. Radio-labelling efficiency was estimated by measuring the radioactivity in the pellets (bound ^{99m}Tc-BP) and supernatants (unbound ^{99m}Tc-BP) of the samples after centrifugation at 17 000 rcf for 30 min. B) Serum (50%) and PBS stability studies of radio-labelled S-MWNT **1–3** after 24 h incubation at 37 °C.

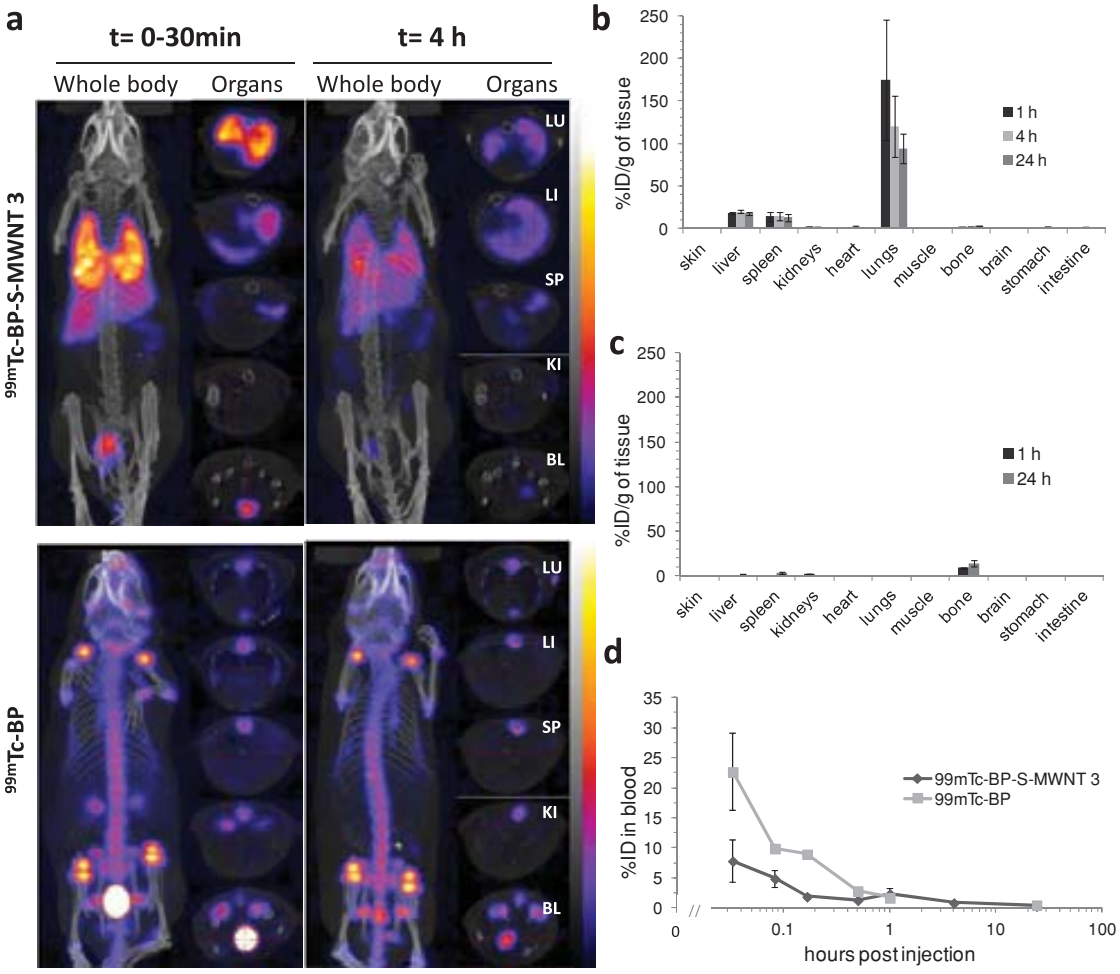

Figure 6. In vivo SPECT/CT and organ biodistribution studies following i.v. injection of ^{99m}Tc-BP-S-MWNT **3** or ^{99m}Tc-BP. A) Whole body 3D SPECT/CT imaging; B) organ biodistribution of ^{99m}Tc-BP-S-MWNT **3** and; C) ^{99m}Tc-BP. D) Blood clearance profile of ^{99m}Tc-BP-S-MWNT **3** and ^{99m}Tc-BP. Cross sections in (A) were taken at lung (LU), liver (LI), spleen (SP), kidney (KI) and bladder (BL). Results are expressed as mean ± S.D. (n = 3).

liver images at different acquisition echo times against Fe concentration (mg/kg) of the hybrid. Like the results obtained in phantoms, MRI signals were darkened over time and the decay effects appeared faster upon increasing iron dosage. The R_2* relaxation rate was plotted in Figure 7B accordingly. The measured in vivo R_2* relaxation rates from liver increased almost linearly in relation to the injected Fe doses.

2.9. Microscopic Examination of S-MWNT 3 in Tissues

To examine the presence of the hybrid in tissues after i.v. injection, tissues of lung, liver and spleen were sampled at various time points up to 30 days and stained by either Perls stain or Neutral Red stain. Mice were administered 400 μg of S-MWNT **3** (5.8 mg Fe/kg), a much higher dose than that used in biodistribution and SPECT studies, in order to be able to detect the hybrids by histological examination.

Perls stain is commonly used to demonstrate iron in tissues in histology. As shown in **Figure 8**A, blue staining indicating the presence of iron (shown by arrows) was observed in the three organs at 24 h, 7 days, and 30 days. Spleen injected with the vehicle alone (1% Pluronic F127 in PBS) lacking the SPION was shown to be the most positive to Perls stain. Moreover, a gradual increase in iron content over time was noted in spleen up to 30 days after injection and more iron was found in the red pulp region than white pulp. Red blood cells, which normally reside in the red pulp were stained with creamy brown colour (Figure 8A). On the contrary, the amount of iron in liver and lung declined over time since very few blue-stained regions were observed after 30 days. In comparison, no iron (blue stain) was observed in Pluronic F127 liver tissues. It was also noted in the liver sections that more blue stain appeared in the cytoplasm of Kupffer cells compared to hepatocytes. This advanced uptake might be due to the phagocytic nature of Kupffer cells.

Separate tissue sections were then stained with Neutral Red as a counter stain to enable visualisation of the MWNTs.[45,46] The results were in agreement with Perls stain that MWNTs (shown by arrows) showed the same pattern as iron in lung and liver with reduction observed in these tissues over time

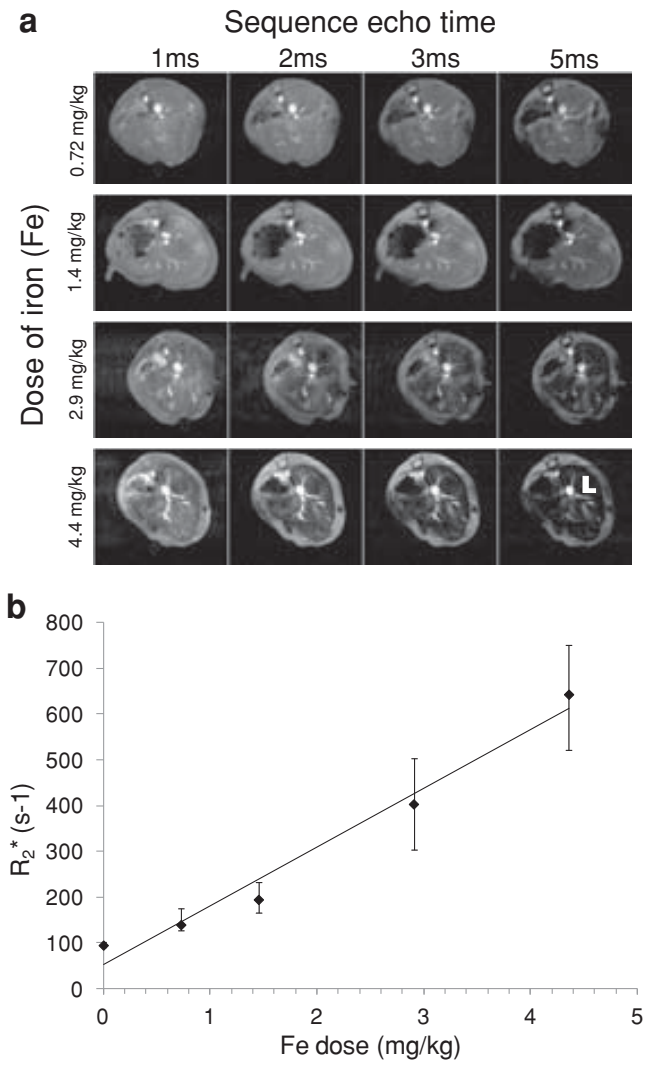

Figure 7. In vivo T_2*-weighted MR studies. A) MR images of mouse liver 48 h after injection with various doses of S-MWNT **3** over time; B) R_2* relaxation rate measurements. L: liver.

(Figure 8B). MWNTs presented in spleen were also found in the red pulp region. Few batches of MWNTs remained in lung at 30 days and were shown as large aggregates.

In summary, a good correlation was demonstrated in the organ biodistribution profile between the MWNTs and iron under microscopic examination, indicating a good stability of SPION-MWNT in vivo. Moreover, additional studies using TEM were carried out to confirm the integrity at the nanoscale level.

2.10. TEM Studies of Mice Organs

To confirm the co-localisation of SPION and MWNT at ultrastructural levels, TEM examination for tissues sampled at 24 h after i.v. injection of 400 μg of S-MWNT **3** (5.8 mg Fe/kg) was carried out. Liver and spleen were chosen here as they showed high accumulation of the hybrid. Interestingly, the results confirmed uptake of the hybrid not only in kupffer cells but also in hepatocytes of the liver. A series of TEM images were taken for hepatocytes at different magnifications (**Figure 9**A,B). Hepatocytes are recognised by the presence of a substantial number of mitocondria. The hybrids were often identified within vesicles. Both SPION and MWNTs were observed in the same endocytic vesicle, suggesting the uptake of MWNTs and SPIOs as an intact hybrid. SPION were shown as electron-dense particles (dotted black arrows) while MWNTs were confirmed with their tubular structures (solid black arrows). At 24 h, SPION were found dissociated from the MWNTs perhaps due to the low pH of endocytic vesicles. Figure 9C,D show a kupffer cell (white dotted line), the professional macrophage cells located in liver, where a similar pattern to that of hepatocytes was observed. TEM images of spleen are shown in Figure 9E,F. Again, SPION and MWNTs were observed in the same endocytic vesicles with some SPION being detached from MWNTs while some remained intact.

Co-localisation observed within the same endocytic vesicles indicated that the hybrids were stable enough to be able to pass through many biological barriers after i.v. administration, enter the same organ and to be internalised as intact hybrids by the same cell within the same endocytic vesicle.

2.11. Histological Examination by H&E

Histological analysis was carried out on H&E stained paraffin embedded tissue sections sampled at various time points up to 30 days after i.v. injections of 400 μg S-MWNT **3** (5.8 mg Fe/kg) (**Figure 10**). No significant histological changes were observed in lung, liver and spleen compared to untreated tissues. Tissues taken from animals treated with 1% Pluronic F127 solution alone were also examined and the results confirm no abnormalities induced. Such results indicated the biocompatibility of the hybrid in vivo under the conditions tested.

3. Discussion

The future of diagnostic applications lies on the use of multimodal approaches by combining different imaging modalities to achieve an accurate diagnosis in cancer, cardiovascular disease and other disorders. These attempts are to integrate the advantages of each imaging tool and compensate their limitations. The best example is the combination of SPECT/PET with MR or X-ray CT. As mentioned previously, the new generation of multimodal imaging equipment is the combination of MRI with SPECT/PET in which pioneer instruments designed for MR/PET hybrid imaging for human have been setup recently.[47] As a result, the collected imaging outcomes would contain excellent tomography from MRI (resolution down to 50–250 μm) and great sensitivity achieved by SPECT/PET (10^{-10} to 10^{-12} mol/L).[14] Another important reason for these imaging techniques being used widely in the clinic is attributed to their unlimited penetration depth. This overcomes the major disadvantages of optical imaging techniques, particularly fluorescence detection, which is highly restricted to the location of

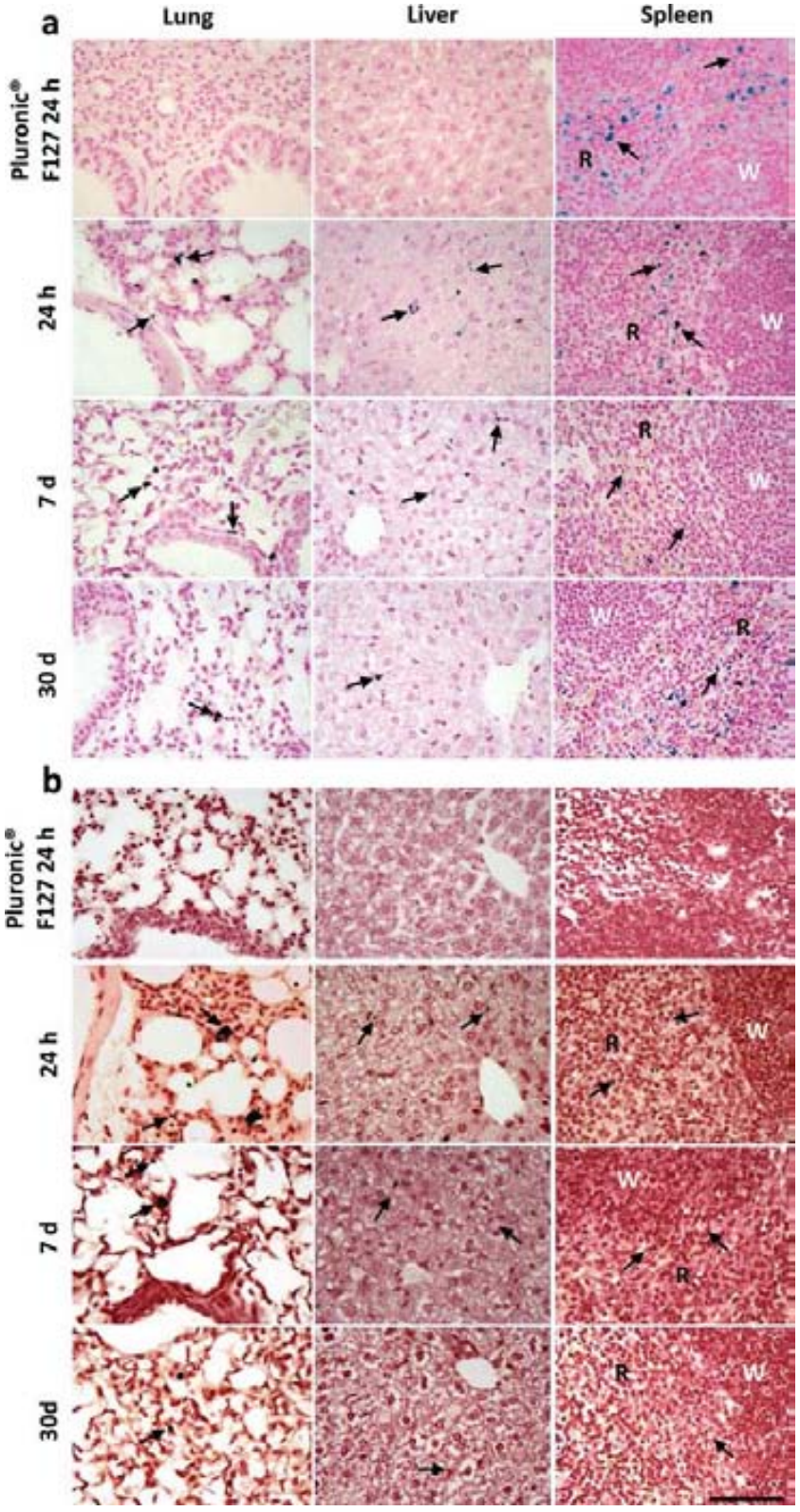

Figure 8. **M**Microscopic examination of liver, lung and spleen sections of C57/Bl6 mice injected with S-MWNT **3.** Animals were injected with the vehicle alone (1% Pluronic F127) or 400 μg of the hybrid (5.8 mg Fe/kg). Selected organs were sampled at 24 h, 7 days, and 30 days after injection and stained with A) Perls staining or B) Neutral Red staining. Arrows in (A) point to the presence of iron (blue colour) and arrows in (B) point to the presence of carbon nanotubes (black dots) in the tissue sections. W: the white pulp region of spleen; R: the red pulp region of spleen. The scale bar corresponds to 50 μm.

the imaging targets, the type of light source used (e.g., laser wavelength), and intrinsic tissue properties (e.g., tissue absorption and scattering).[12]

A recently published study reported the synthesis of CNT/iron oxide hybrids by ligand exchange or click chemistry approaches.[48] In the current study, SPION–MWNT hybrids were prepared by in situ generation. MWNTs were treated with acid to introduce oxygen bearing functionalities on the sidewalls and tips. The decoration of steam purified MWNTs (without the oxygen bearing functionalities) with iron oxide nanoparticles was also carried out as a control. The functionalization of the nanotubes was found to play a key role in providing a homogenous decoration with the nanoparticles. A more uniformed coverage of iron oxide nanoparticles was achieved when employing functionalized MWNTs compared to using the nanotubes lacking oxygen-containing functionalities. The use of iron acetate as a precursor was exploited for the formation of the iron oxide nanoparticles. The procedure involved thermal annealing at high temperature, resulting in the formation of nanoparticles with high crystallinity as confirmed by HRTEM. To determine the degree of nanoparticle loading, TGA under flowing air was performed. As appreciated in the TGA curves (Figure 1A and Figure S1), steam purified MWNT started to oxidize under flowing air at higher temperature (600 °C) than the S-MWNT **1–3** samples with oxidization starting at about 450 °C. The decrease in the onset of combustion temperature, by about 150 °C, was due to the presence of inorganic nanoparticles in the samples. This phenomenon has been observed in samples of carbon nanotubes containing different inorganic materials.[49] Further characterization studies were carried out using HRTEM and XRD. HRTEM allows direct imaging and analysis of nanostructures and provides structural information down to the atomic scale. HRTEM analysis verified the presence of single-phase crystalline iron oxide nanoparticles and discarded the presence of core-shell nanoparticles (Figure 3C) and the diffraction peaks shown in XRD also denoted the presence of carbon and Fe_2O_3/Fe_3O_4 in the bulk sample (Figure 4B). However, both γ-Fe_2O_3

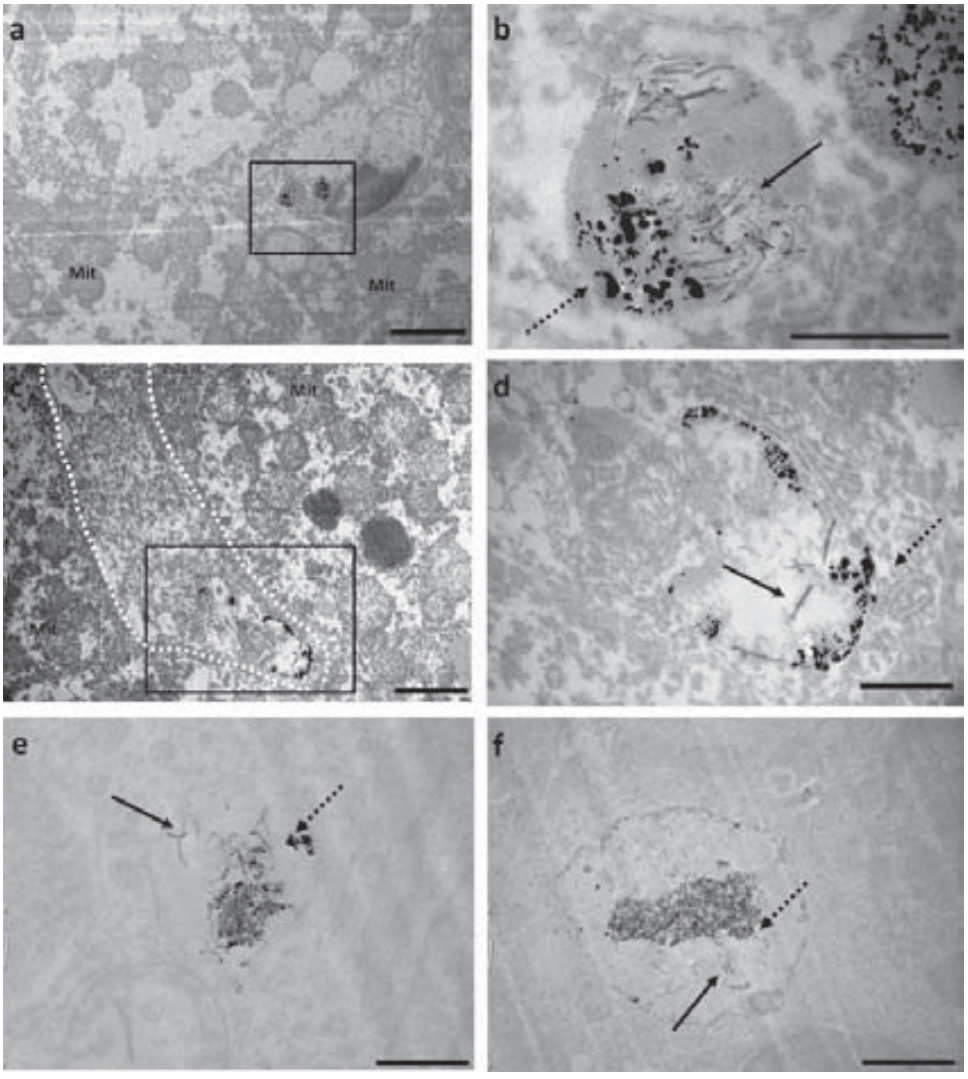

Figure 9. TEM micrographs of liver and spleen sections from animals injected with S-MWNT **3** at 24 h. Animals were injected with 400 μg of S-MWNT **3** (5.8 mg Fe/kg) via a tail vein. Organs were excised, fixed in 3% glutaldehyde in 0.1 M cacodylate buffer, and sectioned for TEM. The presence of S-MWNT was identified in hepatocytes (A,B) and kupffer cells outlined in (C,D) and spleen (E,F). B,D) Higher magnification images from the inset rectangles in (A) and (C), respectively. Dashed arrows point SPION and solid arrows point MWNTs. Mit: mitochondria. Bars are 2 μm in (A) and (C), 0.5 μm in (B) and (D), and 1 μm in (E) and (F).

and Fe_3O_4 possess spinel structures that belong to the Fm-3d space group (cell parameter a(γ-Fe_2O_3) = 8.351 Å; a(Fe_3O_4) = 8.384 Å) and their bulk saturation magnetization are also similar (Ms(γ-Fe_2O_3) = 87 emu g^{-1}; Ms(Fe_3O_4) = 92 emu g^{-1}).[50] It also must be taken into account that the saturation magnetization of small nanoparticles is usually smaller than that of the bulk[51] which prevents the elucidation of the particle type from the performed magnetic measurements. Thus, it was not possible to elucidate the nature of the SPIOs based on diffraction studies and magnetic measurements. The nature of the iron oxide nanoparticles in the SPIO-MWNT hybrids studied was therefore investigated by XPS and identified to be γ-Fe_2O_3 (Figure 4C). Magnetic measurements at 300 K confirmed that the γ-Fe_2O_3 nanoparticles possessed a superparamagnetic behaviour. Such temperature is close to room temperature, i.e., administration condition therefore it was necessary to confirm that no remnant magnetization is present when the magnetic field is removed at such temperature.

Phantom and in vivo MRI of S-MWNT hybrids were both conducted in this study. An intensive exploration of the R_2* relaxation rate was carried out by imaging phantom samples containing different amount of iron prepared in 1% agar and 0.5% Pluronic F127 solution (Figure 2A). S-MWNT **2** containing 28 wt% SPION exhibited a similar r_2* relaxivity to Endorem, and S-MWNT **3** with increased SPION contents displayed a greater value than Endorem (Figure 2B). The phantom study reported r_2* relaxivities of Endorem which appeared to be higher than the values published in some other r_2 studies.[52,53] Such discrepancies are related to several factors. Firstly, R_2* values reflect magnetic susceptibility

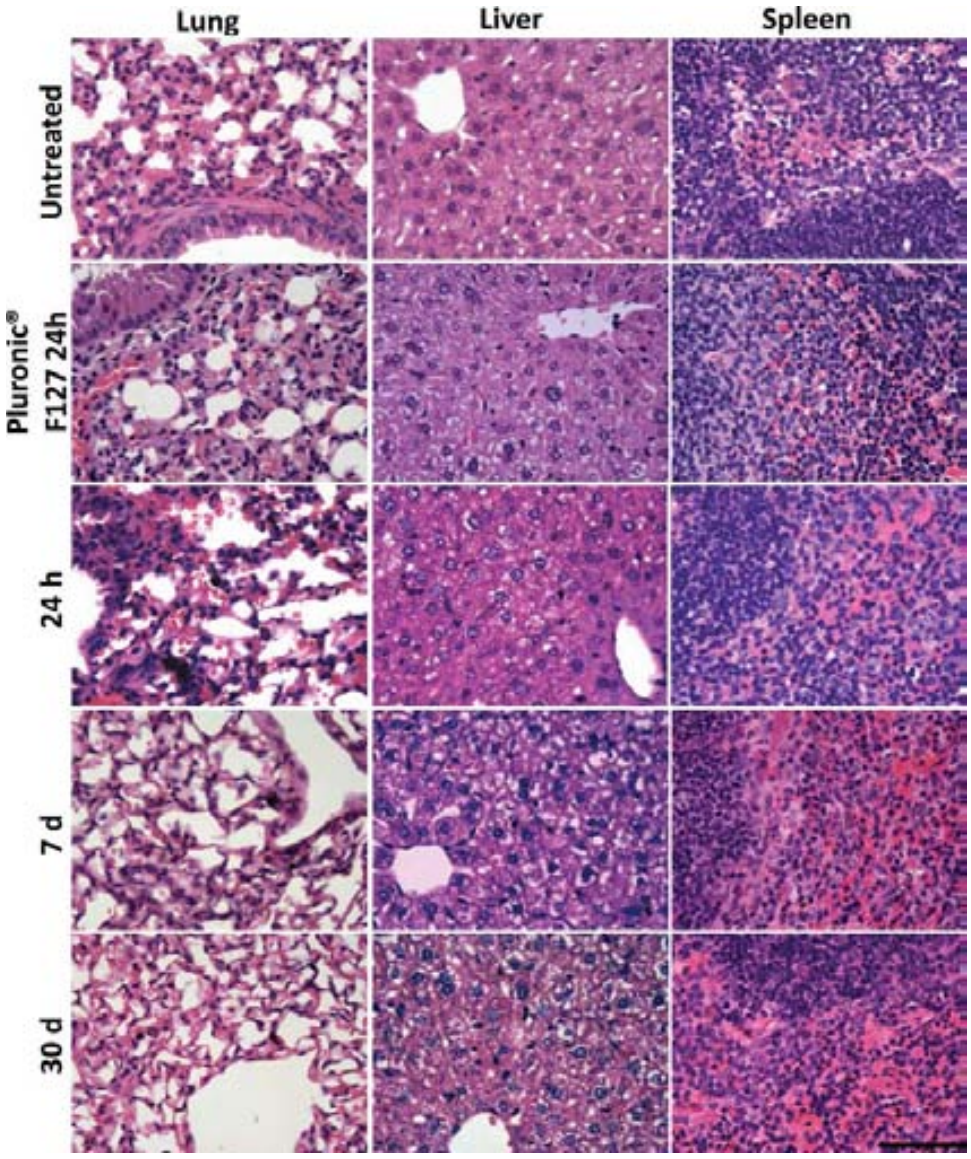

Figure 10. Histological examination of liver, lung, and spleen sections of C57/Bl6 mice injected with S-MWNT **3.** Animals were i.v. injected with 400 µg of the hybrid (5.8 mg Fe/kg). Organs were sampled at 24 h, 7 days, and 30 days, fixed, paraffin embedded and sectioned for H&E staining. Animals injected with 1% Pluronic F-127 were included as controls (at 24 h). The scale bar corresponds to 50 µm. No histological abnormalities were observed in all the organs examined up to 30 days.

effects which are largely avoided when engaging R_2 sequences. R_2* and R_2 are significantly different at high magnetic fields making it difficult to compare. Although R_2 is a more clinically relevant parameter than R_2*, the latter provides higher sensitivity at high fields making it an ideal tool for iron oxide probes investigations. Secondly, the use of agar most probably speed up phantom signal decay thus enhancing r_2* values. In fact, when investigating Endorem in water at 7 T, a r_2* value of 211.18 $s^{-1}mM^{-1}$ was obtained which agreed with what was reported in literature[54] (Figure S4). It also should be mentioned that the relaxivity patterns observed when engaging R_2* techniques should be similar to that observed when engaging R_2 techniques, making, in our case, the S-MWNT **3** highly relevant to in vivo clinical studies. Most importantly, high r_2* relaxivity of S-MWNT **3** implies that lower concentrations of the hybrids were required to achieve signals similar to that of Endorem. Liver T_2*-weighted MR imaging demonstrated time-dependent and concentration-dependent darkening in liver signals (Figure 7A) and an almost linear R_2* relaxation rate was obtained (Figure 7B). Higher relaxation effects were observed in our in vivo liver experiment when compared to two previously reported studies that utilised an equivalent amount of injected Fe.[19,55] A reduction of 60% in R_2* was seen up to 5 h after injection of 2.5 Fe mg/kg compared to 69% reduction value obtained in our study at the 48 h imaging time point.[19,55] In the second study, a reduction of 40% (at 2 h) at the dose of ~2.8 mg Fe/kg was measured compared to 76.5% obtained in our study at the same dose (at 48 h).[19,55] Despite the different

imaging time points which do not allow a direct comparison to be performed, the results showed S-MWNT **3** enhanced liver MRI contrast and confirmed S-MWNT **3** to be suitable as a negative contrast agent.

As far as this study is concerned, this is the first study proving the bimodal MRI/SPECT imaging using SPION-CNT hybrids. Better radio-labelling efficiency was obtained for S-MWNT **2-3** in contrast to S-MWNT **1** with lower SPION content (Figure 5A). This confirmed the radio-labelling approach which introduced ^{99m}Tc-labelled BP to the SPION available on the carbon nanotube surface as opposed to non-selective adsorption of the radio-isotope to the MWNTs. Approximately, 80% labelling efficiency was already obtained for S-MWNT **2** while no enhancement in radio-labelling was achieved in S-MWNT **3** despite of the 1.5 fold increase in iron content of the latter.

The results from SPECT/CT and organ biodistribution studies revealed most of the S-MWNT **3** accumulated in lung, liver and spleen (Figure 6). SPION is known to be taken up by liver and spleen (RES) hence it has been widely used to detect liver diseases by enhancing the negative MRI signals.[56] The prolonged uptake of CNT/iron oxide hybrids in lung has been reported.[19] The lung accumulation may be also due to their tubular and long structure. Long fiber particles tend to cause pulmonary toxicity and fibres with the length longer than 10 μm were reported carcinogenic.[57] The mean length of the MWNTs was measured around 2 ± 1.8 μm (Figure S1) and no histological abnormality was observed from different mice tissues treated with S-MWNT **3** up to 30 days. In a previous study, no physical abnormalities were detected after biochemical analysis of serum and urine samples of mice treated with various MWNTs with the length between 0.5 and 2 μm.[58] Preliminary in vitro cytotoxicity of S-MWNT **3** has been assessed using the mouse macrophage cell line J774 and no significant toxicity was measured at concentrations up to 100 μg/mL after 24 h incubation (unpublished data). Work is currently being undertaken to investigate and compare the MR properties of S-MWNT hybrids with different lengths in vitro and in vivo.

The reduction in S-MWNT **3** accumulation in lung and liver over time was confirmed by microscopic examination of the tissue sections stained with Perls stain and Neutral Red to detect the presence of iron oxide or MWNTs respectively (Figure 8). Unlike lung and liver, contradictory results were obtained in spleen sections following two staining methods where an increase in Perls stain-positive regions were captured up to 30 days while a reduced level of MWNTs was observed in Neutral Red stain. Iron stains were mostly found in the red pulps of spleen. With this regard, spleen is one of the iron storage organs in the body and therefore the red pulps are often Perls stain-positive. Therefore, the blue stains in spleen could be attributed to the iron from S-MWNT hybrids or the natured iron resulted from heme oxidation from dead red blood cells.

TEM examination was further carried out for observation of S-MWNT hybrids in tissues at ultra-structural scale. The observation of SPION-CNT hybrids in vitro by TEM has been reported previously.[48] Prostate cancer cells were incubated with the hybrids for 20 h and TEM images revealed their localisation in endosomes/lysosomes as bundles or individual tubes. Iron oxide nanoparticles were still attached with CNTs at this time point after cellular internalisation. In another study, Wu et al. have used TEM to validate the presence of MWNT/iron oxide constructs in tissues at 4 h after injection.[19] In the present study, more detailed information on cellular localisation of S-MWNT hybrids was disclosed in which co-localisation of SPION and MWNTs within the same endocytic vesicles was clearly observed in spleen cells, liver hepatocytes and kupffer cells at 24 h after injection (Figure 10). The results provided sufficient evidence of the in vivo stability of S-MWNT oxide hybrids so that they were taken up by the same cells as intact hybrids after intravenous injection. The detachment of SPION from MWNTs was also observed which might be due to the acidic environment of these vesicles.

As mentioned previously, CNTs have been developed for biomedical imaging applications[7] and we have also radio-labelled CNTs with Indium-111[45,59] or filled Iodine-125 inside the tube[46] for in vivo imaging and biodistribution studies. The current study presented ^{99m}Tc-labelled SPION-MWNT hybrids as dual MRI and SPECT contrast agents for the first time. The beauty of the design in this construct is the ease in preparation forming a stable construct capable of MRI and SPECT imaging upon reaction with a BP derivative. The BP derivative could be altered so that different radio-isotopes can be utilized[36,60] allowing for SPECT or PET imaging, both considered to be clinically very important modalities in disease diagnosis, staging and monitoring. The current study certainly assures a new prospect for CNTs application in the biomedical imaging field.

4. Conclusions

The present study has developed novel radio-labeled iron oxide nanoparticle decorated multi-walled carbon nanotubes (SPION–MWNT) hybrids for dual MR and SPECT imaging. Efficient and homogeneous loading of SPION were achieved via in situ generation, followed by thorough characterizations of physiochemical and magnetic properties of the prepared hybrids. In MRI studies, the resulting SPION–MWNT showed reduction in T2* signals in both phantom and the liver in vivo which was equivalent in efficacy to a clinically approved MRI contrast agent. Radio-labeling of SPION–MWNT with ^{99m}Tc through a functionalized bisphosphonate was reported, permitting in vivo 3D whole body SPECT/CT imaging and organ biodistribution profiling quantitatively. The TEM observations of SPION and MWNT co-localizing intracellularly in the same vesicles in liver and spleen tissues denoted the in vivo stability. No organ abnormality was found histologically up to 30 days post-adminisitration indicating a good biocompatibility of the hybrids. Findings from this work demonstrated the capability of SPION–MWNT hybrids to be used in dual-modality MR-SPECT imaging thus broadening CNT applications in the biomedical imaging field.

5. Experimental Section

Materials: Chemical vapour deposition multi-walled carbon nanotubes (MWNTs) were supplied as a dry powder (Thomas Swan & Co. Ltd, UK)

with an external average diameter of 10–12 nm (information provided by the supplier). Iron acetate (III), human serum from human male AB plasma, Pluronic F127, agar, 10% neutral buffered formalin, and Perls stain kits were purchased from Sigma-Aldrich (Sigma- Aldrich, UK). Endorem was obtained from Guerbet (Guerbet Laboratories, UK). Dipicolylamine-alendronate (DPA-ale or BP) and ^{99m}Tc -BP were synthesized as previously reported.[27] Na[$^{99m}TcO_4$] in physiological saline was obtained from a ^{99}Mo/^{99m}Tc generator at the Radiopharmacy at Guy's and St Thomas' Hospital NHS Trust, London, UK. Radioactivity in samples was measured using a CRC-25R dose calibrator (Capintec, USA) or a 1282 CompuGamma gamma counter (LKB Wallac, PerkinElmer, USA). [^{99m}Tc $(CO)_3(H_2O)_3$]$^+$ was synthesized using Isolink kits (Mallinckrodt Medical B.V., St. Louis, MO, USA). C57/Bl6 female mice aged 6–8 weeks were used throughout the in vivo studies and were obtained from Harlan Laboratories. Isoflurane for anaesthesia was purchased from Abbott (IsoFlo, Abbott Laboratorie Ltd, UK) and pentobarbital sodium used for lung inflation fixation was from Merial (Euthatal, Merial Animal Health Ltd, UK). For sample preparation for histological and TEM examination, xylene, ethanol, and sodium cacodylate were purchased from Fisher Scientific, DPX used for mounting was obtained from VWR International Ltd, EM grade glutaldehyde was from Merck, and Araldite CY212, tris(dimethylaminomethyl)phenol (DMP30) dodecenyl succinic anhydride (DDSA) were purchased from Agar Scientific.

Synthesis of SPION–MWNT Hybrids: The as-received MWNTs were purified by steam following a previously reported protocol.[30] Briefly, MWNTs were ground with an agate mortar and pestle until a fine powder was obtained. Next, the MWNT sample was spread inside a silica tube (about 40 mm in diameter) which was then introduced into a furnace alumina tube. Steam was introduced by bubbling argon (150 mL min^{-1}) through a flask containing hot distilled water (98 °C). The whole system was initially purged with argon for 2 h to ensure the complete removal of oxygen, before heating the furnace to 900 °C during 1.5 h to allow the purification of the material. The solid powder was collected and treated with 6 M HCl to remove the now exposed metal nanoparticles.[33] The purified MWNTs were collected by filtration through a 0.2 µm polycarbonate membrane and thoroughly washed with water until pH neutral. The purified MWNTs were then functionalized by refluxing with 3 M HNO_3 for 45 h, resulting in the introduction of carboxylic acid groups (–COOH) onto the MWNT tips and side walls.[32] The functionalized MWNTs (*f*-MWNTs) were collected by filtration and washed with water until neutral pH was achieved.

Decoration of the MWNTs with SPION was carried out in situ where SPION were prepared in the presence of the *f*-MWNTs. Iron (II) acetate was employed as the iron precursor for the formation of the SPION since it is water soluble and can be decomposed by thermal annealing. Samples with increasing amount of iron contents were prepared and the loading of SPION onto the MWNTs was subsequently determined. Iron (II) acetate (10, 20, 40, and 50 mg) was added to a round-bottomed flask containing 25 mg of functionalized MWNTs and 15 mL of distilled water. The mixture was bath sonicated for 10 min and stirred at 60 °C for 16 h to allow a uniform coverage of iron (II) acetate onto the surface the MWNTs. Solutions were left to cool down and filtered through a 0.2 µm polycarbonate membrane. Samples were then treated with Ar/H_2 at 500 °C for 2 h and left exposed in air thus affording the formation of the SPION on MWNTs surface.

Analysis and Characterisation of SPION–MWNTs: Thermogravimetric analyses were performed under flowing air at a heating rate of 10 °C/min up to 950 °C (Jupiter, Netzsch Instrument, Germany). X-ray diffraction studies were conducted using a powder diffractometer ($CuK_{\alpha 1}$, λ = 0.1540 nm; Siemens D5000, Germany) with 2θ ranging from 5° to 65°. The PDF (powder data file) database was used to identify the compounds. For transmission electron microscopy studies, samples were prepared by dispersing a small amount of powder in absolute ethanol and sonicated using an ultrasonic power bath. The dispersions were placed dropwise onto lacey carbon grids. Low magnification TEM images were obtained using a JEOL 1210 transmission electron microscope (JEOL SAS, Japan) operating at 120 kV and high resolution TEM analysis was performed in an FEI Tecnai G2 microscope operating at 200 kV (Titan, FEI, the Netherlands). X-ray photoelectron spectra (XPS) were acquired with a Kratos AXIS ultra DLD. The magnetic moment of the samples was measured using a superconducting quantum interference device (SQUID, LOT-QuantumDesign Iberia, Spain) magnetometer. Each sample was placed into a diamagnetic gelatine capsule. Data was acquired with an applied field from –50 000 Oe to 50 000 Oe at temperatures of 10 K and 300 K. The sample holder contribution was subtracted in all the measurements.

Preparation of SPION–MWNT Hybrids Dispersions for MR Studies: SPION–MWNT hybrids dispersed in 1% Pluronic F127 solution were mixed with an equal volume of agar solution (2%, w/v in water) at 95 °C. Samples dispersions prepared at a range of Fe concentrations up to 1.25 mM were transferred to 0.3 mL microtubes within less than one minute before gel solidification occurs. Phantoms were imaged by MRI as described below.

MR Imaging: Phantom and in vivo MR imaging were performed at a 7T horizontal MR scanner (Agilent, Palo Alto, CA). The gradient coil had an inner diameter of 12 cm, gradient strength was 1000 mT/m (100 G/cm) and rise-time of 120 µs. A quadrature transmit/receive coil (RAPID Biomedical GmbH, Germany) with an internal diameter of 39 mm was used. Animals were intravenously injected with 0.72–4.4 mg Fe/kg S-MWNT 3 and imaged at 48 h post injection. This range of injection doses was chosen as reported in several pre-clinical studies.[19,28] Animals were imaged in prone position under constant anesthesia of 1.5% isoflurane/98.5% oxygen. Body temperature was maintained constant at 37 °C using a warm air fan and ECG and respiration monitored (SA Instruments, Stony Brook, NY). R_2* imaging was used in this study as it does not only reflect the spin-spin relaxation but also takes into account the magnetic field inhomogeneity. Cine-FLASH MRI technique with variable echo time (TE) was used to acquire R_2* images and such methods were adopted both in vitro and in vivo. The cine-FLASH parameters for R_2* images in phantoms were: FOV = 30 × 30 mm, matrix size = 96 × 96, slice thickness = 1 mm; number of slice = 1; flip angle = 20°, 1 average, TR = 700 ms; TE = 1, 2, 3, 5, 8, 10 ms; scan time ~ 7 min. Cine-FLASH parameters for in vivo R_2* acquisitions were: FOV = 25 × 25 mm, matrix size = 128 × 128, slice thickness = 1 mm; flip angle = 20°; number of slice = 1; 1 average; TR = 1/heart rate = RR-interval; TE = 1, 2, 3, 5 ms; scan time ~10 min. A short-axis and a long axis view were used for the in-vivo experiment.

MR Image Analysis: MR images were analyzed using the ImageJ software (NIH, USA). R_2* pixel by pixel data was fitted by the following equation:

$$S_n = S_0 * EXP(-TE_n / T_2^*) \quad (1)$$

where S_n is the signal measured, S_0 is the initial signal and TE_n represents the different echo spacing. By selecting a region of interest (ROI) within the phantom area or, for in vivo studies, within the liver area, the software automatically calculates mean T_2* values. R_2* values ($1/T_2$*) were plotted using Excel versus the corresponding iron concentrations. Results are presented as mean ± S.D. (n = 3). In phantom studies such plot resulted in a linear relationship where the slopes corresponded to the r_2*relaxivities.

Radio-Labelling of S-MWNT Hybrid 1–3: The labelling of SPION-MWNT hybrids with ^{99m}Tc-BP was carried out as previously reported by de Rosales et al.[26,28] Hybrids with different iron contents were tested initially to optimise the radio-labelling efficiency. S-MWNT 1–3 (125 µg/125 µL) were first dispersed by sonication (10 min) in 1% Pluronic F127 solution at 1 mg/mL concentration and mixed with 1–10 MBq ^{99m}Tc-BP (500 MBq in 50 µg of BP/125 µL). The mixture was incubated at 37 °C for 30 min with gentle shaking. After cooling to room temperature, ^{99m}Tc-BP-S-MWNT hybrids were separated from unbound ^{99m}Tc-BP by centrifugation at 17 000 rcf for 10 min and the pellets containing ^{99m}Tc-BP-S-MWNT hybrids were washed 4 times (1 mL each wash) with 1% Pluronic F127 until no radioactivity was detected in the supernatant. The total radioactivity in the supernatants and the pellet were measured to determine the radio-labelling efficiency. The pellet was then re-dispersed using 1% Pluronic F127 solution to achieve a final concentration of 1 mg/mL for subsequent in vivo studies (γ-scintigraphy and SPECT/CT imaging).

In Vitro Stability in PBS and Human Serum: To assess the in vitro stability of the radio-labelled hybrids, ^{99m}Tc-BP-S-MWNT 1–3 were mixed with an equal volume of human serum or PBS (at 50% final concentration) and incubated at 37 °C under constant shaking for 24 h. The samples were then centrifuged at 17 000 rcf for 10 min. The radioactivity of the pellets and the supernatants were measured by gamma counting to determine the percentage of ^{99m}Tc-BP remained bound to the S-MWNT hybrids representing stably labelled hybrids.

Whole Body 3D SPECT/CT Imaging of Mice Injected with ^{99m}Tc-BP-S-MWNT 3: All in vivo experiments were conducted under the authority of project and personal licences granted by the UK Home Office and the UKCCCR Guidelines (1998). C57/Bl6 mice were anaesthetised by isofluorane inhalation and injected intravenously with 50 µg of ^{99m}Tc-BP-S-MWNT 3 or ^{99m}Tc-BP in 1% Pluronic F127 solution containing approximately 5 MBq. SPECT imaging was carried out immediately after injection with images taken in 16 projections over 30 min using a four-head scanner with 1.4 mm pinhole collimators (Nano-SPECT/CT scanner, Bioscan, USA). CT scanning was performed with a 45 kV X-ray source and 1000 ms exposure time over 10 min at the end of each SPECT acquisition. SPECT and CT images were reconstructed using the MEDISO software (Medical Imaging Systems) and then merged by the InVivoScope software (Bioscan, USA). Each animal was recovered and further imaged at 4 h and 24 h.

Organ Biodistribution of ^{99m}Tc-BP-S-MWNT 3 *in Mice by Gamma Scintigraphy*: The pharmacokinetic studies including the blood circulation and organ biodistribution of the hybrid were carried out using female C57/Bl6 mice (6–8 weeks old). Mice were given 50 µg of ^{99m}Tc-BP-S-MWNT 3 or ^{99m}Tc-BP (250 µL in 1% Pluronic F127 solution) intravenously *via* tail vein. The blood clearance profile was established by collecting blood samples in heparinised capillaries from 2 min up to 24 h after injection. For organ biodistribution study, major organs including skin, liver, spleen, heart, lung, muscle, bone, brain, stomach, and intestine were excised post mortem at 1 h, 4 h, and 24 h after injection. Samples were weighed and the radioactivity was detected, quantified and corrected for physical radioisotope decay by gamma scintigraphy. The % ID per organ and per gram tissue were calculated and plotted as the mean of triplicate or quadruplicate samples ± SD.

Histological Analysis: For histological examination of organs, C57/Bl6 mice were injected via tail vein with 400 µg of S-MWNT 3 (5.8 mg Fe/kg) dispersed in 1% Pluronic F127 solution and tissues of lung, liver, and spleen were excised at 24 h, 7 days, and 30 days after injection. Lung tissues were sampled by an inflation-fixation method. Mice were given an overdose of pentobarbital sodium intraperitonealy and a small incision in the midline of the trachea was performed. A 24 gauge catheter (Angiocath, BD Biosciences, UK) was placed in the mouse trachea and a solution of 5 mL 10% neutral buffered formalin (Sigma-Aldrich, UK) was directly instilled into the lung using a syringe. Entire inflated lung was removed and stored in 10% neutral buffer formalin. Other organs were immediately fixed in 10% neutral buffer formalin as 5 mm^2 pieces. Samples were then wax-embedded and sectioned for haematoxylin and eosin stains (H&E) or Neutral Red stains according to standard histological protocols at the Royal Veterinary College.

To detect the presence of iron in tissues, Perls staining was carried out using a Perls stain kit used according to the manufacturer's instruction. In brief, sections were deparaffinised and incubated with potassium ferrocyanide solution for 20 min followed by counterstaining with nuclear red solution for 10 min. Sections were then dehydrated using increasing concentrations of ethanol solutions (70%, 90%, and absolute ethanol), cleared by xylene and mounted in DPX.

All stained sections were analysed using a Leica DM 1000 LED Microscope (Leica Microsystems, UK) coupled with CDD digital camera (Qimaging, UK).

TEM Examination of S-MWNT 3 *in Liver and Spleen Tissues*: Mice were injected with 400 µg of S-MWNT 3 (5.8 mg Fe/kg) dispersed in 1% Pluronic F127 solution. At 24 h, mice were killed and liver and spleen were rinsed by PBS. Organs were excised into 2 mm thin pieces and fixed in 2.5% EM grade glutaldehyde in 0.1 M sodium cacodylate buffer for 24 h. Liver and spleen samples were then transferred to 0.1 M sodium cacodylate buffer and stored at 4 °C until further processing. Samples were fixed using 1% osmium oxide solution for 3 h. The samples were rinsed with 0.1 M cacodylate buffer and de-hydrated using increasing concentrations of ethanol solutions (70%, 90%, and absolute ethanol). Propylene oxide was added to the samples for 15 min, followed by infiltration in 1:1 mixture of propylene oxide: epoxy resin (Araldite CY212, DDSA and DMP30) overnight. The samples were then embedded into epoxy resin blocks and left in 60 °C oven for 3 days to polymerise. Ultrathin sections were cut on a microtome (Leica Reichert Ultracut) using a diamond knife and collected on 300-mesh copper grids. The grids were stained using uranyl acetate and imaged using a FEI/Philips CM12 transmission electron microscope (FEI, the Netherlands) at 80 kV.

Supporting Information

Supporting Information is available from the Wiley Online Library or from the author.

Acknowledgements

J. T.-W. Wang and L. Cabana contributed equally to this work. Funding from Biotechnology and Biological Sciences Research Council (BB/J008656/1), Associated International Cancer Research, Spanish Ministerio de Economía y Competitividad (MAT2011-24757), the EU FP7-ITN Marie-Curie Network programme RADDEL (290023), and the EU FP7-Integrated Infrastructure Initiative–I3 programme ESTEEM2 (312483) is acknowledged. H. Kafa is supported by the Atomic Energy Commission of Syria. L. Cabana is supported by a CSIC JAE Predoc Fellowship and is enrolled in the UAB PhD program. R. T. M. de Rosales acknowledges funding by The Centre of Excellence in Medical Engineering funded by the Wellcome Trust and EPSRC under Grant No. WT 088641/Z/09/Z. X. Ke and G. Van Tendeloo acknowledge funding from the European Research Council under the Seventh Framework Program (FP7) ERC Grant No 246791- COUNTATOMS. K. T. Al-Jamal, G. Tobias and R. T. M. de Rosales thank the members of the EU COST actions TD1004 (Theranostics Imaging and Therapy: An Action to Develop Novel Nanosized Systems for Imaging-Guided Drug Delivery) and TD1007 (Bimodal PET-MRI molecular imaging technologies and applications for in vivo monitoring of disease and biological processes) for useful discussions.

Received: August 17, 2013
Revised: October 4, 2013
Published online: November 19, 2013

[1] J. Cheon, J. H. Lee, *Acc. Chem. Res.* **2008**, *41*, 1630.
[2] J. V. Jokerst, S. S. Gambhir, *Acc. Chem. Res.* **2011**, *44*, 1050.
[3] X. Michalet, F. F. Pinaud, L. A. Bentolila, J. M. Tsay, S. Doose, J. J. Li, G. Sundaresan, A. M. Wu, S. S. Gambhir, S. Weiss, *Science* **2005**, *307*, 538.
[4] S. K. Nune, P. Gunda, P. K. Thallapally, Y. Y. Lin, M. L. Forrest, C. J. Berkland, *Expert Op. Drug Deliv.* **2009**, *6*, 1175.
[5] A. Bianco, K. Kostarelos, C. D. Partidos, M. Prato, *Chem. Commun.* **2005**, 571.
[6] K. T. Al-Jamal, F. M. Toma, A. Yilmazer, H. Ali-Boucetta, A. Nunes, M. A. Herrero, B. W. Tian, A. Eddaoui, W. T. Al-Jamal, A. Bianco, M. Prato, K. Kostarelos, *FASEB J.* **2010**, *24*, 4354.
[7] Z. Liu, S. Tabakman, K. Welsher, H. J. Dai, *Nano Res.* **2009**, *2*, 85.
[8] S. Keren, C. Zavaleta, Z. Cheng, A. De La Zerda, O. Gheysens, S. S. Gambhir, *Proc. Natl. Acad. Sci. USA* **2008**, *105*, 5844.
[9] N. W. S. Kam, M. O'Connell, J. A. Wisdom, H. J. Dai, *Proc. Natl. Acad. Sci. USA* **2005**, *102*, 11600.

[10] A. De La Zerda, C. Zavaleta, S. Keren, S. Vaithilingam, S. Bodapati, Z. Liu, J. Levi, B. R. Smith, T. J. Ma, O. Oralkan, Z. Cheng, X. Y. Chen, H. J. Dai, B. T. Khuri-Yakub, S. S. Gambhir, *Nature Nanotechnol.* **2008**, *3*, 557.
[11] L. G. Delogu, G. Vidili, E. Venturelli, C. Ménard-Moyon, M. A. Zoroddu, G. Pilo, P. Nicolussi, C. Ligios, D. Bedognetti, F. Sgarrella, R. Manetti, A. Bianco, *Proc. Natl. Acad. Sci. USA* **2012**, *109*, 16612.
[12] C. Balas, *Meas. Sci. Technol.* **2009**, *20*, 104020.
[13] D. McRobbie, E. Moore, M. Graves, M. Prince, *MRI from Picture to Proton*, Cambridge University Press, UK **2006**.
[14] A. B. de Barros, A. Tsourkas, B. Saboury, V. N. Cardoso, A. Alavi, *EJNMMI Res.* **2012**, *2*, 39.
[15] A. Louie, *Chem. Rev.* **2010**, *110*, 3146.
[16] B. Sitharaman, K. R. Kissell, K. B. Hartman, L. A. Tran, A. Baikalov, I. Rusakova, Y. Sun, H. A. Khant, S. J. Ludtke, W. Chiu, S. Laus, E. Toth, L. Helm, A. E. Merbach, L. J. Wilson, *Chem. Commun.* **2005**, 3915.
[17] B. Sitharaman, B. D. Jacobson, Y. Z. Wadghiri, H. Bryant, J. Frank, *J. Appl. Phys.* **2013**, *113*, 134308.
[18] J. H. Choi, F. T. Nguyen, P. W. Barone, D. A. Heller, A. E. Moll, D. Patel, S. A. Boppart, M. S. Strano, *Nano Lett.* **2007**, *7*, 861.
[19] H. X. Wu, G. Liu, Y. M. Zhuang, D. M. Wu, H. Q. Zhang, H. Yang, H. Hu, S. P. Yang, *Biomaterials* **2011**, *32*, 4867.
[20] B. Chen, H. Zhang, C. Zhai, N. Du, C. Sun, J. Xue, D. Yang, H. Huang, B. Zhang, Q. Xie, Y. Wu, *J. Mater. Chem.* **2010**, *20*, 9895.
[21] B. T. Doan, J. Seguin, M. Breton, R. Le Beherec, M. Bessodes, J. A. Rodriguez-Manzo, F. Banhart, J. C. Beloeil, D. Scherman, C. Richard, *Contrast Media Mol. I.* **2012**, *7*, 153.
[22] M. Yin, M. L. Wang, F. Miao, Y. X. Ji, Z. Tian, H. B. Shen, N. Q. Jia, *Carbon* **2012**, *50*, 2162.
[23] A. Li, C. S. Wong, M. K. Wong, C. M. Lee, M. C. A. Yeung, *Br. J. Radiol.* **2006**, *79*, 368.
[24] A. J. Gauden, P. M. Phal, K. J. Drummond, *J. Clin. Neurosci.* **2010**, *17*, 1097.
[25] Y. X. Wang, *Quant. Imaging Med. Surg.* **2011**, *1*, 35.
[26] L. Lartigue, D. Alloyeau, J. Kolosnjaj-Tabi, Y. Javed, P. Guardia, A. Riedinger, C. Péchoux, T. Pellegrino, C. Wilhelm, F. Gazeaut, *ACS Nano* **2013**, *7*, 3939.
[27] S. W. A. Bligh, P. J. Sadler, J. A. Marriott, I. A. Latham, J. D. Kelly, *Appl. Radiat. Isot.* **1989**, *40*, 751.
[28] J. S. Choi, J. C. Park, H. Nah, S. Woo, J. Oh, K. M. Kim, G. J. Cheon, Y. Chang, J. Yoo, J. Cheon, *Angew. Chem. Int. Ed. Engl.* **2008**, *47*, 6259.
[29] C. Glaus, R. Rossin, M. J. Welch, G. Bao, *Bioconjug. Chem.* **2010**, *21*, 715.
[30] B. R. Jarrett, B. Gustafsson, D. L. Kukis, A. Y. Louie, *Bioconjug. Chem.* **2008**, *19*, 1496.
[31] N. Kohler, C. Sun, A. Fichtenholtz, J. Gunn, C. Fang, M. Q. Zhang, *Small* **2006**, *2*, 785.
[32] J. R. McCarthy, R. Weissleder, *Adv. Drug Deliv. Rev.* **2008**, *60*, 1241.
[33] L. Sandiford, A. Phinikaridou, A. Protti, L. K. Meszaros, X. J. Cui, Y. Yan, G. Frodsham, P. A. Williamson, N. Gaddum, R. M. Botnar, P. J. Blower, M. A. Green, R. T. M. de Rosales, *ACS Nano* **2013**, *7*, 500.
[34] R. Torres Martin de Rosales, C. Finucane, S. J. Mather, P. J. Blower, *Chem. Commun.* **2009**, 4847.
[35] R. Torres Martin de Rosales, R. Tavare, A. Glaria, G. Varma, A. Protti, P. J. Blower, *Bioconjug. Chem.* **2011**, *22*, 455.
[36] R. Torres Martin de Rosales, R. Tavare, R. L. Paul, M. Jauregui-Osoro, A. Protti, A. Glaria, G. Varma, I. Szanda, P. J. Blower, *Angew. Chem. Int. Ed. Engl.* **2011**, *50*, 5509.
[37] G. Tobias, L. D. Shao, C. G. Salzmann, Y. Huh, M. L. H. Green, *J. Phys. Chem. B* **2006**, *110*, 22318.
[38] L. Shao, G. Tobias, C. G. Salzmann, B. Ballesteros, S. Y. Hong, A. Crossley, B. G. Davis, M. L. H. Green, *Chem. Commun.* **2007**, 5090.
[39] J. Liu, A. G. Rinzler, H. J. Dai, J. H. Hafner, R. K. Bradley, P. J. Boul, A. Lu, T. Iverson, K. Shelimov, C. B. Huffman, F. Rodriguez-Macias, Y. S. Shon, T. R. Lee, D. T. Colbert, R. E. Smalley, *Science* **1998**, *280*, 1253.
[40] B. Ballesteros, G. Tobias, L. Shao, E. Pellicer, J. Nogues, E. Mendoza, M. L. H. Green, *Small* **2008**, *4*, 1501.
[41] R. M. Lago, S. C. Tsang, K. L. Lu, Y. K. Chen, M. L. H. Green, *J. Chem. Soc. Chem. Comm.* **1995**, *0*, 1355.
[42] T. Kolodiazhnyi, M. Pumera, *Small* **2008**, *4*, 1476.
[43] A. Ambrosi, M. Pumera, *Chemistry* **2010**, *16*, 10946.
[44] A. P. Grosvenor, B. A. Kobe, M. C. Biesinger, N. S. McIntyre, *Surf. Interface Anal.* **2004**, *36*, 1564.
[45] K. T. Al-Jamal, A. Nunes, L. Methven, H. Ali-Boucetta, S. Li, F. M. Toma, M. A. Herrero, W. T. Al-Jamal, H. M. M. ten Eikelder, J. Foster, S. Mather, M. Prato, A. Bianco, K. Kostarelos, *Angew. Chem. Int. Ed.* **2012**, *51*, 6389.
[46] S. Y. Hong, G. Tobias, K. T. Al-Jamal, B. Ballesteros, H. Ali-Boucetta, S. Lozano-Perez, P. D. Nellist, R. B. Sim, C. Finucane, S. J. Mather, M. L. Green, K. Kostarelos, B. G. Davis, *Nat. Mater.* **2010**, *9*, 485.
[47] B. J. Pichler, A. Kolb, T. N gele, H. P. Schlemmer, *J. Nucl. Med.* **2010**, *51*, 333.
[48] G. Lamanna, A. Garofalo, G. Popa, C. Wilhelm, S. Begin-Colin, D. Felder-Flesch, A. Bianco, F. Gazeau, C. Ménard-Moyon, *Nanoscale* **2013**, *5*, 4412.
[49] B. Ballesteros, G. Tobias, M. A. H. Ward, M. L. H. Green, *J. Phys. Chem. C* **2009**, *113*, 2653.
[50] R. M. Cornell, U. Schwertmann, *The Iron Oxides: Structure, Properties, Reactions, Occurrence and Uses* USA: John Wiley & Sons, Ltd., **1996**.
[51] X. Batlle, A. Labarta, *J. Phys. D—Appl. Phys.* **2002**, *35*, R15.
[52] C. W. Jung, P. Jacobs, *Magn. Reson. Imaging* **1995**, *13*, 661.
[53] M. Rohrer, H. Bauer, J. Mintorovitch, M. Requardt, H. J. Weinmann, *Invest. Radiol.* **2005**, *40*, 715.
[54] R. Misri, D. Meier, A. Yung, P. Kozlowski, U. Haumlfeli, *Nanomed. Nanotechnol. Biol. Med.* **2012**, *8*, 1007.
[55] C. Chambon, O. Clement, A. Leblanche, E. Schoumanclaeys, G. Frija, *Magn. Reson. Imaging* **1993**, *11*, 509.
[56] P. Reimer, B. Tombach, *Eur. Radiol.* **1998**, *8*, 1198.
[57] K. Donaldson, F. A. Murphy, R. Duffin, C. A. Poland, *Part. Fibre Toxicol.* **2010**, *7*, 5.
[58] L. Lacerda, H. Ali-Boucetta, M. A. Herrero, G. Pastorin, A. Bianco, M. Prato, K. Kostarelos, *Nanomedicine* **2008**, *3*, 149.
[59] L. Lacerda, A. Soundararajan, R. Singh, G. Pastorin, K. T. Al-Jamal, J. Turton, P. Frederik, M. A. Herrero, S. L. A. Bao, D. Emfietzoglou, S. Mather, W. T. Phillips, M. Prato, A. Bianco, B. Goins, K. Kostarelos, *Adv. Mater.* **2008**, *20*, 225.
[60] V. Kubíček, J. Rudovský, J. Kotek, P. Hermann, L. Vander Elst, R. N. Muller, Z. I. Kolar, H. T. Wolterbeek, J. A. Peters, I. Lukeš, *J. Am. Chem. Soc.* **2005**, *127*, 16477.

Synthesis of PbI_2 Single-Layered Inorganic Nanotubes Encapsulated Within Carbon Nanotubes

*Laura Cabana, Belén Ballesteros, Eudar Batista, César Magén, Raúl Arenal, Judith Oró-Solé, Riccardo Rurali, and Gerard Tobias**

The isolation and growth of single layers of a wide variety of inorganic materials is of interest for both fundamental research and advanced applications.[1] When an individual layer is seamlessly wrapped into a cylinder, the resulting single-layered nanotube combines the characteristics of both two-dimensional (2D) and one-dimensional (1D) materials.[2] Yet, despite their interest, reports on single-walled inorganic nanotubes are scarce because their multiwalled counterparts are in general favoured during growth.[3] Here we report on a versatile approach that allows the formation of high-quality, single-crystalline single-layered inorganic nanotubes. To achieve this, we employed a solvent-free high temperature route using the inner cavities of carbon nanotubes as a hosting templates. Lead iodide single-layered nanotubes, ranging from 3.5 to 7.5 nm in diameter, were prepared by this methodology. Using aberration-corrected electron microscopy and first-principles quantum mechanical calculations we have explored the fundamental physics and chemistry of the resulting materials. Remarkably, our theoretical studies show that the single-layered nanotubes are stable without the presence of the sheathing carbon and their electronic structure is found to be diameter independent. The method presented here offers wide versatility towards the formation of tubular single-layered nanomaterials of different nature whose diameter is merely determined by the host.

Carbon nanotubes (CNTs) are a highly versatile platform for the template assisted growth of nanomaterials, given that both their internal space and the outer surface allow the formation of tailored nanostructures.[4] The encapsulation of materials inside CNTs results in the formation of extremely narrow 1D nanowires[5] that can go down to a chain of single atoms forming an "atomic necklace".[6] The use of filled carbon nanotubes has been recently explored in radiology,[7] nanothermometry,[8] molecular electronics,[9] water confinement,[10] cell tracking[11] and as nanoscale reaction vessels for the controlled growth of graphene nanoribbons.[12] However, in spite of the versatility that the nanoencapsulation into CNTs offers, the use of the inner cavities for the growth of single-layered inorganic materials has not been realized to date. In this report, we present the template-assisted growth of single-layered lead iodide crystals. Lead iodide is a semiconducting material with interest for its electroluminescence, photoluminiscence and non-linear optical effects.[13] It is a good candidate for X-ray and γ-ray detectors, thin film transistors and, more recently, organo-lead iodide perovskites are employed in efficient hybrid solar cells.[14] Multiwalled nanotubes and nanoclusters of lead iodide have recently been prepared by template assisted growth using WS_2 nanotubes for the former[15] and supramolecular cages for the latter,[16] but their single-walled counterparts have not been observed. We reasoned that this could be achieved by using the cavities of multiwalled carbon nanotubes (MWCNTs) due to their narrower cavity compared to that of WS_2.

The tubular single-layers of PbI_2 were prepared by molten phase capillary wetting[5] using steam purified and open-ended CNTs.[17] The successful growth of single-layered nanotubes within the CNT walls was confirmed by aberration-corrected high-resolution transmission electron microscopy (HRTEM) and scanning transmission electron microscopy (STEM) at 80 kV. First-principles density functional theoretical calculations allowed the determination of the stability and electronic properties of the prepared materials.

The structure of the single-layered PbI_2 nanotubes was initially analyzed by HRTEM. In **Figure 1**a, a single-layered nanotube with an outermost external diameter of 3.94 nm is observed (area A). Taking into account that each layer of PbI_2 is actually composed by a I-Pb-I repeating unit in which a layer of Pb atoms is sandwiched between two layers of I atoms (see schematic representation), an external diameter of 3.94 nm actually corresponds to a nanotube of about 3.5 nm (taking Pb as the central point). We will therefore refer to the diameter of the PbI_2 nanotubes to this central Pb layer. It is worth noticing the ease in which the tubular structure of PbI_2 accommodates in the core of the host, overcoming for instance a narrowing of the CNT (area B) or even a dramatic 30% increase in diameter from 3.5 nm to 4.5 nm (area C). A high magnification image of the tip of the PbI_2 nanotube is presented in Figure 1b, where its high degree of crystallinity can be better appreciated. Image simulation along with the employed model structure is also included for comparison. Since the chirality of each of the layers

L. Cabana, E. Batista, Dr. J. Oró-Solé, Dr. R. Rurali, Dr. G. Tobias
Institut de Ciència de Materials de Barcelona (ICMAB-CSIC), Campus UAB, 08193, Bellaterra, Barcelona, Spain
E-mail: gerard.tobias@icmab.es
Dr. B. Ballesteros
ICN2 – Institut Catala de Nanociencia i Nanotecnologia
Campus UAB, 08193, Bellaterra, Barcelona, Spain
Dr. C. Magén, Dr. R. Arenal
Laboratorio de Microscopías Avanzadas (LMA)
Instituto de Nanociencia de Aragón (INA)-ARAID
Universidad de Zaragoza, 50018 Zaragoza, Spain
Dr. C. Magén
Departamento de Física de la Materia Condensada
Universidad de Zaragoza
50009, Zaragoza, Spain

To the memory of Prof. John D. Corbett, Distinguished Professor at Iowa State University.

DOI: 10.1002/adma.201305169

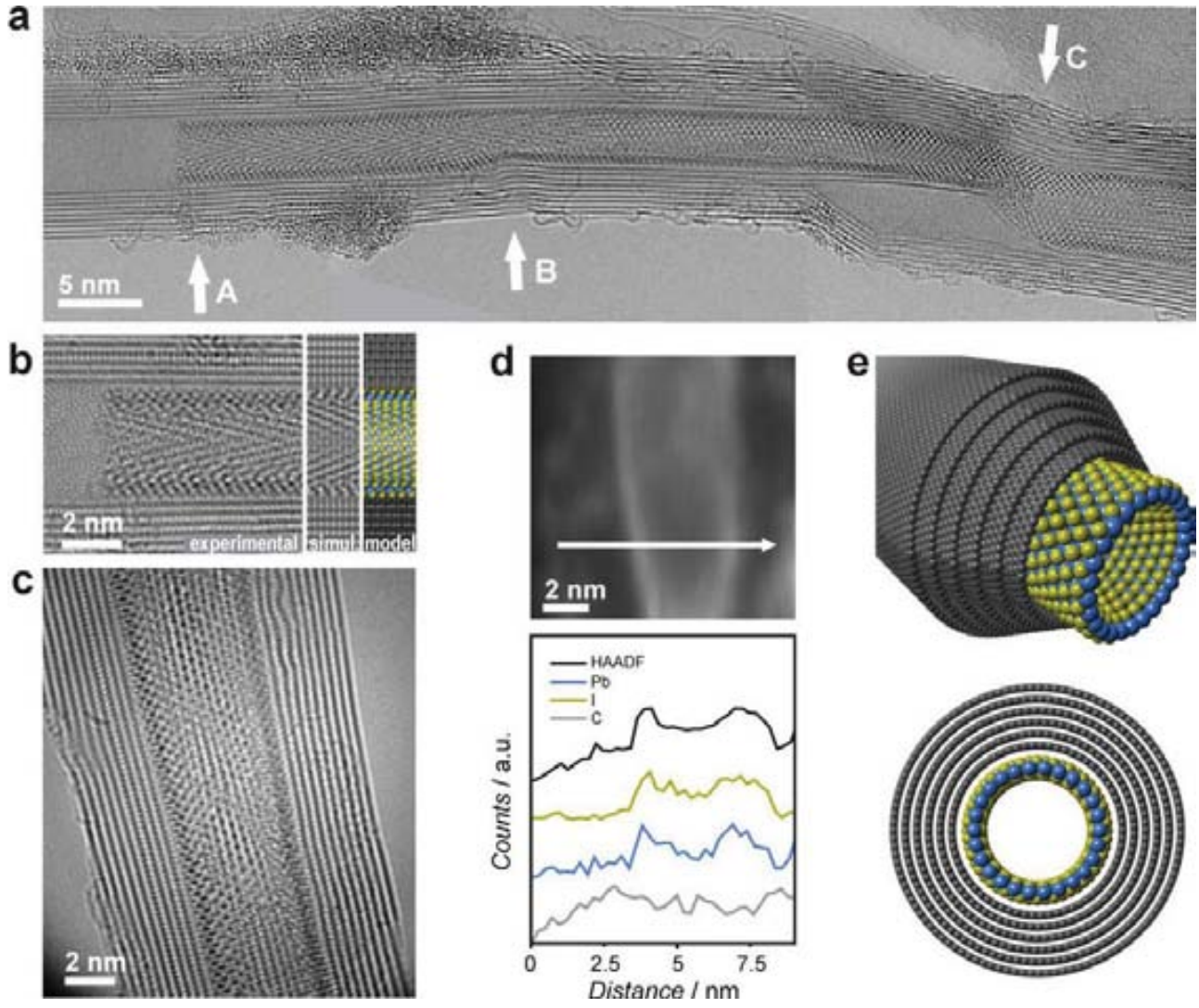

Figure 1. HRTEM and STEM analysis of the synthesised materials. a) Aberration-corrected HRTEM images of a single-layered PbI_2 nanotube. b) Detail of the HRTEM image (area A) with its corresponding simulation and model (cross section along the main axis). c) Aberration-corrected HRTEM image of another single-layered PbI_2 nanotube d) STEM-EDS line profiles confirming the presence of a PbI_2 nanotube. e) Schematic representation of the grown single-layered PbI_2 tubular materials (cyan and green spheres representing Pb and I atoms, respectively) within the inner cavities of a multiwalled carbon nanotube (grey spheres). A cross section across the main axis of the tube is also included for clarity.

of the carbon nanotube is unknown, all the CNTs were taken as zig-zag. Despite small differences, the simulated image is indeed in good agreement with the presence of a lead iodide single-layered nanotube. The distinctive curvature of the prepared inorganic nanotubes can also be directly appreciated by both HRTEM (Figure 1c; average diameter 4.38 nm) and by high-angle annular dark field (HAADF) imaging in high-resolution STEM (see Supporting Information, Figure S1). HAADF imaging provides Z-contrast images which scale with a power of the atomic number, thus facilitating the detection of heavy elements confined within carbon nanotubes or attached to their external walls down to the atomic scale.[18] Therefore in HAADF STEM a large contrast is observed between PbI_2 and C from the host. The wall thickness measured in the HAADF STEM image is about 0.4 nm (Figure S1), consistent with that of a single-layer of PbI_2. Bulk PbI_2 has an interlayer spacing of 0.6986 nm which takes into account the van der Waals spacing,[19] therefore a smaller thickness is expected when measuring an individual single layer. In order to unambiguously determine the successful formation of the tubular structures, HAADF imaging in STEM and x-rays energy dispersive spectroscopy (EDS) experiments were combined to produce elemental profiles of a region of the sample presenting a white tubular contrast (Figure 1d). As expected, a higher intensity of both constituent elements, I and Pb, is detected at the edges compared to the central space confirming the tubular nature of the grown material. For comparison we also analyzed a nanorod of PbI_2 within the CNT host, where the highest intensity for both elements is encountered at the center of the profile, at variance with the hollow structures discussed thus far (see Supporting Information, Figure S2).

Encouraged by the successful formation of PbI_2 nanotubes, we further investigated the role that the diameter of the

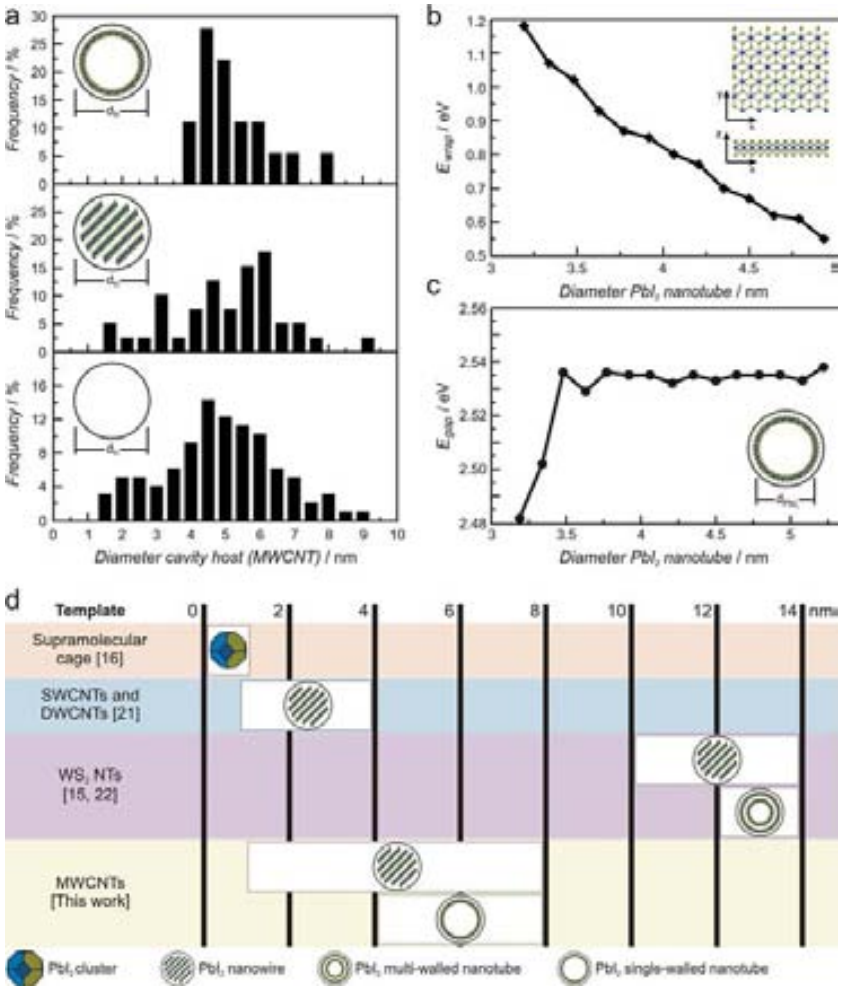

Figure 2. Role of the diameter on the formation, stability, and properties of single-layered inorganic nanotubes. a) Histograms of the MWCNT cavity (cavity of the host), when PbI_2 nanotubes (top) or PbI_2 nanorods (center) are observed; empty MWCNTs (bottom) are also included for comparison. b) Wrapping energy as a function of the PbI_2 nanotube diameter. The wrapping energy is defined as $E_{wrap} = E_{NT}$-E_{ML}, where E_{NT} is the total energy of the PbI_2 nanotube and E_{ML} is the total energy of a flat stand-alone PbI_2 monolayer of the same size, i.e. the unrolled nanotube. The wrapping axis is x (inset) and the energy is given for unit cell of the nanotube. Note that the x, y, z axis correspond to the fragment of PbI_2 layer used to model the nanotubes and not to the bulk PbI_2 structure. c) Band-gap vs diameter of the PbI_2 single-layered nanotube. d) Summary on the formation of PbI_2 nanostructures using template-assisted growth (from this and previous works) with respect to the diameter of the hosts.

confining cage has on the formation of the inorganic nanocrystals. For that purpose, a sample of open-ended CNTs with inner diameters ranging from 1.5 nm to 9 nm was employed, having a larger proportion of nanotubes between 4 and 6 nm. We measured the diameter of the inner cavity of the CNT host when either a nanorod or a single-layered nanotube was present and the resulting histograms are plotted in **Figure 2**a. Interestingly, despite the confined growth of nanorods can take place irrespective of the diameter of the host, the formation of nanotubes preserve a threshold at 4 nm. A large fraction of PbI_2 nanotubes are present within CNTs with diameters of about 4.5–5 nm merely reflecting the diameter distribution of the host in the starting material. Taking into account that the grown PbI_2 nanotubes are about 0.5 nm narrower than the host, single-layered PbI_2 nanotubes from 3.5 to 7.5 nm in diameter can be successfully prepared with this approach. Therefore one can envisage that tailored PbI_2 nanotubes with regular diameters are indeed possible to prepare by using a hosting template with uniform diameters.

To understand the role of the tubular template, we have performed first-principles electronic structure calculations of PbI_2 nanotubes with diameters ranging from 3 to 5 nm. The metal halide nanotubes were modeled by rolling up a fragment (of variable size) of an individual layer of bulk PbI_2.[19] Initially we have calculated the wrapping energy, the energy required to roll up a flat monolayer into a tube (Figure 2b). The energy cost of the wrapping is rather moderate (it is larger than 1 eV per nanotube unit cell only for the narrower systems investigated) and, as expected, it decreases as the diameter of the nanotube increases. This energy is always largely exceeded by the *encapsulation energy* of the PbI_2 nanotubes, the van der Waals PbI_2–C interlayer interaction that we found to be approximately 2.75 eV nm^{-2} (we obtain a very similar value for the interlayer interaction in graphite), thus easing the formation of the nanotubes. This difference decreases at smaller diameters and makes the synthesis of narrow tubes less likely, favoring the higher relative stability of PbI_2 nanorods in such a size range. The theoretical calculations also predict stability for the single-layered PbI_2 nanotubes in case the template was removed: all the stand-alone nanotubes considered turned out to be stable. All the tubes studied are wide band-gap semiconductors, with an energy band-gap very similar to the one of bulk PbI_2 and scarcely dependent on the tube diameter or wrapping axis (see Figure 2c), as previously observed for BN nanotubes.[20] All the calculated band-gaps are within 0.056 eV, a range further reduced to 0.09 eV if the two narrowest, and at present, unrealistic diameters are discarded.

The possibility of growing single-layered nanotubes using nanotubular templates in such a range of diameters (3.5 to 7.5 nm) is remarkable. Figure 2d summarizes the PbI_2 nanostructures that have been prepared so far using their template-assisted growth. Within the 0-dimensional range, nanoclusters of PbI_2 (with molecular formula $Pb_{10}I_{20}$) have recently been prepared employing supramolecular cages.[16] More examples are available with 1-dimensional nanostructures. When employing either single-walled or double-walled carbon nanotubes (1–4 nm in diameter), PbI_2 nanorods, and not nanotubes, are always observed.[21] The use of inorganic WS_2 nanotubes (inner and outer diameters of about 10 nm and 20 nm respectively) as hosts allows the formation of multiwalled PbI_2 nanotubes (3–5 layers)

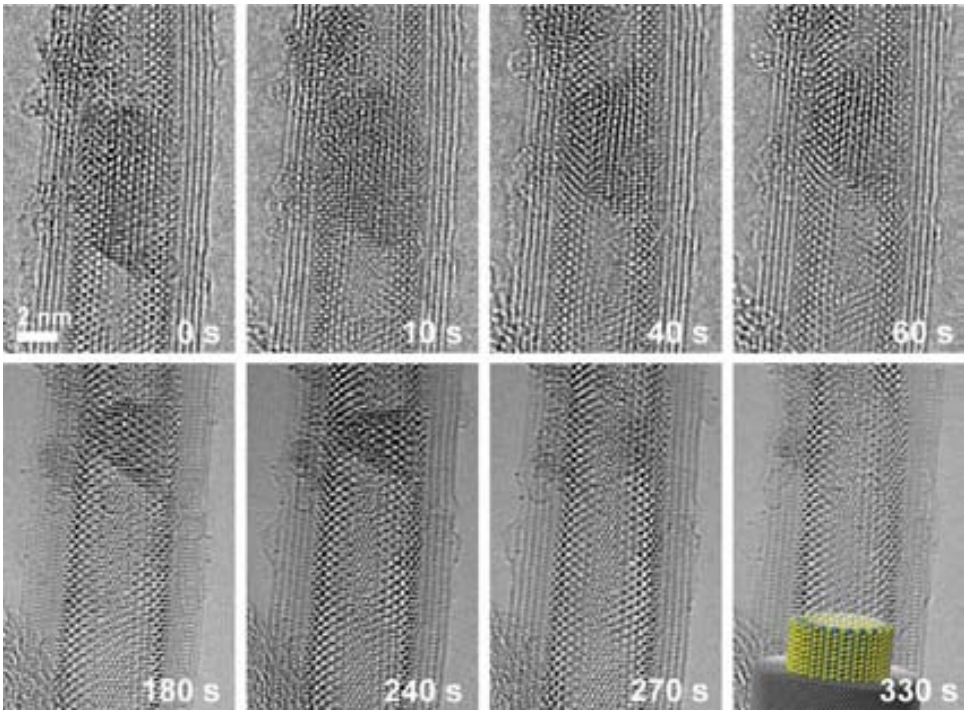

Figure 3. Dynamics under the electron beam radiation. Sequence of images showing the transformation from a nanorod fragment onto a single-layered nanotube using an electron dose of ~$0.6 \cdot 10^4$ e^- $Å^{-2}$. A schematic representation is included in the last image; cyan, green and grey spheres representing Pb, I and C atoms, respectively.

as well as PbI_2 inorganic nanorods.[15] Model calculations indicate that PbI_2 multiwalled nanotubes become stable inside MoS_2 (model for WS_2) only when the diameter of the host is larger than 12 nm; below this diameter the PbI_2 crystallizes as a nanorod.[22] This is in agreement with the experimental observations.[22] Other metal halides, including BiI_3 and SbI_3 have also been confined within the WS_2 nanocapillaries leading also to the formation of multiwalled nanotubes and nanorods.[22] It is only when carbon nanotubes are employed, that single-layered PbI_2 can be prepared. The filling of PbI_2 occurs in a fast and effective manner and can be achieved after annealing the bulk metal halide in the presence of carbon nanotubes in only 10 minutes. Higher encapsulation efficiencies are obtained after annealing for longer periods of time. The formation of single-layered PbI_2 tubular structures is also accompanied by the presence of PbI_2 nanorods, and several nanotube-nanorod junctions are present. Molecular dynamic simulations suggested that PbI_2 initially fills as a molten drop into tubular templates; this can then lead to the spread of melt over the inner surface of the host with crystallization of PbI_2 nanotubes on cooling (into chalcogenide hosts).[23] The diameter of the CNT models employed for the simulations lie within the diameters encountered with single- and double-walled CNTs. In this range of diameters, only the formation of tubular structures of one-atom in thickness (graphene-like) has been described by dynamic and static simulations.[24] Therefore molecular dynamic studies with CNTs of larger diameter, such as those used in the present study, are needed to get further insights in these systems.

A great deal of interest is devoted towards the study of physical transformations that materials undergo in a confined nanoscale geometry.[25,26] Electron microscopy has proven to be a powerful tool to directly monitor these changes in real time.[27] Therefore, we next studied the dynamic effect of electron beam irradiation on several nanotube-nanorod junctions. **Figure 3** presents a sequence of images of a PbI_2 nanorod confined within an envolving PbI_2 nanotube. Upon irradiation by the electron beam at 80 kV (to reduce knock-on damage), a continuous blending of the nanorod onto the nanotube takes place until its complete dissolution, thus resulting in the formation of a continuous PbI_2 nanotube. The conversion process has been observed in other nanotube-nanorod-nanotube junctions. The inverse phenomenon has also been observed, where a fragment of nanotube confined within two nanorods is "filled" resulting in a continuous nanorod (Supporting Figure S3). In both cases, the transformation from one type of nanostructure to the other takes place due to the irradiation by the electron beam. HAADF STEM analysis reveals that PbI_2 nanorods can be composed of a narrower nanorod confined within a PbI_2 single-layered nanotube (Supporting Figure S4). In this scenario, upon beam irradiation, the inner nanorod could be displaced within the PbI_2 nanotube, filling an empty void, as seems to be the case of the in-situ study presented in Figure S3. The opposite mechanism where the inner nanorod breaks apart leaving the shielding inorganic tube visible could also be considered but the nanotube to nanorod transformation observed in Figure 3 does not seem to fall in this scenario. In this sequence of images rather an atomic migration from the nanorod to the nanotube seems to occur. To allow the accommodation of additional lead and iodine atoms into the tubular structure an atomic migration within the top/bottom part of the nanotube would be necessary.

The motion of confined materials, including metal halides, within the cavities of CNTs has been widely investigated. The displacement can be stimulated by either electron beam irradiation, like in the present study, or driven for instance by heat or electrical currents.[26,28,29] A wide variety of metal halides have been encapsulated within CNTs being electron microscopy the most commonly used technique for their investigation.[5,21,30] In some cases electron beam irradiation has been reported to lead to chemical changes, typically after prolonged irradiation or under high acceleration voltages.[29,31] Therefore the use of low voltage is desired when investigating these systems under the electron beam. The mechanism of transformation from nanotubes to nanorods and viceversa needs further investigation and even chemical changes cannot be disregarded at this stage.

As discussed, all the PbI_2 nanotubes studied are wide band-gap semiconductors. Projections of the density of states (DOS) on the different chemical species reveal a peculiar localization of the band-edge states of different layers, for instance similarly to what have been reported for SiGe heterostructures.[32] As can be seen in **Figure 4**a, valence states are almost exclusively made of I orbitals, while conduction states are mostly made of Pb orbitals. This is also evident in the real space representation of the wave-function of the higher (valence band) and lower (conduction band) states shown in Figure 4b. This behaviour can be in principle exploited in all those applications where an efficient charge separation is required, such as solar cells where the efficiency of recombination of a created electron-hole pair must be minimized. The contribution of outer and inner I atoms is different, but of course this difference vanishes as the diameter increases and the curvature drops. Additionally, we observe that the conduction states exhibit a larger dispersion than the rather flat valence band (Figure 4c), thus electrons are expected to be more efficient charge carriers than holes in these tubular systems.

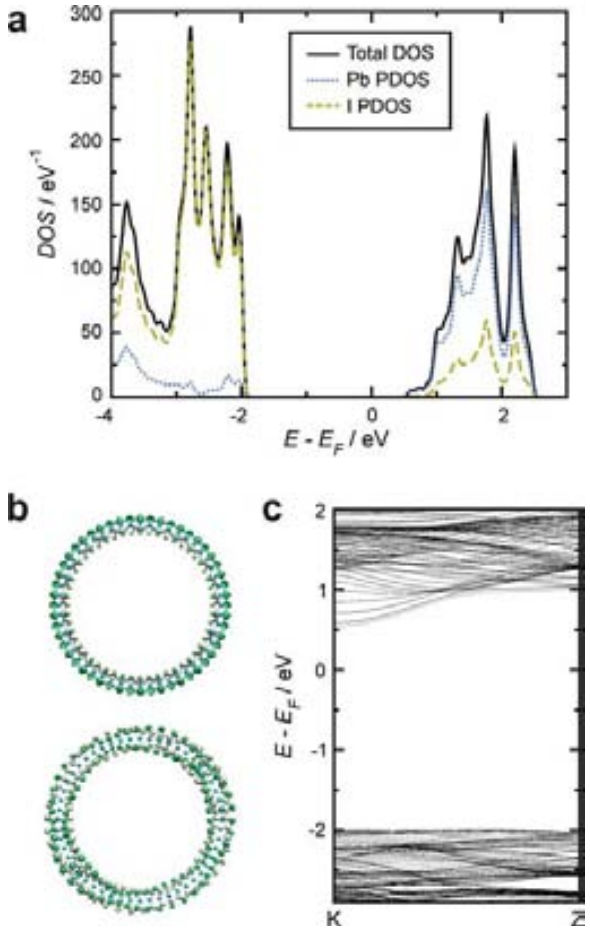

Figure 4. Electronic structure of single-layered PbI_2 nanotubes. a) Total density of states and projections on Pb and I atoms. b) The wave-function of HOMO (bottom) and LUMO (top) shows the different localization: on I atoms the former, on Pb atoms the latter. c) Band structure diagram. The data presented correspond to a nanotube of 3.77 nm in diameter.

In conclusion, a solvent-free high temperature route has been explored that allows the formation of high-quality, single-crystalline inorganic nanotubes. We have produced an interesting hybrid core-shell structure combining two different tubular materials: single-layered PbI_2 nanotubes@CNTs. Above the threshold of 3.5 nm, the single-layers of PbI_2 can be easily moulded to the inner diameter of the hosting CNT template. The diameter of the inorganic nanotubes prepared herein is merely dependent on the diameter of the host. Therefore inorganic nanotubes of a given diameter can be prepared by simply using a sample of CNTs with uniform inner diameter. These coupled 1D nanostructures will offer very promising technological applications where materials having well defined electronic, optic or optoelectronic properties are required. The method is highly versatile opening up new horizons in the preparation of single-layered nanostructures of a wide variety of materials.

Experimental Section

Growth of PbI_2 Single-Layered Nanotubes: Chemical vapour deposition multiwalled carbon nanotubes (Thomas Swan Co.Ltd.) were steam treated in order to open their ends and purify the as-received material.[17] Next the sample was treated with HCl to remove the now exposed catalytic metal nanoparticles.[33] In an argon-filled glove box, purified CNTs (6 mg) and PbI_2 (140 mg) were ground with an agate mortar and pestle until the mixture presented a uniform color. The mixture was transferred into a silica ampoule, evacuated and sealed under vacuum. The ampoule was placed into a furnace where it dwelled at 500 °C (above the melting point of lead iodide; mp 408 °C) for different periods of time (from 10 min up to 86 h). Finally, the samples were cooled at room temperature.

HRTEM and STEM Studies: Initial TEM characterisation of the samples was performed on a JEOL JEM 1210 operated at 120 kV. HRTEM images were acquired in an image corrected FEI Titan Cube 60–300 microscope. STEM imaging and EDS chemical analyses were carried out in a probe corrected FEI Titan 60–300 microscope and a FEI Tecnai G2 F20 microscope. Both FEI Titan instruments were operated at 80 kV with a point resolution of 0.14 nm. Samples for TEM characterisation were prepared by sonication of a small amount of powder in ethanol absolute. The dispersions were placed dropwise onto lacey carbon grids.

First-Principles Calculations: First-principles electronic structure calculations were performed within density-functional theory, as implemented in the siesta and vasp packages,[34] expanding the one-electron wave function using a double-ζ polarized basis set of numerical atomic orbitals and a plane-wave cutoff of 400 eV, respectively. We used the Local Density Approximation (LDA) for the exchange-correlation energy.[35] The Brillouin zone was sampled with a grid of 12 points along the k_z (z being the nanotube axis). The interlayer interaction between a C and a PbI_2 nanotube was approximated with the

graphene-PbI_2 monolayer interaction energy (flat geometry) within the semi-empirical dispersion correction of Grimme.[36] Due to the intrinsic incommensurability of graphene and lead iodide, we constructed the hybrid system by placing a 4 × 4 supercell of the flat PbI_2 monolayer on top of a 7 × 7 supercell of graphene, with a compressive strain of 0.88% on the latter. The atomic positions were relaxed until all the forces were lower than 0.04 eV $Å^{-1}$ and the lattice parameter was optimized in all the structures discussed.

Supporting Information

Supporting Information is available from the Wiley Online Library or from the author.

Acknowledgements

This work was supported by MINECO (MAT2011–24757, FIS2012–37549-C05–05), EU FP7-ITN RADDEL (290023) and Nanoaracat. The authors are grateful to Thomas Swan Co. Ltd. for supplying the MWCNT samples. L.C. acknowledges a JAE-Predoc fellowship (CSIC) and E.B. the CSIC-CITMA training and mobility program. L.C. is enrolled in the UAB PhD program. Aberration-corrected electron microscopy studies were conducted in the *Laboratorio de Microscopías Avanzadas* (LMA) at the *Instituto de Nanociencia de Aragón* (INA) – *Universidad de Zaragoza* (Spain).

Received: October 17, 2013
Published online: December 16, 2013

[1] a) A. H. C. Neto, K. Novoselov, *Rep. Progr. Phys.* **2011**, *74*, 082501; b) O. Minoru, S. Takayoshi, *Adv. Mater.* **2012**, *24*, 210; c) Q. H. Wang, K. Kalantar-Zadeh, A. Kis, J. N. Coleman, M. S. Strano, *Nature Nanotech.* **2012**, *7*, 699; d) J. L. Dattatray, L. Bin, L. Jiajun, Y. Aiming, H. S. S. R. Matte, G. Matthew, C. N. R. Rao, P. D. Vinayak, *Adv. Mater.* **2013**, *24*, 3549.
[2] J. Goldberger, R. Fan, P. Yang, *Acc. Chem. Res.* **2006**, *39*, 239.
[3] C. N. R. Rao, A. Govindaraj, *Adv. Mater.* **2009**, *21*, 4208.
[4] D. Eder, *Chem. Rev.* **2010**, *110*, 1348.
[5] R. R. Meyer, J. Sloan, R. E. Dunin-Borkowski, A. I. Kirkland, M. C. Novotny, *Science* **2000**, *289*, 1324.
[6] R. Kitaura, R. Nakanishi, T. Saito, H. Yoshikawa, K. Awaga, H. Shinohara, *Angew. Chem. Int. Ed.* **2009**, *48*, 8298.
[7] S. Hong, G. Tobias, K. Al-Jamal, B. Ballesteros, H. Ali-Boucetta, S. Lozano-Perez, P. Nellist, R. Sim, C. Finucane, S. Mather, K. Kostarelos, B. Davis, *Nature Mater.* **2010**, *9*, 485.
[8] J. Y. Chen, A. Kutana, C. P. Collier, K. P. Giapis, *Science* **2005**, *310*, 1480.
[9] M. del Carmen Giménez-López, F. Moro, A. La Torre, C. J. Gómez-García, P. D. Brown, J. van Slageren, A. N. Khlobystov, *Nature Commun.* **2011**, *2*, 407.
[10] Y. Maniwa, K. Matsuda, H. Kyakuno, S. Ogasawara, T. Hibi, H. Kadowaki, S. Suzuki, Y. Achiba, H. Kataura, *Nature Mater.* **2007**, *6*, 135.
[11] A. E. Porter, M. Gass, K. Muller, J. N. Skepper, P. A. Midgley, M. Welland, *Nature Nanotech.* **2007**, *2*, 713.
[12] a) A. Chuvilin, E. Bichoutskaia, M. C. Gimenez-Lopez, T. W. Chamberlain, G. A. Rance, N. Kuganathan, J. Biskupek, U. Kaiser, A. N. Khlobystov, *Nature Mater.* **2011**, *10*, 687; b) A. N. Khlobystov, *ACS Nano* **2013**, *5*, 9306.
[13] a) A. M. Guloy, Z. Tang, P. B. Miranda, V. I. Srdanov, *Adv. Mater.* **2001**, *13*, 833; b) L.-M. Wu, X.-T. Wu, L. Chen, *Coord. Chem. Rev.* **2009**, *253*, 2787.
[14] a) M. M. Lee, J. l. Teuscher, T. Miyasaka, T. N. Murakami, H. J. Snaith, *Science* **2012**, *338*, 643; b) J. Jun-Yuan, C. Yi-Fang, L. Mu-Huan, P. Shin-Rung, G. Tzung-Fang, C. Peter, W. Ten-Chin, *Adv. Mater.* **2013**, *25*, 3727.
[15] R. Kreizman, S. Y. Hong, J. Sloan, R. Popovitz-Biro, A. Albu-Yaron, G. Tobias, B. Ballesteros, B. G. Davis, M. L. H. Green, R. Tenne, *Angew. Chem. Int. Ed.* **2009**, *48*, 1230.
[16] Y. Liu, C. Hu, A. Comotti, M. D. Ward, *Science* **2011**, *333*, 436.
[17] G. Tobias, L. Shao, C. Salzmann, Y. Huh, M. L. H. Green, *J. Phys. Chem. B* **2006**, *110*, 22318.
[18] a) X. Fan, E. C. Dickey, P. C. Eklund, K. A. Williams, L. Grigorian, R. Buczko, S. T. Pantelides, S. J. Pennycook, *Phys. Rev. Lett.* **2000**, *84*, 4621; b) S. Y. Hong, G. Tobias, B. Ballesteros, F. El Oualid, J. C. Errey, K. J. Doores, A. I. Kirkland, P. D. Nellist, M. L. H. Green, B. G. Davis, *J. Am. Chem. Soc.* **2007**, *129*, 10966.
[19] B. Palosz, *J. Phys.: Cond. Matter* **1990**, *2*, 5285.
[20] a) A. Rubio, J. L. Corkill, M. L. Cohen, *Phys. Rev. B* **1994**, *49*, 5081; b) X. Blase, A. Rubio, S. G. Louie, M. L. Cohen, *Phys. Rev. B* **1995**, *51*, 6868; c) R. Arenal, O. Stéphan, M. Kociak, D. Taverna, A. Loiseau, C. Colliex, *Phys. Rev. Let.* **2005**, *95*, 127601; d) R. Arenal, X. Blase, A. Loiseau, *Adv. Phys.* **2010**, *59*, 101.
[21] E. Flahaut, J. Sloan, S. Friedrichs, A. I. Kirkland, K. S. Coleman, *Chem. Mater.* **2006**, *18*, 2059.
[22] R. Kreizman, A. N. Enyashin, F. L. Deepak, A. Albu-Yaron, R. Popovitz-Biro, G. Seifert, R. Tenne, *Adv. Funct. Mater.* **2010**, *20*, 2459.
[23] A. N. Enyashin, R. Kreizman, G. Seifert, *J. Phys. Chem. C* **2009**, *113*, 13664.
[24] M. Wilson, *Nano Lett.* **2004**, *4*, 299.
[25] V. C. Holmberg, M. G. Panthani, B. A. Korgel, *Science* **2009**, *326*, 405.
[26] P. M. F. J. Costa, U. K. Gautam, Y. Bando, D. Golberg, *Nature Commun.* **2011**, *2*, 421.
[27] E. Nakamura, *Angew. Chem. Int. Ed.* **2013**, *52*, 236.
[28] a) A. N. Khlobystov, K. Porfyrakis, M. Kanai, D. A. Britz, A. Ardavan, H. Shinohara, T. J. S. Dennis, G. A. D. Briggs, *Angew. Chem. Int. Ed.* **2004**, *43*, 1386; b) D. Golberg, P. M. F. J. Costa, M. Mitome, S. Hampel, D. Haase, C. Mueller, A. Leonhardt, Y. Bando, *Adv. Mater.* **2007**, *19*, 1937; c) P. M. F. J. Costa, D. Golberg, M. Mitome, S. Hampel, A. Leonhardt, B. Buchner, Y. Bando, *Nano Lett.* **2008**, *8*, 3120; d) J. Sloan, G. Matthewman, C. Dyer-Smith, A. Y. Sung, Z. Liu, K. Suenaga, A. I. Kirkland, E. Flahaut, *ACS Nano* **2008**, *2*, 966; e) P. M. F. J. Costa, U. K. Gautam, Y. Bando, D. Golberg, *Carbon* **2011**, *49*, 3747.
[29] J. L. Hutchison, N. Grobert, R. M. Zakalyukin, A. A. Eliseev, M. V. Chernisheva, A. S. Kumskov, Y. V. Grigoriev, A. V. Krestinin, B. Freitag, N. A. Kiselev, *AIP Conference Proceedings* **2008**, *999*, 79.
[30] a) J. Sloan, A. I. Kirkland, J. L. Hutchison, M. L. H. Green, *Chem. Commun.* **2002**, 1319; b) B. Ballesteros, G. Tobias, M. A. H. Ward, M. L. H. Green, *J. Phys. Chem. C* **2009**, *113*, 2653; c) E. Fidiani, P. M. F. J. Costa, A. U. B. Wolter, D. Maier, B. Buechner, S. Hampel, *J. Phys. Chem. C* **2013**, *117*, 16725.
[31] a) G. Brown, S. R. Bailey, J. Sloan, C. Xu, S. Friedrichs, E. Flahaut, K. S. Coleman, J. L. Hutchison, R. E. Dunin-Borkowski, M. L. H. Green, *Chem. Commun.* **2001**, 845; b) A. Ilie, J. S. Bendall, K. Nagaoka, S. Egger, T. Nakayama, S. Crampin, *ACS Nano* **2011**, *5*, 2559.
[32] M. Amato, S. Ossicini, R. Rurali, *Nano Lett.* **2011**, *11*, 594.
[33] B. Ballesteros, G. Tobias, L. Shao, E. Pellicer, J. Nogués, E. Mendoza, M. L. H. Green,*Small* **2008**, *4*, 1501.
[34] a) J. M. Soler, E. Artacho, J. D. Gale, A. García, J. Junquera, P. Ordejón, D. Sánchez-Portal, *J. Phys.: Cond. Matter* **2002**, *14*, 2745; b) G. Kresse, J. Furthmüller, *Comput. Mat. Sci.* **1996**, *6*, 15.
[35] D. M. Ceperley, B. J. Alder, *Phys. Rev. Lett.* **1980**, *45*, 566.
[36] S. Grimme, *J. Comp. Chem.* **2006**, *27*, 1787.

Annex I

Submitted and under review articles

The role of steam treatment on the structure, purity and length distribution of multi-walled carbon nanotubes

Laura Cabana[1], Xiaoxing Ke[2], Dejan Kepić[1,3], Judith Oro-Solé[1], Ester Tobías-Rossell[4], Gustaaf Van Tendeloo[2], Gerard Tobias[1*]

[1]*Institut de Ciència de Materials de Barcelona (ICMAB-CSIC), Campus UAB, 08193 Bellaterra, Barcelona, Spain.*

[2]*Electron Microscopy for Materials Science (EMAT), University of Antwerp, Groenenborgerlaan 171, B-2020, Antwerp, Belgium.*

[3]*Vinča Institute of Nuclear Sciences, University of Belgrade, Mike Alasa 12-14, Belgrade, Serbia*

[4]*Escola Universitària de Ciències de la Salut de Manresa, Universitat de Vic-Universitat Central de Catalunya, Av. Universitària 4-6, 08242 Manresa, Barcelona, Spain*

*Corresponding author. E-mail: **gerard.tobias@icmab.es** (Gerard Tobias); Tel. +34 93 580 1853

Abstract

Purification and shortening of carbon nanotubes have attracted a great deal of attention to increase the biocompatibility and performance of the material in several applications. Steam treatment has been employed to afford both purification and shortening of multi-walled carbon nanotubes (MWCNTs). Steam removes the amorphous carbon and the graphitic particles that sheath catalytic nanoparticles, facilitating their removal by a subsequent acidic wash. The amount of metal impurities can be reduced in this manner below 0.01 wt.%. Electron microscopy analysis allowed the assessment of the length distribution of MWCNTs after different steam treatment times (from 1 h to 15 h). Samples with a median length of 0.57 μm have been prepared with the reported methodology whilst preserving the integrity of the tubular wall structure.

1. Introduction

Bulk synthesis of carbon nanotubes (CNTs) results in samples that contain several impurities, namely amorphous carbon, graphitic particles in the form of fullerenes or nano-onions, and metal nanoparticles when employed for the catalytic growth of CNTs. The presence of these impurities is detrimental for further processing and application of CNTs. Metal nanoparticles not only might induce cytotoxicity [1-3] but can also dominate the electrochemical response of the material [4] along with graphitic particles [5-7]. On the other hand, the presence of amorphous carbon alter the adhesion properties of the nanotubes [8] and might lead to the formation of oxidation debris preventing the sidewall functionalization of CNTs [9]. A wide range of purification strategies have been employed to remove these side products; liquid phase treatments in oxidising acidic conditions being the most widely used. For instance, the combination of HCl and HNO_3 has been shown to simultaneous remove non-nanotube carbon material along with metal and metal oxide nanoparticles present in samples of multi-walled carbon nanotubes (MWCNTs) [10], leading to purities above 96 wt.% [11]. Other liquid phases treatments for the purification of MWCNTs involve the use of hydrogen peroxide, followed by an HCl wash [12] or chlorine and ammonia water [13]. Gas phase reactions not only reduce the amount of chemical waste but also present some advantages compared to liquid phase treatments [14, 15]. Gas phase purification of MWCNTs commonly involve air [16] but steam [17], carbon dioxide [18], chlorine [19], hydrogen [20], and plasma-thermal purification [21] have also been explored. Purification studies on as-produced single-walled carbon nanotubes (SWCNTs) have revealed that air-oxidation can remove the associated impurities while inflicting considerably less damage than oxidising acid-treatment, and avoid the formation of oxidation debris [15]. Unlike liquid phase oxidation the gas phase process preferentially oxidizes SWCNTs without introducing sidewall defects [22]. Oxygen reacts with carbon in a fast manner, above a given temperature. Therefore when air is employed for the purification of CNT samples a careful optimization of the temperature and treatment time is necessary from batch to batch to avoid the complete oxidation and loss of the carbon material.

Steam, being a milder oxidizing agent, allows a better control of the purification with reactions with as-produced SWCNTs that can last for several hours [23]. Steam has been combined with oxidizing acid treatments for the purification of cloth-like soot SWCNTs from arc discharge [24], because steam can efficiently remove the functionalities introduced by the acid treatment [17]. Steam treatment has also been used for the controlled etching of multi-walled carbon nanotubes decorated with iron nanoparticles [25]. The etching occurred only at the interface between the iron nanoparticles and the nanotubes. Steam purified carbon nanotubes are being employed for a wide range of applications such as lithium-ion batteries [26], supercapacitors [27, 28], ceramic composites [29], templated growth of novel structures [30], biomedical applications [31, 32] or even for the formation of graphene by unzipping steam purified nanotubes [28]. Furthermore, initial studies reveal that short SWCNTs can be obtained after prolonged steam treatment [23]. Short CNTs have an increased biocompatibility and are desired for a wide range of applications including biomedicine [33, 34], sensors [35], membranes [36] and electrode materials [37]. As such, a toolbox of cutting and shortening strategies is nowadays available including ball milling [38], lithography [39], fluorination [40] and oxidation [41].

From just the few examples noted above, it becomes clear that there is a growing interest in the use of steam for the post-synthesis processing of CNT material. Steam is actually widely employed as an oxidative additive during the synthesis of carbon nanotubes by chemical vapor deposition (CVD). When steam is added into the reactor, not only the formation of amorphous carbon is suppressed, but also the activity and lifetime of the catalysts are greatly improved [42, 43]. Thus, using steam is possible to synthesize high-purity CNTs and is an efficient additive for the supergrowth of aligned SWCNTs [44]. However, the role of steam onto the post-synthesis treatment of MWCNT samples has barely been studied. As in the case of their SWCNT counterparts, it has been shown that steam removes the amorphous carbon and opens the ends of MWCNTs [17]. Here we report for the first time on the effect of the steam treatment on the length distribution of MWCNTs, wall structure, and residual inorganic content of the samples.

2. Experimental and methods

Chemical vapour deposition Elicarb® MWCNTs from Thomas Swan & Co. Ltd. were supplied as dry powder, with an average diameter of 10-12 nm (value provided by the company). The samples contained amorphous carbon, graphitic particles (carbonaceous crystalline materials having few graphitic layers) and inorganic particles. CoMoCAT® CVD MWCNTs from SouthWest NanoTechnologies were purchased from Sigma-Aldrich as dry powder. The CoMoCAT MWCNTs have an average diameter of 10 nm ± 1 nm and a purity of ≥98% carbon basis (values provided by the company). The as-received material was finely grounded with an agate mortar and pestle and spread on the center part inside a silica tube of 5 cm in diameter. The silica tube, opened at both ends, was then placed into the alumina tube of the furnace and purged with argon (150 mL min^{-1}) for 2 h to allow the complete removal of air. Steam was introduced by flowing the incoming argon through a bubbler with hot water (98 ºC). Therefore, a mixture of Ar/steam gets in contact with the sample. The temperature of the furnace was then increased up to 900 ºC and dwelled for different periods of time between 1 to 15 h. The sample was next treated with 6 M HCl to remove catalytic particles. Finally the powder was collected by filtration through a 0.2 μm polycarbonate membrane and washed with distilled water until the pH of the filtrate was neutral.

Thermogravimetric analysis (TGA) were performed on Netzsch instrument, model STA 449 F1 Jupiter® (Elicarb MWCNTs) or in a Mettler Toledo TGA/SDTA851e/SF/1100 (CoMoCAT MWCNTs). Experiments were conducted under a flow of air at a heating rate of 10 ºC min^{-1} up to 950 ºC. To examine the stability of as-received Fe-growth MWCNTs, TGA was performed on SETARAM Setsys Evolution instrument. Sample was heated up to 1100 °C with a heating rate of 10 °C min^{-1} under Ar/steam flow (190 mL min^{-1} of argon and 2 g h^{-1} of steam).

Magnetic measurements were done in a Superconducting Quantum Interference Device (SQUID) magnetometer (LOT-QuantumDesign Iberia). A diamagnetic gelatine capsule was filled with 3-4

mg of sample. Data was acquired with an applied field from -50.000 Oe to +50.000 Oe at 10 K to obtain the hysteresis loops. The sample holder contribution was subtracted in all the measurements.

Raman spectra were recorded with a LabRam HR 800 Raman spectrometer, Jobin Yvon® equipped with a microscope, through a 100-fold magnification objective. A 20 mW He-Ne red laser (633 nm) and - Ar^+ green laser (514 nm) were used. The spectra were recorded from 100 to 2000 cm^{-1}. The abscissa was calibrated with a silicon standard. Samples for Raman were prepared by sonicating the material with 2-propanol, in an ultrasonic power bath. Afterwards, these were drop dried onto a glass substrate, building up a film of the material. To check homogeneity of the samples, three spectra at different spots on the sample were recorded. Spectra were fitted using OriginPro 8 software. Each spectrum was fitted with one Gaussian and four Lorentzian functions until satisfactory fitting criteria.

Elemental Analysis was conducted with an elemental analyzer EA 1108 Instrument and a microbalance Mettler Toledo MX5. For the measurement, 1 mg of sample was weighed and a mixture of vanadium pentoxide and tin was added to ease the combustion. Sulfanilamide was used as a pattern.

XPS were acquired with a Kratos AXIS ultra DLD spectrometer with an Al Kα X ray font and a power of 120 W. Samples were measured as dry powder. Survey-scan was conducted with a Pass Energy of 160 eV and high resolution scans at a Pass Energy of 20 eV. Hybrid-slot lens mode was employed, with an area of analysis of 700 x 300 microns.

Low magnification TEM images were obtained using a JEOL 1210 and operating at 120 kV. HRTEM images were acquired using an FEI Tecnai G2 microscope operating at 200 kV. TEM

and HRTEM samples were prepared by dispersing a small amount of powder in absolute ethanol and sonicated in an ultrasonic power bath. Afterwards, the dispersion was drop dried onto a lacey carbon TEM grid.

3. Results and discussion

The reactivity of MWCNTs towards steam was assessed by TGA analysis of as-received Elicarb® Fe-grown MWCNTs under Ar/steam flow (Figure 1). As it can be seen, MWCNTs present an excellent stability in the presence of steam until about ~900 ºC were the sample starts to oxidize. Therefore, all the subsequent treatments were performed at 900 °C.

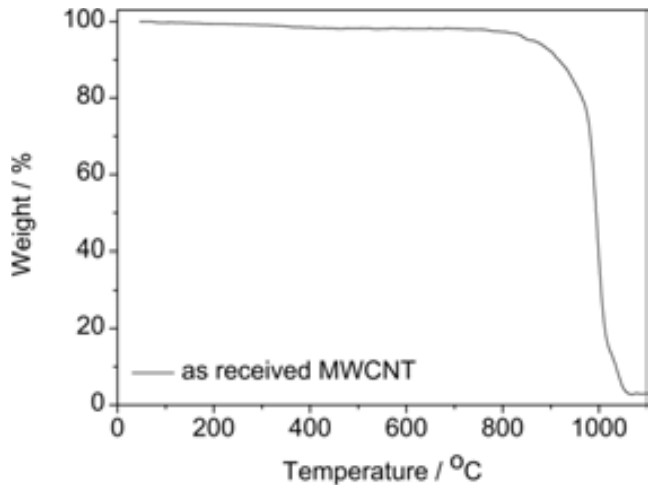

Figure 1. TGA of as-received Fe-growth CVD MWCNTs under Ar/steam flow.

Thermogravimetric analysis (TGA) under flowing air was used to assess the amount of solid residue in both as-received and steam purified samples for different periods of time, namely 1 h, 1.5 h, 2 h, 2.5 h, 5 h, 10 h and 15 h (Figure 2a). All the samples were treated with HCl before TGA measurements. Taking into account that all carbon species are oxidized to carbon dioxide, the residue from the TGA analysis must correspond to inorganic impurities from the synthesis of the nanotubes. Compared to as-received material, which contains 2.8 wt.% of inorganic solid residue, a decrease is observed up to 1.5 h of steam treatment, down to 0.5 wt.%. Longer

treatments result in an increase of the inorganic content which levels off at about 1.9 wt.% for prolonged treatments (10-15 h). The solid residue obtained after the thermogravimetric analysis of the samples in air is typically attributed to the oxidation of the metal employed for the growth of the CNTs. Therefore, in the present case the residue would correspond to iron oxide (Fe_2O_3) since iron is used for the synthesis of the nanotubes. The amount of iron would then be 2.0 wt.% (as-made), 0.4 wt.% (1.5 h steam) and 1.3 wt.% (10 h). To independently assess the amount of metal content in the samples we performed magnetic measurements which have been shown to be the most accurate statistical method for quality control of CNTs [45]. Contrary to TGA, magnetic measurements are non-destructive and preserve the sample. Figure 2b presents the hysteresis loops of both as-received MWCNTs and after 1.5 h steam purification followed by HCl treatment. The as-received MWCNTs present a clear ferromagnetic behaviour superposed on a paramagnetic contribution, whereas in the purified sample a weak diamagnetic response from the holder starts to prevail. This illustrates a dramatic decrease in the amount of metal catalyst present in the sample. The saturation magnetization (M_S) of the samples after removing the linear background is 2.19 emu·g_{sample}^{-1} for the as-received material and 0.049 emu·g_{sample}^{-1} for the purified sample. Considering that the nature of the catalyst particles is pure Fe, and with iron having a bulk saturation magnetization of 221.7 emu·g^{-1} [46], the amount of metal catalyst in samples would be 0.99 wt.% for the as-received material and 0.022 wt.% for the 1.5 h steam purified sample. In contrast to their SWCNT counterparts where both TGA and SQUID revealed the same amount of catalytic impurities [23], the quantity of Fe assessed by magnetic measurements in the steam purified MWCNTs results to be an order of magnitude lower than that obtained by TGA. The same trend occurs after a prolonged 10 h steam treatment where a 0.007 wt.% of Fe is determined by SQUID measurements (0.016 emu·g_{sample}^{-1}) in contrast to a 1.3 wt.% Fe as per TGA. If the nature of the impurities present in the sample were iron oxide or iron carbide, with bulk M_S(γ-Fe_2O_3) = 87 emu·g^{-1}; $M_S(Fe_3O_4)$ = 92 emu·g^{-1} and $M_S(Fe_3C)$ = 140 emu·g^{-1} [46], then the observed saturation magnetization after 10 h treatment would correspond to about 0.018 wt.% of

iron oxide and 0.011 wt.% of iron carbide; still well below the inorganic residue observed by TGA. The observed differences between TGA and SQUID determination of the catalytic impurities can not only arise from the fact that the M_S values of nanoparticles are typically smaller than that of the bulk material [47]. Therefore, we performed XPS analysis of the 10 h steam treated sample to determine the presence of any other inorganic species. Whereas the amount of iron was below the detection limit of this technique, an aluminium peak is clearly visible (Figure S1). Most likely aluminium is present in the sample in the oxide form as alumina, a commonly employed refractory material for high temperature syntheses. The presence of alumina impurities would indeed contribute to the TGA residue but not to the SQUID analysis, and accounts for the differences observed between both methods. Table 1 summarizes the inorganic content of representative samples. The presence of alumina in the samples becomes more visible after prolonged treatments because the carbon content diminishes with time due to its continuous removal by steam. The steam treatment followed by HCl wash is indeed an efficient approach for the removal of catalytic particles reaching levels below 0.01 wt.% Fe. The catalytic particles present in the as-received CNTs are sheathed by graphitic layers that are difficult to be oxidized even under strong acidic conditions [48]. Steam reacts with these graphitic shells leaving the metal particles exposed and susceptible to be dissolved by HCl wash. The very low residual amount of iron particles after the steam and HCl treatments makes the whole range of steam purified samples interesting for further application.

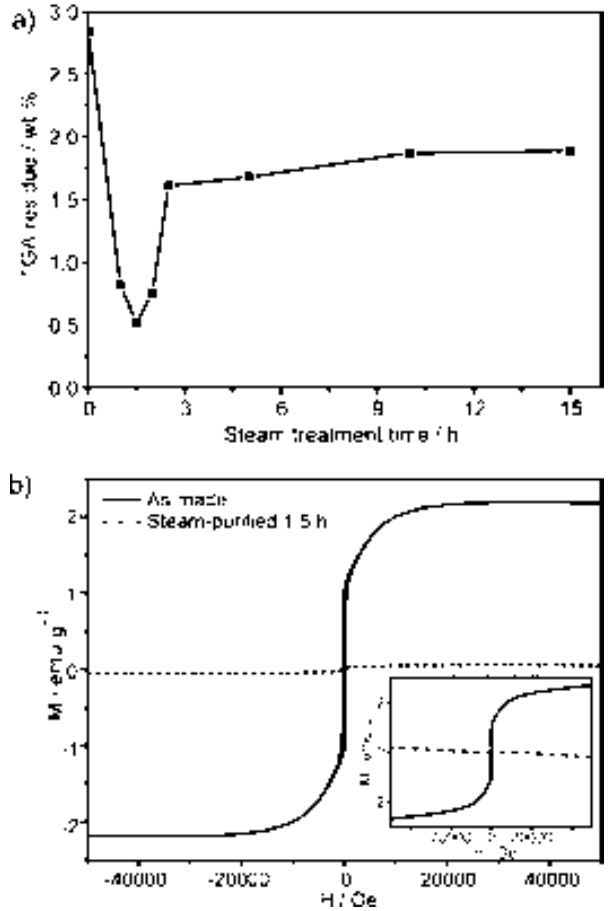

Figure 2. TGA and SQUID analysis of as-received and steam purified MWCNTs. a) Amount of residue present in the MWCNTs before (0 h) and after steam treatment (1 h up to 15 h) followed by an HCl wash, determined from TGA. b) Hysteresis loops at 10 K for as-made MWCNTs and 1.5 h steam and HCl purified MWCNTs, after linear substraction. Raw data are presented in the inset.

Table 1. Inorganic impurities present in as-received and steam treated samples (after HCl wash) as determined by SQUID (wt.% Fe) and TGA. The Al_2O_3 content has been calculated by subtraction of the wt.% of Fe_2O_3 (product of the oxidation of Fe during the TGA analysis) from the total TGA residue.

Sample	TGA residue (wt.%)	Fe (wt.%) SQUID	Al_2O_3 (wt.%)
as-made	2.84	0.99	1.42
1.5 h	0.52	0.022	0.48
10 h	1.87	0.007	1.86
15 h	1.89	0.013	1.87

Both the amount of inorganic particles and amorphous carbon present in the samples of CNTs can influence the onset of the combustion temperature observed by TGA. Samples with a higher amount of inorganic material, such as metal nanoparticles, start to oxidize at lower temperatures [49, 50]. The same trend is also observed when amorphous carbon is present because it is more easily oxidized than carbon nanotubes [51]. In agreement, the onset of combustion of all the purified samples is higher than that of raw material (Figure S2), showing the higher quality of the steam-treated nanotubes. For the ease of comparison, TGA data of the sample holding the lowest residual content (1.5 h steam) along with the data for the as-received material are shown in Figure 3. Whereas the as-received material presents an onset of combustion at 571 ºC, an increase of 63 ºC up to 634 ºC is observed for the purified material. A detailed analysis of the shape of the TGA curve via the 1st derivative (inset) indicates two distinctive peaks for the as-received material: the first one at about 608 ºC can be assigned to the combustion of amorphous carbon and the second one at about 642 ºC can be attributed to the oxidation of carbon nanotubes [51]. Accordingly, the 1st derivative of the steam purified sample presents a single peak indicating a higher homogeneity and the successful removal of the amorphous carbon during the steam treatment.

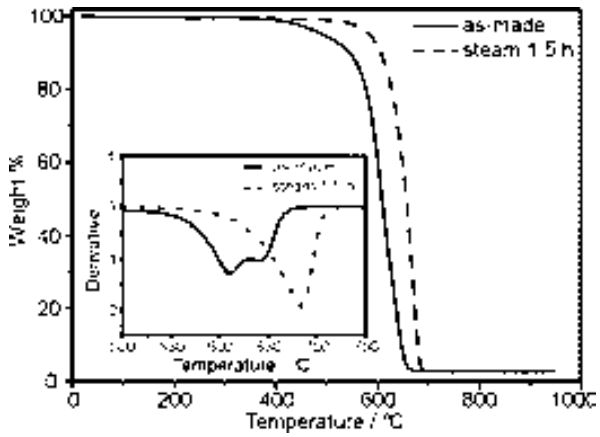

Figure 3. TGA curves in air and 1st derivative (inset) of as-received and 1.5 h steam and HCl purified MWCNTs.

In order to confirm that the steam purification was not sample dependent, CoMoCAT MWCNTs were steam treated for 1.5 h at 900 ºC, followed by an HCl wash. As it can be seen in Figure 4, the steam treated sample presents a higher onset of the combustion temperature compared to the as-received MWCNTs, indicating the removal of the amorphous carbon by the steam treatment. In agreement with the Fe grown MWCNTs, a decrease in the solid residue is also observed for the steam treated CoMoCAT MWCNTs, from 0.2 wt.% in the as-received material down to 0.004 wt.% for the steam purified sample. SQUID data also reveals a dramatic decrease in the content of magnetic catalytic particles in the sample, from a Ms of 0.54 emu·g_{sample}^{-1} in the non-treated sample down to a Ms of 0.017 emu·g_{sample}^{-1} for the purified MWCNTs.

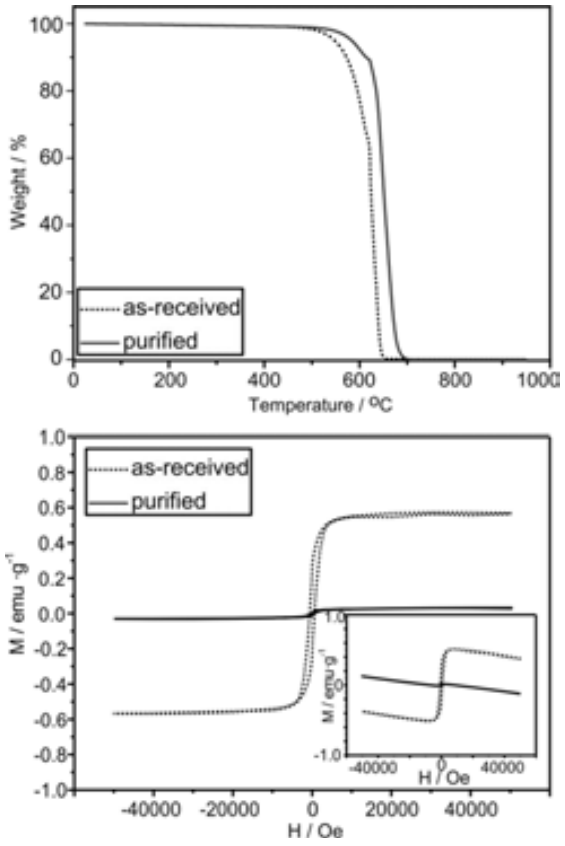

Figure 4. a) TGA curves in air and b) hysteresis loops at 10 K, of as-received and 1.5h steam and HCl purified CoMoCAT MWCNTs.

We next investigated the effect of the steam treatment time on the length distribution of the MWCNTs. We focused on the Fe-growth MWCNTs for this and subsequent studies. For comparison we analysed the as-received material, the sample presenting the lowest amount of solid residue (1.5 h steam), and three additional samples with longer steam treatments (5 h, 10 h and 15 h). Visual inspection of the low magnification transmission electron microscopy (TEM) images presented in Figure 5 reveals a marked decrease of the MWCNTs' length with increased steam treatment time. Note that images are presented at different scales to allow observing the entire MWCNTs and contain a large amount of nanotubes for ease of inspection. For each sample, the length of about 175 individual nanotubes was measured to quantitatively assess the decrease

(Figure S3), and the results are presented as histograms in the figure. Since the samples present a non-symmetric length distribution it is not possible to determine an average mean length and a box plot analysis was performed (Figure 6, Table S1). An initial inspection of the box plot indicates a similar degree of outliers/faroutliers in all the samples, indicating that all the samples present a small amount of nanotubes that have a much longer length than the majority of the nanotubes present in each of the samples. Both as-received (0 h treatment) and 1.5 h steam treated MWCNTs are statistically similar and therefore this treatment can be employed to purify the as-received material without a significant alteration on the length distribution of the sample. As-received MWCNTs contain a high fraction of long nanotubes, with 32.2 % above 2.5 μm and a median length of 1.9 μm. When steam purification is carried out for a prolonged time, not only the length of the resulting MWCNTs is extremely diminished but also a much narrower length distribution is observed. For instance after 10 h most of the nanotubes are shorter than 2.07 μm (maximum adjacent observation, Table S1) and a median length of 0.58 μm is achieved for MWCNT samples treated with steam for 15 h. Therefore the length of the MWCNTs can be easily modulated by applying a given steam treatment time.

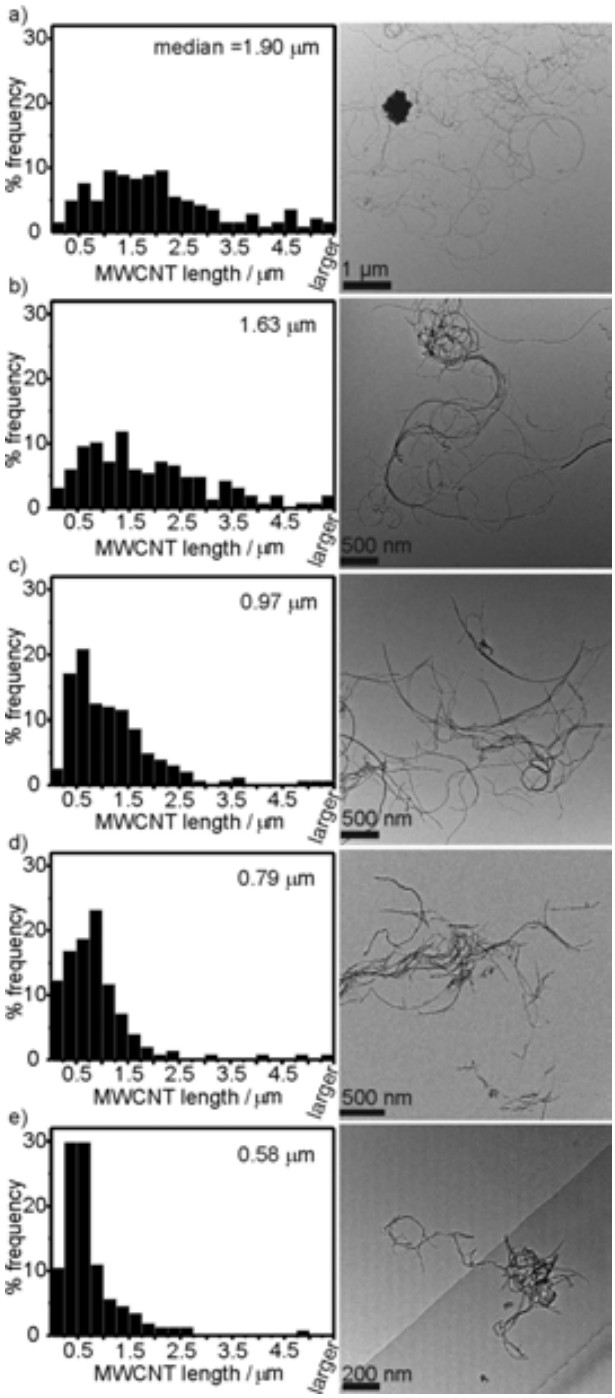

Figure 5. Low magnification TEM images and length distribution histograms of a) as-received MWCNTs, b) steam-treated MWCNTs for 1.5 h, c) 5 h, d) 10 h and e) 15h. All samples have

undergone an HCl wash. Note that image magnification is different for each image to make visible the whole MWCNTs.

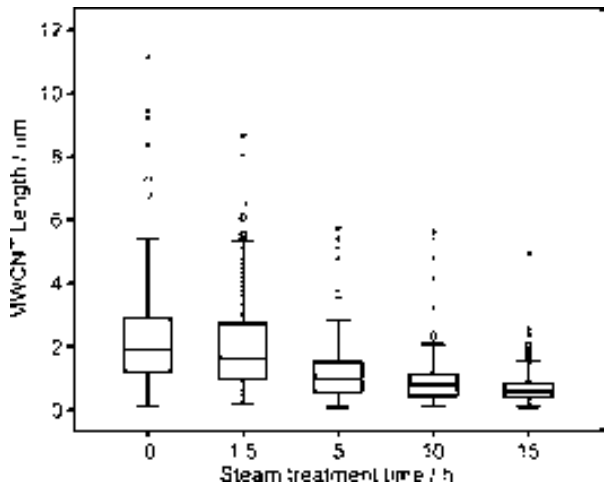

Figure 6. Box plot analysis of the as-received MWCNTs (0 h) and steam-treated MWCNTs for 1.5 h, 5 h, 10 h and 15h. All samples have undergone an HCl wash. Empty circles indicate outliers and asterisks faroutliers in the samples.

Most shortening and cutting strategies take place via a progressive introduction of defects/functionalities into the wall structure until a complete cutting is achieved [52, 53]. From the TGA curves of the steam treated samples it becomes clear that this is not the case for the steam shortened nanotubes. All the samples are completely stable under air until their complete combustion above 500 ºC (Figure S2). To determine the amount of functional groups, if any, on the samples we performed both elemental analysis and X-ray photoelectron spectroscopy (XPS). Any functionality derived from the steam treatment should contain hydrogen and/or oxygen as constituent elements. Elemental analysis gives information on the amount of C, N, H and S in the sample. Steam treated samples during 1.5 h and 15 h were measured after being treated in HCl (Table 2). From these analyses it can be seen that the quantity of hydrogen in the samples is negligible (<0.2 wt.%), indicating that no functional groups containing this element are present on

the MWCNTs. The threshold of <0.2 wt.% used for hydrogen quantification is the same than that of N and S which are certainly not expected in these samples. Next, XPS analysis was carried out to determine the presence/absence of oxygen in the steam treated samples. Integration of the high resolution spectra in the C1s and O1s regions (Figure S4) indicate similar levels of oxygen for as-received (1.3 % O/C) and steam treated samples for 1.5 h (1.0 % O/C) and 15 h (1.5 % O/C). It is therefore likely that such small levels of oxygen arise from the alumina impurities because the O/C ratio in the different samples follow the same trend than the alumina content as determined by TGA. Contribution from absorbed atmospheric species is also expected since the samples were exposed to atmospheric moisture and oxygen. Analysis of the C1s high resolution spectra allows the detection of different functional groups [54]. For instance, oxygen-bearing functionalities that could have been introduced during the treatment would be observed at binding energies below 290 eV. As it can be observed in Figure 7 there are no differences between the C1s peaks of as-made MWCNTs and the steam treated ones. Therefore, combining both XPS and elemental analysis we can conclude that no detectable functional groups are introduced in the MWCNT structure even after 15 h of steam exposure.

Table 2. Amount of carbon, hydrogen, nitrogen, and sulfur obtained by elemental analysis of steam-treated samples for 1.5 h and 15 h (after HCl wash).

	at.% C	at.% H	at.% N	at.% S
Steam 1.5 h	97.79	<0.2	<0.2	<0.2
Steam 15 h	95.4	<0.2	<0.2	<0.2

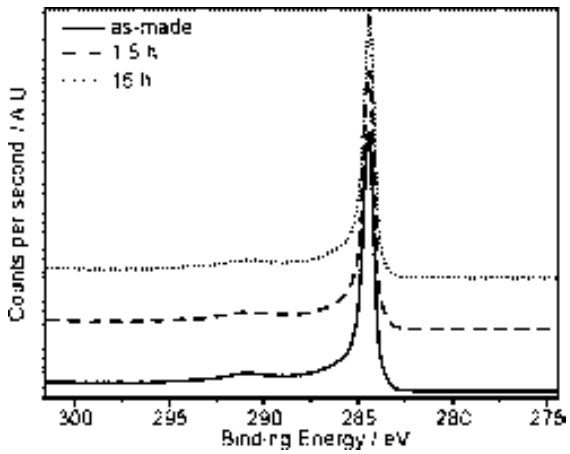

Figure 7. XPS spectra on the C 1s region of as-received MWCNTs and steam-purified MWCNTs during 1.5 h and 15 h. Spectra have been normalized for an ease of comparison.

Because no functionalities are detected either by XPS or by elemental analysis, we next performed Raman spectroscopy which provides information on the wall structure and purity of the MWCNTs. The two most prominent features in the Raman spectrum of MWCNTs are the G band arising at about 1575 cm^{-1}, which is related to well-ordered sp^2 graphite-type structures, and the D band centred at about 1341 cm^{-1}, which is commonly attributed to disordered sp^3-hybridized carbon material from defects and functionalities [55]. Beside those, in the Raman spectrum of MWCNTs it can be found a band at ~1620 cm^{-1} which appears as a shoulder on the G band and is denoted as D' band [56], a broad band at ~1200 cm^{-1} [57], and a band located between G and D band which is denoted as D" band [58]. Whereas the origin of D band can be attributed to both tube-related defects and amorphous carbon, D" band at ~1500 cm^{-1} originates only from the presence of amorphous carbon [58, 59]. Therefore, Choi et al. used intensity ratios of D" and G bands to estimate the purity of MWCNT samples [60]. It has been previously established that D" band has a Gaussian line shape [56, 58], in contrast to all the other aforementioned bands in Raman spectrum of MWCNT that have a Lorentzian line shape.

Figure 8 displays Raman spectra of all the steam treated samples along with the as-received

material. For the ease of inspection all the spectra are normalized to the G band intensity for both the green (514 nm; Fig. 6a) and red lasers (633 nm; Fig. 6b). Raman spectra measured with both laser for the as-received, 1.5 h and 15 h steam treated MWCNTs (followed by HCl wash) were fitted using four Lorentzian and one Gaussian component (Figure S5). The relative intensities of D and G bands are considered as probes of the CNT wall integrity and their degree of functionalization. The D/G intensity ratios derived from the fitted spectra are summarized in Figure 8c and Table S1. As expected, the D/G intensity ratio of a given sample is higher when measured at 633 nm than at 514 nm illustrating the dependence of this ratio on the laser excitation frequency [61]. An increase in the D/G intensity ratios can be observed for the steam treated samples which appears to be more pronounced at higher steam treatment times. As mentioned earlier, an increase in the D/G intensity ratios is typically attributed to disordered sp^3-hybridized carbon. From the analysis performed so far, it is clear that the functional groups present in the samples after the steam treatment are very limited. On the other hand, if side-wall defects were introduced onto the MWCNTs the reactivity of the resulting material with oxygen would be increased, and this is not the case according to TGA. Therefore, although side-wall defects cannot be discarded, it appears that the increase in the D/G intensity ratio is associated with the end-opening and shortening of the nanotubes. We advocate that MWCNTs oxidation takes place through the ends of the tubes, and, when opened, MWCNTs exhibit a higher amount of C sp^3. Moreover, this oxidation leads to a decrease of the CNT length during the treatment and an increase of the end-to-wall carbon ratio on the MWCNTs that gets reflected on the D-band. To estimate the content of amorphous carbon in our samples, the D"/G ratios are presented in Figure 8d and summarized in Table S2. As it can be seen, for both Raman lasers D"/G ratios decrease for the steam treated samples compared to the as-received material. The decrease is more prominent when using the 633 nm Raman laser. Therefore, analysis of the Raman data also allows us to confirm that steam decreases the amount of amorphous carbon present in samples of as-received MWCNT.

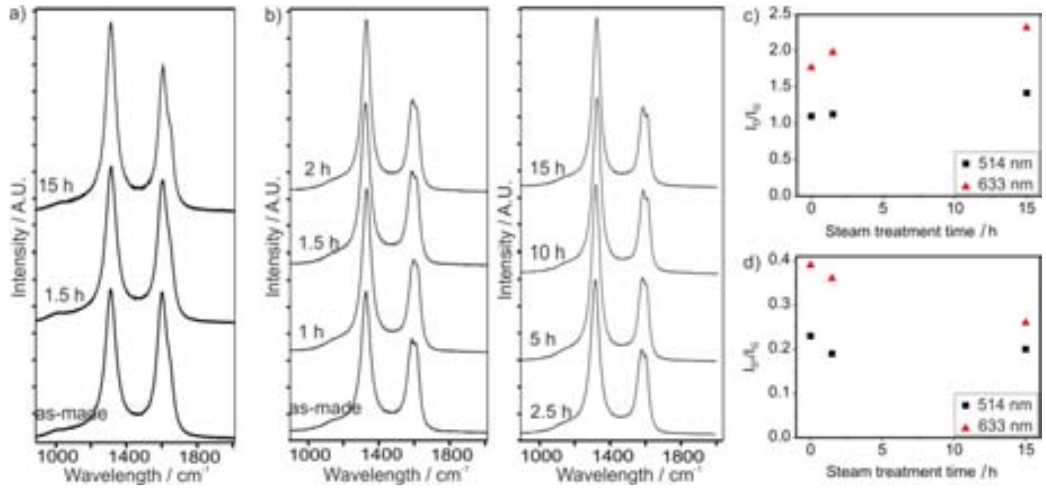

Figure 8. Raman spectra of as-made MWCNTs and steam-treated MWCNTs for different periods of time. a) Spectra obtained with green laser (514 nm). b) Spectra obtained with red laser (633 nm). c) Summary of the D/G band intensity ratio with respect of steam purification time for both lasers. d) Summary of the D''/G band intensity ratio with respect of steam purification time for both lasers.

To get further insight on this aspect, we analysed several individual MWCNTs by high resolution TEM (HRTEM) before and after a prolonged steam treatment. This technique allows the direct visualization of the carbon nanotube structure [62, 63] and provides information down to the atomic scale [64-66]. Figure 9 displays HRTEM images of a MWCNT from the as-received material where the walls are clearly visible, and a MWCNT after a prolonged steam treatment (10 h). Albeit it is a long treatment, the MWCNT structure has been well preserved. The walls have no apparent breaks and the tubular structure remains intact. From a qualitative point of view the steam-treated MWCNTs have comparable structural integrity compared to as-received CNTs, which also natively contain defects (additional images are included in Figure S6). Therefore HRTEM confirms that the amount of defects introduced during the steam purification is sensibly low and that the observed increase in the D/G intensity ratio by Raman spectroscopy is most likely related to the end-opening and shortening of the MWCNTs.

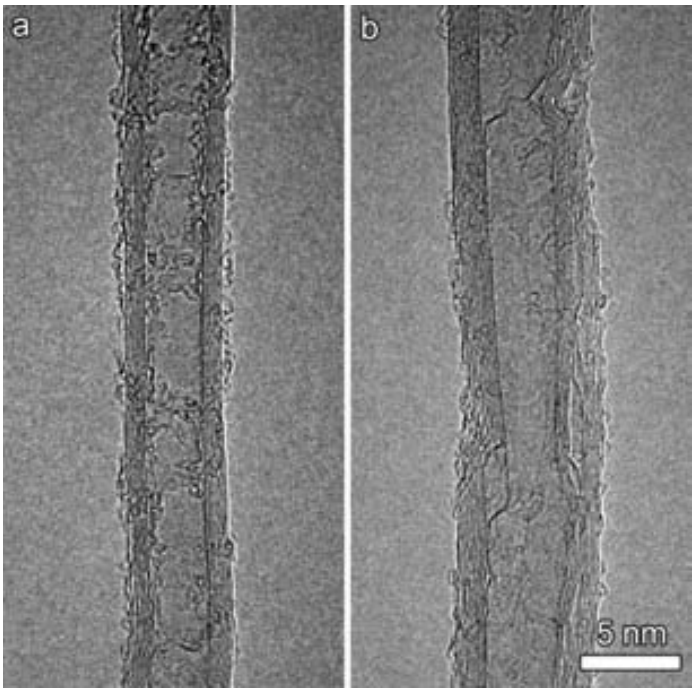

Figure 9. HRTEM images of a) as-received MWCNTs and b) Steam treated MWCNTs during 10 h.

4. Conclusions

We investigated the role that the steam treatment time plays on the purification, wall structure and length distribution of MWCNTs. Steam allows the removal of graphitic particles that sheath the metal catalysts (impurities from the CNTs' growth) and the amorphous carbon whilst reducing its impact on the wall structure of the MWCNTs. Oxygen- and hydrogen-bearing functionalities have not been detected on steam treated samples; neither by XPS nor by elemental analysis. Samples with a metal content below 0.01 wt% have been achieved by steam purification followed by an HCl wash. The steam purification treatment has been successfully achieved in both Fe-grown and CoMoCAT MWCNTs. Steam is a simple, economic, and environmentally friendly method that results in end-opened high-quality nanotubes, the length of which can be easily modulated by a mere change of the treatment time. Open-ended CNTs with a low degree of functionalities are of interest for subsequent filling experiments since functional groups at the tips have been shown to

block the entry ports of the nanochannels [67]. Therefore, steam further expands the toolbox of purification, end-opening and shortening strategies that allow the preparation of tailored MWCNT samples for selected applications.

Acknowledgements

The authors are grateful to Thomas Swan Co. & Ltd. for supplying the Elicarb® MWCNT samples. The research leading to these results has received funding from MINECO (MAT2011-24757) and the European Union Seventh Framework Programme under Grant Agreements 290023 - RADDEL (FP7-ITN) and 312483 - ESTEEM2 (Integrated Infrastructure Initiative-I3). L.C. acknowledges a JAE-Predoc fellowship (CSIC) and D.K. the financial support of the Ministry of Education, Science and Technological Development of Republic of Serbia for postdoctoral research. This work was performed in the frame of the Materials Science PhD program of the Universitat Autònoma de Barcelona (L.C.). The XPS data was acquired at the Laboratorio de Microscopías Avanzadas (LMA) - Instituto de Nanociencia de Aragón (INA), EA at the Centres Científics i Tecnològics - Universitat de Barcelona, and TGA of CoMoCAT MWCNTs at the Universitat d'Alacant, in Spain.

References

[1] Koyama S, Kim YA, Hayashi T, Takeuchi K, Fujii C, Kuroiwa N, et al. In vivo immunological toxicity in mice of carbon nanotubes with impurities. Carbon 2009;47(5):1365-72.
[2] Wörle-Knirsch JM, Pulskamp K, Krug HF. Oops They Did It Again! Carbon Nanotubes Hoax Scientists in Viability Assays. Nano Letters 2006;6(6):1261-8.
[3] Sharma H, Hussain S, Schlager J, Ali S, Sharma A. Influence of Nanoparticles on Blood–Brain Barrier Permeability and Brain Edema Formation in Rats. In: Czernicki Z, Baethmann A, Ito U, Katayama Y, Kuroiwa T, Mendelow D, eds. *Brain Edema XIV*: Springer Vienna 2010:359-64.
[4] Banks CE, Crossley A, Salter C, Wilkins SJ, Compton RG. Carbon Nanotubes Contain Metal Impurities Which Are Responsible for the "Electrocatalysis" Seen at Some Nanotube-Modified Electrodes. Angewandte Chemie International Edition 2006;45(16):2533-7.
[5] Henstridge MC, Shao L, Wildgoose GG, Compton RG, Tobias G, Green MLH. The Electrocatalytic Properties of Arc-MWCNTs and Associated 'Carbon Onions'. Electroanalysis 2008;20(5):498-506.
[6] Ambrosi A, Pumera M. Nanographite Impurities Dominate Electrochemistry of Carbon Nanotubes. Chemistry – A European Journal 2010;16(36):10946-9.
[7] Scott CL, Pumera M. Carbon nanotubes can exhibit negative effects in electroanalysis due to presence of nanographite impurities. Electrochemistry Communications 2011;13(5):426-8.
[8] An Z, Furmanchuk Ao, Ramachandramoorthy R, Filleter T, Roenbeck MR, Espinosa HD, et al. Inherent carbonaceous impurities on arc-discharge multiwalled carbon nanotubes and their implications for nanoscale interfaces. Carbon 2014;80(0):1-11.
[9] Shao L, Tobias G, Salzmann CG, Ballesteros B, Hong SY, Crossley A, et al. Removal of amorphous carbon for the efficient sidewall functionalisation of single-walled carbon nanotubes. Chemical Communications 2007;(47):5090-2.
[10] Ko FH, Lee CY, Ko CJ, Chu TC. Purification of multi-walled carbon nanotubes through microwave heating of nitric acid in a closed vessel. Carbon 2005;43(4):727-33.
[11] Chen XH, Chen CS, Chen Q, Cheng FQ, Zhang G, Chen ZZ. Non-destructive purification of multi-walled carbon nanotubes produced by catalyzed CVD. Materials Letters 2002;57(3):734-8.
[12] Feng Y, Zhang H, Hou Y, McNicholas TP, Yuan D, Yang S, et al. Room temperature purification of few-walled carbon nanotubes with high yield. ACS Nano 2008;2(8):1634-8.
[13] Yuan JM, Chen XH, Fan ZF, Yang XG, Chen ZH. An easy method for purifying multi-walled carbon nanotubes by chlorine oxidation. Carbon 2008;46(9):1266-9.
[14] Ming J, Wu Y, Yu Y, Zhao F. Steaming multiwalled carbon nanotubesvia acid vapour for controllable nanoengineering and the fabrication of carbon nanoflutes. Chemical Communications 2011;47(18):5223-5.
[15] Suri A, Coleman KS. The superiority of air oxidation over liquid-phase oxidative treatment in the purification of carbon nanotubes. Carbon 2011;49(9):3031-8.
[16] Ebbesen TW, Ajayan PM, Hiura H, Tanigaki K. Purification of nanotubes. Nature 1994;367(6463):519-.
[17] Tobias G, Shao L, Salzmann CG, Huh Y, Green MLH. Purification and Opening of Carbon Nanotubes Using Steam. The Journal of Physical Chemistry B 2006;110(45):22318-22.
[18] Babu DJ, Yadav S, Heinlein T, Cherkashinin G, Schneider JJ. Carbon Dioxide Plasma as a Versatile Medium for Purification and Functionalization of Vertically Aligned Carbon Nanotubes. The Journal of Physical Chemistry C 2014;118(22):12028-34.
[19] Chng ELK, Poh HL, Sofer Z, Pumera M. Purification of carbon nanotubes by high temperature chlorine gas treatment. Physical Chemistry Chemical Physics 2013;15(15):5615-9.
[20] Vivekchand SRC, Govindaraj A, Seikh MM, Rao CNR. New Method of Purification of Carbon Nanotubes Based on Hydrogen Treatment. The Journal of Physical Chemistry B 2004;108(22):6935-7.

[21] Meyer-Plath A, Orts-Gil G, Petrov S, Oleszak F, Maneck H-E, Dörfel I, et al. Plasma-thermal purification and annealing of carbon nanotubes. Carbon 2012;50(10):3934-42.
[22] Wiltshire JG, Khlobystov AN, Li LJ, Lyapin SG, Briggs GAD, Nicholas RJ. Comparative studies on acid and thermal based selective purification of HiPCO produced single-walled carbon nanotubes. Chemical Physics Letters 2004;386(4–6):239-43.
[23] Ballesteros B, Tobias G, Shao L, Pellicer E, Nogués J, Mendoza E, et al. Steam Purification for the Removal of Graphitic Shells Coating Catalytic Particles and the Shortening of Single-Walled Carbon Nanotubes. Small 2008;4(9):1501-6.
[24] Guo W, Dou Z, Li H, Shi Z, Sun H, Liu Y. An efficient strategy for the purification of cloth-like single walled carbon nanotube soot produced by arc discharge. Carbon 2010;48(13):3769-77.
[25] Xia W, Hagen V, Kundu S, Wang Y, Somsen C, Eggeler G, et al. Controlled Etching of Carbon Nanotubes by Iron-Catalyzed Steam Gasification. Advanced Materials 2007;19(21):3648-52.
[26] Ponrouch A, Palacín MR. Optimisation of performance through electrode formulation in conversion materials for lithium ion batteries: Co3O4 as a case example. Journal of Power Sources 2012;212(0):233-46.
[27] Mendoza-Sánchez B, Rasche B, Nicolosi V, Grant PS. Scaleable ultra-thin and high power density graphene electrochemical capacitor electrodes manufactured by aqueous exfoliation and spray deposition. Carbon 2013;52(0):337-46.
[28] Huang C, Grobert N, Watt AAR, Johnston C, Crossley A, Young NP, et al. Layer-by-layer spray deposition and unzipping of single-wall carbon nanotube-based thin film electrodes for electrochemical capacitors. Carbon 2013;61(0):525-36.
[29] Chu BTT, Tobias G, Salzmann CG, Ballesteros B, Grobert N, Todd RI, et al. Fabrication of carbon-nanotube-reinforced glass-ceramic nanocomposites by ultrasonic in situ sol-gel processing. Journal of Materials Chemistry 2008;18(44):5344-9.
[30] Cabana L, Ballesteros B, Batista E, Magén C, Arenal R, Oró-Solé J, et al. Synthesis of PbI_2 Single-Layered Inorganic Nanotubes Encapsulated Within Carbon Nanotubes. Advanced Materials 2014;26(13):2016-21.
[31] Pascu SI, Arrowsmith RL, Bayly SR, Brayshaw S, Hu Z. Towards nanomedicines: design protocols to assemble, visualize and test carbon nanotube probes for multi-modality biomedical imaging. Philosophical Transactions of the Royal Society A: Mathematical, Physical and Engineering Sciences 2010;368(1924):3683-712.
[32] Wang JT-W, Cabana L, Bourgognon M, Kafa H, Protti A, Venner K, et al. Magnetically Decorated Multiwalled Carbon Nanotubes as Dual MRI and SPECT Contrast Agents. Advanced Functional Materials 2014;24(13):1880-94.
[33] Heister E, Brunner EW, Dieckmann GR, Jurewicz I, Dalton AB. Are Carbon Nanotubes a Natural Solution? Applications in Biology and Medicine. ACS Applied Materials & Interfaces 2013;5(6):1870-91.
[34] Tobias G, Martincic M. Filled carbon nanotubes in biomedical imaging and drug delivery. Expert Opinion on Drug Delivery 2015;12:563-81.
[35] Zhang X, Jiao K, Wang X. Paste Electrode Based on Short Single-Walled Carbon Nanotubes and Room Temperature Ionic Liquid: Preparation, Characterization and Application in DNA Detection. Electroanalysis 2008;20(12):1361-6.
[36] Fonseca A, Reijerkerk S, Potreck J, Nijmeijer K, Mekhalif Z, Delhalle J. Very short functionalized carbon nanotubes for membrane applications. Desalination 2010;250(3):1150-4.
[37] Wang X, Wang J, Chang H, Zhang Y. Preparation of Short Carbon Nanotubes and Application as an Electrode Material in Li-Ion Batteries. Advanced Functional Materials 2007;17(17):3613-8.
[38] Kim YA, Hayashi T, Fukai Y, Endo M, Yanagisawa T, Dresselhaus MS. Effect of ball milling on morphology of cup-stacked carbon nanotubes. Chemical Physics Letters 2002;355(3–4):279-84.

[39] Lustig SR, Boyes ED, French RH, Gierke TD, Harmer MA, Hietpas PB, et al. Lithographically Cut Single-Walled Carbon Nanotubes: Controlling Length Distribution and Introducing End-Group Functionality. Nano Letters 2003;3(8):1007-12.
[40] Gu Z, Peng H, Hauge RH, Smalley RE, Margrave JL. Cutting Single-Wall Carbon Nanotubes through Fluorination. Nano Letters 2002;2(9):1009-13.
[41] Marega R, Accorsi G, Meneghetti M, Parisini A, Prato M, Bonifazi D. Cap removal and shortening of double-walled and very-thin multi-walled carbon nanotubes under mild oxidative conditions. Carbon 2009;47(3):675-82.
[42] Hata K, Futaba DN, Mizuno K, Namai T, Yumura M, Iijima S. Water-Assisted Highly Efficient Synthesis of Impurity-Free Single-Walled Carbon Nanotubes. Science 2004;306(5700):1362-4.
[43] Yamada T, Maigne A, Yudasaka M, Mizuno K, Futaba DN, Yumura M, et al. Revealing the Secret of Water-Assisted Carbon Nanotube Synthesis by Microscopic Observation of the Interaction of Water on the Catalysts. Nano Letters 2008;8(12):4288-92.
[44] Amama PB, Pint CL, McJilton L, Kim SM, Stach EA, Murray PT, et al. Role of water in super growth of single-walled carbon nanotube carpets. Nano Letters 2009;9(1):44-9.
[45] Kolodiazhnyi T, Pumera M. Towards an Ultrasensitive Method for the Determination of Metal Impurities in Carbon Nanotubes. Small 2008;4(9):1476-84.
[46] Cornell R, Schwertmann U. The Iron Oxides: Structure, Properties, Reactions, Occurences and Uses: Wiley-VCH 2004.
[47] Xavier B, Amílcar L. Finite-size effects in fine particles: magnetic and transport properties. Journal of Physics D: Applied Physics 2002;35(6):R15.
[48] Pumera M. Carbon Nanotubes Contain Residual Metal Catalyst Nanoparticles even after Washing with Nitric Acid at Elevated Temperature Because These Metal Nanoparticles Are Sheathed by Several Graphene Sheets. Langmuir 2007;23(11):6453-8.
[49] Chiang IW, Brinson BE, Smalley RE, Margrave JL, Hauge RH. Purification and Characterization of Single-Wall Carbon Nanotubes. The Journal of Physical Chemistry B 2001;105(6):1157-61.
[50] Ballesteros B, Tobias G, Ward MAH, Green MLH. Quantitative Assessment of the Amount of Material Encapsulated in Filled Carbon Nanotubes. The Journal of Physical Chemistry C 2009;113(7):2653-6.
[51] Brukh R, Mitra S. Kinetics of carbon nanotube oxidation. Journal of Materials Chemistry 2007;17(7):619-23.
[52] Shuba MV, Paddubskaya AG, Kuzhir PP, Maksimenko SA, Ksenevich VK, Niaura G, et al. Soft cutting of single-wall carbon nanotubes by low temperature ultrasonication in a mixture of sulfuric and nitric acids. Nanotechnology 2012;23(49):495714.
[53] Rubio N, Fabbro C, Herrero MA, de la Hoz A, Meneghetti M, Fierro JLG, et al. Ball-Milling Modification of Single-Walled Carbon Nanotubes: Purification, Cutting, and Functionalization. Small 2011;7(5):665-74.
[54] T.I.T. Okpalugo, P. Papakonstantinou, H. Murphy, J. McLaughlin, Brown NMD. High resolution XPS characterization of chemical functionalised MWCNTs and SWCNTs. Carbon 2005;43:153-61.
[55] Kim UJ, Furtado CA, Liu X, Chen G, Eklund PC. Raman and IR Spectroscopy of Chemically Processed Single-Walled Carbon Nanotubes. Journal of the American Chemical Society 2005;127(44):15437-45.
[56] Sadezky A, Muckenhuber H, Grothe H, Niessner R, Pöschl U. Raman microspectroscopy of soot and related carbonaceous materials: Spectral analysis and structural information. Carbon 2005;43(8):1731-42.
[57] Schwan J, Ulrich S, Batori V, Ehrhardt H, Silva SRP. Raman spectroscopy on amorphous carbon films. Journal of Applied Physics 1996;80(1):440-7.
[58] Jawhari T, Roid A, Casado J. Raman spectroscopic characterization of some commercially available carbon black materials. Carbon 1995;33(11):1561-5.

[59] Cuesta A, Dhamelincourt P, Laureyns J, Martínez-Alonso A, Tascón JMD. Raman microprobe studies on carbon materials. Carbon 1994;32(8):1523-32.
[60] Choi YC, Min K-I, Jeong MS. Novel Method of Evaluating the Purity of Multiwall Carbon Nanotubes Using Raman Spectroscopy. Journal of Nanomaterials 2013;2013:6.
[61] Brown SDM, Jorio A, Dresselhaus MS, Dresselhaus G. Observations of the D-band feature in the Raman spectra of carbon nanotubes. Physical Review B 2001;64(7):073403.
[62] Suarez-Martinez I, Ewels CP, Ke X, Van Tendeloo G, Thiess S, Drube W, et al. Study of the Interface between Rhodium and Carbon Nanotubes. ACS Nano 2010;4(3):1680-6.
[63] Felten A, Gillon X, Gulas M, Pireaux J-J, Ke X, Van Tendeloo G, et al. Measuring Point Defect Density in Individual Carbon Nanotubes Using Polarization-Dependent X-ray Microscopy. ACS Nano 2010;4(8):4431-6.
[64] Börrnert F, Gorantla S, Bachmatiuk A, Warner JH, Ibrahim I, Thomas J, et al. In situ observations of self-repairing single-walled carbon nanotubes. Physical Review B 2010;81(20):201401.
[65] Allen CS, Robertson AW, Kirkland AI, Warner JH. The Identification of Inner Tube Defects in Double-Wall Carbon Nanotubes. Small 2012;8(24):3810-5.
[66] Hong SY, Tobias G, Ballesteros B, El Oualid F, Errey JC, Doores KJ, et al. Atomic-Scale Detection of Organic Molecules Coupled to Single-Walled Carbon Nanotubes. Journal of the American Chemical Society 2007;129(36):10966-7.
[67] Kuznetsova A, Mawhinney DB, Naumenko V, Yates Jr JT, Liu J, Smalley RE. Enhancement of adsorption inside of single-walled nanotubes: opening the entry ports. Chemical Physics Letters 2000;321(3–4):292-6.

- SUPPLEMENTARY MATERIAL -

The role of steam treatment on the structure, purity and length distribution of multi-walled carbon nanotubes

Laura Cabana[1], Xiaoxing Ke[2], Dejan Kepić[1,3], Judith Oro-Solé[1], Ester Tobías-Rossell[4], Gustaaf Van Tendeloo[2], Gerard Tobias[1*]

[1]*Institut de Ciència de Materials de Barcelona (ICMAB-CSIC), Campus UAB, 08193 Bellaterra, Barcelona, Spain.*

[2]*Electron Microscopy for Materials Science (EMAT), University of Antwerp, Groenenborgerlaan 171, B-2020, Antwerp, Belgium.*

[3]*Vinča Institute of Nuclear Sciences, University of Belgrade, Mike Alasa 12-14, Belgrade, Serbia*

[4]*Escola Universitària de Ciències de la Salut de Manresa, Universitat de Vic-Universitat Central de Catalunya, Av. Universitària 4-6, 08242 Manresa, Barcelona, Spain*

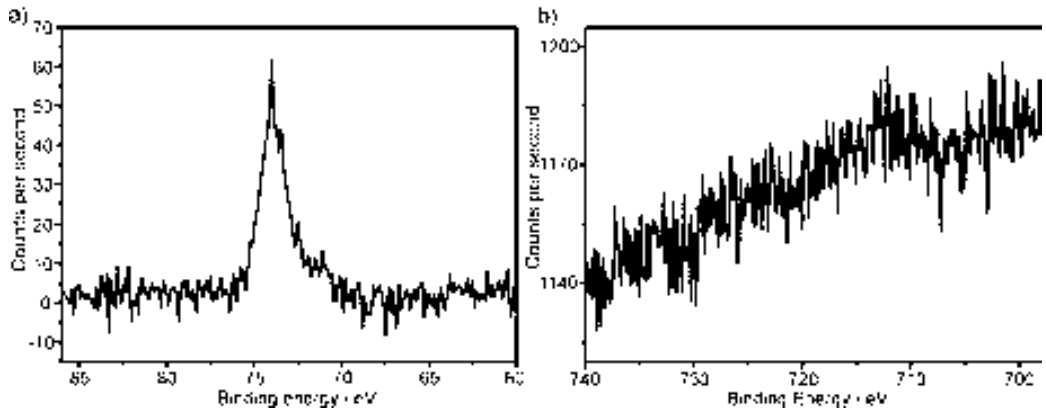

Figure S1. XPS spectra on the a) Al 2p region and b) Fe 2p region of steam-treated MWCNTs during 10 h followed by an HCl wash.

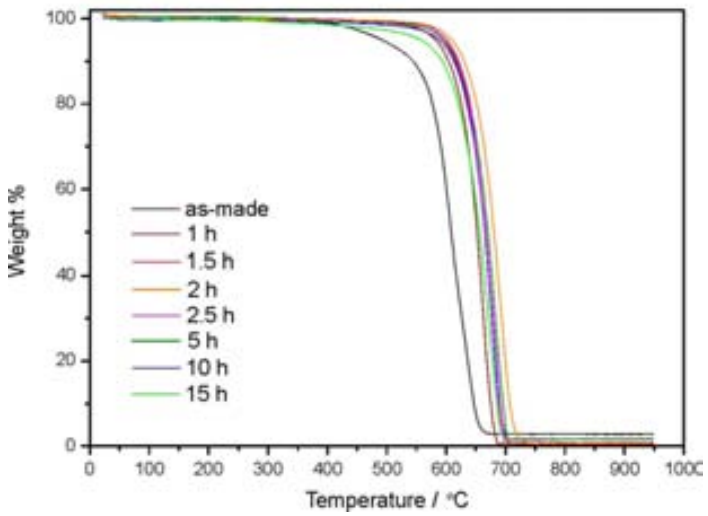

Figure S2. TGA in air of as-received MWCNTs and steam-purified MWCNTs from 1.5 h up to 15 h (after HCl wash).

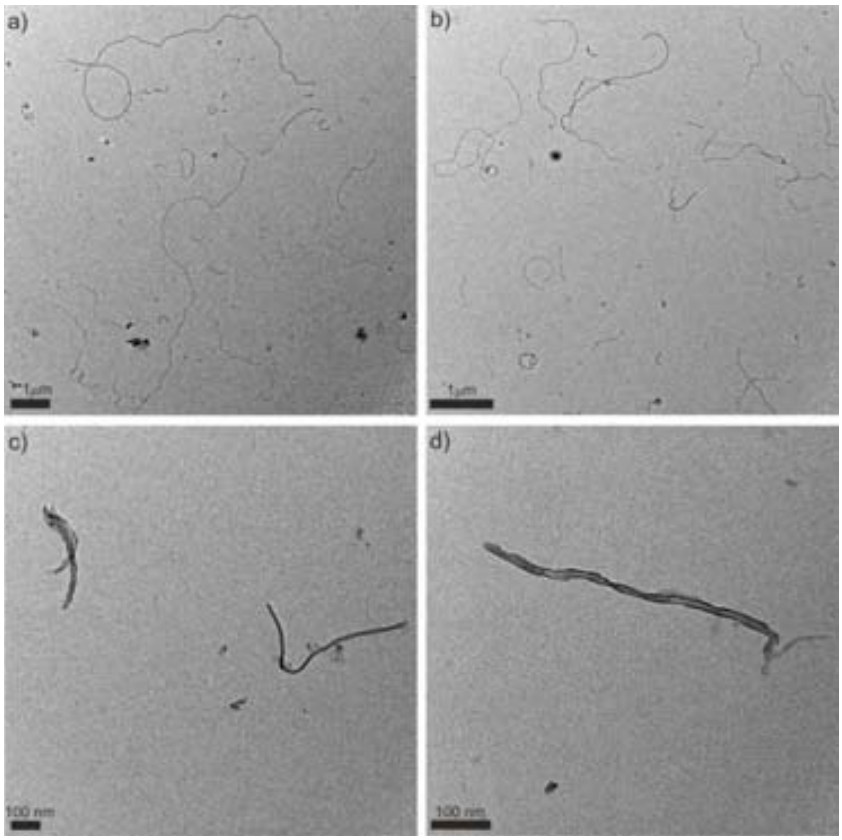

Figure S3. Low resolution TEM images of a,b) as-received MWCNTs and c,d) steam-purified MWCNTs for 15 h.

Table S1 . Descriptive analysis of the length distribution for as-received MWCNTs (0 h) and steam-treated MWCNTs for 1.5 h, 5 h, 10 h and 15h. All samples have undergone an HCl wash.

Sample	N	Median	Lower adjacent observation	Q1 25^{th} percentile	Q3 25^{th} percentile	Maximum adjacent observation	Maximum observation
As-received	149	1.90	0.10	1.20	2.88	5.39	11.13
1.5 h	173	1.63	0.17	0.95	2.72	5.34	8.66
5 h	214	0.97	0.08	0.55	1.51	2.82	5.72
10 h	156	0.79	0.09	0.42	1.11	2.07	5.62
15 h	183	0.58	0.09	0.37	0.85	1.53	4.93

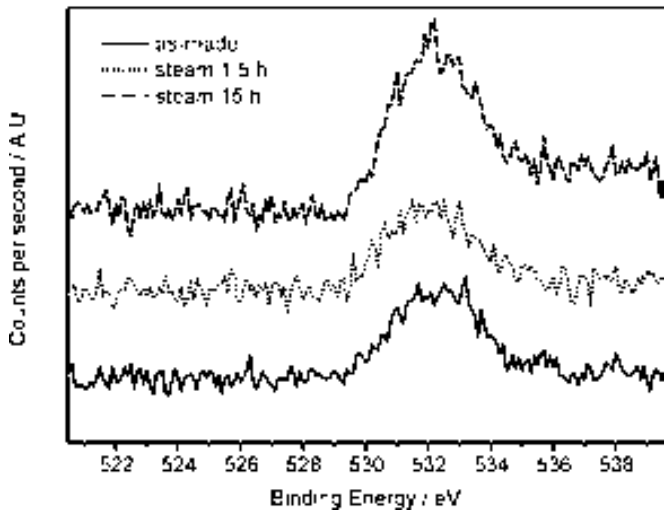

Figure S4. XPS spectra on the O 1s region of as-received MWCNTs and steam-purified MWCNTs during 1.5 h and 15 h.

Sample	514 nm		633 nm	
	D"/G	D/G	D"/G	D/G
As-received	0.23±0.03	1.10±0.06	0.39±0.02	1.77±0.04
Steam purified (1.5 h)	0.19±0.02	1.13±0.05	0.36±0.03	1.98±0.03
Steam purified (15 h)	0.20±0.03	1.42±0.10	0.26±0.01	2.32±0.11

Table S2. Summary of D"/G and D/G intensity ratios with respect of steam purification time for both lasers. Fitted spectra are presented in Figure S5.

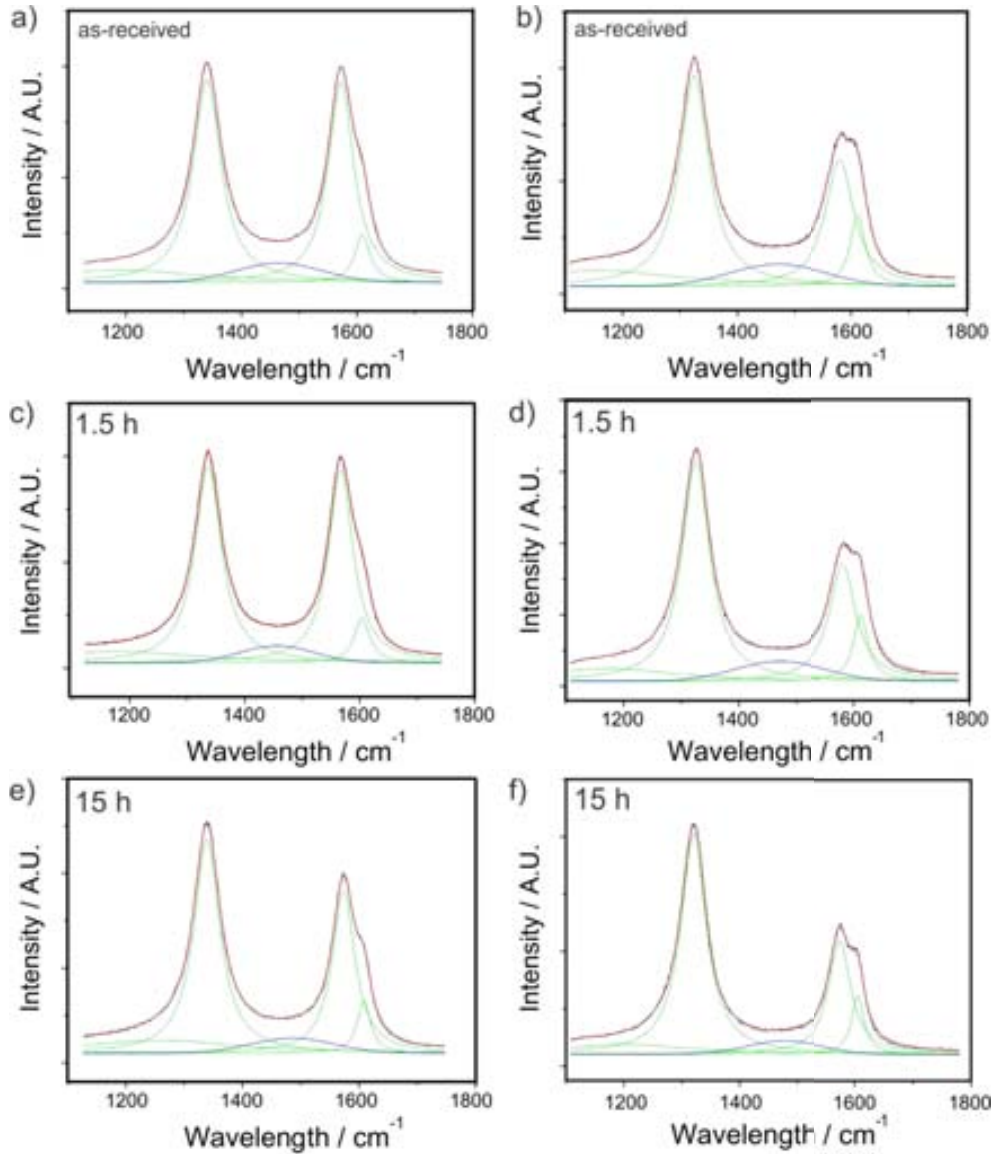

Figure S5. Fitted Raman spectra of as-received MWCNTs and MWCNTs subjected to steam purification for 1.5 and 15 h. Spectra are measured using 514 nm (a, c, e) and 633 nm (b, d, f) Raman laser and normalized to the G band intensity. Black line represents original curve, red line resulting fitted curve, green lines Lorentzian components and blue line Gaussian component.

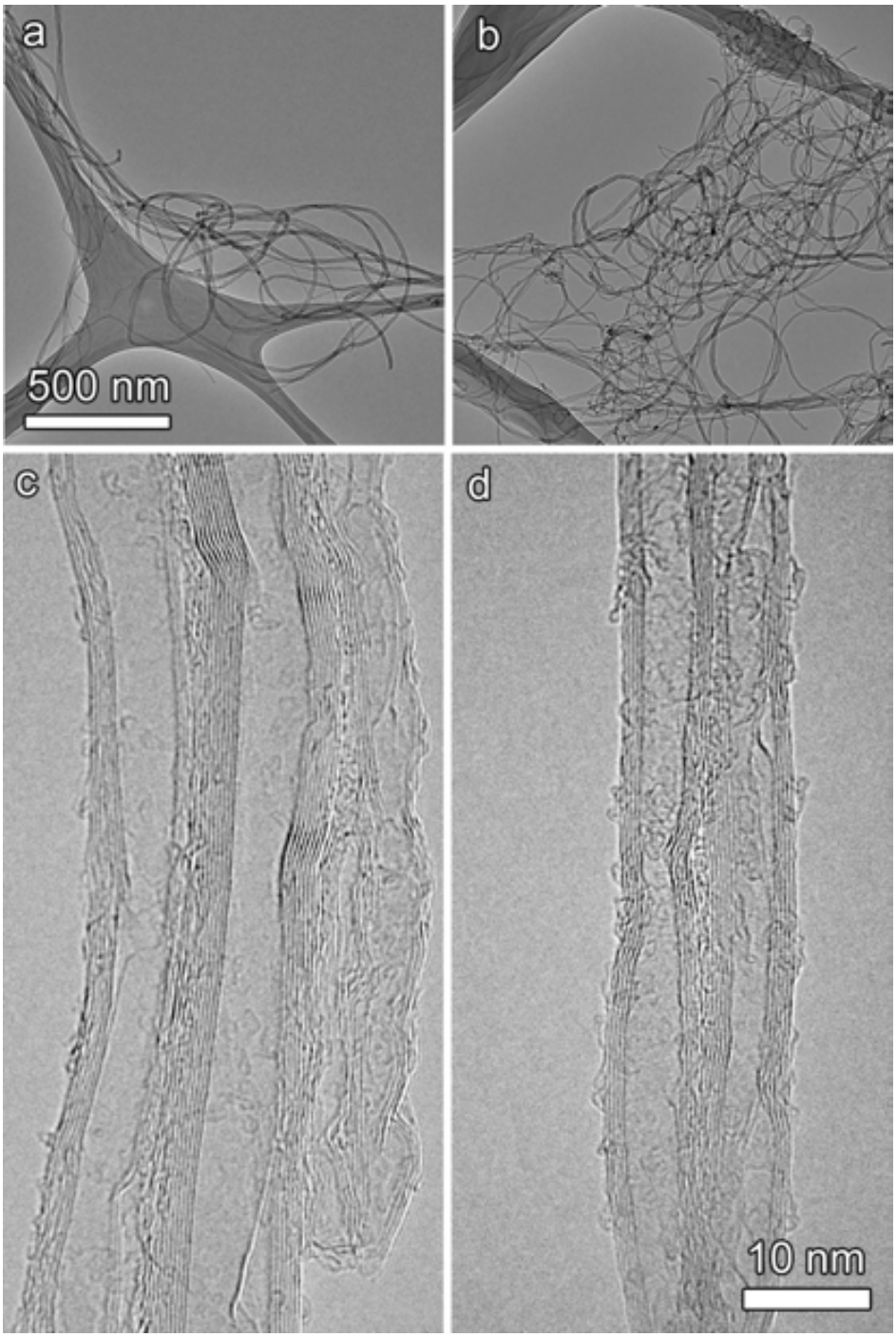

Figure S6. Low resolution TEM images at the same magnification of a) as-received MWCNTs and b) steam-treated MWCNTs (10 h). High resolution TEM images at the same magnification of c) as-received MWCNTs and d) steam-treated MWCNTs (10 h).

DOI: 10.1002/ ((please add manuscript number))
Full Paper

The Shortening of MWNT-SPION Hybrids by Steam Treatment Improves their Magnetic Resonance Imaging Properties *In vitro* and *In Vivo*

Laura Cabana‡, Maxime Bourgognon‡, Julie T-W. Wang, Andrea Protti, Rafael T. M. de Rosales, Ajay M. Shah, Josep Fontcuberta, Ester Tobías-Rossell, Jane K. Sosabowski, Khuloud T. Al-Jamal* and Gerard Tobias*

L. Cabana, Prof. J. Fontcuberta, Dr. G. Tobias
Institut de Ciència de Materials de Barcelona (ICMAB-CSIC)
Campus UAB, 08193 Bellaterra, Barcelona, Spain
E-mail: **gerard.tobias@icmab.es**

M. Bourgognon, Dr. J. T-W. Wang, Dr. K. T. Al-Jamal
Institute of Pharmaceutical Science
King's College London
London, SE1 9NH, UK
E-mail: **khuloud.al-jamal@kcl.ac.uk**

Dr. A. Protti, Dr. R. T. M. de Rosales
Division of Imaging Sciences and Biomedical Engineering
King's College London
St. Thomas' Hospital, London, SE1 7EH, UK

Prof. A. M. Shah, Dr. A. Protti
Cardiovascular Division, James Black Centre
British Heart Foundation Centre of Excellence, King's College London
London, SE5 9NU, UK

E. Tobías-Rossell
Escola Universitària de Ciències de la Salut de Manresa
Universitat de Vic-Universitat Central de Catalunya
Av. Universitària 4-6, 08242 Manresa, Barcelona, Spain

Dr. J. K. Sosabowski
Centre for Molecular Oncology
Barts Cancer Institute
Queen Mary University of London
London, EC1A 7BE, UK

Keywords: carbon nanotubes, MRI, shortening, SPECT, dual-imaging

1. Introduction

Carbon nanotubes (CNTs) are being widely investigated for a diverse array of biomedical applications.[1] Their high surface area, nanoscopic dimensions with a hollow core, excellent mechanical properties and good electrical conductivity make them appealing for diversified biological purposes. These include tissue scaffolds, bone prosthetics, neural interfaces, cellular growth, stem cell differentiation, biosensors, drug delivery and biomedical imaging.[1,2] Both drug delivery and imaging take advantage of the needle-like shape of the CNTs which confers these materials with superior flow dynamics and an enhanced capacity to penetrate cellular membranes compared to spherical nanoparticles. CNTs are flexible structures and as such can bend and allow the interaction with cells through multiple binding sites.[2]

As a consequence of its use for biomedical applications, a lot of concern has raised on their potential cytotoxicity. As-produced CNTs contain several impurities, namely amorphous, graphitic nanoparticles and metal particles (from the catalysts employed in the CNT's growth). Early pharmacological studies reported on the cytoxicity of as-prepared CNTs, but it was later shown that the observed toxicity was likely to be due to the presence of metal nanoparticles or from long nanotubes (> 15 μm). The effect of as-prepared CNTs on human epidermal keratinocytes cells was investigated back in 2003,[3] showing the presence of free radicals and peroxidative products. As these nanotubes contained iron and nickel catalyst in a high dose, the oxidative stress and loss of cell viability was imminent.[4] The presence of impurities is not the unique source of potential cytotoxicity, since long CNTs could induce acute and chronic peritoneal inflammation in mice.[5-7] Other studies suggest that if the length of the CNTs is superior to the size of a phagocytic cell these nanosystems can induce an inflammatory response.[8] It has also been reported that long fibers cannot be completely engulf by macrophages leading to an incomplete internalisation of the CNTs, and consequently this could impair the plasma membrane.[9] Hence, despite pharmacological studies are continuously in progress, there is a

general consensus within the scientific community that CNTs hold great potential in biomedical imaging provided they have been properly purified, shortened and dispersed either via covalent or non-covalent strategies; thus rendering a biocompatible nanoplatform.[10-13]

Apart from affecting the biocompatibility, the length of the CNTs has been shown to have a major impact on key pharmacological aspects including cell internalization, in-vivo biodistribution and pharmacokinetic profile. By exposing cells to multi-walled CNTs (MWNTs) of different lengths, it was shown by Bussy et al. that the percentage of cells containing MWNTs was significantly higher for short CNTs, meaning that these are more easily internalized by the cells.[8] Moreover, it has also been reported that short CNTs are less accumulated in the tissues and undergo a faster renal excretion than their long counterparts.[14-16]

Several strategies have been developed to purify and shorten CNTs to efficiently obtain biocompatible CNTs including treatment with oxidizing acids, fluorination and steam. Steam has been proposed as a method to remove the impurities present during the CNT growth whilst reducing the impact on the wall structure of the CNTs.[17] In addition, the length of the nanotubes can be easily modulated by a mere change in the steam exposure time.[18]

A commonly employed approach towards the development of diagnostic agents for biomedical imaging consists on the formation of hybrid nanostructures. One can take advantage of the hollow cavity of CNTs, susceptible of being filled with a wide variety of materials,[19-22] to encapsulate to chosen imaging agent.[23-26] In this way the external walls remain available for the attachment of dispersing and targeting moieties. The second strategy consists on the external decoration with inorganic nanoparticles or molecular tags.[27-29] Following the latter, CNT-based imaging agents have been developed aiming to improve the sensitivity and contrast of clinically relevant modalities including nuclear imaging (single photon emission computed tomography (SPECT) and positron emission tomography (PET)) and magnetic resonance imaging (MRI). Nuclear medicine has marked advantages over other modalities for both diagnosis (imaging) and therapy.

In terms of imaging, nuclear medicine records radiation emitted from a radiopharmaceutical within the body (inside-out) rather than radiation that is generated by external sources and crosses the body (like X-rays). In terms of therapy, the use of radiopharmaceuticals allows a shorter treatment, with a lower dosage and frequency, and with less side-effects than pharmaceutical drugs. In this line, several radiolabelled-CNTs have been developed by chelation of chosen radionuclides to the external CNT walls for both diagnosis and therapeutic pourposes.[28-30] On the other hand, MRI does not use any ionizing radiation and is experiencing a sustained increase in demand with over 25.000 scanners in use worldwide.[31] Inherent MRI contrast is a function of proton density, relaxation times, and magnetic susceptibility. Since it is rather difficult to alter the water content of tissues many diagnostic questions require the use of external contrast agents (CAs). Contrast agents based on gadolinium and iron have been the main focus of attention. Positive contrast agents based on gadolinium-loaded CNTs have shown promising results up to the pre-clinical level.[26,32] Several studies have reported the preparation and use of superparamagnetic iron oxide nanoparticles (SPION) attached to CNTs for biomedical imaging applications.[27] These behave as negative contrast agents, increasing the R_2 and R_2^* relaxation rates. Choi et al. prepared Fe catalyst-grown SWNT (length not reported) and confirmed the formation of paramagnetic iron oxide at the tip of CNTs. Phagocytic cells incubated with Fe catalyst-grown SWNTs were then imaged by MRI and near-infrared fluorescence.[33] Yin et al. conjugated SPION (7-8 nm in diameter) to MWNTs (100-300 nm length) and actively targeted the hybrids to cancer cells using folic acid.[34] After incubation with cells over-expressing folate receptor (HeLa cells), the targeted magnetic hybrid increased the in vitro R_2 relaxation rate of incubated cells. Wu et al. loaded Fe_3O_4 nanoparticles (average size of 4.5 nm) to the surface of MWNTs (0.5-2 μm length) and showed an MR signal enhancement in liver and spleen after intravenous injection of the hybrid, highlighting the accumulation of such hybrid into the reticular endothelial system (RES).[35] Recently, Liu et al. conjugated SPION (diameter of 9 nm) to MWNTs

(length not reported) by electrostatic interaction, which were injected intravenously into mice bearing liver metastases.[36] Increases in liver tumor contrast ratio between tumor and healthy tissue region facilitated the diagnosis of liver metastases. To further expand the capabilities of CNTs contrast agents, we have recently shown that CNTs can serve as a nanoplatform to combine both imaging modalities (SPECT/CT and MRI) thus affording dual imaging. This was achieved by radiolabelling SPION-decorated MWNTs with ^{99m}Tc. In the present report, we take advantage of this newly introduced concept to get further insights on the role that the CNTs' length has on the development of novel contrast agents. The use of steam shortened MWNTs not only allows the modulation of the pharmacological profile of the resulting contrast agents but is found to enhance the R_2^* magnetic properties both *in vitro* and *in vivo* compared to their long counterparts.

2. Results and Discussion

2.1. Synthesis of different length of iron oxide-MWNTs hybrids

As-received MWNTs were treated by steam to remove carbonaceous impurities that are present as secondary products during the CNTs' growth; namely, amorphous carbon and graphitic particles. The graphitic particles can in turn cover catalytic particles and inhibit their dissolution by an acid wash. After the steam treatment the metal particles become exposed and can be easily removed by HCl.[37] The length of the MWNTs can be modulated by changing the time of the steam treatment. For the preparation of long MWNTs (L-MWNTs) the sample was exposed to steam for 1.5 hours, whereas for short MWNTs (S-MWNTs) an steam treatment of 15 h was employed. Afterwards, oxygen bearing functionalities were added onto the CNTs by treatment with nitric acid.[38] In this respect, the removal of amorphous carbon is necessary to allow a proper functionalization of the CNTs' walls.[39] Next, the synthesis of the iron oxide nanoparticles was conducted *in situ* following a previously reported protocol.[40] The presence of oxygen bearing functionalities on the backbone structure of the MWNTs facilitates the coating since these moieties act as anchoring groups

during the formation of the nanoparticles. The iron oxide nanoparticles were prepared in situ by decomposition of iron acetate, which was employed as an iron precursor.

2.2. Physicochemical Characterization of L-SPION-MWNT and S-SPION-MWNT

The length distribution of both the short and long MWNTs was determined by measuring individual nanotubes from low resolution transmission electron microscopy (TEM) images (**Figures 1A, 1B**). The insets show the resulting histograms from measuring about 165 nanotubes for each sample. The median lengths for the long and short nanotubes are 1.9 μm and 0.6 μm respectively. Actually the decrease in length becomes apparent by visual inspection of the images which need to be displayed at different scale to be able to observe the full length of the MWNTs. It is interesting to note that the short nanotubes appear to present a larger amount of π-π interactions leading to the formation o small bundles; both after the steam treatment and after their sidewall functionalization and decoration with the inorganic nanoparticles (**Figures 1C, 1D**). The amount of nanoparticles present in the resulting hybrids was quantitatively determined by thermogravimetric analysis (TGA) (**Figure S1**). The samples were heated under flowing air until their complete combustion. Therefore, considering that the nanoparticles are Fe_2O_3, the residue obtained after the TGA analysis corresponds to the iron oxide present in each sample. In the case of L-SPION-MWNTs the residue is of 33.5 wt.% and for S-SPION-MWNTs 29.5 wt.%. Since both hybrids present a similar degree of loading, the amount of SPION present for a given length of nanotube will be the same. Therefore, each individual long nanotube (L-MWNTs) will at the end have a larger amount of nanoparticles on its surface than a single nanotube present in the sample of S-MWNT.

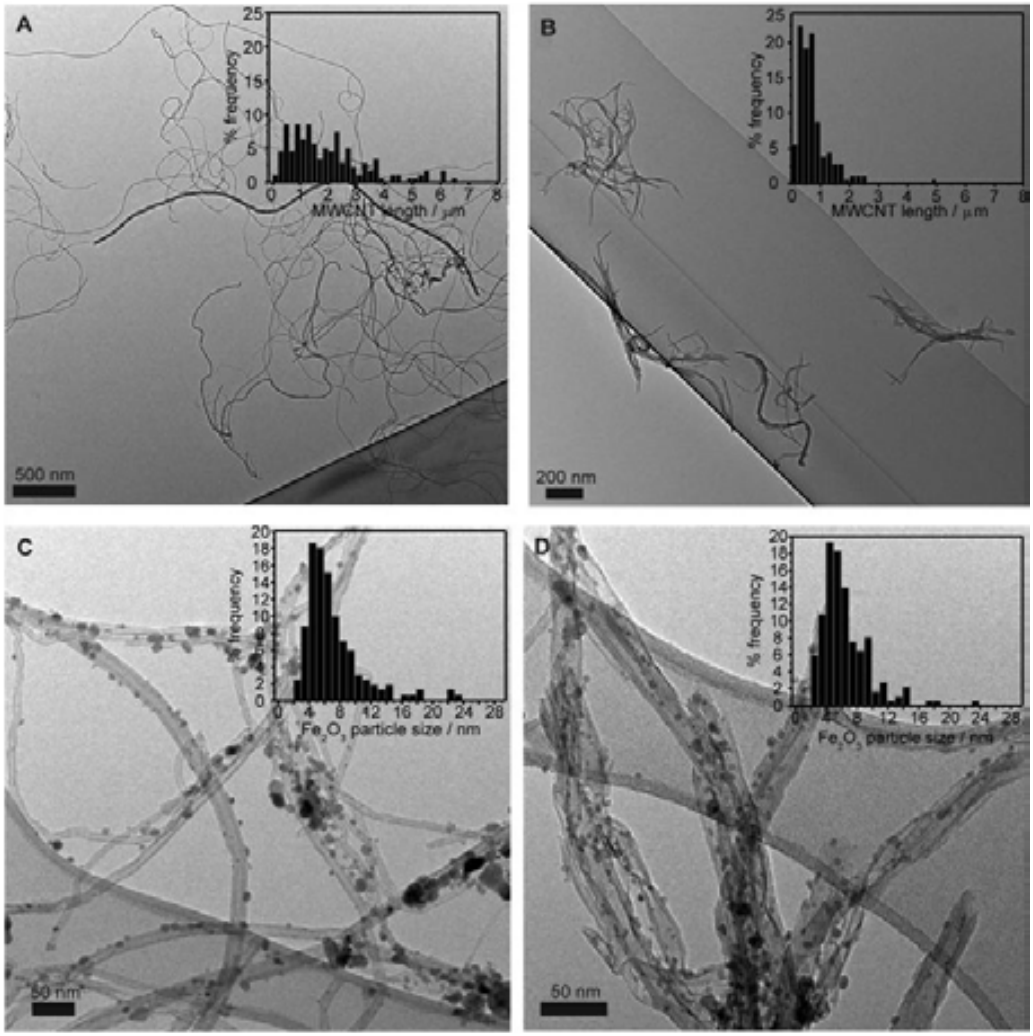

Figure 1: Transmission Electron Microscopy (TEM) images and length distribution histograms (top). TEM images and SPION particle size distribution histograms. (A,C) L-MWNTs, (B,D)- S-MWNTs. The histograms presented in the insets of C and D are fitted with a log-normal function.

The size, shape and distribution of the nanoparticles was examined by TEM (**Figures 1C, 1D**). The nanoparticles appear to be well spread along the MWNT walls. The diameter of about 180 nanoparticles was evaluated for each sample and the resulting histograms are displayed as an inset in the figures. Since the samples present a non-symmetric length distribution it is not possible to

determine an average mean length and a box plot analysis was performed (Figure 2, Table S1). Box plot analysis reveals a statistically similar size distribution of the nanoparticles regardless of the length of the MWNTs, with almost no particles being bigger than 13.1 nm (maximum adjacent observation for both samples). The median particle size in both samples is about 5.9 nm (5.7 nm in the S-MWCNTs and 6.1 nm in the L-MWNTs). The structure of the prepared nanoparticles was further investigated by X-ray diffraction (XRD) and X-ray photoelectron spectroscopy (XPS) (**Figure 2**). The two hybrids present the same diffraction patterns with peaks arising from the carbon nanotubes (pdf – powder diffraction file– 750444) and from the presence of iron oxide nanoparticles which are in agreement with both maghemite (γ-Fe_2O_3; pdf 391346) and magnetite (Fe_3O_4; pdf 740748). The small particle size the nanoparticles is also reflected by the broad peaks present in the diffraction pattern. A cumulative XPS scan in the Fe 2p region serves as an indicator to differentiate between maghemite and magnetite.[41] Again, the two hybrids present the same features in the XPS spectra further confirming that both samples contain the same type of nanoparticles. The "shake-up" satellite structure at 720 eV is distinctive of maghemite (γ-Fe_2O_3).

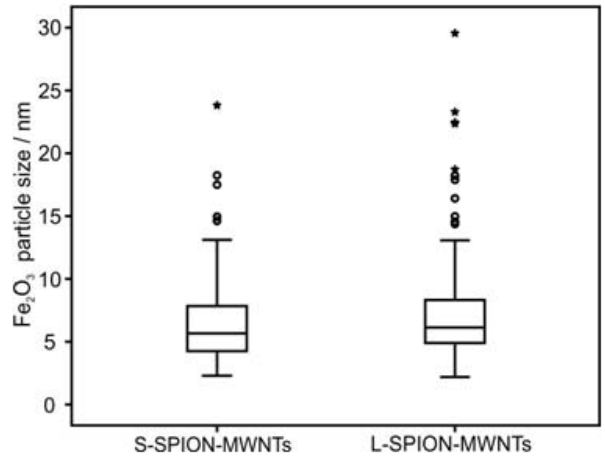

Figure 2: Box plot analysis of the particle size distribution in S-SPION-MWNTs and L-SPION-MWNTs. Empty circles indicate outliers and asterisks faroutliers in the samples.

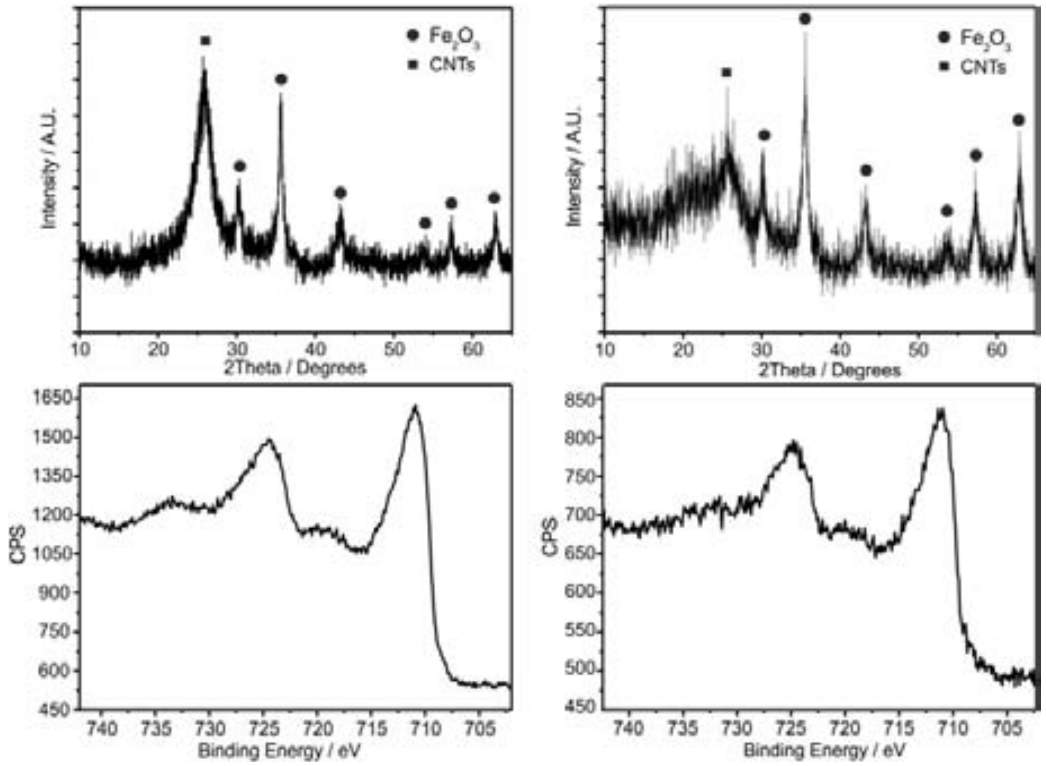

Figure 2: X -ray diff raction (XRD) pa ttern (top) and X-ray P hotoelectron spectroscopy (XPS) of the Fe 2p region. (A,C) L-SPION-MWNTs, (B,D) S-SPION-MWNTs.

2.3. Phantom MR Imaging and R_2* Relaxation Measurements

To compare the MR imaging properties of hybrids, samples with concentrations ranging from 0.125 to 1.25 mM (Fe) were prepared and imaged in a preclinical scanner at 7 Tesla. L-SPION-MWNT, S-SPION-MWNT and Endorem® were dispersed by sonication before being resuspended in 1% Agar solution (phantoms) avoiding any sedimentation effect leading to imprecise relaxation measurements. Relaxation times (R_2*) of L-SPION-MWNT, S-SPION-MWNT and Endorem® calculated from their signal decay were plotted against Fe concentration (**Figure 3**).

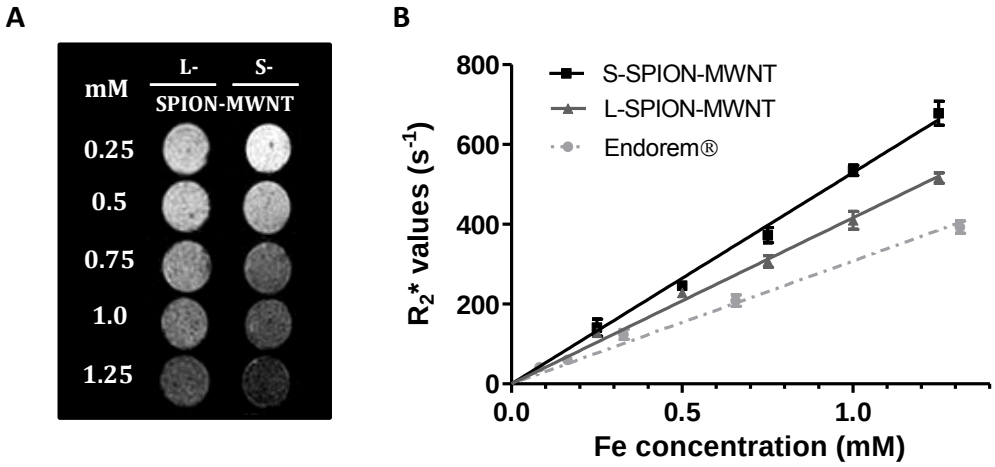

Figure 3: Phantom MR imaging of hybrids and Endorem®. Samples were dispersed in 1% agar solution and imaged using a 7 Tesla (7T) preclinical MR scanner. **(A)** Phantom MR imaging of Endorem®, S-SPION-MWNT and L-SPION-MWNT; **(B)** R_2* relaxation rate analysis as a function of Fe concentration. Results are presented as mean ± S.D showed higher r_2* relaxivity for S-SPION-MWNT (n=3).

R_2* measurements are significantly higher than R_2 at high field, but their relaxivity pattern should be comparable. Even though R_2 is a more clinically relevant parameter, R_2* is preferred to explore relaxation properties of iron oxide contrast agent at high field as it increases the measurement sensitivity. Good linear regressions ($R^2 > 0.98$) were obtained and their slopes, defined as relaxivity values (r_2*), indicated that S-SPION-MWNT exhibits higher r_2* value (530 s^{-1} mM^{-1}) compared to L-SPION-MWNT (417 s^{-1} mM^{-1}). Both hybrids displayed higher r_2* values compared to Endorem® (308 s^{-1} mM^{-1}). To investigate if the enhanced r_2* value of S-SPION-MWNT resulted from the magnetic properties of pristine MWNT (pMWNT), relaxivity measurements of S-MWNT and L-MWNT (without SPION decoration) were carried out (**Figure S2**). R_2 relaxivity measurements of L-MWNT and S-MWNT were very low (< 1 s^{-1} mM^{-1}) and not different for both hybrids.

2.4. Magnetic properties of L-SPION-MWNT and S-SPION-MWNT

The higher r_2* values observed for the S-SPION-MWNT compared to the L-SPION-MWNT cannot be explained from the physico-chemical characterization performed so far since both samples contain particles of Fe_2O_3 with similar sizes, as assessed by box plot analysis. Wilson et al. reported that ultrashort SWNTs (60-80 nm) have an intrinsic and significant contribution to the MRI signal.[42] In our case a negligible MRI signal was observed in both of the steam treated samples (L-MWNTs and S-MWNTs) in the absence of SPION (Figure S3). Therefore, we next performed magnetic measurements of both hybrids to understand the origin of the enhanced relaxivity when short nanotubes are employed.

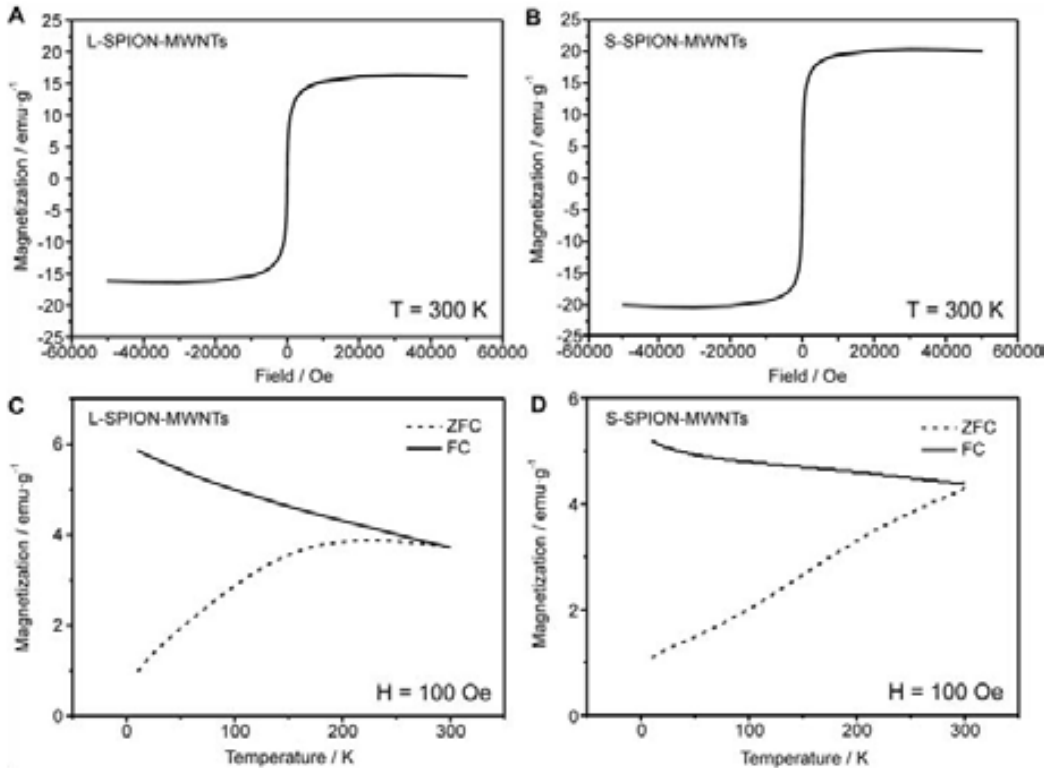

Figure 4: Hysteresis loops at 300 K after subtracting the linear background (top) and zero field-cooling and field-cooling curves (100 Oe), recorded using a field of 100 Oe (bottom). (A,C) L-SPION-MWNTs, (B,D) S-SPION-MWNTs.

Hysteresis loops at 300 K are shown in **Figures 4A, 4B**. No remnant magnetization is observed at room temperature after removal of the external magnetic field confirming the superparamagnetic behaviour of the nanoparticles. Hysteresis loops at 10 K were also recorded and are presented in Figure S2. **Figures 4C,4D** present the zero-field cooling and field cooling (ZFC-FC) curves of both hybrids. The ZFC curve is measured upon warming using a field of 100 Oe, after cooling down the sample in nominally zero magnetic field; in the FC study there is an applied field of 100 Oe. The observed splitting of the ZFC and FC data is the common behaviour of a system of superparamagnetic particles. A gradual increase of magnetization is observed in FC data when decreasing the temperature, reflecting the reduction of the thermally-induced magnetic disorder. In contrast, in the ZFC curves the magnetization increases. In the ZFC measurement, when cooling, at some temperature the thermal energy becomes smaller that the magnetic anisotropy energy and the magnetic moment of the nanoparticle gets blocked in a direction dictated by its magnetic anisotropy axis. For a collection of non-interacting SPIONs and in absence of any magnetic field (ZFC) this direction is randomly distributed and thus the overall magnetization should vanish. When warming and measuring under field, the sample magnetization gradually increases and displays a maximum (so called blocking temperature T_B) and merges the FC curve. For a system on non-interacting SPIONs, T_B is determined by the magnetic anisotropy energy ($E_a = K_aV$) where K_a is the anisotropy constant of the nanoparticle and V its volume. In the present case, the composition of SPIONs is seen to be identical in both samples (as inferred for the structural and spectroscopic data in Fig. 2, and the saturation magnetization of Figs 4a, b) and their shape, size and size-distributions are also virtually identical. Therefore, E_a should be similar in both samples and correspondingly T_B would be the same. However, it is obvious in Fig. 4c and 4d that of L-SPION-MWNTs and S-SPION-MWNTs display a distinctive ZFC-FC response. In L-SPION-MWNTs is T_B of is well visible at ≈ 175 K and ZFC-FC data approach each other at T > 175 K whereas in S-SPION-MWNTs where ZFC and FC only merge at the highest temperature.

This conduct has been previously described for nanoparticles presenting a broad size distribution.[43] However, as state above, our samples present a narrow and statistically similar size distribution. The presence of outliers/faroutliers in the samples is also found to have no effect on the magnetic response of the material (11in L-SPION-MWNTs and 7 in S-SPION-MWNTs; Figure 2). Differences in T_B should thus be related to differences on magnetic interactions among SPIONs; indeed nanoparticle interaction has an important influence in boosting stability of arrangement of magnetic nanoparticles. Since the amount of nanoparticles is similar in both samples, the distance between particles that are randomly distributed should also be similar in each individual nanotube; the "total the length" of nanotubes is the same in both samples for a given mass ("total length" = sum of the length of all the nanotubes present in the sample). Therefore interparticle interactions might arise from nanoparticles sitting on different nanotubes. As detailed above, during TEM analysis of the long and short samples we observed that S-MWNTs tend to form small bundles and as a consequence, the S-SPION-MWNTs would have more interparticle interactions. This interaction makes them to behave as a cluster, producing an increase of the blocking temperature.[44] Phantom MR imaging of the hybrids significantly revealed a higher relaxivity values for S-SPION-MWNTs. This could be explained by the higher interaction between the SPION when MWNTs have shorter length in agreement with the magnetic measurements. As a result of this interaction, the cluster itself might be considered as a large magnetized sphere. The total magnetization is aligned to the magnetic field and due to the large size the secular term of the relaxation rate is affected.

$$\boldsymbol{R_2} = \frac{\mathbf{1}}{\boldsymbol{T_2}} = \frac{\mathbf{16} f_a \Delta\boldsymbol{\omega}^2 \boldsymbol{\tau_D}}{\mathbf{45}} \quad (1)$$

The secular contribution derives from the the outesphere diffusion theory.[45,46] This refers to $\Delta\omega\tau_D < 1$, where $\Delta\omega$ is the difference between the frequencies of the local field experienced by a proton in the cluster surface and the one experienced by a proton in the bulk, and τ_D is the diffusion time

around the cluster, which increases with cluster size.[47] In equation 1, f_a is the volume fraction occupied by the cluster. This secular contribution significantly describes an increase in R_2 values at high fields.[48,49] Consequently, for S-SPION-MWNTs the values were higher than for L-SPION-MWNTs, which have a more diffused cluster. A similar phenomenum has been reported for gadofullerenes (gadolinium endohedralmetallofullerenes) which have been also investigated as paramagnetic MRI contrast agents. Gadofullerenes tend to form aggregates, which is at the origin of much of their relaxivity enhancement.[50-52] As a result, when the gadofullerenes are disaggregated (individualized), the substantial enhancement over the clinically available contrast agents is mostly lost.

2.5. *In Vitro* MR Imaging and Uptake Ability of Hybrids by ICP-MS in J774A.1 cells

The ability of SPION-MWNT hybrids to be internalized within cells and conserve their imaging properties *in vitro* was then studied. L-SPION-MWNT, S-SPION-MWNT and Endorem® were incubated with J774A.1 cells at 12 and 24 μg (Fe)/mL for 24h. Perls' staining demonstrated the co-localisation of CNTs and Fe within J774A.1 cells (**Figure 5A**).

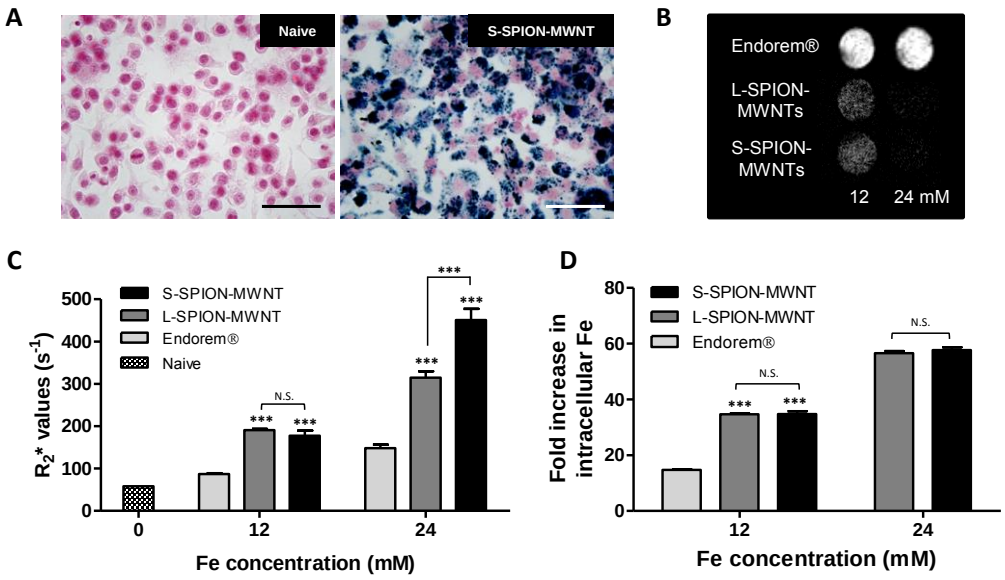

Figure 3: ***In vitro*** **MR imaging of J774A.1 cells exposed to SPION-MWNT and Endorem®.** J774 cells were incubated with Endorem®, L-SPION-

Figure 5: In vitro MR imaging of J774A.1 cells exposed to SPION-MWNT and Endorem®. J774 cells were incubated with Endorem®, L-SPION-MWNT or S-SPION-MWNT at 12 or 24 µg/ml (Fe) for 24 h. **(A)** Perl's staining of J774A.1 cells exposed to 24 µg/ml (Fe) of S-SPION-MWNT for 24 h; **(B)** In vitro T_2*-weighted MR images of J774A.1 cells exposed to SPION-MWNT and Endorem®. After treatment, cells were washed with PBS, resupended in 0.5% Agarose at a density of 1 x 10^6 cells per 200 µL. Resulting phantoms were imaged at 7 Tesla; **(C)** In vitro R_2* relaxation rate measurements. J774A.1 cells incubated with SPION-MWNT displayed higher R_2* values compared to cells exposed to Endorem®. Cells exposed to S-SPION-MWNT at 24 µg/ml displayed the highest R_2* value (n=3); **(D)** Intracellular iron measurement of J774A.1 cells treated with SPION-MWNT or Endorem®. Phantoms were digested overnight in nitric acid (>65%) and their iron content was assessed using ICP-MS. J774A.1 cells incubated with SPION-MWNT displayed a 2,3 fold intracellular Fe concentration increase compared to cells incubated with Endorem® but no significant difference was observed between cells treated with short and long hybrids (n=3). *P<0.05, **P<0.01, ***P<0.001 are relative to Endorem® treated samples at equal Fe concentration or are calculated from the comparison between samples using analysis of variance (ANOVA) with post hoc analysis by the Tukey test. The scale bar corresponds to 50 µm.

To measure the MR imaging properties of internalized hybrids, J774A.1 cells were detached, fixed and resuspended in 0.5 % Agarose solution at a final density of 1 x 10^6 cells per 200 µL and imaged at 7 Tesla. **Figure 5B** and **5C** represent the *in vitro* phantom imaging and the relaxation rates measured from their signal decays. J774A.1 cells incubated with both hybrids showed higher R_2* relaxation rate compared to cells exposed to Endorem®. J774A.1 treated with S-SPION-

MWNT displayed higher relaxation rate (R_2*) than cells exposed to L-SPION-MWNT and Endorem® (at 24 μg/mL). These results confirmed that the shortening of SPION-MWNT increased the *in vitro* negative contrast imaging properties of hybrids. The intracellular Fe content (per 1 x 10^5 cells) was then measured by ICP-MS to assess if MR enhancement effect was due to higher uptake capacity of S-SPION-MWNT into cells or due to their intrinsically enhanced MR properties. J774A.1 cells treated with S-SPION-MWNT and L-SPION-MWNT showed higher iron uptake than cells incubated with Endorem® (**55D**). However, no significant difference in intra-cellular Fe content was observed between the two types of the hybrid, suggesting that the enhanced MR signal of S-SPION-MWNT was due to intrinsic enhancement in MR signals agreeing with phantom studies.

2.6. Relaxation rate of S-SPION-MWNT in Mice

Magnetic properties of S-SPION-MWNT and Endorem® were compared in liver tissue after intravenous injection of both hybrids at 1.4 or 2.9 mg(Fe)/kg in mice. R_2* values were measured in living animals at 30 min, 24 h and 8 days post-injection. Relaxation rate measurements of liver injected with Endorem® at 1.4 mg(Fe)/kg showed highest value (326.9 ± 12.4 s^{-1}) at earliest scan time, i.e., 30 min after injection which progressively decreased to background at 8 days post injection (120.3 ± 25.2 s^{-1}) (**Figure 6**).

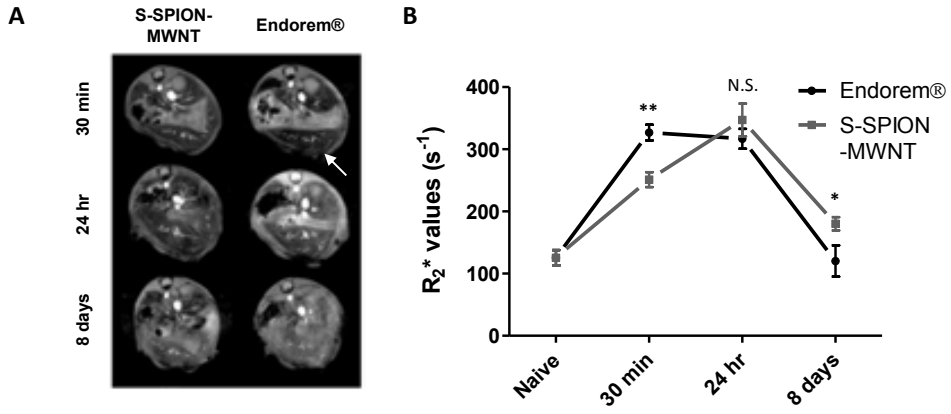

Figure 6: In vivo R_2*-weighted MR studies in liver after intravenous injection of S-SPION-MWNT (1.4 mg (Fe)/kg). (A) In vivo T_2*-weighted MR images at 7T; **(B)** *In vivo* R_2* relaxation rate measurements. R_2* relaxation rate analysis in the liver showed non significantly different R_2* values between S-SPION-MWNT and Endorem®, 24 h after injection (n=5). *P<0.05, **P<0.01 relative to the naïve condition by analysis of variance (ANOVA) with post hoc analysis by the Tukey test.

Such results were indicative of the rapid and vast accumulation of Endorem® in the reticular endothelial system (RES) within 30 min. Following intravenous injection of S-SPION-MWNT in mice, relaxation rates in liver tissue increased from 251.1 ± 12.0 s^{-1} (30 min) to 347.1 ± 26.2 s^{-1} (24 h) before decreasing to 180.1 ± 10.6 s^{-1} (8 days). S-SPION-MWNT displayed uptake in the lung with a percentage reaching liver and spleen, as will be presented later. Interestingly, 24 h after injection, the relaxation rate of liver injected with S-SPION-MWNT (347.1 ± 26.2 s^{-1}) was comparable to that of Endorem® (316.9 ± 15.9 s^{-1}). Furthermore, the relaxation rate of liver treated with S-SPION-MWNT was consistently higher than that of Endorem® at 8 days (*p<0.05). When the injected dose of S-SPION-MWNT was increased from 1.4 to 2.9 mg(Fe)/kg, R_2* measurements in livers reached 495.3 ± 51.5 s^{-1} at 24 h (**Figure S3)**. Both injected dose of S-SPION-MWNT showed an increase in R_2* measurements from 30 min to 24 h and significantly higher R_2* values at 8 days compared to Endorem®. R_2* measurements in the spleen of mice

injected with 2.9 mg(Fe)/kg displayed consistently higher relaxation time for Endorem® compared to S-SPION-MWNTs.

2.7. Biodistribution Study of ^{99m}Tc-BP-S-MWNT in Mice after Intravenous Injection

To assess the fraction of short hybrids contributing to MR signals within the liver, S-SPION-MWNT biodistribution was investigated using the method we previously reported for L-SPION-MWNT adopted from Rosales *et al.*[40,53] A functionalized biphosphonate (BP) named dipicolylamine-alendronate (DPA-ale) was utilized as linker between the radioisotope ^{99m}Tc and SPION. The ^{99m}Tc-BP complex was mixed with S-SPION-MWNT for 30 minutes at 37° C to form ^{99m}Tc-BP-S-MWNT. The radio-labelled hybrid was then washed to remove unbound ^{99m}Tc-BP and its stability in PBS and serum was confirmed (**Figure S4**). Whole body SPECT/CT imaging was carried out at 30 min, 4 h and 24 h after intravenous injection of ^{99m}Tc-BP-S-MWNT (4 MBq, 10 mg/kg hybrid) or ^{99m}Tc-BP (10 MBq) alone in C57BL/6 mice (**Figure 7A**).

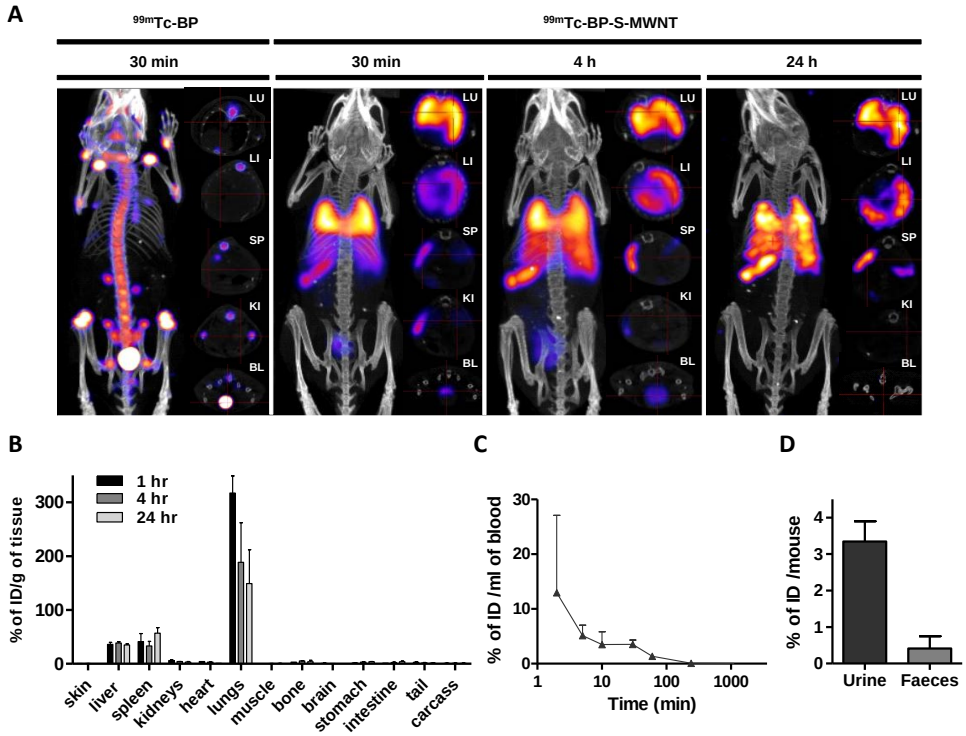

Figure 6: ***In vivo*** **SPECT/CT images and organ biodistribution studies following i.v. injection of ^{99m}Tc-BP-S-MWNT-Fe_2O_3.** ^{99m}Tc-BP and S-MWNT-

Figure 7: In vivo SPECT/CT images and organ biodistribution studies following intravenous injection of ^{99m}Tc-BP-S-MWNT. ^{99m}Tc-BP and S-MWNT-SPION were mixed for 30 min at 37 °C to form ^{99m}Tc-BP-S-MWNT. Unbound ^{99m}Tc-BP was removed following 4 centrifugation steps until limited amount of radioactivity (<1% of the total activity) was measured in the supernatant. Hybrids as 200 µg (4 MBq) or 100 µg (0.2 MBq) were injected intravenously for SPECT/CT imaging and γ-counting study, respectively. **(A)** Whole body 3D SPECT/CT imaging; **(B)** Organ biodistribution of ^{99m}Tc-BP-S-MWNT by γ-counting; **(C)** Blood clearance profile. Blood samples from 2 min up to 24 h were collected after injection of ^{99m}Tc-BP-S-MWNT (n=3); D) Excretion profile. Injected mice were kept in metabolic cages to collect urine and faeces. Cross sections in **(A)** were taken at lung (LU), liver (LI), spleen (SP), kidney (KI) and bladder (BL). Results are expressed as mean ± SD (n=3).

The affinity of bisphosphonates molecules (^{99m}Tc-BP) for bone mineral tissue led to the accumulation of free ^{99m}Tc-BP into bone tissue. The high signal within the bladder revealed the predominant urinary excretion of the free ^{99m}Tc-BP. This result agrees with our previously published data.[53] In comparison, ^{99m}Tc-BP-S-MWNT accumulated mostly into lungs, followed by liver and spleen after 30 min of injection. A small fraction of ^{99m}Tc-BP-S-MWNT was found in the bladder, indicating that a fraction of the hybrid was excreted *via* the urinary tract. Because of the rapid decay of ^{99m}Tc (half-life = 6 h), the "virtual" loss of radioactivity was compensated by adjusting the signal intensity of later time points. At 4 and 24 hr, ^{99m}Tc-BP-S-MWNT was translocated from lungs to the liver and spleen.

To assess quantitatively the organ biodistribution profile of S-SPION-MWNT, post-mortem γ-scintigraphy was conducted. Major mouse organs were excised at 1, 4 and 24 h time points. As observed with SPECT/CT results, lung, liver and spleen were the organs showing the highest accumulation with 317.2 ± 32.0, 36.1 ± 3.4 and 41.2 ± 14.8 % ID/g, respectively (**Figure 7B**). Despite significant accumulation of ^{99m}Tc-BP-S-MWNT into the lungs, the hybrid was progressively cleared from this organ. In contrast, no clearance of ^{99m}Tc-BP-S-MWNT was observed for the liver and spleen. Blood clearance profile showed that 3.5 ± 0.8 % ID was measured 30 min after injection (**Figure 7C**). Only 3.3 ± 0.4 % ID were excreted *via* the urine whereas only 0.41 ± 0.5 % ID were measured in faeces. To summarize, ^{99m}Tc-BP-S-MWNT

predominantly accumulated into lung but also into the liver and spleen. Relocation of the hybrid from lungs into liver and spleen was observed over the 30 min - 24 h period.

3. Experimental Section

Materials: Chemical vapour deposition (CVD) multi-walled carbon nanotubes (MWNTs) were supplied as a dry powder (Thomas Swan & Co. Ltd, UK) with an external average diameter of 10–12 nm (information provided by the supplier). Iron acetate (III), propidium iodide, human male AB plasma, Triton® X-100, ribonuclease A, agar, agarose, nitric acid, citric acid, sodium phosphate dibasic (Na_2HPO_4), Pluronic® F-127, 10% neutral buffered formalin, paraformaldehyde (PFA), DPX, nuclear red solution and Accustain® kit were purchased from Sigma-Aldrich. Xylene and ethanol were purchased from Fisher Scientific (UK). Dulbecco's Modified Eagle Medium (DMEM), phosphate buffered saline (PBS), penicillin-streptomycin, Glutamax® and sodium pyruvate were obtained from Invitrogen®, Life Sciences (UK). Plasma derived bovine serum (FBS) was obtained from First-Link, UK Ltd. Cytotox 96® Non-Radio Cytotoxicity Assay was bought from Promega UK Ltd. Endorem® was obtained from Guerbet (UK). Dipicolylamine-alendronate (DPA-ale or BP) and ^{99m}Tc -BP were synthesized as previously reported.[16] Na[$^{99m}TcO_4$] in physiological saline was obtained from a ^{99}Mo/ ^{99m}Tc generator at the Radiopharmacy of Saint Bartholomew's Hospital and The London School of Medicine & Dentistry Queen Mary University, London, UK. Radioactivity in samples was measured using a CRC-15R dose calibrator (Capintec, USA). [^{99m}Tc $(CO)_3$ $(H_2O)_3$]$^+$ was synthesized using Isolink kits prepared by Mallinckrodt Medical B.V. (USA). Isoflurane (IsoFlo®) for anaesthesia was purchased from Abbott Laboratorie Ltd (UK).

Preparation of S-SPION-MWNT and L-SPION-MWNT: The as-received MWNTs were purified by steam treatment followed by an HCl wash, as previously described.[37] Briefly, MWNTs were ground with an agate mortar and pestle until a fine powder was obtained and introduced inside an

horizontal tubular furnace. Steam was introduced by bubbling argon through hot distilled water. To prepare long MWNTs the sample was exposed to steam at 900 ºC for 1.5 h whereas short MWNTs were achieved after 15 h of steam treatment.[18] The solid powder was next treated with HCl to remove catalytic nanoparticles and washed with water until the pH of the filtrate was neutral. Both S-MWNTs and L-MWNTs were independently treated with with 3 M HNO_3 for 45 h under refluxing conditions. This results in the introduction of oxygen bearing functionalities onto the CNT structure, mainly carboxylic acid groups (–COOH).[38] The functionalized MWNTs (*f*-MWNTs) were collected by filtration and thoroughly washed with distilled water until neutral pH of was achieved. The MWNTs were decorated with SPION by *in-situ* formation of the nanoparticles following a previously reported protocol that employs iron (II) acetate as a precursor.[40]

Analysis and Characterisation of SPION–MWNTs: Thermogravimetric analysis (TGA) were performed on a Netzsch instrument, model STA 449 F1 Jupiter®. Experiments were conducted under a flow of air at a heating rate of 10 ºC min^{-1} up to 950 ºC.

Low magnification TEM images were obtained using a JEOL 1210 and operating at 120 kV. TEM samples were prepared by dispersing a small amount of powder in absolute ethanol and sonicated in an ultrasonic power bath. Afterwards, the dispersion was drop dried onto a lacey carbon TEM grid.

X-ray diffraction studies were conducted using a powder diffractometer ($CuK_{\alpha 1}$, λ = 0.1540 nm; Siemens D5000, Germany) with 2θ ranging from 5° to 65°. The PDF (powder data file) database was used to identify the compounds.

X-ray Photoelectron spectra were acquired with a Kratos AXIS ultra DLD spectrometer with an Al Kα X ray font and a power of 120 W. Samples were measured as dry powder. Survey-scan was conducted with a Pass Energy of 160 eV and high resolution scans at a Pass Energy of 20 eV. Hybrid-slot lens mode was employed, with an area of analysis of 700 x 300 microns.

Magnetic measurements were done in a Superconducting Quantum Interference Device (SQUID) magnetometer (LOT-QuantumDesign Iberia). A diamagnetic gelatine capsule was filled with 3-4 mg of sample. Data was acquired with an applied field from -50.000 Oe to +50.000 Oe at 10 K to obtain the hysteresis loops. The sample holder contribution was subtracted in all the measurements.

MWNT-SPION Phantom Preparation: S-MWNT-SPION and L-MWNT-SPION in 1% Pluronic® F-127 solution were dispersed for 30 min using a bath sonicator (UT-300H) purchased from VWR (UK). Dispersed MWNT-SPION were mixed with an equal volume of melted agar solution (2%, w/v in water) to achieve final phantom concentrations ranging from 0.25 mM to 1.25 mM (Fe) in 1% agar in water.

Magnetic Resonance (MR) Imaging of Phantoms. Phantoms were imaged using a 7 Tesla horizontal MR scanner obtained from Varian Inc. (USA). The gradient coil had an inner diameter of 12 cm, gradient strength was 1000 mT/m (100 G/cm) and rise-time was 120 μs. Quadrature transmit/receive coil (RAPID) with an internal diameter of 39 mm was obtained from Biomedical GmbH (Germany). Cine-FLASH MRI technique with variable echo time (TE) was used to acquire T_2* images. Cine-FLASH parameters for T_2* images were: FOV = 30 x 30 mm, matrix size = 96 x 96, slice thickness = 1 mm; number of slice = 1; flip angle = 20°, 1 average, TR = 700 ms; TE = 1, 2, 3, 5, 8, 10 ms; scan time ~ 7 min.

Phantom MR Imaging Analysis: MR images were analyzed using ImageJ (USA). T_2* pixel by pixel data was fitted by the following equation: $S_n = S_0 \times \exp(-TE_n/T_2^*)$. Where S_n is the signal measured, S_0 is the initial signal and TE_n is the echo spacing. Regions of interest (ROI) in the phantom were selected, three T_2* maps were averaged to provide the mean corresponded T_2* values of such area. R_2* values (corresponding to $1/T_2$*) were calculated and consequently related to the iron concentrations.

Cell Culture and Treatment: J774A.1 cell line (ATCC® TIB-67™) was cultured in DMEM media supplemented with 10% FBS, 50 U/mL penicillin, 50 µg/mL streptomycin and 1 % L-glutamax®, at 37°C in 5 % CO_2. Cells were routinely grown in 75 cm^2 canted-neck tissue culture flasks and passaged twice a week by scraping cells at 80 % confluency. S-SPION-MWNT and L-SPION-MWNT were dispersed for 30 min in a bath sonicator before use. J774A.1 cells were incubated with SPION-MWNT or Endorem® for 24 h, at 12 and 24 µg/mL of Fe, in J774A.1 cells at 37° C and 5% CO_2.

Perls' Prussian blue staining of J77A.1 cells: To detect the presence of iron in cells, the Accustain® kit obtaned from Sigma-Aldrich (UK) was used with minor modifications to the manufacturer's instructions. Treated cells on coverslip were fixed in 4% PFA, washed in PBS and stained with potassium ferrocyanide solution/HCl solution mixed at 1:1 ratio (v/v) for 20 min to reveal the presence of iron by blue staining. Then, cells were washed in PBS and counterstained after incubation with the Nuclear Red Solution for 10 min. Coverslips were then dehydrated by sequential incubation for 1 min in solutions of ethanol (50%, 70%, 100%) and xylene (2 incubations) before being mounted in DPX mounting media. All stained sections were analyzed using a DM 1000 LED Microscope obtaned from Leica Microsystems (UK) coupled with CCD camera purchased from Qimaging (UK).

In Vitro Phantom Preparation and Imaging: After treatment, J774A.1 cells were scraped, washed in PBS and fixed in 4% PFA. Cells were counted and resuspended in 1% Agarose solution to achieve a final density of 1 x 10^6 cells per 200 µl of 0.5% Agarose. Phantoms containing J774.A.1 cells were imaged by MRI and analyzed using ImageJ following the same method described above for SPION-MWNT phantoms.

In Vitro Uptake Study using Inductively Coupled Plasma Mass Spectrometry (ICP-MS) Detection: The intracellular amount of iron was quantified by ICP-MS to compare the *in vitro* uptake ability of SPION-MWNT hybrids. J774.A.1 cells were digested in HNO_3 (10:1) at 65 °C overnight. ICP-

MS was carried out on Sciex Elan 6100DRC with AS93+ autosampler and crossflow nebuliser obtained from Perkin Elmer Ltd (UK). Results were analyzed using Elan v3.3 software provided by Perkin Elmer Lts (UK). ^{56}Fe was measured in samples using sample flow of 0.4 ml/min, nebuliser gas flow of 0.98 L/min, plasma gas flow of 15 L/min, aux gas flow 0.8 L/min, RF power 1200W and cell gas NH_3 at 0.7 ml/min. Triplicates were averaged for each sample, each replicate being 30 sweeps with 100 ms dwell time.

Animals: All *in vivo* experiments were carried out under the authority of project and personal licences granted by the UK Home Office and the UKCCCR Guidelines (1998). All *in vivo* studies were conducted using female C57BL/6 mice (6-8 weeks old) supplied from Harlan Laboratories (UK).

In Vivo MR Imaging: In vivo MR imaging was performed using a 7 Tesla horizontal MR scanner used for phantom MR imaging. Animals were injected with 1.4 or 2.9 mg(Fe)/Kg of SPION-MWNT or Endorem® followed by imaging after 30 min, 24 h and 8 days in prone position under anaesthesia maintained with 1.5% isoflurane / 98.5% oxygen. The body temperature was maintained at 37 °C using a warm air fan. Cine-FLASH MRI technique with variable echo time (TE) was used to acquire T_2* images for *in vivo* studies. ECG was monitored *via* two metallic needles placed subcutaneously in the front paws. A pressure-transducer for respiratory gating was placed on the animal abdomen. To synchronize data acquisition with the ECG and to compensate for respiratory motion, simultaneous ECG triggering and respiration gating were applied. Cine-FLASH parameters for T_2* images were: FOV = 25 x 25 mm, matrix size = 128 x 128, slice thickness = 1 mm; flip angle = 20°; number of slice = 1; 1 average; TR = 1 / heart rate = RR-interval; TE = 1, 2, 3, 5 ms; scan time ~ 5 min.

In vivo MR imaging analysis: MR images were analyzed using ImageJ as described above for phantom MR imaging analysis. ROI in the liver and spleen were selected, five T_2* maps were

averaged to provide the mean corresponded T_2* values of such area. R_2* values (corresponding to $1/T_2$*) were calculated and related to the acquisition time points.

Radio-labelling and In Vitro Stability of S-SPION-MWNT: The labelling of S-SPION-MWNT with ^{99m}Tc-BP was carried out as previously reported.[40] A dispersion of S-SPION-MWNT (1 mg/mL) was obtained by sonication for 10 minutes in 1% Pluronic® F-127/0.9% NaCl solution concentration (w/v) and mixed with ^{99m}Tc-BP (200-500 MBq in 50 μg of BP/125 μL). The mixture was incubated at 37° C for 30 min with gentle shaking. After cooling to room temperature, ^{99m}Tc-BP-S-MWNT hybrids were separated from unbound ^{99m}Tc-BP by centrifugation at 14 000 rcf for 20 min and the pellets containing ^{99m}Tc-BP-S-MWNT hybrids were washed 5 times (1 mL each wash) with distilled water until less than 1% of the radioactivity was detected in the supernatant. The pellet was then re-dispersed using 1% Pluronic® F-127 solution to achieve a final concentration of 1 mg/mL for subsequent *in vivo* studies (γ-scintigraphy and SPECT/CT imaging).

Serum-stability of the Radio-labelled Hybrids: The *in vitro* stability of short hybrids was confirmed by mixing ^{99m}Tc-BP-S-MWNT with an equal volume of human serum or PBS (at 50% final concentration) and incubating samples at 37 ° C for 24 h. After sample centrifugation at 14 000 rcf for 20 min, γ-counting was used to measure the radioactivity of the pellets and the supernatants. The percentage of ^{99m}Tc-BP remaining bound to S-SPION-MWNT was above 80% in PBS and 85 % in serum, indicating the good stability of short hybrids in PBS and human serum.

Whole Body 3D SPECT/CT Imaging of Mice Injected with ^{99m}Tc-BP-S-MWNT: To assess the biodistribution of ^{99m}Tc-BP-S-MWNT in C57BL/6 mice, 10 mg/kg (~ 200 μg per mouse) of ^{99m}Tc-BP-S-MWNT or ^{99m}Tc-BP in 1% Pluronic® F-127 solution containing 5-10 MBq were injected intravenously *via* tail vein. SPECT imaging was carried out immediately after injection with images taken in 16 projections over 30 min using a four-head scanner Nano-SPECT/CT

scanner provided by Bioscan (USA) with 1.4 mm pinhole collimators. CT scanning was performed with a 45 kV X-ray source and 1000 ms exposure time over 10 min at the end of each SPECT acquisition. SPECT and CT images were reconstructed using the MEDISO® software supplied by Medical Imaging Systems (Hungary) and then merged by the InVivoScope® software obtained from Bioscan (USA). Each animal was recovered and further imaged at 4 and 24 h.

Organ Biodistribution of ^{99m}Tc-BP-S-MWNT in Mice by γ-Scintigraphy: The pharmacokinetic profile of ^{99m}Tc-BP-S-MWNT was measured by γ-scintigraphy after intravenous injection of ^{99m}Tc-BP-SPION-MWNT dispersed in 1% Pluronic® F-127/0.9% NaCl *via* tail vein. The blood clearance profile was obtained by collecting blood samples in heparinised capillaries from 2 min up to 24 h after injection. In order to study the organ biodistribution, major organs including skin, liver, spleen, heart, lung, muscle, bone, brain, stomach, and intestine were excised *post mortem* at 1 h, 4 h, and 24 h after injection. Injected mice were kept in metabolic cages for 24 h after injection to collect urine and faeces. Samples were weighed and the radioactivity was detected, quantified and corrected for physical radioisotope decay by γ-scintigraphy. The % ID per gram tissue was calculated and plotted as the mean of triplicate samples ± SD.

Statistical Analysis: The quantitative *in vitro* and *in vivo* data were statistically analyzed by one-way ANOVA with post hoc analysis using the Tukey test and presented as mean ± SD. The data quantitative data were also analyzed by one-way ANOVA (*$p<0.05$, **$p<0.01$, ***$p<0.001$).

Supporting Information

Supporting Information is available from the Wiley Online Library or from the author.

Acknowledgements

The authours are grateful to Thomas Swan Co. & Ltd for supplying the Elicarb MWNT samples. L. Cabana acknowledges a CSIC JAE Predoc Fellowship and is enrolled in a Materials science PhD program of the Universitat Autònoma de Barcelona. M. Bourgognon is a Marie Curie fellow.

Funding from FP7-ITN Marie-Curie Network programme RADDEL (290023), Biotechnology and Biological Sciences Research Council (BB/J008656/1), Worldwide Cancer Research (12-1054), Spanish Ministerio de Economía y Competitividad (MAT2011-24757) are acknowledged. R. T. M. de Rosales acknowledges funding by The Centre of Excellence in Medical Engineering funded by the Wellcome Trust and EPSRC under Grant No. WT 088641/Z/09/Z. K. T. Al-Jamal, G. Tobias and R. T. M. de Rosales thank the members of the EU COST actions TD1004 (Theranostics Imaging and Therapy: An Action to Develop Novel Nanosized Systems for Imaging-Guided Drug Delivery) and TD1007 (Bimodal PET-MRI molecular imaging technologies and applications for *in vivo* monitoring of disease and biological processes) for useful discussions. The XPS data was acquired at the Laboratorio de Microscopías Avanzadas (LMA) - Instituto de Nanociencia de Aragón (INA) (Spain).

Received:

Revised:

Published online:

References

(1) Heister, E.; Brunner, E. W.; Dieckmann, G. R.; Jurewicz, I.; Dalton, A. B. Are Carbon Nanotubes a Natural Solution? Applications in Biology and Medicine. *ACS Applied Materials & Interfaces* **2013**, *5*, 1870-1891.

(2) Liu, Z.; Tabakman, S.; Welsher, K.; Dai, H. Carbon nanotubes in biology and medicine: In vitro and in vivo detection, imaging and drug delivery. *Nano Res.* **2009**, *2*, 85-120.

(3) Shvedova, A.; Castranova, V.; Kisin, E.; Schwegler-Berry, D.; Murray, A.; Gandelsman, V.; Maynard, A.; Baron, P. Exposure to Carbon Nanotube Material: Assessment of Nanotube Cytotoxicity using Human Keratinocyte Cells. *Journal of Toxicology and Environmental Health, Part A* **2003**, *66*, 1909-1926.

(4) Pulskamp, K.; Diabaté, S.; Krug, H. F. Carbon nanotubes show no sign of acute toxicity but induce intracellular reactive oxygen species in dependence on contaminants. *Toxicology Letters* **2007**, *168*, 58-74.

(5) Poland, C. A.; Duffin, R.; Kinloch, I.; Maynard, A.; Wallace, W. A. H.; Seaton, A.; Stone, V.; Brown, S.; MacNee, W.; Donaldson, K. Carbon nanotubes introduced into the

abdominal cavity of mice show asbestos-like pathogenicity in a pilot study. *Nat Nano* **2008**, *3*, 423-428.

(6) Palomäki, J.; Välimäki, E.; Sund, J.; Vippola, M.; Clausen, P. A.; Jensen, K. A.; Savolainen, K.; Matikainen, S.; Alenius, H. Long, Needle-like Carbon Nanotubes and Asbestos Activate the NLRP3 Inflammasome through a Similar Mechanism. *ACS Nano* **2011**, *5*, 6861-6870.

(7) Kostarelos, K. The long and short of carbon nanotube toxicity. *Nature biotechnology* **2008**, *26*, 774-776.

(8) Bussy, C.; Pinault, M.; Cambedouzou, J.; Landry, M. J.; Jegou, P.; Mayne-L'hermite, M.; Launois, P.; Boczkowski, J.; Lanone, S. Critical role of surface chemical modifications induced by length shortening on multi-walled carbon nanotubes-induced toxicity. *Part Fibre Toxicol* **2012**, *9*, 46.

(9) Hirano, S.; Kanno, S.; Furuyama, A. Multi-walled carbon nanotubes injure the plasma membrane of macrophages. *Toxicology and Applied Pharmacology* **2008**, *232*, 244-251.

(10) Ali-Boucetta, H.; Nunes, A.; Sainz, R.; Herrero, M. A.; Tian, B.; Prato, M.; Bianco, A.; Kostarelos, K. Asbestos-like Pathogenicity of Long Carbon Nanotubes Alleviated by Chemical Functionalization. *Angewandte Chemie International Edition* **2013**, *52*, 2274-2278.

(11) Sitharaman, B.; Shi, X.; Walboomers, X. F.; Liao, H.; Cuijpers, V.; Wilson, L. J.; Mikos, A. G.; Jansen, J. A. In vivo biocompatibility of ultra-short single-walled carbon nanotube/biodegradable polymer nanocomposites for bone tissue engineering. *Bone* **2008**, *43*, 362-370.

(12) Kostarelos, K. The long and short of carbon nanotube toxicity. *Nat Biotech* **2008**, *26*, 774-776.

(13) Bianco, A.; Kostarelos, K.; Prato, M. Making carbon nanotubes biocompatible and biodegradable. *Chemical Communications* **2011**, *47*, 10182-10188.

(14) Lacerda, L.; Herrero, M. A.; Venner, K.; Bianco, A.; Prato, M.; Kostarelos, K. Carbon-Nanotube Shape and Individualization Critical for Renal Excretion. *Small* **2008**, *4*, 1130-1132.

(15) Kolosnjaj-Tabi, J.; Hartman, K. B.; Boudjemaa, S.; Ananta, J. S.; Morgant, G.; Szwarc, H.; Wilson, L. J.; Moussa, F. In Vivo Behavior of Large Doses of Ultrashort and Full-Length Single-Walled Carbon Nanotubes after Oral and Intraperitoneal Administration to Swiss Mice. *ACS Nano* **2010**, *4*, 1481-1492.

(16) Lacerda, L.; Ali-Boucettal, H.; Herrero, M. A.; Pastorin, G.; Bianco, A.; Prato, M.; Kostarelos, K. Tissue histology and physiology following intravenous administration of different types of functionalized multiwalled carbon nanotubes. *Nanomedicine* **2008**, *3*, 149-161.

(17) Tobias, G.; Shao, L.; Salzmann, C. G.; Huh, Y.; Green, M. L. H. Purification and Opening of Carbon Nanotubes Using Steam. *The Journal of Physical Chemistry B* **2006**, *110*, 22318-22322.

(18) Cabana, L.; Ke, X.; Kepic, D.; Oro-Solé, J.; Van Tendeloo, G.; Tobias, G. The role of steam treatment on the structure, purity and length distribution of multi-walled carbon nanotubes. **2015**, submitted.

(19) Datta, S.; Marty, L.; Cleuziou, J. P.; Tilmaciu, C.; Soula, B.; Flahaut, E.; Wernsdorfer, W. Magneto-Coulomb Effect in Carbon Nanotube Quantum Dots Filled with Magnetic Nanoparticles. *Physical review letters* **2011**, *107*, 186804.

(20) Spencer, J. H.; Nesbitt, J. M.; Trewhitt, H.; Kashtiban, R. J.; Bell, G.; Ivanov, V. G.; Faulques, E.; Sloan, J.; Smith, D. C. Raman Spectroscopy of Optical Transitions and Vibrational Energies of ~1 nm HgTe Extreme Nanowires within Single Walled Carbon Nanotubes. *ACS Nano* **2014**, *8*, 9044-9052.

(21) Cabana, L.; Ballesteros, B.; Batista, E.; Magén, C.; Arenal, R.; Oró-Solé, J.; Rurali, R.; Tobias, G. Synthesis of PbI_2 Single-Layered Inorganic Nanotubes Encapsulated Within Carbon Nanotubes. *Advanced Materials* **2014**, *26*, 2016-2021.

(22) Golberg, D.; Costa, P. M. F. J.; Wang, M.-S.; Wei, X.; Tang, D.-M.; Xu, Z.; Huang, Y.; Gautam, U. K.; Liu, B.; Zeng, H.; Kawamoto, N.; Zhi, C.; Mitome, M.; Bando, Y. Nanomaterial Engineering and Property Studies in a Transmission Electron Microscope. *Advanced Materials* **2012**, *24*, 177-194.

(23) Hong, S.; Tobias, G.; Al Jamal, K.; Ballesteros, B.; Ali Boucetta, H.; Lozano Perez, S.; Nellist, P.; Sim, R.; Finucane, C.; Mather, S.; Green, M. L. H.; Kostarelos, K.; Davis, B. Filled and glycosylated carbon nanotubes for in vivo radioemitter localization and imaging. *Nature Materials* **2010**, *9*, 485-490.

(24) Martincic, M.; Tobias, G. Filled carbon nanotubes in biomedical imaging and drug delivery. *Expert Opinion on Drug Delivery* **2015**, doi:10.1517/17425247.17422015.17971751.

(25) Liu, X.; Marangon, I.; Melinte, G.; Wilhelm, C.; Ménard-Moyon, C.; Pichon, B. P.; Ersen, O.; Aubertin, K.; Baaziz, W.; Pham-Huu, C.; Bégin-Colin, S.; Bianco, A.; Gazeau, F.; Bégin, D. Design of Covalently Functionalized Carbon Nanotubes Filled with Metal Oxide Nanoparticles for Imaging, Therapy, and Magnetic Manipulation. *ACS Nano* **2014**, *8*, 11290-11304.

(26) Law, J. J.; Guven, A.; Wilson, L. J. Relaxivity enhancement of aquated Tris(β-diketonate)gadolinium(III) chelates by confinement within ultrashort single-walled carbon nanotubes. *Contrast Media & Molecular Imaging* **2014**, *9*, 409-412.

(27) Lamanna, G.; Garofalo, A.; Popa, G.; Wilhelm, C.; Begin-Colin, S.; Felder-Flesch, D.; Bianco, A.; Gazeau, F.; Menard-Moyon, C. Endowing carbon nanotubes with superparamagnetic properties: applications for cell labeling, MRI cell tracking and magnetic manipulations. *Nanoscale* **2013**, *5*, 4412-4421.

(28) Julie T-W. Wang; Ciara Fabbro; Enrica Venturelli; Cécilia Ménard-Moyon; Olivier Chaloin; Tatiana Da Ros; Laura Methven; Antonio Nunes; Jane K. Sosabowski; Stephen J. Mather; Martyn K. Robinson; Julien Amadou; Maurizio Prato; Alberto Bianco; Kostas Kostarelos; Al-Jamal, K. T. The relationship between the diameter of chemically-functionalized multi-walled carbon nanotubes and their organ biodistribution profiles in vivo. *Biomaterials* **2014**, *35*, 9517-9528.

(29) Liu, Z.; Cai, W.; He, L.; Nakayama, N.; Chen, K.; Sun, X.; Chen, X.; Dai, H. In vivo biodistribution and highly efficient tumour targeting of carbon nanotubes in mice. *Nat Nano* **2007**, *2*, 47-52.

(30) McDevitt, M. R.; Chattopadhyay, D.; Kappel, B. J.; Jaggi, J. S.; Schiffman, S. R.; Antczak, C.; Njardarson, J. T.; Brentjens, R.; Scheinberg, D. A. Tumor Targeting with Antibody-Functionalized, Radiolabeled Carbon Nanotubes. *Journal of Nuclear Medicine* **2007**, *48*, 1180-1189.

(31) Rinck, P. A. *Magnetic Resonance in Medicine. The Basic Textbook of the European Magnetic Resonance Forum* **2014**, Electronic version 8.2. 8th edition.

(32) Tran, L. A.; Hernández-Rivera, M.; Berlin, A. N.; Zheng, Y.; Sampaio, L.; Bové, C.; Cabreira-Hansen, M. d. G.; Willerson, J. T.; Perin, E. C.; Wilson, L. J. The use of gadolinium-carbon nanostructures to magnetically enhance stem cell retention for cellular cardiomyoplasty. *Biomaterials* **2014**, *35*, 720-726.

(33) Choi, J. H.; Nguyen, F. T.; Barone, P. W.; Heller, D. A.; Moll, A. E.; Patel, D.; Boppart, S. A.; Strano, M. S. Multimodal Biomedical Imaging with Asymmetric Single-Walled Carbon Nanotube/Iron Oxide Nanoparticle Complexes. *Nano Letters* **2007**, *7*, 861-867.

(34) Yin, M.; Wang, M.; Miao, F.; Ji, Y.; Tian, Z.; Shen, H.; Jia, N. Water-dispersible multiwalled carbon nanotube/iron oxide hybrids as contrast agents for cellular magnetic resonance imaging. *Carbon* **2012**, *50*, 2162-2170.

(35) Wu, H.; Liu, G.; Zhuang, Y.; Wu, D.; Zhang, H.; Yang, H.; Hu, H.; Yang, S. The behavior after intravenous injection in mice of multiwalled carbon nanotube / Fe3O4 hybrid MRI contrast agents. *Biomaterials* **2011**, *32*, 4867-4876.

(36) Liu, Y.; Hughes, T. C.; Muir, B. W.; Waddington, L. J.; Gengenbach, T. R.; Easton, C. D.; Hinton, T. M.; Moffat, B. A.; Hao, X.; Qiu, J. Water-dispersible magnetic carbon nanotubes as T2-weighted MRI contrast agents. *Biomaterials* **2014**, *35*, 378-386.

(37) Ballesteros, B.; Tobias, G.; Shao, L.; Pellicer, E.; Nogués, J.; Mendoza, E.; Green, M. L. H. Steam Purification for the Removal of Graphitic Shells Coating Catalytic Particles and the Shortening of Single-Walled Carbon Nanotubes. *Small* **2008**, *4*, 1501-1506.

(38) Liu, J.; Rinzler, A. G.; Dai, H. J.; Hafner, J. H.; Bradley, R. K.; Boul, P. J.; Lu, A.; Iverson, T.; Shelimov, K.; Huffman, C. B.; Rodriguez-Macias, F.; Shon, Y. S.; Lee, T. R.; Colbert, D. T.; Smalley, R. E. Fullerene pipes. *Science* **1998**, *280*, 1253-1256.

(39) Shao, L.; Tobias, G.; Salzmann, C. G.; Ballesteros, B.; Hong, S. Y.; Crossley, A.; Davis, B. G.; Green, M. L. H. Removal of amorphous carbon for the efficient sidewall functionalisation of single-walled carbon nanotubes. *Chemical Communications* **2007**, 5090-5092.

(40) Wang, J. T. W.; Cabana, L.; Bourgognon, M.; Kafa, H.; Protti, A.; Venner, K.; Shah, A. M.; Sosabowski, J. K.; Mather, S. J.; Roig, A.; Ke, X. X.; Van Tendeloo, G.; Rosales, R. T. M.; Tobias, G.; Al-Jamal, K. T. Magnetically Decorated Multiwalled Carbon Nanotubes as Dual MRI and SPECT Contrast Agents. *Advanced Functional Materials* **2014**, *24*, 1880-1894.

(41) Grosvenor, A. P.; Kobe, B. A.; Biesinger, M. C.; McIntyre, N. S. Investigation of multiplet splitting of Fe 2p XPS spectra and bonding in iron compounds. *Surface and Interface Analysis* **2004**, *36*, 1564-1574.

(42) Ananta, J. S.; Matson, M. L.; Tang, A. M.; Mandal, T.; Lin, S.; Wong, K.; Wong, S. T.; Wilson, L. J. Single-Walled Carbon Nanotube Materials as T2-Weighted MRI Contrast Agents. *The Journal of Physical Chemistry C* **2009**, *113*, 19369-19372.

(43) Lemine, O. M.; Omri, K.; Iglesias, M.; Velasco, V.; Crespo, P.; de la Presa, P.; El Mir, L.; Bouzid, H.; Yousif, A.; Al-Hajry, A. γ-Fe2O3 by sol–gel with large nanoparticles size for magnetic hyperthermia application. *Journal of Alloys and Compounds* **2014**, *607*, 125-131.

(44) Si, S.; Kotal, A.; Mandal, T.; Giri, S.; Nakamura, H.; Kohara, T. Size-Controlled Synthesis of Magnetite Nanoparticles in the Presence of Polyelectrolytes. *Chemistry of Materials* **2004**, *16*, 3489-3496.

(45) Sethi, R.; Mackeyev, Y.; Wilson, L. J. The Gadonanotubes revisited: A new frontier in MRI contrast agent design. *Inorg. Chim. Acta* **2012**, *393*, 165-172.

(46) Brooks, R. A. T(2)-shortening by strongly magnetized spheres: a chemical exchange model. *Magnetic resonance in medicine : official journal of the Society of Magnetic Resonance in Medicine / Society of Magnetic Resonance in Medicine* **2002**, *47*, 388-391.

(47) Gillis, P.; Moiny, F.; Brooks, R. A. On T(2)-shortening by strongly magnetized spheres: a partial refocusing model. *Magnetic resonance in medicine : official journal of the Society of Magnetic Resonance in Medicine / Society of Magnetic Resonance in Medicine* **2002**, *47*, 257-263.

(48) Matsumoto, Y.; Jasanoff, A. T2 relaxation induced by clusters of superparamagnetic nanoparticles: Monte Carlo simulations. *Magn Reson Imaging* **2008**, *26*, 994-998.

(49) Chen, D. X.; Taboada, E.; Roig, A. Experimental study on T2 relaxation time of protons in water suspensions of iron-oxide nanoparticles: Cases of composite nanospheres. *Journal of Magnetism and Magnetic Materials* **2011**, *323*, 2487-2492.

(50) Laus, S.; Sitharaman, B.; Tóth, É.; Bolskar, R. D.; Helm, L.; Asokan, S.; Wong, M. S.; Wilson, L. J.; Merbach, A. E. Destroying Gadofullerene Aggregates by Salt Addition in Aqueous Solution of Gd@C60(OH)x and Gd@C60[C(COOH2)]10. *Journal of the American Chemical Society* **2005**, *127*, 9368-9369.

(51) Laus, S.; Sitharaman, B.; Tóth, É.; Bolskar, R. D.; Helm, L.; Wilson, L. J.; Merbach, A. E. Understanding Paramagnetic Relaxation Phenomena for Water-Soluble Gadofullerenes. *The Journal of Physical Chemistry C* **2007**, *111*, 5633-5639.

(52) Bolskar, R.: Gadolinium Endohedral Metallofullerene-Based MRI Contrast Agents. In *Medicinal Chemistry and Pharmacological Potential of Fullerenes and Carbon Nanotubes*; Cataldo, F., Da Ros, T., Eds.; Carbon Materials: Chemistry and Physics; Springer Netherlands, 2008; Vol. 1; pp 157-180.

(53) Torres Martin de Rosales, R.; Finucane, C.; Mather, S. J.; Blower, P. J. Bifunctional bisphosphonate complexes for the diagnosis and therapy of bone metastases. *Chemical Communications* **2009**, 4847-4849.

- Supplementary Information -

The Shortening of MWNT-SPION Hybrids by Steam Treatment Improves their Magnetic Resonance Imaging Properties *In vitro* and *In Vivo*

Laura Cabana‡, Maxime Bourgognon‡, Julie T-W. Wang, Andrea Protti, Rafael T. M. de Rosales, Ajay M. Shah, Josep Fontcuberta, Ester Tobías-Rossell, Jane K. Sosabowski, Khuloud T. Al-Jamal* and Gerard Tobias*

L. Cabana, Prof. J. Fontcuberta, Dr. G. Tobias
Institut de Ciència de Materials de Barcelona (ICMAB-CSIC)
Campus UAB, 08193 Bellaterra, Barcelona, Spain
E-mail: **gerard.tobias@icmab.es**

M. Bourgognon, Dr. J. T-W. Wang, Dr. K. T. Al-Jamal
Institute of Pharmaceutical Science
King's College London
London, SE1 9NH, UK
E-mail: **khuloud.al-jamal@kcl.ac.uk**

Dr. A. Protti, Dr. R. T. M. de Rosales
Division of Imaging Sciences and Biomedical Engineering
King's College London
St. Thomas' Hospital, London, SE1 7EH, UK

Prof. A. M. Shah, Dr. A. Protti
Cardiovascular Division, James Black Centre
British Heart Foundation Centre of Excellence, King's College London
London, SE5 9NU, UK

E. Tobías-Rossell
Escola Universitària de Ciències de la Salut de Manresa
Universitat de Vic-Universitat Central de Catalunya
Av. Universitària 4-6, 08242 Manresa, Barcelona, Spain

Dr. J. K. Sosabowski
Centre for Molecular Oncology
Barts Cancer Institute
Queen Mary University of London
London, EC1A 7BE, UK

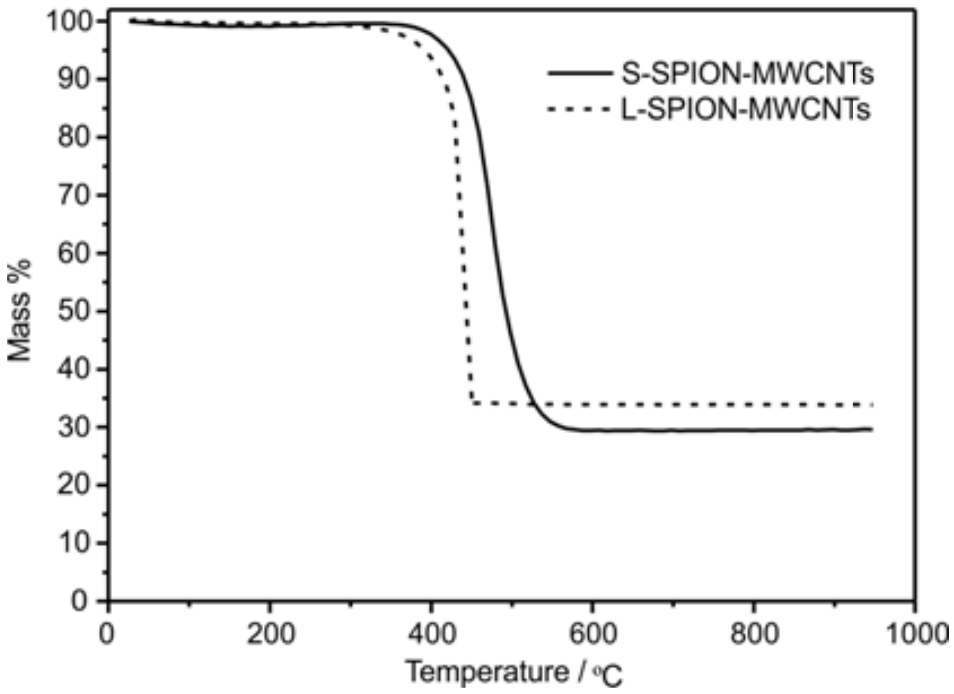

Figure S1: Thermogravimetric analysis under air of S-SPION-MWNTs and L-SPION-MWNTs.

Sample	N Number of measured SPION	Median	Lower adjacent observation	Q1 25th percentile	Q3 75th percentile	Maximum adjacent observation	Maximum observation
S-SPION-MWNTs	186	5.66	2.29	4.25	7.84	13.11	23.82
L-SPION-MWNTs	172	6.13	2.19	4.90	8.32	13.07	29.56

Table S1. Descriptive analysis of particle size distribution for S-SPION-MWNTs and L-SPION-MWNTs

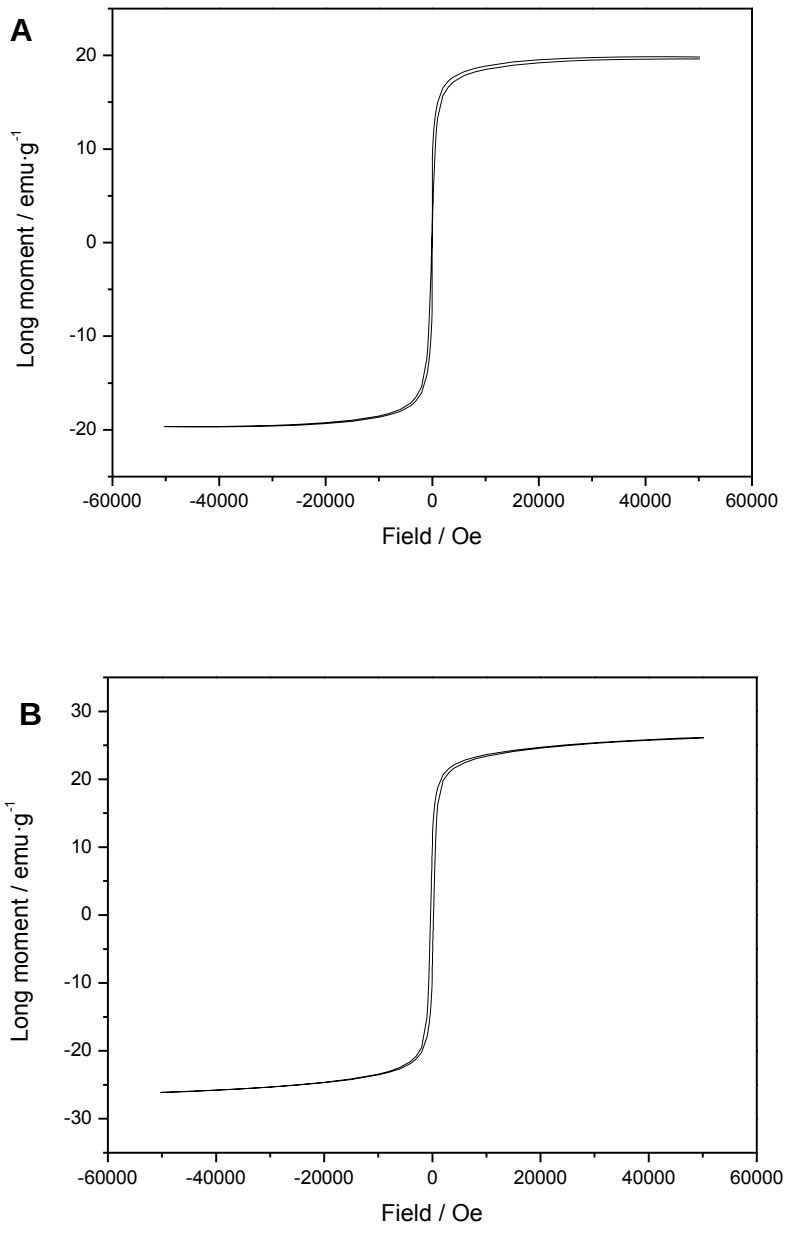

Figure S2: Hysteresis loops at 10 K after subtracting the linear background. (A) L-SPION-MWNTs, (B) S-SPION-MWNTs.

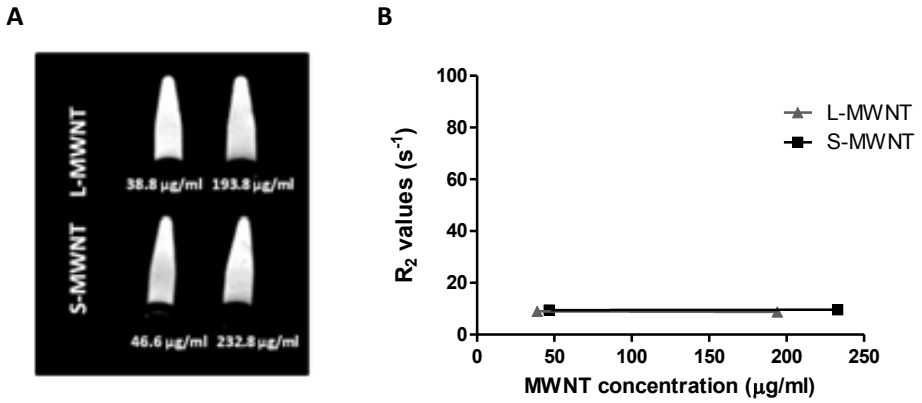

Figure S3: Phantom MR imaging of pristine MWNTs (L-MWNTs and S-MWNTs). Samples were dispersed in 1% agar solution and imaged using a 7 Tesla (7T) preclinical MR scanner. Both pMWNT showed long relaxation times where R_2* measurements were affected by the external magnetic field inhomogeneity. In order to obtain reliable measurements, R_2 was preferred to R_2*. **(A)** Phantom MR imaging of S-MWNT and L-MWNT at same MWNT concentration used for relaxation rate measurements of S-SPION-MWNT and L-SPION-MWNT; **(B)** R_2 relaxation rate analysis as a function of Fe concentration. Results are presented as mean ± S.D. Both hybrids show negligible r_2 values (n=3).

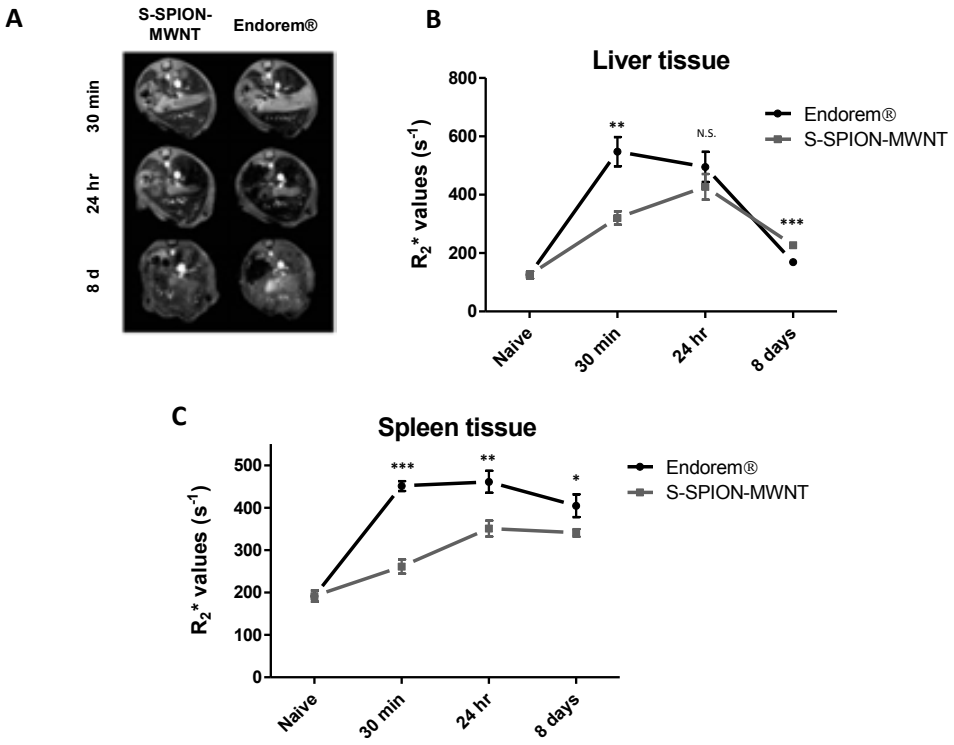

Figure S4: *In vivo* R_2*-weighted MR studies in liver and spleen after intravenous injection of S-SPION-MWNT (2.9 mg (Fe)/kg). (A) *In vivo* T_2*-weighted MR images of liver at 7T; **(B)** *In vivo* R_2* relaxation rate measurements in liver tissue. **(C)** *In vivo* R_2* relaxation rate measurements in spleen tissue. Results are expressed as mean ± SD (n=3). *P<0.05, **P<0.01 relative to the naïve condition by analysis of variance (ANOVA) with post hoc analysis by the Tukey test.

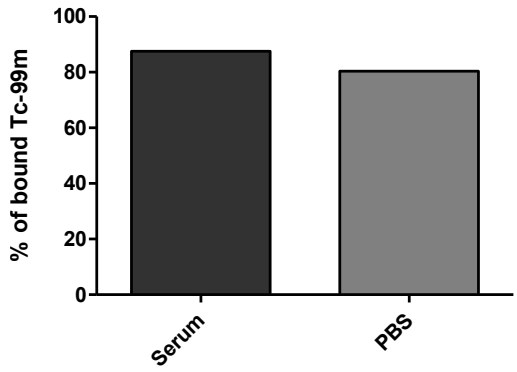

Figure S5: Stability of ^{99m}Tc-BP-S-MWNT. Serum (50%) and PBS stability studies of radio-labelled S-SPION-MWNT after 24 h incubation at 37°C.

Journal Name

RSCPublishing

COMMUNICATION

Localized Metallacarboranes on Single-Wall Carbon Nanotubes for Boron Carriers

Cite this: DOI: 10.1039/x0xx00000x

Laura Cabana,[a,†] Arántzazu González-Campo,[a,†] Xiaoxing Ke,[b] Gustaaf Van Tendeloo,[b] Rosario Núñez,*[a] Gerard Tobias,*[a]

Received 00th January 2012,
Accepted 00th January 2012

DOI: 10.1039/x0xx00000x

www.rsc.org/

Herein we covalently functionalize single-walled carbon nanotubes with cobaltabisdicarbollide anions by different methods in order to develop new boron carrier agents. The functionalized SWCNTs can be dispersed in water and localization of boron clusters on the walls has been corroborated using high-resolution transmission electron microscopy

Preparation of boron carriers has attracted high interest due to their application in a wide range of fields such as materials science, nanotechnology and medicine.[1] One of the most used boron clusters for boron delivery are the carborane clusters and derivatives due to their high thermal and chemical stability together with their low toxicity.[2] Several strategies have been followed to prepare boron-enriched molecules using carborane clusters with high solubility in water for mainly biomedical applications.[1] One important strategy is the functionalization of dendrimers with neutral and anionic carborane clusters to have a control of the number of boron atoms with the combination of the properties of the dendritic molecule.[3] Furthermore, metallacarboranes have become also important thanks to variety of metals used and modulation of their final properties. From all of them, the cobaltabisdicarbollide sandwich anion, [3,3'-$Co(C_2B_9H_{11})_2]^-$, has emerged as a suitable building block for the preparation of boron carries drugs. It has been used in medicine as specific inhibitor of HIV protease and for boron neutron capture therapy (BNCT).[4] Noticeable are the recent studies demonstrating that it can assemble into monolayer vesicles in water, can cross through synthetic lipid membranes without disrupting membrane integrity to accumulate *in vitro* within living cells, ant it can be visualized *in vivo*.[5] On the other hand, Single-Walled Carbon Nanotubes (SWCNTs) are promising materials for biomedical applications,[6] as they are able to penetrate biological barriers and to be internalized by the nucleus without any toxic effects.[7] Because of its high surface area it is possible to chemically modify them to increase its biocompatibility.[8] Hence, SWCNTs are promising nanomaterials for both therapy (drug delivery) and diagnosis.[9] However, the main drawback of this family of nanomaterials is that its biomedical applications are discouraged due to its tendency to form bundles and its hydrophobicity.[10] Many studies have been conducted with the purpose to increase solubility of SWCNTs in water,[11] including covalent[12] and non-covalent[13] functionalization and chemical oxidation.[14] However, there is still more improvement to be done in this sense, because the dispersion stability is not ensured to be enough for *in vivo* studies. The combination of boron clusters and SWCNTs could entail an improvement in the group of boron carriers, due to the exceptional properties of both. First attempts of incorporation of boron clusters to SWCNTs were made by the encapsulation of *o*-carborane clusters into SWCNTs with the inconvenient for the boron release process.[15] Additionally, side walls attachment of neutral and anionic *o*-carborane clusters were tried via covalent bonds or physisorption onto functionalized SWCNTs.[16,17] Although initially the results obtained showed that the covalently modified SWCNTs with neutral and anionic *o*-carboranes were tumor-specific, modifications to improve the solubility and the boron concentration are still necessary.[16]

With the aim of using SWCNTs as potential carriers for delivery of boron in the current work we explore a strategy to increase the amount of boron as well as improving their solubility in water by covalently functionalizing the nanotubes with

a Institut de Ciència de Materials de Barcelona (ICMAB-CSIC), Campus Universitari de la UAB. 08193, Bellaterra (Spain)
b Electron Microscopy for Materials Research (EMAT), University of Antwerp, Groenenborgerlaan 171, B-2020, Antwerp (Belgium)
† Equal contribution
Electronic Supplementary Information (ESI) available: Experimental details, supplementary figures (FT-IR and XPS spectra, TGA curves). See DOI: 10.1039/c000000x/

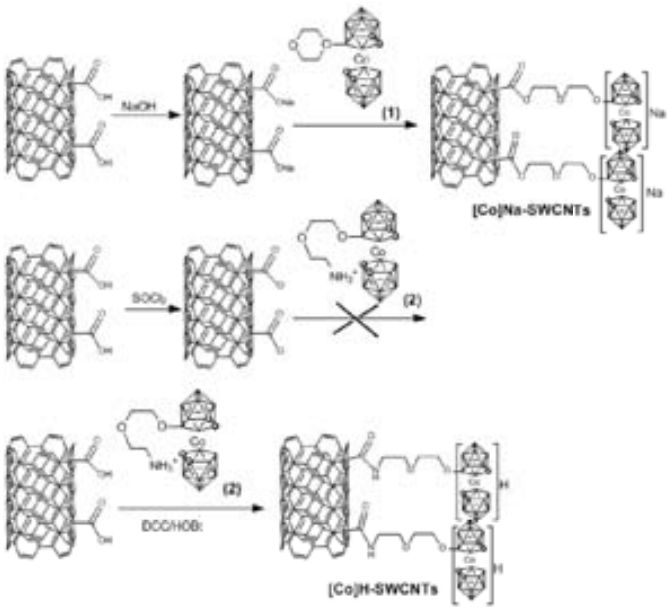

Scheme 1. Synthetic strategies to functionalize SWCNTs with [3,3-Co(1,2-$C_2B_9H_{11})_2$)]$^-$ anions

cobaltabisdicarbollide anions. Furthermore, we assess the enhancement in the individualization of SWCNTs when incorporating these clusters to the structure and the location of the clusters on the sidewalls of the carbon nanotubes.

The three strategies developed to functionalize covalently SWCNTs with cobaltabisdicarbollide anions (Co), are outlined in Scheme 1. The first one involved the *in situ* ring-opening of **1**[18] by reaction with preactivated COONa-SWCNTs in anhydrous DME, which allowed successful immobilization of cobaltabisclicarbolide anions as sodium salts ([Co]Na-SWCNTs). For the second strategy and in order to control the ring-opening step, the dioxane ring was opened to obtain **2**[19] before the reaction with preactivated COCl-SWCNTs. However, this strategy was unsuccessful, due to the instability of **2** in presence of $SOCl_2$. As an alternative, **2** was reacted with preactivated COOH-SWCNTs with DCC/HBOBt, allowing to obtain the corresponding functionalized SWCNTs ([Co]H-SWCNTs), as protonated salts .

One way to successfully assess the functionalization of the SWCNTs was to use FTIR spectroscopy (Figure S1). The observation of the ν(B–H) vibration band at 2525 and 2535 cm^{-1} for ([Co]Na-SWCNTs and ([Co]H-SWCNTs respectively, confirmed the presence of the carborane anions. On the other hand, the band at 1620 cm^{-1} related to the C=C stretching mode for the fundamental SWCNT mode was downshifted to 1587 cm^{-1} for the functionalized SWCNTs. Furthermore, a decrease of the relative intensive of the C=O stretching in the carboxylic acid groups band at 1740 cm^{-1} together with the appearance of a band at 1621 cm^{-1} for the [Co]H-SWCNTs assigned to the ν(NC=O) vibration band also indicated the right functionalization.

By conducting thermogravimetric analysis (TGA) and X-ray Photoelectron Spectroscopy (XPS) measurements, it was also possible to assess the presence of the cobaltabisdicarbollide

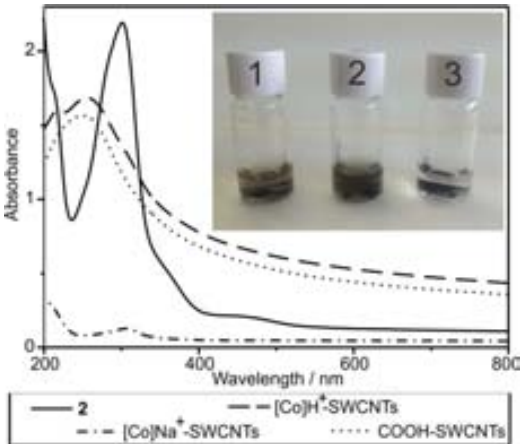

Fig. 1: UV-Vis spectra of oxidized SWCNTs, **2**, COOH-SWCNTs, [Co]H-SWCNTs and [Co]Na-SWCNTs. Inset picture: 1 mg/ml dispersions in water of COOH-SWCNTs (vial 1), [Co]H-SWCNTs (vial 2), [Co]Na-SWCNTs (vial 3).

anions. The TGA analysis of the functionalized SWCNTs showed one-step weight losses at around 450 ºC and the weight recovered at 900 ºC was 12.83 for [Co]Na-SWCNTs % and 9.00 % and for [Co]H-SWCNTs, indicating a similar degree of functionalization (Figure S2). Moreover, the XPS measurements showed that both B and Co were detected in the acquired hybrids. Even more, it can be clearly stated that the ratio between B and Co was of around 20:1 in both cases (Figure S3-S4 and Table S1). This value is the same than in cobaltabisdicarbollide anion before the functionalization, meaning that it remains its structure during the whole process.

One of the main issues when using CNTs for biomedical applications is its lack of dispersibility in aqueous media. In order to assess the dispersibility of the functionalized SWCNTs in water, UV-Vis spectroscopy studies were performed with solutions of 1 mg/ml (Figure 1). Hence, freshly aqueous solutions (1 mg/ ml) were prepared and only [Co]H-SWCNTs presented a good dispersibility (inset Figure 1). Therefore, the absorption value at λ = 500 nm was selected to value the degree of dispersion of [Co]Na-SWCNTs and [Co]H-SWCNTs compared to the COOH-SWCNTs.[7c] In water, the relative absorbance value of COOH-SWCNTs was fixed as 100 % and higher dispersibility was obtained for [Co]HSWCNTs (117 %), confirming the correct functionalization and the effect of the cobaltabisdicarbollide anions. However, the [Co]Na-SWCNTs presented lower degree of dispersion (8 %). This suggests that besides the functionalization with cobaltabisdicarbollide anions, the counterion used is essential to define the properties and the further application of the functionalized SWCNTs. On the other hand, **2** presented two bands with maximum absorbance at 213 nm and 300 nm. The UV-Vis spectrum of [Co]H-SWCNTs presented two broad bands at 217 and 256 nm, which also confirm the correct functionalization. While the band at 217 nm indicates the presence of cobaltabisdicarbollide anion, the broad band at 256 nm exhibits higher intensity and was shifted with respect to the COOH-SWCNTs confirming that functionalization provides better dispersed and more individualized SWCNTs in aqueous solution. On the contrary, for [Co]Na-SWCNTs there is no absorbance in

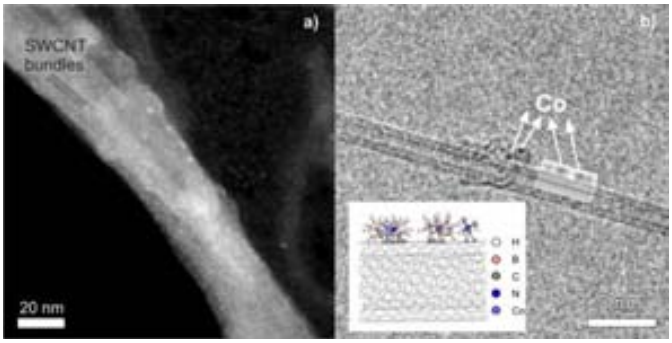

Fig. 2. STEM and HRTEM analysis of the material a) Dark field STEM image of $[Co]H^+$-SWCNTs. b) HRTEM of a carborane cluster attached to the wall of a DWCNT with the corresponding simulation (inset) and model.

the UV-Vis region due to the poor solubility of the functionalized nanotubes. However, the presence of a band at 305 nm from the cobaltabisdicarbollide anion suggests that a small fraction of the [Co]Na-SWCNTs are dispersed in the aqueous solution. It is important to highlight that after 3 months the dispersion of [Co]H-SWCNTs and COOH-SWCNTs solutions were still of very dark colour, being then very stable dispersions (Figure S5).

Besides the general bulk techniques, direct imaging of the cobaltabisdicarbollide anions immobilized on the side-walls of the SWCNTs was performed using high-resolution transmission electron microscopy (HRTEM) and scanning transmission electron microscopy (STEM) of [Co]H-SWCNTs (Figure 2). From our best knowledge it is the first time that carborane clusters are visualized and localized upon immobilization on SWTNs. The Z-constrast dark field STEM images a bundle of SWCNTs was detected with various bright dots surrounding the walls, Figure1a. Those evidently correspond to each of the Co atoms from the carborane structure, as they are much heavier than the rest of the elements in the cluster. To better display the attachment of the cluster to the nanotube, HRTEM imaging was also done (Figure 2b). Hence, one SWCNT was displayed, containing several aggregates on top of its walls. In this scenario, Co presents in the carborane structure will originate dark contrast. This was further confirmed, by conducting HRTEM simulation (inset Figure2b), in which it was illustrated how the Co in a dark contrast was surrounded by lower contrast agglomerates, related to the clustered structure, and being in good agreement with the experimental HRTEM imaging. Moreover, a model of the hybrid was constructed for comparison, indeed fitting with the experimental results. Therefore, we have demonstrated that the SWCNTs have been successfully functionalized with the cobaltabisdicarbollide anions

In summary, we have demonstrated that cobaltabisdicarbollide anions have been chemically linked to the walls of SWCNTs, leading new hybrids with higher dispersibility in water than the pure oxidized nanotubes. Moreover, we have observed that the dispersity of the new functionalized carbon nanotubes depends on the counterion of the metallacarboranes. Different techniques have been used to confirm the successful functionalization and composition of the modified nanotubes. Notably, the visualization for the first time of the cobaltabisdicarbollide anions on the nanotubes was achieved using HRTEM and STEM, which clearly evidences the attachment of the anionic boron clusters. Therefore, this new hybrid is a very suitable agent as boron carrier for cancer treatment and drug-resistant infection. Further studies in this direction are underway.

The research leading to these results has received funding from MINECO (MAT2011-24757) and (CTQ2013-44670-R), Generalitat de Catalunya (2014/SGR/149) and the European Union Seventh Framwork Programme under Grant Agreements 90023-RADDEL (FP7ITN). L.C. and A.G-C acknowledge a JAE-Predoc and a JAE-DOC fellowship (CSIC).

Notes and references

This work is involved in the Materials Science PhD Program of the Universitat Autònoma de Barcelona

1. (a) R. N. Grimes, in *Carboranes (Second Edition)*, ed. R. N. Grimes, Academic Press, Oxford, 2011, pp. 1053-1082; (b) R. F. Barth, J. A. Coderre, M. G. H. Vicente and T. E. Blue, *Clin. Cancer Res.*, 2005, **11**, 3987. c) N. A. Hosmane, in Boron Science, New Technologies and Applications, CRC Press, Taylor & Francis Group, New York, 2012.

2. G. Calabrese, J. J. Nesnas, E. Barbu, D. G. Fatouros and J. Tsibouklis, *Drug Discovery Today*, 2011, **17**, 153.

3. a) A. González-Campo, C. Viñas, F. Teixidor, R. Núñez, R. Kivekäs, R. Sillanpää, *Macromolecules* 2007, 40, 5644; b) A. González-Campo, A. Ferrer-Ugalde, C. Viñas, F. Teixidor, R. Sillanpää, J. Rodríguez-Romero, R. Santillan, N. Farfán, R. Núñez, *Chem. Eur. J.*, 2013, **19**, 6299.

4. a) P. Cígler, M. Kožíšek, P. Řezáčová, J. Brynda, Z. Otwinowski, J. Pokorná, J. Plešek, B. Grüner, L. Dolečková-Marešová, M. Máša, J. Sedláček, J. Bodem, H.-G. Kräusslich, V. Král and J. Konvalinka, *Proceedings of the National Academy of Sciences*, 2005, **102**, 15394. b) P. Farràs, E. J. Juárez-Pérez, M. Lepsik, F. Luque, R. Núñez, F. Teixidor, *Chem. Soc. Rev.* 2012, **41**, 3445.

5 a) P. Bauduin, S. Prevost, P. Farràs, F. Teixidor, O. Diat and T. Zemb, Angew. Chem., Int. Ed., 2011, 50, 5298. b) M. Tarrés, E. Canetta, C. Viñas, F. Teixidor and A. J. Harwood, Chem. Commun., 2014, 50(51), 3370. c) K. B. Gona, A. Zaulet, V. Gómez-Vallejo, F. Teixidor, J. Llop, C. Viñas, Chem. Commun. 2014, 50, 11415-11417.

6. (a) A. Bianco, K. Kostarelos, C. D. Partidos and M. Prato, *Chemical Communications*, 2005, 571; (b) Z. Liu, S. Tabakman, K. Welsher and H. J. Dai, *Nano Res.*, 2009, **2**, 85; (c) M. Adeli, R. Soleyman, Z. Beiranvand and F. Madani, *Chem Soc Rev*, 2013, **42**, 5231

7. (a) N. W. S. Kam, M. O'Connell, J. A. Wisdom and H. J. Dai, *Proceedings of the National Academy of Sciences of the United States of America*, 2005, **102**, 11600; (b) C. Klumpp, K. Kostarelos, M. Prato and A. Bianco, *Biochimica et Biophysica Acta (BBA) - Biomembranes*, 2006, **1758**, 404; (c) K. Kostarelos, L. Lacerda, G. Pastorin, W. Wu, WieckowskiSebastien, J. Luangsivilay, S. Godefroy, D. Pantarotto, J.-P. Briand, S. Muller, M. Prato and A. Bianco, *Nat Nano*, 2007, **2**, 108; (d) M. Mahmood, Y. Xu, V. Dantuluri, T. Mustafa, Y. Zhang, A. Karmakar, D. Casciano, S. Ali and A. Biris, *Nanotechnology*, 2013, **24**, 045102.

8. (a) N. W. S. Kam, M. Shim, N. Shi Kam, R. Chen, Y. Li and H. Dai, *Nano Letters*, 2002, **2**, 285; (b) A. Battigelli, C. Ménard-Moyon, T. Da Ros, M. Prato and A. Bianco, *Advanced Drug Delivery Reviews*, 2013, **65**, 1899; (c) P. Luksirikul, B. Ballesteros, G. Tobias, M. Moloney and M. L. H. Green, *Journal of materials chemistry*, 2011, **21**, 19080; (d)M.

Prato, K. Kostarelos and A. Bianco, *Accounts of chemical research*, 2007, **41**, 60.

9. (a) Z. Liu, K. Yang and S.-T. Lee, *Journal of Materials Chemistry*, 2011, **21**, 586; (b) K. Kostarelos, A. Bianco and M. Prato, *Nat Nano*, 2009, **4**, 627; (c) A. De La Zerda, C. Zavaleta, S. Keren, S. Vaithilingam, S. Bodapati, Z. Liu, J. Levi, B. R. Smith, T. J. Ma, O. Oralkan, Z. Cheng, X. Y. Chen, H. J. Dai, B. T. Khuri-Yakub and S. S. Gambhir, *Nature nanotechnology*, 2008, **3**, 557; (d) S. R. Ji, C. Liu, B. Zhang, F. Yang, J. Xu, J. Long, C. Jin, D. L. Fu, Q. X. Ni and X. J. Yu, *Biochimica et biophysica acta*, 2010, **1806**, 29.

10. M. O'Connell, P. Boul, L. Ericson, C. Huffman, Y. Wang, E. Haroz, C. Kuper, J. Tour, K. Ausman and R. Smalley, *Chemical Physics Letters*, 2001, **342**, 265.

11. (a) C. G. Salzmann, B. T. T. Chu, G. Tobias, S. A. Llewellyn and M. L. H. Green, *Carbon*, 2007, **45**, 907; (b) Y. Maeda, S.-i. Kimura, Y. Hirashima, M. Kanda, Y. Lian, T. Wakahara, T. Akasaka, T. Hasegawa, H. Tokumoto, T. Shimizu, H. Kataura, Y. Miyauchi, S. Maruyama, K. Kobayashi and S. Nagase, *The journal of physical chemistry. B*, 2004, **108**, 18395.

12. P. Singh, S. Campidelli, S. Giordani, D. Bonifazi, A. Bianco and M. Prato, *Chemical Society Reviews*, 2009, **38**, 2214.

13. P. Bilalis, D. Katsigiannopoulos, A. Avgeropoulos and G. Sakellariou, *RSC Advances*, 2014, **4**, 2911.

14. (a) V. Datsyuk, M. Kalyva, K. Papagelis, J. Parthenios, D. Tasis, A. Siokou, I. Kallitsis and C. Galiotis, *Carbon*, 2008, **46**, 833; (b) G. Tobias, L. Shao, B. Ballesteros and M. L. H. Green, *Journal of nanoscience and nanotechnology*, 2009, **9**, 6072.

15 D. A. Morgan, J. Sloan and M. L. H. Green, *Chemical Communications*, 2002, 2442.

16. Z. Yinghuai, A. Peng, K. Carpenter, J. Maguire, N. Hosmane and M. Takagaki, *Journal of the American Chemical Society*, 2005, **127**, 9875.

17. S. N. Yannopoulos, G. D. Zouganelis, S. Nurmohamed, J. R. Smith, N. Bouropoulos, G. Calabrese, D. G. Fatouros and J. Tsibouklis, *Nanotechnology*, 2010, **21**, 85101.

18. P. Farràs, F. Teixidor, R. Kivekäs, R. Sillanpää, C. Viñas, B. Grüner, I. Cisarova, *Inorg. Chem*., 2008, **47**, 9497.

19. E.J. Juárez-Pérez, M. Granier, C. Viñas, P.H. Mutin, R. Núñez, *Chem Asian J.*, 2012, **7**, 277.

-Supporting Information-

Localized Metallacarboranes on Single-Wall Carbon Nanotubes for Boron Carriers

Laura Cabana,[a] Arantzazu Gonzalez-Campo,[a] Xiaoxing Ke,[b] Gustaaf Van Tendeloo,[b] Gerard Tobias,[a] Rosario Núñez[a]

a Institut de Ciència de Materials de Barcelona (ICMAB-CSIC), Campus Universitari de la UAB. 08193, Bellaterra (Spain)

b Electron Microscopy for Materials Research (EMAT), University of Antwerp, Groenenborgerlaan 171, B-2020, Antwerp (Belgium)

† Equal contribution

Experimental Section

Materials:

Carbon nanotube (CNTs) samples were supplied by Thomas Swan & Co. Ltd as a dry powder. The average diameter of the CNTs is about 2.1 nm (value provided by the supplier). As-made samples contain impurities like amorphous carbon, graphitic particles (carbonaceous crystalline materials having few graphitic layers) and some metal particles. Moreover, the metal catalyst particles used for the SWCNT synthesis, are covered by graphitic shells which inhibit their dissolution during a simple acid wash. Therefore, the as-received SWCNT material was steam purified.[1,2] Briefly, SWCNTs were ground with an agate mortar and pestle, and placed into a silica tube (about 40 mm diameter) which was then introduced into the alumina tube of the furnace. Steam was introduced by bubbling argon (190 mL min^{-1}) through a flask containing hot water (98 ºC). The whole system was initially purged with argon for 2 h to ensure the complete removal of oxygen, before heating the furnace to 900 ºC to allow the purification of the material. This treatment is known to remove the amorphous carbon present in the sample and the graphitic shells that are covering the metal particles. The removal of amorphous carbon is an essential step for further functionalization.[3] The solid powder was collected and treated with HCl to remove the now exposed metal nanoparticles. The purified SWCNTs were then refluxed with nitric acid for 45 h in order to functionalize them. This treatment introduces oxygen bearing functionalities onto the SWCNT tips and sidewalls, mainly carboxylic acid groups (-COOH).[4] The functionalized SWCNTs were collected by filtration through a 0.2 μm polycarbonate membrane and thoroughly washed with water until neutral pH. In order to eliminate any possible humidity present in the

SWCNTs due to atmosphere exposure, those were heated overnight in a round bottom flask at 100 ºC. Afterwards, the flask was purged with bubbling argon and vacuum for 3 times to remove any traces of oxygen. Then, sample is left under vacuum for 6 hours to finally obtain a completely dry powder.

The synthesis of the metallacarboranes and the funtionzalization of the SWCNTs were carried under N_2 atmosphere using standard Schelenck techniques. Solvents were reagent grade and were purified by distillation over appropriate drying agents before use. $Cs[3\text{-}Co\text{-}1,2\text{-}(C_2B_9H_{11})_2]$ was purchased from Katchem Ltd. (Prague) and used as received. $[3,3'\text{-}Co(8\text{-}C_4H_8O_2\text{-}1,2\text{-}C2B_9H_{10})(1',2'\text{-}C_2B_9H_{11})]^{5\text{-}7}$ (**1**) and $[H][8\text{-}NH_2\text{-}C_4H_8O_2\text{-}3,3\text{-}Co(1,2\text{-}C_2B_9H_{10})(1,2\text{-}C_2B_9H_{11})]^{8}$ (**2**) were prepared according to the literature procedures. All the reactions were performed under inert atmosphere otherwise it is indicated.

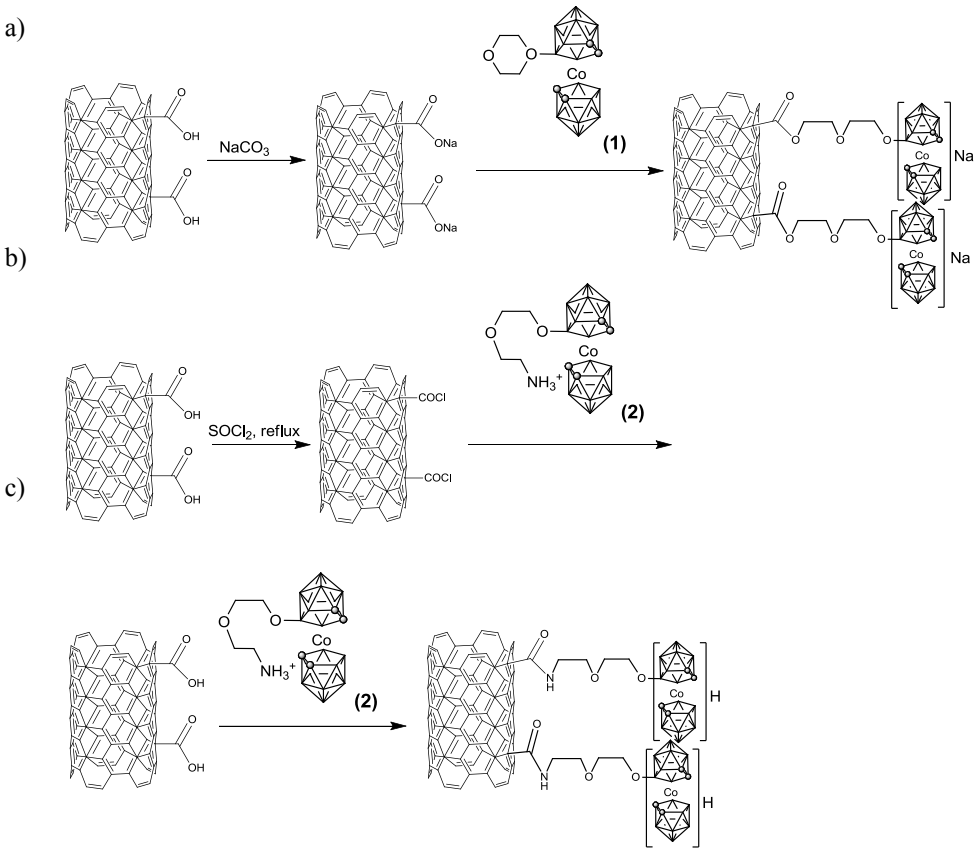

Scheme 1. Functionalization of SWCNTs with carborane clusters

Methology A:

SWCNTs were activated following literature methods.[9] Briefly, acid treated SWCNTs (15 mg) were mixed with a solution of 10 M NaOH in water (10 mL) for 5h at 90 ºC. The mixture was filtered through a 0.2 μm polycarbonate membrane and thoroughly washed with water. Then, the collected CNTs-COONa were dried under vacuum at 60ºC to remove the traces of water. Afterwards, the flask was purged with bubbling argon and vacuum for 3 times to remove any traces of oxygen and a solution of **1** (22 mg) in anhydrous DME (5 mL) was added dropwise. The mixture was then stirred at room temperature for 72h. The solvent was removed and the final [Co]Na-SWCNTs were washed with EtOH, filtered through the polycarbonate membrane, washed with MeOH and dried.

Methology B:

SWCNTs were activated following literature methods.[10] Briefly, acid treated SWCNTs (15 mg) were heated at 65 ºC in thionyl chloride (5 mL) for 24h. After this time the solvent was removed under vacuum and a solution of **2** (46.3 mg) in dried DMF (5 mL) was added to the thionyl chloride treated SWCNTs. After 96h, the mixture was cooled at room temperature and 10 mL of MeOH was added. The product was filtered through the polycarbonate membrane, washed with MeOH and dried.

Methology C:

SWCNTs were activated following literature methods.[10] Briefly, acid treated SWCNTs (15 mg) were preactivated with DCC/HOBt (20.6 mg/13.5 mg) in dried DMF (5 mL). After 45 min, a solution of **2** (24 mg) in dried DMF (3 mL) was added. The mixture was then stirred at room temperature for 72h. After this time, the solvent was removed under vacuum and 10 mL of MeOH was added. The final mixture was filtered through the polycarbonate membrane, washed with MeOH and dried to get the final functionalized [Co]H-SWCNTs.

Instrumentation:

Fourier Transform Infrared Spectroscopy (FTIR)

FTIR spectra were recorded in the transmission mode with a Perkin Elmer Spectrum One spectrometer at 4 cm^{-1} resolution by co-ading 10 scans. Thin films of carborane-SWCNT hybrids were prepared on top of a ZnSe disk (2 mm thickness) by drop-drying sample dispersions on 2-propanol onto the preheated substrate at 80 ºC.[11]

Thermogravimetric Analysis (TGA)

TGA analyses were performed under flowing air at a heating rate of 10°C/min up to 950°C (Jupiter®, Netzsch Instrument, Germany).

X-ray Photoelectron Spectroscopy

XPS were acquired with a Kratos AXIS ultra DLD spectrometer with an Al Kα X ray font and a power of 120 W. Samples were measured as dry powder. Survey-scan was conducted with a Pass Energy of 160 eV and high resolution scans at a Pass Energy of 20 eV. Hybrid-slot lens mode was employed, with an area of analysis of 700 x 300 microns.

Electron Microscopy

HRTEM images were acquired using an FEI Tecnai G2 microscope operating at 200 kV. STEM and HRTEM samples were prepared by dispersing a small amount of powder in absolute ethanol and sonicated in an ultrasonic power bath. Afterwards, the dispersion was drop dried onto a lacey carbon TEM grid.

Ultraviolet-Visible spectroscopy

The dispersions of the hybrids were characterized using a Cary 5 Varian UV/Vis/NIR spectrophotometer, operating between 200-800 nm.

Supplementary figures

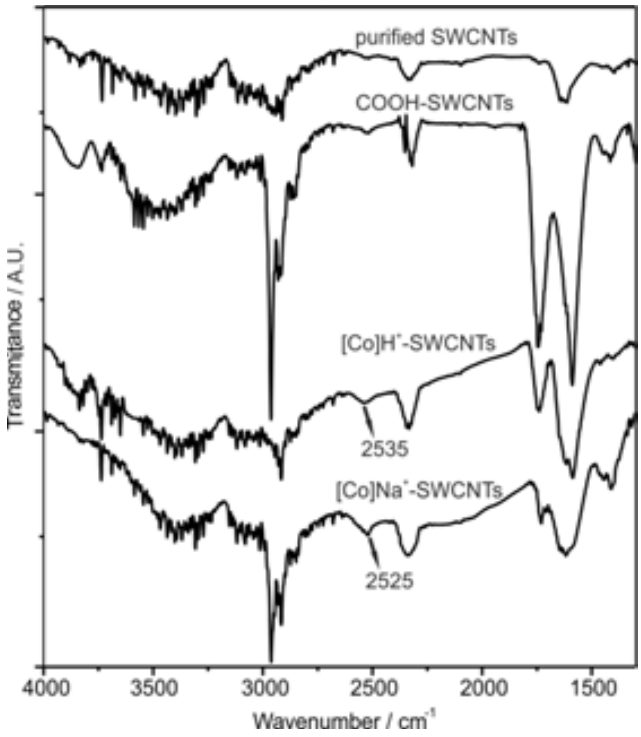

Figure S1 . FT-IR spectra of purified SWCNTs, COOH-SWCNTs, of [Co]Na-SWCNTs and [Co]H-SWCNTs.

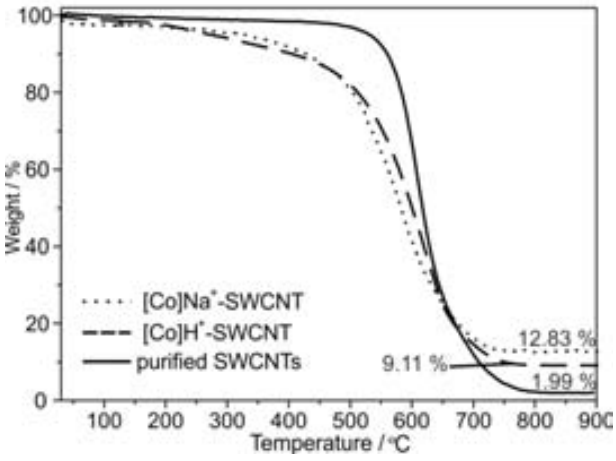

Figure S2. TGA curves of purified SWCNTs, $[Co]H^+$-SWCNTs and $[Co]Na^+$-SWCNTs.

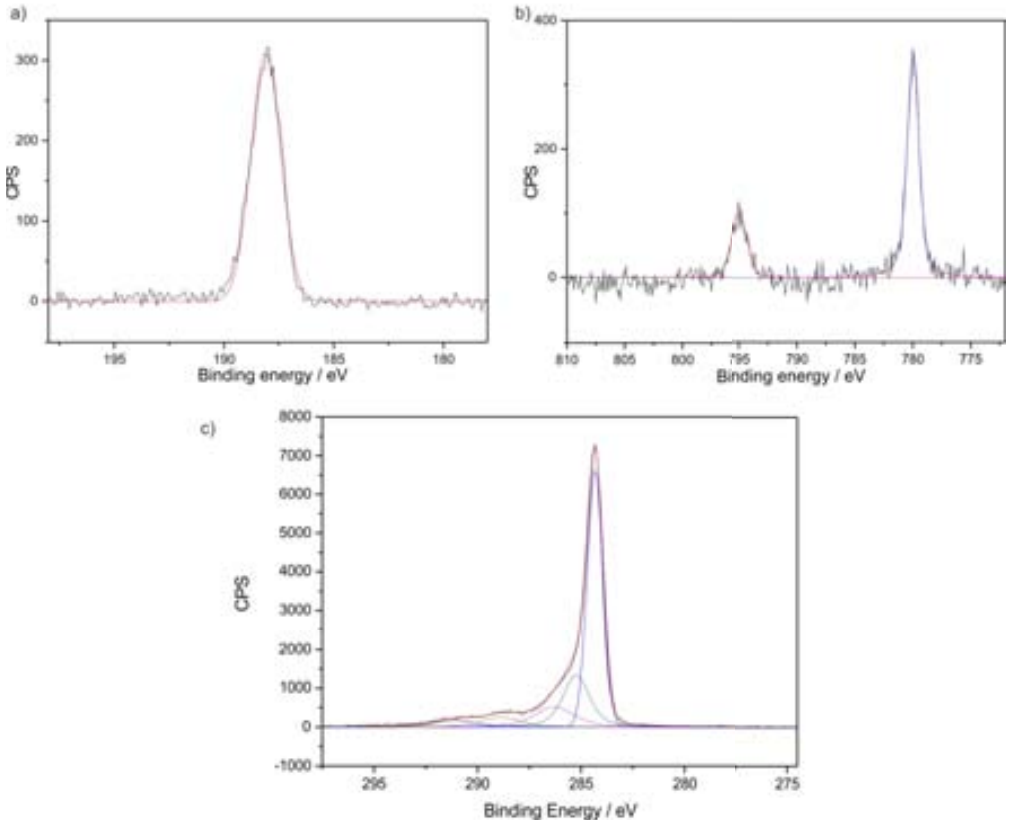

Figure S2. XPS spectra of [Co]Na-SWCNTs of (a) B1s, (b) Co 2p and (c) C1s

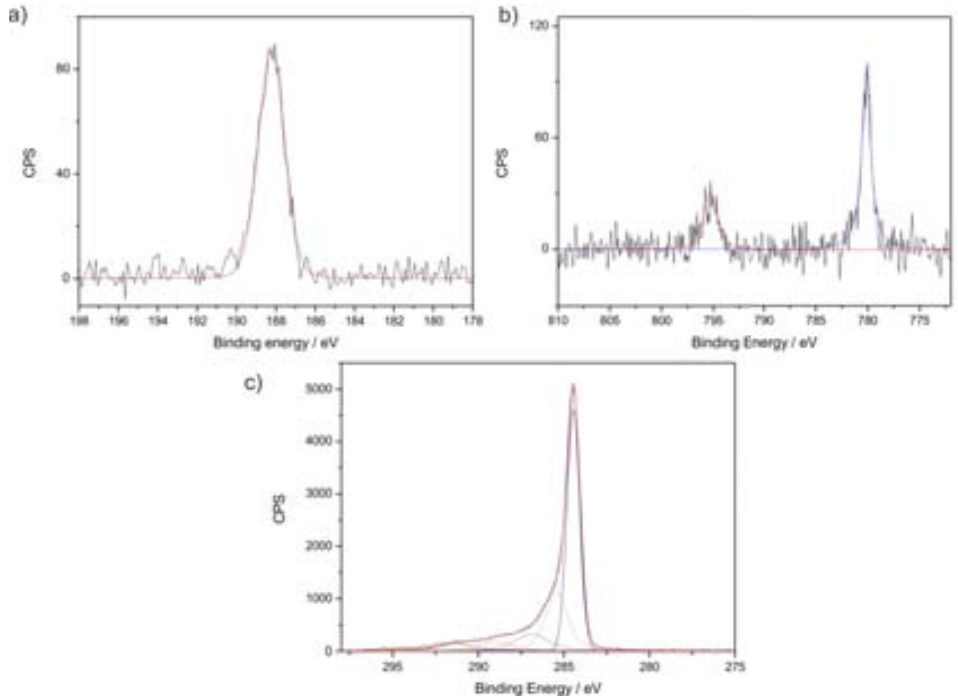

Figure S3. XPS spectra of [Co]H-SWCNTs of (a) B1s, (b) Co 2p and (c) C1s

Table 1: B:Co atomic ratio determined by integration over the high resolution B 1s and the Co 2p3/2 regions in the XPS spectra.

	Atomic ratio	
Element	**[Co] H^+-SWCNTs**	**[Co]Na^+-SWCNTs**
B	20	19
Co	1	1

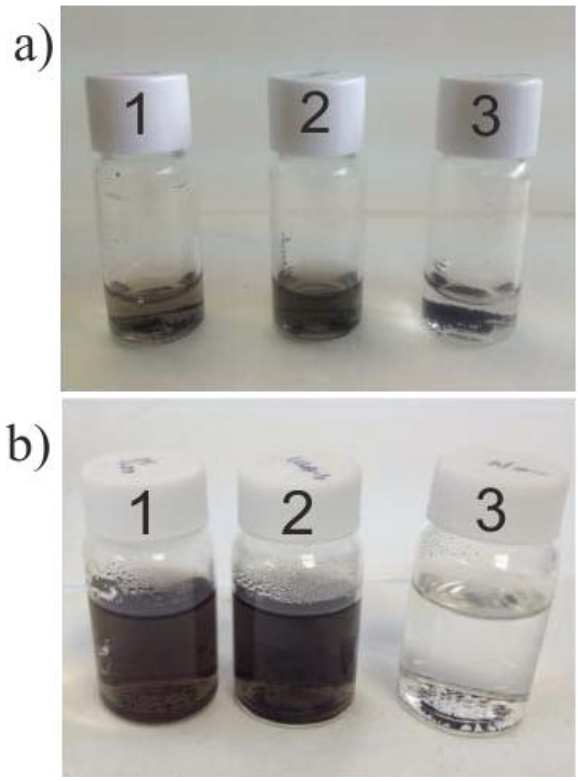

Figure S4 : 1 mg/ml dispersions of 1- COOH-SWNTs, 2- $[Co]H^+$-SWCNTs, 3- $[Co]Na^+$-SWCNTs a) in fresh solutions and b) after 3 months of its preparation.

References

1. G. Tobias, L. Shao, C. G. Salzmann, Y. Huh and M. L. H. Green, *The Journal of Physical Chemistry B*, 2006, 110, 22318-22322.
2. B. Ballesteros, G. Tobias, L. Shao, E. Pellicer, J. Nogués, E. Mendoza and M. L. H. Green, *Small*, 2008, 4, 1501-1506.
3. L. Shao, G. Tobias, C. G. Salzmann, B. Ballesteros, S. Y. Hong, A. Crossley, B. G. Davis and M. L. H. Green, *Chemical Communications*, 2007, DOI: 10.1039/b712614j, 5090-5092.
4. G. Tobias, L. Shao, B. Ballesteros and M. L. H. Green, *Journal of nanoscience and nanotechnology*, 2009, 9, 6072-6077.
5. A. A. Semioshkin, I. B. Sivaev and V. I. Bregadze, *Dalton Transactions*, 2008, DOI: 10.1039/b715363e, 977-992.
6. J. Plesek, S. Hermanek, I. Cisarova, J. Plešek, S. Heřmánek, A. Franken, I. Císařová and C. Nachtigal, *Collection of Czechoslovak Chemical Communications*, 1997, 62, 47-56.
7. F. Teixidor, J. Pedrajas, I. Rojo, C. Viñas, R. Kivekäs, R. Sillanpää, I. Sivaev, V. Bregadze and S. Sjöberg, *Organometallics*, 2003, 22, 3414-3423.
8. A. Semioshkin, E. Nizhnik, I. Godovikov, Z. Starikova and V. Bregadze, *Journal of Organometallic Chemistry*, 2007, 692, 4020-4028.

9. B. Zhao, J. Wang, Z. Li, P. Liu, D. Chen and Y. Zhang, *Materials letters*, 2008, 62, 4380-4382.
10. Y. H. Sung, S. Hong, G. Tobias, B. Ballesteros, F. El Oualid, J. Errey, K. Doores, A. Kirkland, P. Nellist, M. L. H. Green and B. Davis, *Journal of the American Chemical Society*, 2007, 129, 10966-10967.
11. U. J. Kim, C. A. Furtado, X. Liu, G. Chen and P. C. Eklund, *Journal of the American Chemical Society*, 2005, 127, 15437-15445.

We can destroy what we have written, but we cannot unwrite it

A Clockwork orange. Anthony Burgess